Studies on the Design of Frequency Selective Rasorbers/Absorbers for Radar Cross Section Reduction of Radiating Systems

Thesis submitted for the award of the Degree
of

Doctor of Philosophy

by

Mehran Manzoor Zargar
(2018REE0044)

भारतीय प्रौद्योगिकी संस्थान जम्मू
INDIAN INSTITUTE OF TECHNOLOGY JAMMU
विद्याधनं सर्वधन प्रधानम्

Department of Electrical Engineering
Indian Institute of Technology Jammu

November 2022

Declaration

I hereby declare that the matter embodied in this thesis entitled **"Studies on the Design of Frequency Selective Rasorbers/Absorbers for Radar Cross Section Reduction of Radiating Systems"** is the result of investigations carried out by me in the Department of Electrical Engineering, Indian Institute of Technology Jammu, India, under the supervision of **Dr. Kushmanda Saurav** (IIT Jammu), **Dr. Archana Rajput** (NIT Srinagar), and **Prof. Shiban K. Koul** (IIT Delhi) and it has not been submitted elsewhere for the award of any degree or diploma, membership etc. In keeping with the general practice in reporting scientific observations, due acknowledgements have been made whenever the work described is based on the findings of other investigators. Any omission that might have occurred due to oversight or error in judgment is regretted. A complete bibliography of the books and journals referred in this thesis is given at the end of the thesis.

November 2022 | Mehran Manzoor Zargar
Indian Institute of Technology Jammu | (2018REE0044)

Dedicated to My Parents

SYNOPSIS

Name of the student: **Mehran Manzoor Zargar** Enrollment No: **2018REE0044**

Degree for which submitted: **Ph.D.** Department: **Electrical Engineering**

Thesis title: **Studies on the Design of Frequency Selective Rasorbers / Absorbers for Radar Cross Section Reduction of Radiating Systems**

Thesis supervisor: **Dr. Kushmanda Saurav**

Thesis co-supervisors: **Dr. Archana Rajput (National Institute of Technology Srinagar)** , **Prof. Shiban K. Koul (Indian Institute of Technology Delhi)**

Month and year of submission: **November 2022**

Electromagnetic (EM) absorption is of essential requirement in many areas like stealth technology, EM shielding, interference and radar cross section (RCS) reduction, etc. Earlier components like Salisbury Screen, Jaumann absorber, carbon foam based pyramidal absorbers have shown the capability of EM absorption. The FSS (frequency selective surface) based absorbers are thin, light as compared to the conventional absorbers and can be engineered depending upon the requirements.

The general FSS based absorber is typically a periodic array of resonant structures on the dielectric substrate with complete metallic lamination at the back side. The FSS absorbers completely restrains the transmission through it thereby depriving the possibility of communication. In order to overcome the limitation of communication blockade the FSS absorber is combined with the bandpass FSS and the resultant structure is known as frequency selective rasorber (FSR) or AFST (absorptive frequency selective transmission) or simply rasorber. The FSR due to the presence of bandpass FSS is capable of exhibiting transmission in addition to absorption.

The FSR exhibiting a transmission band can be used with a radiating system as a radome for reducing the out-of-band RCS. The FSRs can be classified based on the number and the relative position of transmission/absorption bands. This includes FSR with lower transmission and upper absorption band (T-A), lower absorption and higher transmission band (A-T), absorption band lying within two transmission bands (T-A-T), transmission frequency positioned between the two absorption bands (A-T-A), multiple absorptions and multiple transmission bands in an alternate form (A-T-A-T) and so on.

Table 1: Summary of Proposed Polarization-Insensitive Rasorber/Absorber Designs

Absorption	Rasorber Type	Achieved Parameters
Narrowband	T-A-T	Single Layer; Absorption: 6.2 GHz; B.W= 110 MHz (1.75 %) Transmission 1: 3.1 GHz; I.L = 0.6 dB Transmission 2: 8.4 GHz; I.L = 1.2 dB
	A-T-T-A (2T2A)/A-T-A-T-A (2T3A)	Single Layer; Flexible; Conformal Response Tested up to 180^o curvature angle. **2T2A:** A- 6.4 and 14.7 GHz; T- 9.6 and 13.4 GHz **2T3A:** A- 6.6,11.1 and 14.7 GHz: T- 9.6 and 13.4 GHz
Broadband	A-T	Absorption: 3.1−8.7 GHz (94.91%) Transmission: 11.4 GHz; I.L = 0.7 dB
	T-A-T	Absorption: 3.6−7.4 GHz (69.09%) Transmission 1: 2.1 GHz; I.L =1.4 dB Transmission 2: 8.8 GHz; I.L = 1.5 dB
	A-T-A	Absorption 1: 3.4−7.5 GHz (75.22%) 80% Absorption 2: 9.2−10.8 GHz; 16% Transmission: 8.4 GHz; I.L = 0.7 dB **FSR + Patch Antenna:** Average Monostatic RCS Reduction = 11.92 dB (Lower Band) and 5.04 dB (Upper Band) Average Bistatic RCS Reduction = 77% (Lower Band) and 60% (Upper Band)
	A-T-A-T	Absorption 1: 5.2−10.1 GHz (64.05%) Absorption 2: 10.7−14.4 GHz; (29.48%) Transmission 1: 10.4 GHz; I.L = 1.9 dB Transmission 2: 15.2 GHz; I.L = 0.9 dB
	AFSR	Absorption 1: 4.2−7.0 GHz (50%) Absorption 2: 9.2−11.5 GHz (22.2%) Reflection: 8.2 GHz Attenuation = 1.5 dB **AFSR + Crossed Dipole:** Average Monostatic RCS Reduction = 12 dB Average Bistatic RCS Reduction = 80%

A: Absorption; T: Transmission; B.W: Bandwidth; I.L: Insertion Loss

The low out-of-band RCS system can also be designed with the use of band-notched absorber also called as AFSR (absorptive frequency selective reflection) structures having a reflection band within a broad absorption band.

The motivation of this thesis is to pursue systematic studies on the rasorber/absorber designs for addressing the various limitations and further performance improvement of the existing designs. Polarization-Insensitive rasorber/absorber designs studied in the thesis are outlined below:

1. Narrowband flat/flexible FSR on a single layer substrate.

2. Design of A-T/T-A-T rasorbers with improved performances.

3. Highly selective A-T-A/ A-T-A-T FSRs

4. Low RCS radiation system co-designed with A-T-A FSR.

5. Low RCS dual-polarized radiation system co-designed with AFSR Structure.

The outcome of the research work presented in the thesis is summarized in Table 1.

Single Layer Dual-Band Transmissive Rasorber

Initially, in this thesis, a frequency selective surface based rasorber has been proposed by combining the designs of split-ring absorber and dual bandpass FSS, which are printed on the front and backside of 0.8-mm thick FR-4 substrate, respectively as depicted in Figure 1. The proposed FSS-based rasorber is a thin single layer structure and also exhibits the polarisation-insensitive behaviour due to its four-fold symmetry. The response of the proposed rasorber is given in Figure 1(d). The split-ring structure at the front contributes to the resonant absorption at 6.2 GHz, while the bandpass FSS structure at the backside provides two transmission windows at 3.1 and 8.4 GHz, respectively. The parameters of the design are optimized such that at the absorption frequency, the bandpass FSS acts as a complete metallic ground. The operating principle of the proposed rasorber is analyzed using an equivalent circuit model. The effects of design parameters on the performance of the rasorber are studied, and accordingly, optimum ranges of lower and upper transmission bands with respect to the absorption band are determined. A 21×21 array of the proposed rasorber unit cell is fabricated, and the results are experimentally verified.

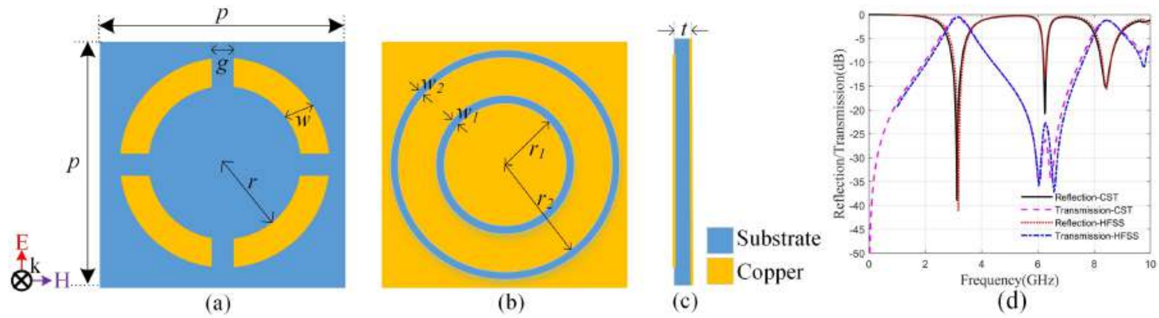

Figure 1: Unit cell schematic representation of the proposed FSS based rasorber. (a) Front, (b) back, and (c) side views. (d) Reflection and transmission response of the proposed rasorber. $p = 20$, $r = 6.6$, $w = 3.2$, $g = 1$, $r_1 = 4$, $r_2 = 8.5$, $w_1 = 0.8$, $w_2 = 0.8$ and $t = 0.8$ (All dimensions are in mm).

Single-Layered Flexible Multi-Band Rasorbers for Conformal Applications

Next, the thesis discusses flexible frequency selective surface (FSS) based rasorbers exhibiting dual/triple absorption bands along with dual-band transmission. The proposed rasorbers are designed by combining the individual designs of dual-/triple-band resonant absorber and dual bandpass FSS on the two sides of a flexible substrate. The unit schematic for the dual/triple absorption rasorbers are provided in Figure 2. The front schematic for the dual and triple absorption rasorbers are represented in Figure 2(a) and 2(c), respectively while the back side design given in Figure 2(b) is same for both the case. The perspective views of dual and triple absorption rasorber are shown in Figure 2(d) and 2(e), respectively while Figure 2(f) depicts the fabricated flexible prototype. At the absorption frequencies, the bandpass FSS acts as reflective metallic ground. The transmission and reflection coefficients for the dual and triple absorption rasorbers are depicted in Figure 2(g) and 2(h), respectively. The two transmission bands in both the rasorbers are located at 9.6 and 13.4 GHz. The absorption bands for the dual rasorber are located at 6.4 and 14.7 GHz, while for the triple absorption rasorber, the third band lies at 11.1 GHz. The proposed FSS based rasorbers are flexible, single-layer structures having a thickness of $0.005\lambda_0$ at the lowest absorption frequency and can serve as suitable candidates for the much practical conformal applications. The working of the proposed rasorbers is analyzed using an equivalent circuit model. Further, an optimum range at each absorption frequency is determined by studying the parametric effects on the proposed design. Prototypes consisting of 17×25 unit cells are fabricated and experimental validation is achieved. The performance of the rasorbers is also studied by bending their

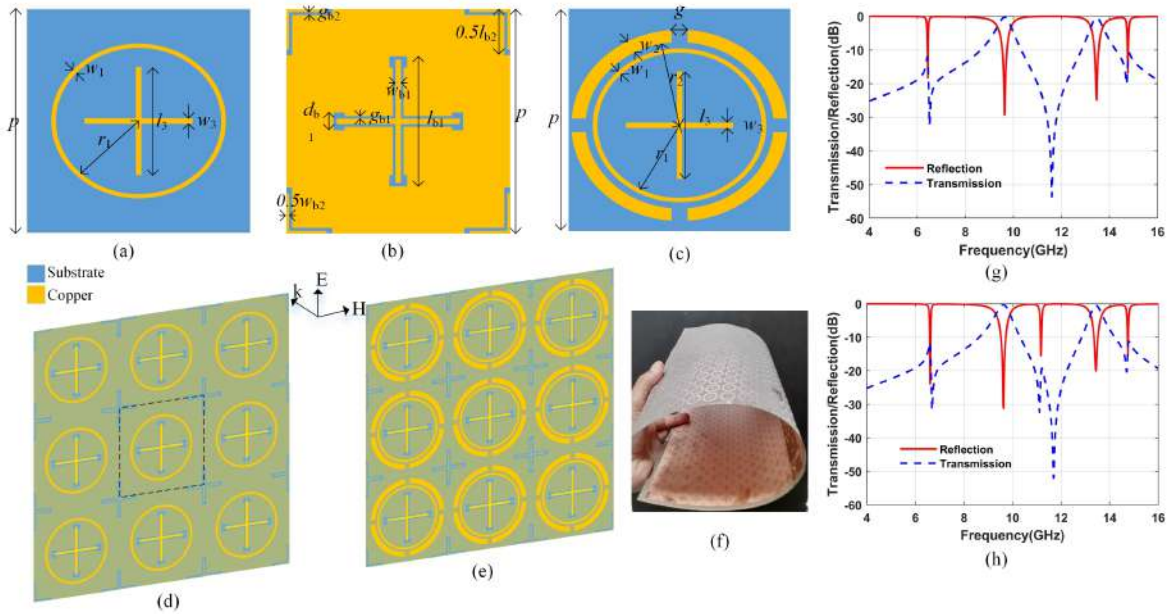

Figure 2: Unit cell schematic of the proposed rasorbers. (a) Front view of 2T2A rasorber. (b) Back view of both 2T2A and 2T3A rasorber. (c) Front view of 2T3A rasorber. (d) Perspective view of 2T2A rasorber. (e) Perspective view of 2T3A rasorber. (f) Fabricated flexible prototype. (g) Reflection and transmission response of the proposed 2T2A rasorber. (h) Reflection and transmission response of the proposed 2T3A rasorber. p = 15, r_1 = 5.0, w_1 = 0.5, l_3 = 7.0, w_3 = 0.4, r_2 = 5.9, w_2 = 0.9, g = 0.8, r_1 = 5.0, w_1 = 0.5, l_3 = 7.0, w_3 = 0.4 (All dimensions are in mm).

fabricated prototypes with 120^o, 150^o, and 180^o degrees of curvatures.

A-T FSR

A frequency selective rasorber is proposed in this thesis where a transmission band at a higher frequency is achieved besides the lower broadband absorption. The FSR is designed by combining the individual designs of broadband absorber and bandpass FSS. The schematic and response of the proposed FSR is shown in Figure 3. The broadband absorption is achieved by placing the resistive and ground layer at a distance of around $\lambda/4$ at center frequency. The unit cell of bandpass FSS is designed by etching a double cross slot (Figure 3(a)). The performance parameters at the transmission band are improved by a modified double cross slot, wherein a quarter of the slot is replicated on each corner of the unit cell. The bandpass FSS replaces the ground plane of broadband absorber, in the design of proposed FSR. The proposed FSR is a polarization-independent structure exhibiting a broadband absorption from 3.1−8.7 GHz (94.91%) along with a transmission band at 11.4 GHz (Figure 3(b)). The working principle of proposed FSR is illustrated by an equivalent circuit model. A range for higher transmission frequency is

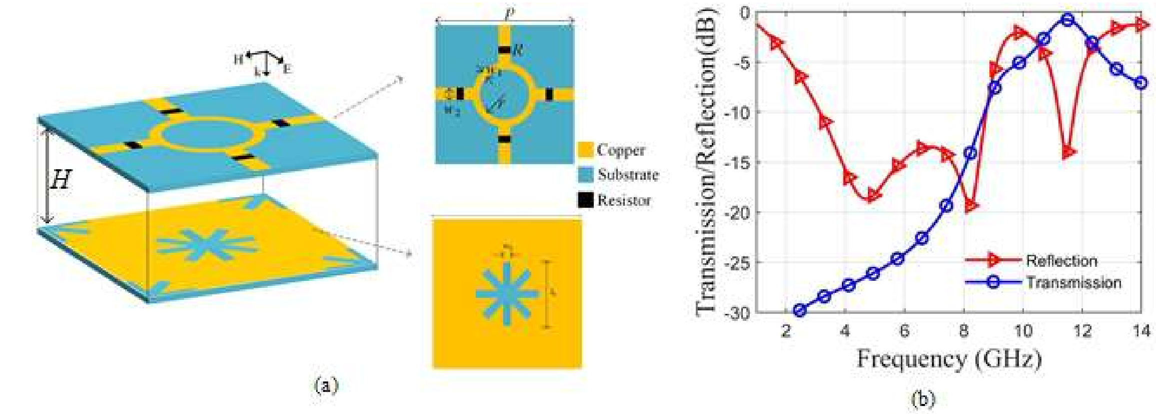

Figure 3: Proposed A-T FSR. (a) Unit cell schematic, and (b) reflection and transmission response. p = 20, r = 5, w_1 = 0.5, w_2 = 1, t = 0.8, w_b = 1.2 , l_b = 9, H = 12. (All dimensions are in mm).

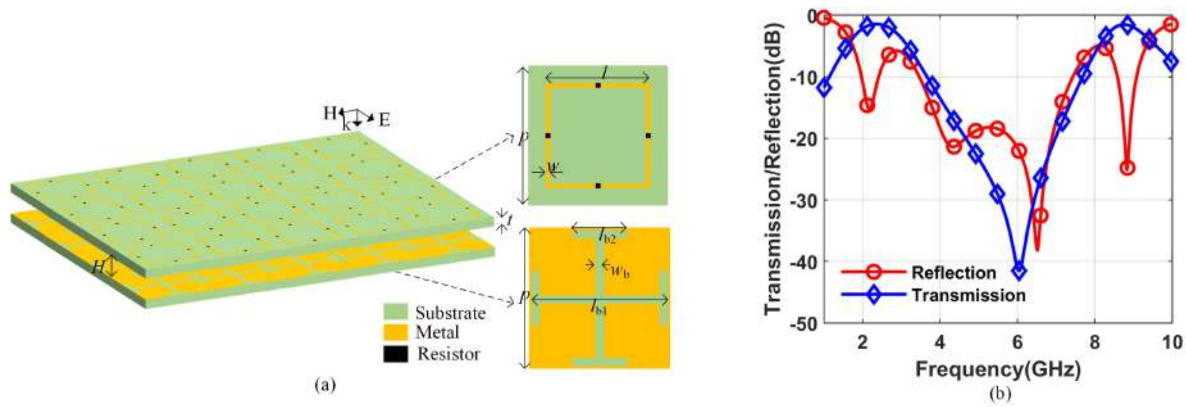

Figure 4: Proposed T-A-T FSR. (a) Unit cell schematic, and (b) reflection and transmission response. p = 25, l_{b1} = 24, l_{b2} = 12, w_b = 1.3, l = 15, w = 0.5, t = 0.8, H = 12 (All dimensions are in mm)

determined for the proposed FSR, by studying the effects of bandpass FSS parameters on the transmission performance. A prototype of the proposed FSR is fabricated, and the results are experimentally verified.

T-A-T FSR

Next in this thesis, a compact and polarization-insensitive FSR is proposed with dual transmission bands located at the two sides of a broad absorption band. The proposed FSR as shown in Figure 4(a) is a two-layer structure designed by combining the Jerusalem cross based dual bandpass frequency selective surface (FSS) with a broadband resistive square loop absorber, such that both the absorption and transmission characteristics are retained. The proposed FSR has a thickness and size of $0.09\lambda_L$ and $0.026\lambda_L^2$, respectively at the lowest frequency of 10 dB reflection (1.97 GHz). As observed from Figure 4(b), the dual transmission bands are obtained at 2.1 and 8.8 GHz with an in-between absorption

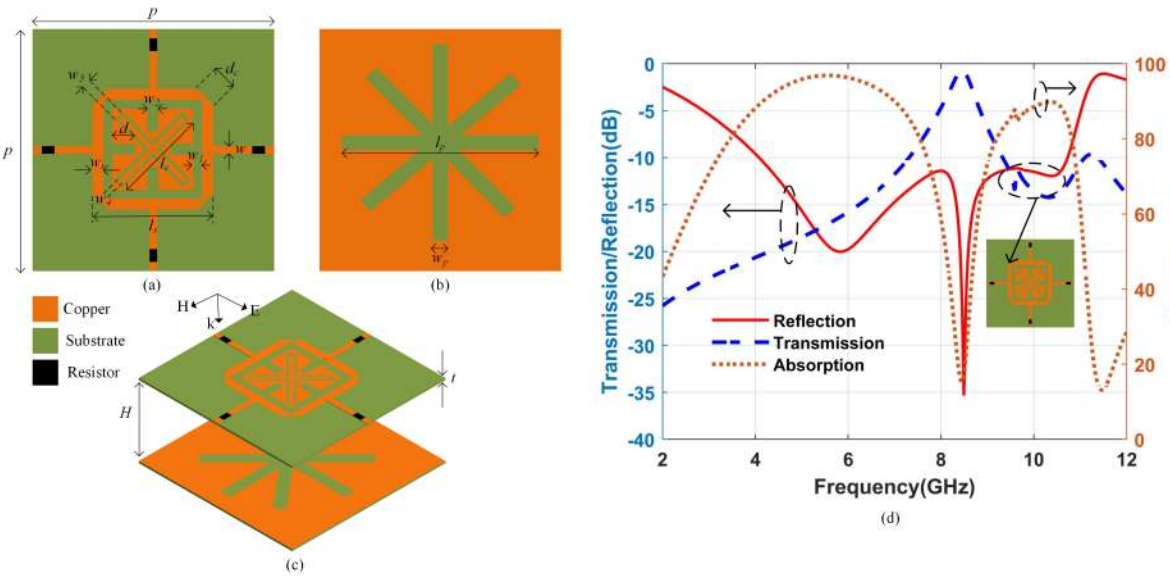

Figure 5: Proposed A-T-A FSR. (a) Top, (b) bottom, and (c) perspective views. (d) Reflection and transmission response. p = 15, w = 0.5, w_s = 0.8, l_s = 7.1, w_1 = 0.3, w_2 = 0.3, l_c = 5.8, w_3 = 0.6, w_4 = 0.2, d = 1.6 (All dimensions are in mm).

band ranging from 3.6 to 7.4 GHz (69.09%). The working principle of the proposed FSR is analyzed using an equivalent circuit model. Furthermore, a range of lower and upper transmission bands with respect to the absorption band is determined by carrying out the parametric studies on the geometrical parameters of the bandpass FSS. A prototype of the proposed FSR consisting of an array of 10×10 unit cells is fabricated and the results are experimentally verified.

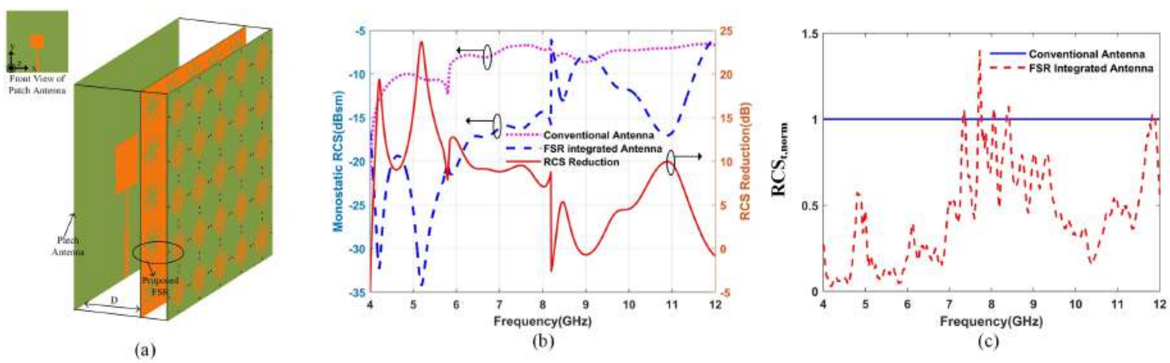

Figure 6: (a) Schematic of the FSR integrated patch antenna. (b) Monostatic RCS, and (c) normalized total bistatic RCS of the FSR integrated antenna with reference to the conventional antenna. (D = 18 mm)

A-T-A FSR for Low RCS Radiating System

Further, in this thesis, a novel design of compact frequency-selective rasorber exhibiting absorption–transmission–absorption characteristics and having high passband selectivity has been proposed. A square-loop resonator with mounted lossy elements serves as the elemental broadband absorber from 4 to 12 GHz. The unit schematic and response of the proposed FSR are shown in Figure 5. The transmission frequency at 8.4 GHz is realized by printing a Minkowski fractal-shaped resonator with a high-Q factor on the resistive layer (Figure 5(a)), which provides a transmission pole at the frequency corresponding to the passband of a double-cross-slot-shaped bandpass layer (Figure 5(b)). The lower and the upper absorption bands of the proposed FSR are from 3.4 to 7.5 GHz and 9.2 to 10.8 GHz, respectively while the center transmission notch is at 8.4 GHz. The functioning of the proposed frequency-selective rasorbers (FSR) is explained by a corresponding equivalent circuit model. The proposed FSR exhibits higher selectivity at the passband, thus making it a suitable candidate for shielding the narrowband radiating system. Measurements performed on the fabricated prototype of a 17×17 unit cell array provides experimental validation. Further, as represented by schematic in Figure 6(a), a low radar cross-section antenna is realized by integrating a patch antenna with the proposed FSR, which achieves an average out-of-band monostatic radar cross-section (RCS) reduction of 11.92 and 5.04 dB in the lower (4–7.5 GHz) and upper (9.2–10.8 GHz) absorption bands, respectively (Figure 6(b)), while maintaining the other antenna parameters. Furthermore, as depicted from the plot in Figure 6(c), the bistatic total RCS reduction of 77% and 60% are achieved in the lower and upper frequency bands, respectively.

A-T-A-T FSR

Furthermore, as an extension to the previously proposed FSR, a novel design strategy for realizing a polarization-independent and compact absorption-transmission-absorption-transmission (A-T-A-T) type FSR is presented in thesis. A resonator with cross-loop slot in the Minkowski fractal (MF) design is studied and incorporated within the top resistive layer of the square loop broadband absorber (Figure 7(a)). The proposed MF resonator incorporated within the resistive layer is capable of realizing a dual transmission pole inside the broad absorption band. A cross slot based bandpass layer depicted in Figure

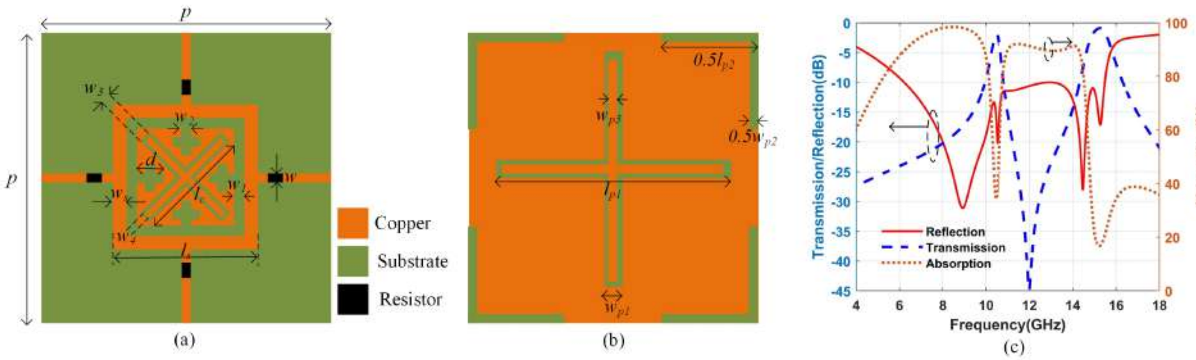

Figure 7: Proposed A-T-A-T FSR. (a) Top, and (b) bottom views. (d) Reflection and transmission response. $p = 10$, $w = 0.5$, $w_s = 0.3$, $l_s = 4.6$, $w_1 = 0.2$, $w_2 = 0.2$, $l_c = 4.3$, $w_3 = 0.5$, $w_4 = 0.2$, $d = 1.2$, $l_{p1} = 6.1$, $l_{p2} = 6.2$, $w_{p1} = 0.8$, $w_{p2} = 0.4$, $w_{p3} = 0.4$ (All dimensions are in mm).

7(b) is replaced with the ground layer of absorber as such the desired transmission bands are achieved, while acting as ground plane outside the passbands. The response of the proposed A-T-A-T FSR is shown in Figure 7(c). The proposed FSR design realizes two transmission windows at 10.4 and 15.2 GHz with the adjacent absorption bands from 5.2 to 10.1 GHz and 10.7 to 14.4 GHz. Measurements carried on the fabricated 15 x 15 array prototype experimentally validates the design. The proposed rasorber is a suitable contender for shielding and radar cross section reduction of the dual-band radiating systems.

Low RCS Crossed Dipole antenna Co-Designed with AFSR Structure

This thesis also proposes a novel strategy for realizing a reduction in radar cross-section of dual-polarized crossed dipole antenna. At first, a compact and polarization-insensitive AFSR structure is proposed by incorporating a bandstop ring resonator within the circular-cross based broadband absorber as shown by the unit schematic provided in Figure 8. The bandstop ring resonator is designed on the backside of the resistive layer due to which a reflection window is realized at a frequency of 8.2 GHz between the two broadband absorptions (4.2−7.0 GHz and 9.2−11.5 GHz) (Figure 8(d)). A dual-polarized crossed dipole antenna is designed with operating frequency lying within the reflecting notch of the AFSR structure. As shown in Figure 9, a 6 x 6 AFSR structure array is truncated at the center where from which the crossed dipole is connected through a feed substrate. The

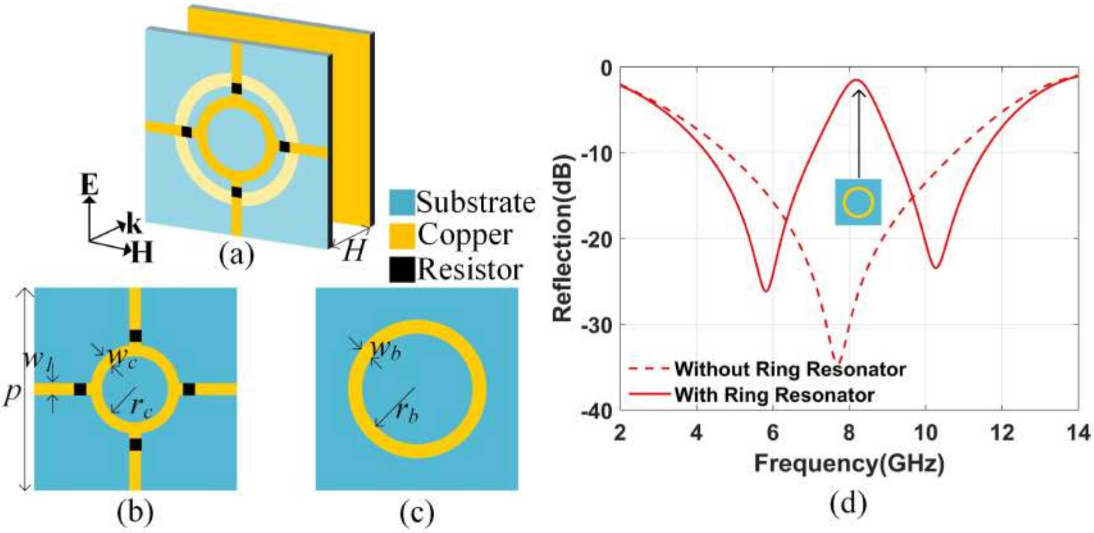

Figure 8: Proposed AFSR structure. (a) Perspective, (a) front, and (b) back views. (d) Reflection and transmission response. $p = 15$, $r_c = 2.2$, $w_c = 1$, $r_b = 3.2$,$w_1 = 0.8$, $w_b = 0.6$, and $H = 8$ (All dimensions are in mm).

AFSR structure enacts as a modified ground plane to the crossed dipole antenna. The monostatic and bistatic RCS for the AFSR integrated antenna in comparison with the conventional reflector backed antenna for the TE incident waves are provided in Figures 9(c) and 9(d), respectively. The proposed AFSR integrated antenna achieves an average mono-static RCS reduction of 12.51 dB and 12.62 dB for the TE and TM incident waves, respectively. Further, the AFSR based antenna is also measured for the bi-static RCS, wherefrom the average total RCS reduction of 80% for TE and TM incidence is attained in the frequency band of 4.2 to 11.5 GHz.

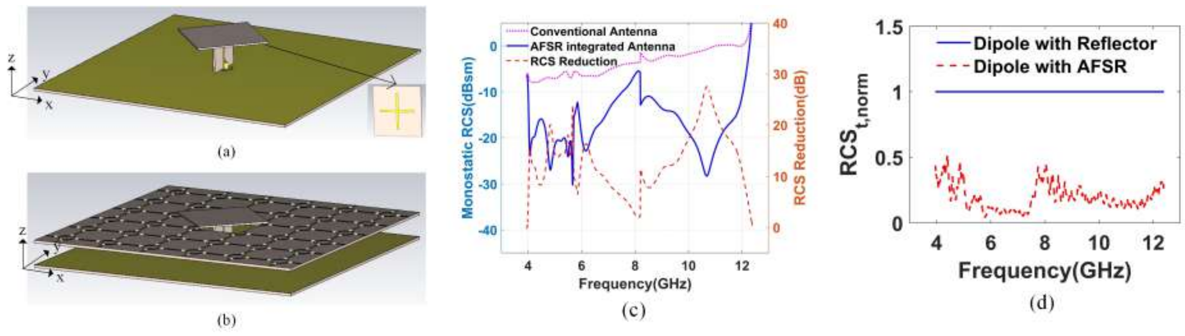

Figure 9: (a) Schematic representation of the crossed dipole antenna with (a) reflector, and (b) AFSR structure. (c) Monostatic RCS, and (d) normalized total bistatic RCS of the AFSR integrated antenna with reference to the conventional antenna.

Acknowledgements

All praise is for Allah, The Most Compassionate, The Most Merciful. This is by the Grace of my Lord.

At the outset, I would like to express my sincere gratitude and respect to my thesis supervisor *Dr. Kushmanda Saurav*, Department of Electrical Engineering, Indian Institute of Technology (IIT) Jammu whose guidance, and constant efforts have been invaluable throughout this study and have made this an inspiring experience for me. His persistent and tireless dedication to the work has made it possible to complete the thesis work. His regular and dedicated attention to my work showed me the path and also enhanced my experience in the research field. I am highly thankful that I had the opportunity of working under his guidance.

I am highly thankful to my co-supervisor *Dr. Archana Rajput*, for constantly guiding and supporting me in the thesis work. All the discussions and her suggestions related to the research work had made a significant impact in improving the quality and technical aspects of the work.

I also want to express my high regards to my co-supervisor *Prof. Shiban K. Koul*, Centre for Applied Research in Electronics, Indian Institute of Technology Delhi, for being highly supportive during all times of the thesis work. During my course work at IIT Delhi, his quality teaching made a high impact on my understanding of the subject and laid a strong foundation on the basics of RF and Microwave. His guidance along with constant motivation throughout the thesis work helped in overcoming all the technical hindrances which I faced at various levels of my work.

I am highly grateful to *Dr. Zamir Ahmad Wani*, currently Post Doc Fellow at IIT Jammu (Formerly Research Scholar at IIT Delhi) for being a senior friend cum technical mentor during the initial and later stages of my research work. The interactions and discussions I had with him have directly helped me in overcoming the various barriers faced during the research period. He was always there in sharing his expertise, knowledge, and skills which eased all the technical difficulties.

I would like to thank the Department of Electrical Engineering IIT Jammu for providing the lab facilities and financial support in the completion of my thesis work. A special word of mention for my SRC faculties, *Dr. Badri Narayan Subudhi* and *Dr. Rahul R. Salunke* from whom I received positive support and suggestions all the time.

I thank my senior colleague *Dr. Mohammad Ayoub Sofi* with whom I spent a good time during my Ph.D. course and whose guidance was beneficial to me both in personal and professional areas. I am thankful to my junior colleague *Mr. Javid Ahmad Ganie* who is a close friend and with whom I shared all the moments whether high or low, personal or professional. I thank my fellow mates *Mr. Ankit Kumar Pandey*, *Mr. Gazali Bashir* and *Ms. Amina Girdhar* for all the good fruitful discussions and fun we together had in time between working hours. I also thank other fellow scholars *Mr. Burhan ud din Wafai Mr. Abdul Haseeb Wani*, *Mr. Suhaib ul Riyaz*, *Dr. Mohit Pal*, *Mr. Shashi Bushan Kotwal Mr. Ajaz Ahmad Mir*, *Mr. Hardeep Kumar Maurya*, *Mr. Harshvardhan Singh*, *Mr. Satyendra Kumar Singh*, *Mr. Tawseef Ahmad Wani*, *Ms. Insha Wani*, *Ms. Insha Amin*, *Ms. Deebha Mumtaz*, *Ms. Sadhbhawna*, *Ms. Ambreen Bashir*, *Ms. Sapna Thapar*, *Ms. Aditi Gupta*, *Dr. Manoj Panda*, *Dr. Gaurav Sharma*, *Ms. Sonam Gupta*, *Mr. Murtiza Ali* and all others for the good moments we shared.

I had some good friends *Mr. Rahul Bharadwaj*, *Ms. Kirpa Garg*, *Mr. Mukul Dwivedi*, *Ms. Tanu Gupta*, *Ms. Shreya Mudgil*, *Ms. Aditi Magotra*, *Mr. Bijendar Dharan*, *Ms. Sheriya Sareen*, *Ms. Saima ut un Nisa*, *Mr. Ankit Upadhyay*, *Mr. Rajaram Kumar Gupta*, *Mr. Nitesh Kumar*, *Mr. Hridesh Kumar*, *Mr. Pummy Sharma* and others in the Scholars Lab, with all I had serious as well as light-hearted interactions which created a positive working ambiance.

I also want to mention my long time fast friends *Mr. Mohd Aarish Shaheen*, *Mr. Aarif Ashraf Wani* from my school days and *Dr. Furqan Zahoor*, *Mr. Ehtisham Bashir Mr. Itmenon Towfeeq*, *Mr. Tajamul Bashir*, *Mr. Talib Hussian Beigh*, *Mr. Afzan Hussain Hamdani*, *Mr. Rabie Malik*, and *Mr. Mudasir Ahmad Bakshi* from my B.Tech days.

Last but not the least, I want to express my deep regard to my family members which includes my Grandmom *Amijan*, my parents *Mr. Manzoor Ahmed Zargar* and *Mrs. Abida* for their unconditional love, utmost care, endless sacrifice, ceaseless support wholehearted blessing throughout.

Contents

List of Figures

List of Tables

List of Symbols

Symbol	Description
E	Electric field
H	Magnetic field
K	Electromagnetic wave vector
ε_r	Real part of permittivity of the dielectric
$tan\delta$	Loss tangent of the dielectric
A	Absorptivity
β	Propagation constant
Q	Quality factor
σ	Conductivity
λ	Guided wavelength
λ_0	Free space wavelength

List of Abbreviations

Abbreviation	Description
EM	Electromagnetic
EMI	Electromagnetic Interference
FSS	Frequency Selective Surface
FSR	Frequency Selective Rasorber
AFST	Absorptive Frequency Selective Transmission
AFSR	Absorptive Frequency Selective Reflection
RCS	Radar Cross-Section
2T2A	Dual Transmission Dual Absorption
2T3A	Dual Transmission Triple Absorption
A-T	Absorption-Transmission
T-A-T	Transmission-Absorption-Transmission
A-T-T-A	Absorption-Transmission-Transmission-Absorption
A-T-A-T-A	Absorption-Transmission-Absorption-Transmission-Absorption
A-T-A	Absorption-Transmission-Absorption
A-T-A-T	Absorption-Transmission-Absorption-Transmission
DCS	Double Cross Slot
MDCS	Modified Double Cross Slot
MF	Minkowski Fractal
BW	Bandwidth
PCR	Polarization Conversion Ratio
RFID	Radio Frequency Identification
SRR	Split Ring Resonator

Chapter 1

Introduction

Electromagnetic (EM) absorbers are primarily defined as those entities that are capable of absorbing the incident electromagnetic waves. The EM waves get trapped inside the absorbers leading to zero reflection and zero transmission of the incident EM wave. Traditionally, many components like Salisbury Screen, Jaumann absorber, carbon foam based pyramidal absorbers have shown the capability of EM absorption. The absorption phenomenon of the EM wave has significant applications in many areas like stealth technology, EM shielding, interference reduction, etc. However, the bulky size of conventional absorbers severely limits their usage in many applications. The breakthrough gained in the studies on frequency selective surface (FSS) has made a tremendous role in the development of microwave absorbers [1]. The FSS based absorbers have the unique features of being thin, lightweight and can be well engineered depending upon the desired requirements. Due to these features, the FSS based absorbers are found to be well suitable for many applications in stealth technology, shielding and others [2]. In the last decade, studies have been carried out in the field of FSS based absorbers for characterizing, analyzing, and enhancing the performance parameters associated with them.

The FSS based absorbers suffer from communication blockade limitations as they are not capable of allowing selective transmission through them. The limitation of absorbers can be addressed by integrating them with the FSS based spatial bandpass filter. The combination of absorbers and bandpass FSS has been given the name of frequency selective rasorber (FSR) or simply rasorber. This name has been derived from the two words 'radome' and 'absorber' which suggests the radome as well as the absorber characteristics in a single entity. Since, the advent of FSR, studies on its designs have gained tremendous popularity among researchers. Plenty of extensive works carried on the FSR design have been reported in the recent literature. The objective of this thesis is to focus on the designs of the FSR depending upon various requirements and improved performance as compared to the existing literature. Moreover, studies on the integration of the proposed FSR with the antenna system has also been carried out in this thesis.

This chapter introduces the work presented in the thesis in a systematic manner. In the initial part, a brief overview of the FSS has been presented which is followed by the theory of FSS based absorbers along with the reported literature. Next, this chapter introduces FSRs followed by a detailed literature survey. Further, the motivation behind the thesis work along with the outcome is comprehensively laid down. The last part of this chapter provides the organization of the thesis.

1.1 Frequency Selective Surface

Frequency selective surface (FSS) is a periodic structure which contains an array of metallic patterns on a dielectric material. These FSS structures when excited with the incident EM wave exhibit the property of selective reflection/transmission depending on the dimensions, geometry as well as the orientation of incident wave [3]. The FSS structure has found huge applications in various areas like design of radomes [4]−[6], dichroic sub-reflectors [7], radio frequency identification (RFID) [8], lens [9, 10], absorbers [11], cloaks [12, 13], sensors [14]−[16], polarizers [17]−[23], reflect-array antennas [24], and EM shielding [25, 26]. Recently many other applications of FSS have been explored thereby increasing its importance [27]−[42]. The behaviour of FSS is largely dependent on shape and size of its one period, known as unit cell. The principle of operation in FSS is generally illustrated by the resonance phenomenon even though shapes may vary in different structures. The incidence of EM wave on the FSS causes the elements of the structure to resonate at a particular frequency which is dependent on the geometry/material properties of the structure and the incident wave orientation [43].

The characteristics of FSS design is illustrated using two structures shown in Figure 1.1(a) and Figure 1.1(b) which consists of an array of patches and slots, respectively. It can be observed from Figure 1.1(c) that for the array of patches the bandstop response is obtained in which the transmission coefficient (S_{21}) takes a dip at the associated resonance

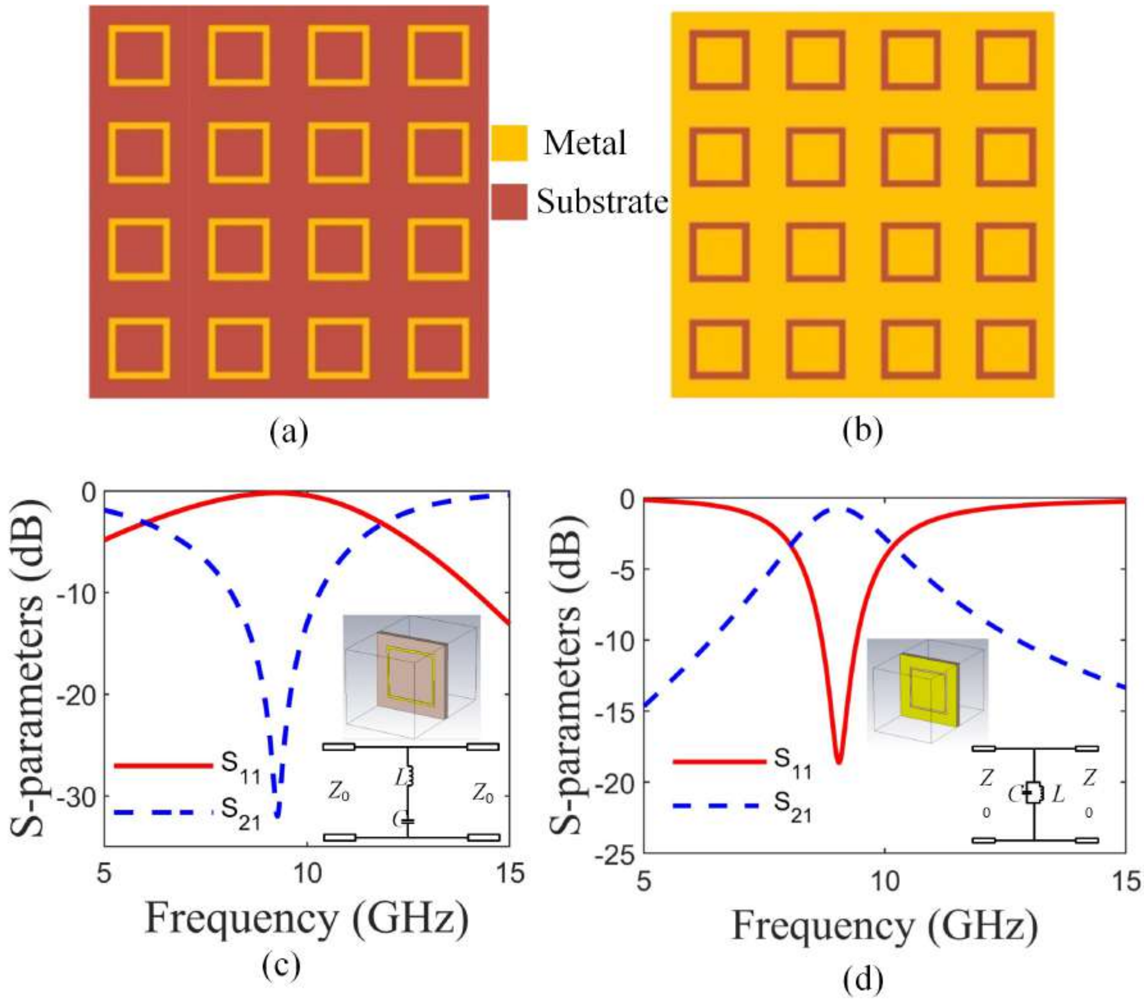

Figure 1.1: FSS Structures: (a) Array of patches, and (b) array of slots. S-parameter responses: (c) Array of patches, and (d) array of slots.

frequency while the reflection coefficient (S_{11}) at that point is maximum. The induced inductive and capacitive effects are generated due to incident EM wave. The response of the metal array (Figure 1.1(a)) corresponds to the series combination of an inductor and a capacitor. On the other hand, complimentary design of slots in Figure 1.1(b) realizes a bandpass response. As illustrated in Figure 1.1(d), at the associated resonance frequency, the reflection coefficient (S_{11}) is minimized while the transmission coefficient (S_{21}) is high, thus causing the bandpass effect. The response for the array of slots can be related with the response across the parallel combination of an inductor and a capacitor.

1.2 FSS based Absorbers

One of the key application of FSS lies in its significant feature of being used as a EM absorber. The FSS based absorbers consist of various shapes of metallic pattern printed on the dielectric substrate, the other side of which is generally laminated with copper ground. The copper ground on the other side ensures zero transmission of EM wave through the structure. It can be deduced that since the transmission through the structure is zero, hence for absorption to increase, the reflection from the surface should decrease. So the basic objective in FSS based absorbers is to control the geometry and material properties in such a way that the reflection is minimized at desired frequencies. The absorptivity of the structure can be given from the following equation:

$$A(\omega) = 1 - |S_{11}|^2 - |S_{21}|^2. \tag{1.1}$$

Since transmission is nullified so $S_{21} = 0$

Therefore,

$$A(\omega) = 1 - |S_{11}|^2. \tag{1.2}$$

Where $|S_{11}|^2$, $|S_{21}|^2$, and $A(\omega)$ are the reflectance, transmittance and absorptivity, respectively at a particular frequency. Thus, at the particular frequency the absorption of structure can be maximized by minimizing the reflectance from the surface.

The reflection coefficient at the surface is given as:

$$S_{11}(\omega) = \frac{Z_{in}(\omega) - Z_0}{Z_{in}(\omega) + Z_0}. \tag{1.3}$$

Where Z_{in} is the input impedance of the structure and Z_0 is the free space impedance. From the above equation (1.3), it is implied that for reflections to be zero, the input impedance of the structure must be perfectly matched to free space impedance. Therefore in FSS absorber design, the input impedance of the structure can be controlled by varying the geometrical parameters to enable a proper match with the free space impedance at the frequency of interest.

1.3 Literature Survey on FSS based Absorbers

Based upon successive studies reported in the literature, FSS based absorbers can be categorized into three different types: narrow-band FSS absorbers [44]−[58], bandwidth-enhanced absorbers [59]−[61], and broadband absorbers [62]−[65]. The primary FSS absorber exhibits a narrowband absorption phenomenon at the resonance frequency. Bandwidth-enhanced absorbers have been designed using multi-resonating structures and exhibit an enhancement in absorption bandwidth. Broadband FSS absorbers are designed using circuit analog absorber (CAA) concept using lumped ohmic components and multi-layer geometry. In this section, brief literature works corresponding to each of them are presented sequentially.

1.3.1 Narrow-band FSS Absorbers

The split ring resonator (SRR) based structure shown in Figure 1.2, was the first FSS based absorber reported in 2006 [44]. This structure consists of an array of SRRs attached to a resistive sheet. The resistor sheet has a thickness of 1 mm and its impedance is 377 Ω. The incident magnetic field is kept perpendicular to plane of the SRR for exhibiting a magnetic resonance. This structure gives rise to narrow-band absorption at around 2 GHz as shown in Figure 1.2(d). This absorber however has limitations of being non-planar and having large thickness.

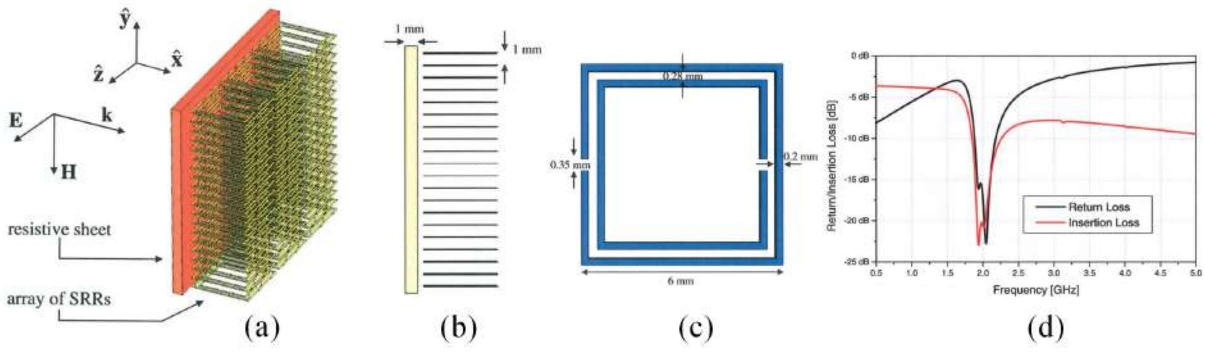

Figure 1.2: SRR based absorber. (a) Perspective, (b) side, and (c) top view of the unit cell. (d) Simulated response [44].

The perfect narrow-band absorber structure had been reported in 2008 [45]. The reported structure is shown in Figure 1.3 which consists of a metallic ELC resonator and thin strip printed on the front and back side of a dielectric substrate, respectively

(Fig. 1.3(a) and 1.3(b)). The simulated response is depicted in Figure 1.3(d). The absorber structure in this case is thin and planar in comparison with [44]. The electric resonance causes the structure to resonate. The parameters of the structure and the material properties are determined such that at a particular frequency, reflection and transmission is minimized so that the absorption dominates. For the given structure single-band absorption takes place at 11.65 GHz producing an absorption peak of 96%.

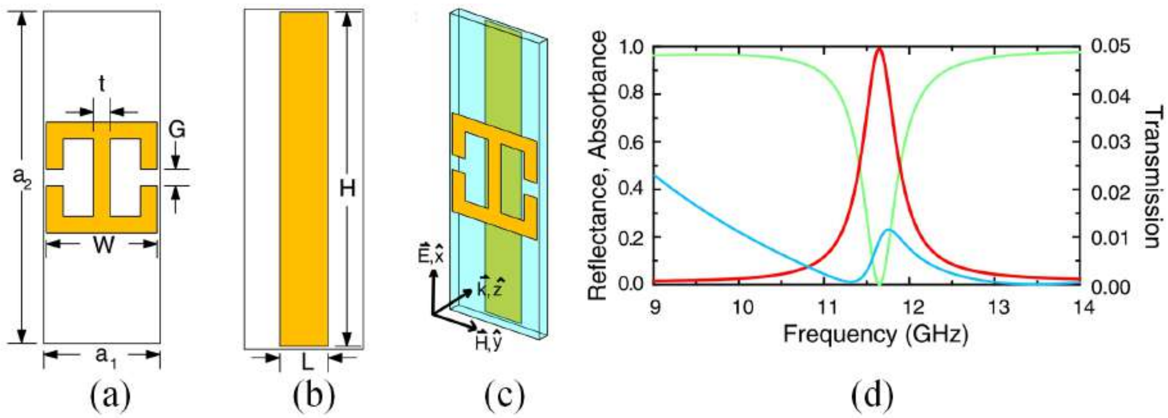

Figure 1.3: Perfect narrow-band absorber. (a) Top, (b) back, and (c) perspective view. (d) Simulated response [45]

Another electric-field-coupled-LC (ELC) resonator based FSS absorber has been reported in which the back side has been completely copper laminated [46]. The basic ELC structure (Figure 1.4(a)) exhibits single narrow-band absorption at 9.92 GHz (Figure 1.4(b)). The ELC resonator further arranged in an array with the scaling factor k1 realizes the multi-band absorption. A 2 x 2 array of ELC resonator (Figure 1.4(c)) exhibits a dual-band absorption response at 9.18 and 12.36 GHz (Figure 1.4(d)), while the 3 x 3 array of ELC resonator (Figure 1.4(e)) provides a triple-band absorption response at 7.44, 10.37 and 12.27 GHz (Figure 1.4(f)).

A conformal and polarization-insensitive triple-band absorber using modified triple circular ring resonator is shown is Figure 1.5 [47]. The modified triple circular ring resonator printed on the thin GML 1000 substrate of 0.502 mm thickness and with a full metallic layer at the backside exhibits a triple narrow absorption bands at 4.19, 6.64, and 9.95 GHz.

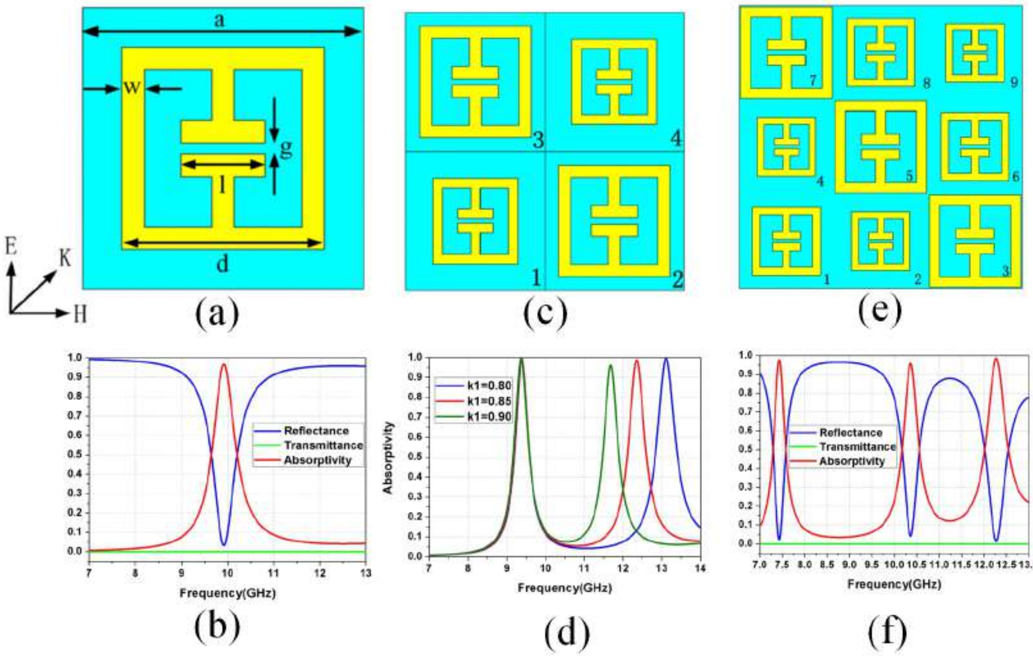

Figure 1.4: ELC resonator based absorber. Single-band: (a) Unit cell front view, and (b) simulated response. Dual-band: (c) Unit cell front view, and (d) simulated responsriple-band: (e) Unit cell front view, and (f) simulated response [46].

1.3.2 Bandwidth-Enhanced FSS Absorber

Various techniques have been implemented to widen the bandwidth of the FSS based absorber [59]−[61]. In case of bandwidth-enhanced techniques one of the conventional method is to design two resonating structures on the single unit cell. The design parameters are chosen in such a way that two absorption frequencies are brought closer to each other thus obtaining a bandwidth enhanced absorber. Figure 1.6 depicts one of such reported bandwidth-enhanced absorber and its response [59]. In this reported structure, the unit cell consists of two ELC resonators of similar shapes but different dimensions arranged in a 2 x 2 array.

The technique of using array of resonating structure however is associated with limitation of having large unit cell dimensions. To realize the bandwidth-enhanced absorber without increasing the unit cell size, multi-resonating structures are employed. One such absorber (Figure 1.7) has been reported in [60], where a hexagonal interdigital resonator realizes a double resonance which are then brought closer to realize a bandwidth-enhancement type absorber.

Some other techniques have been reported for the bandwidth-enhanced case in which

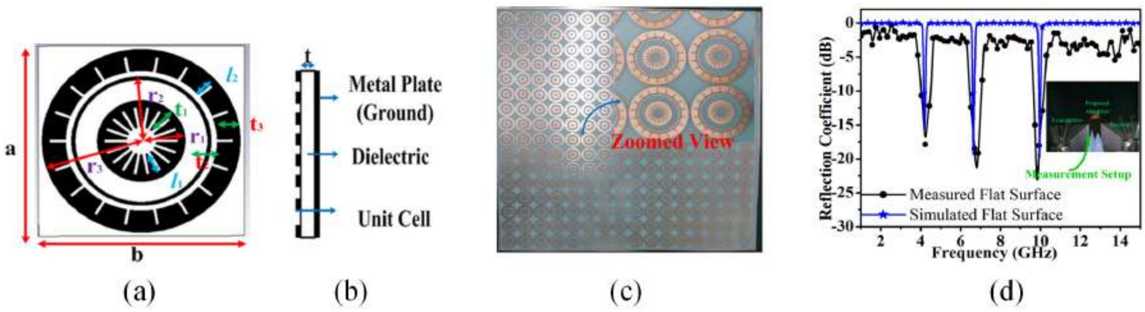

Figure 1.5: Triple-band conformal absorber: (a) Top, and (b) side view. (c) Fabricated prototype. (d) Reflection coefficient [47].

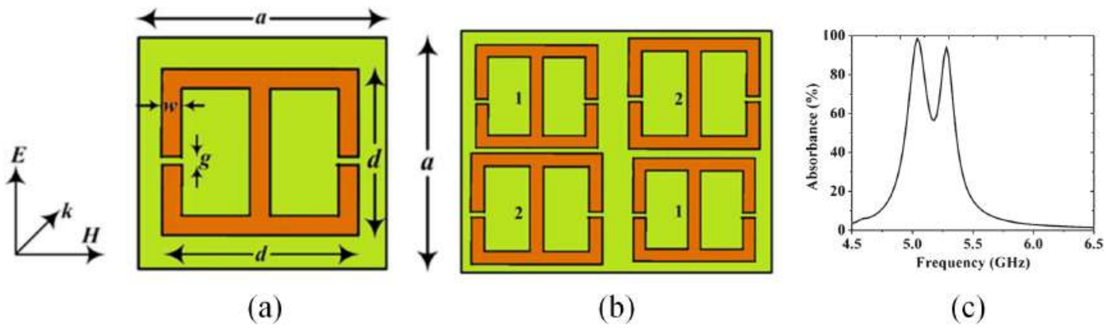

Figure 1.6: Bandwidth enhanced absorber using ELC resonator. (a) Basic structure, (b) 2 x 2 array, and (c) absorptivity response [59].

multilayer geometry is employed. Figure 1.8 shows one such reported bandwidth- enhanced absorber in which six alternate metal-dielectric layers are stacked together [61]. In this structure (Figure 1.8(c)) absorptivity is above 80% in the frequency range of 8.8 to 10.8 GHz, with a relative full width at half maximum (FWHM) absorption bandwidth of 23%.

1.3.3 Broadband FSS Absorbers

In the bandwidth-enhanced absorber the absorption bandwidth is limited to a few hundred MHz only. In view of the demand for various practical applications, various absorbers have been reported in which the absorption bandwidth is in the order of few GHz. Circuit analog absorber (CAA) is utilised for the broadband mechanism in which lumped resistors are mounted across the gaps in the metallic pattern on the dielectric substrate. The broadband absorbers are generally a two-layer structure in which a ground layer is placed at some distance from the resistive layer. One of the earlier reported broadband absorbers which uses the concept of CAA is shown in Figure 1.9 [62]. This reported absorber exhibits

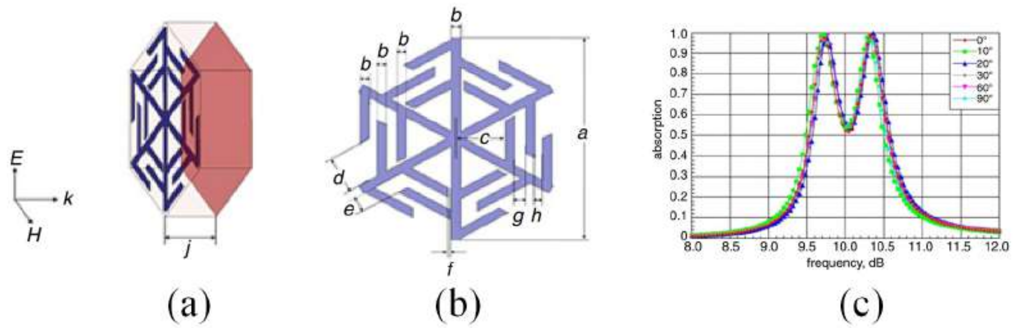

Figure 1.7: Bandwidth enhanced absorber using double resonance. (a) Perspective, and (b) top view. (c) Absorptivity response [60].

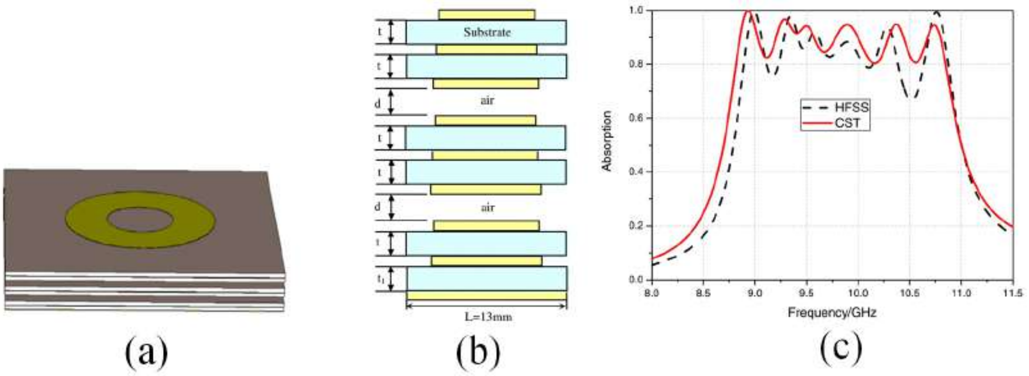

Figure 1.8: Bandwidth enhanced absorber using multi-layer geometry. (a) Perspective, and (b) side view. (c) Absorptivity response [61].

1.5 GHz absorption bandwidth under normal incidence with absorptivity over 90%. The lumped resistor with high ohmic loss results in the absorption over broad frequency range. This reported absorber is polarisation-insensitive and also possess high angular stability.

For further increasing the bandwidth of FSS absorber, the reported structure in [63] is designed by combining the concept of multiple resonators and multi-layer geometry. The reported work as shown in Figure 1.10 is a multi-layer structure in which top and bottom layer consists of resistor loaded double and single square loop, respectively. The back side of bottom layer is completely metal plated. A broadband absorption of 114.40% (4.96 to 18.22 GHz) is obtained (Figure 1.10(e)).

Another absorber has been reported in [64] where the capacitive reactance associated with the square loop geometry is utilized to reduce the thickness of the structure. The reported design (Figure 1.11) consists of multiple pair of square loop resonators connected through lumped resistors in the top layer and achieves an absorption bandwidth of 100.26% from 1.91 to 5.75 GHz.

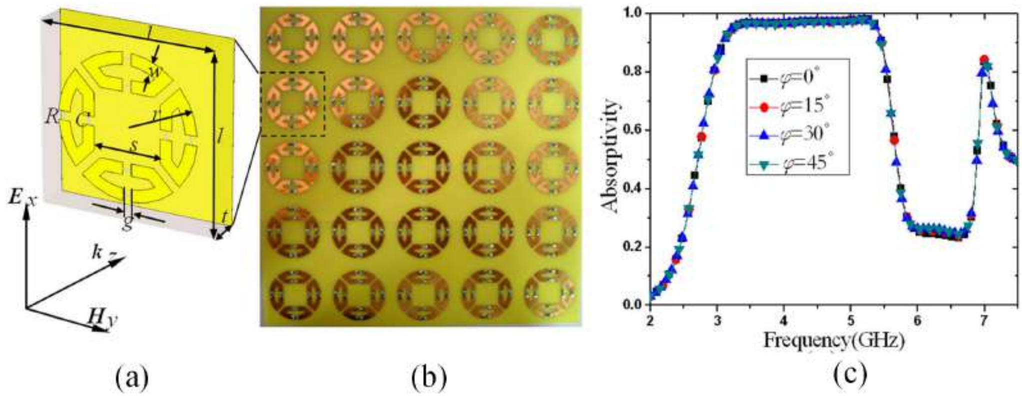

Figure 1.9: Broadband absorber using lumped elements. (a) Unit cell perspective view, (b) fabricated prototype, and (c) absorptivity plots at different polarization angles [62].

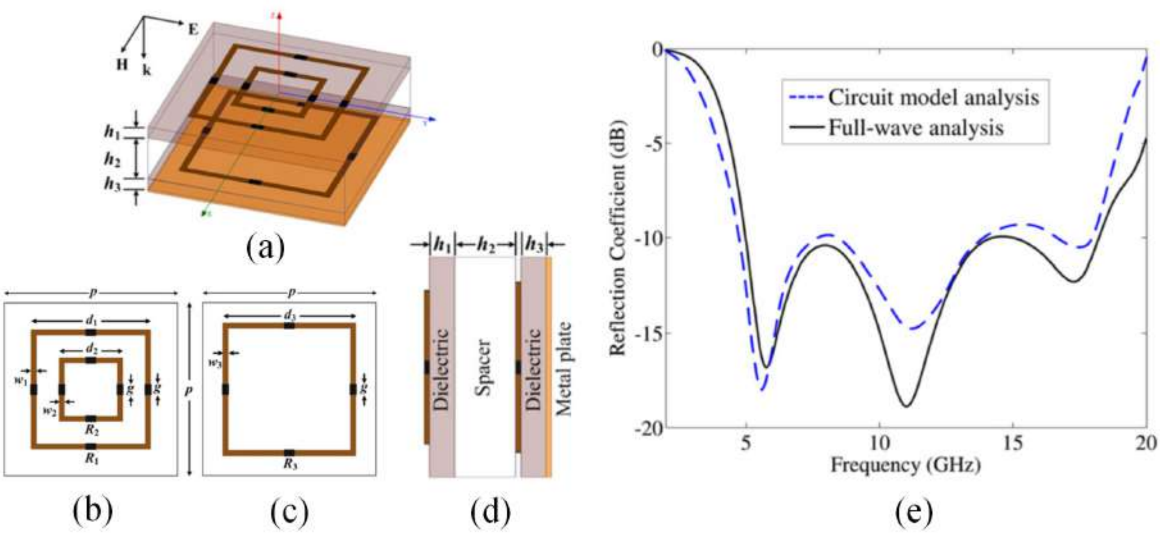

Figure 1.10: Multi-layer broadband absorber. (a) Perspective view , (b) top view of first layer, (c) top view of second layer, (d) side view, and (e) reflection coefficient of full wave and circuit model. [63].

A dual-polarized absorber is reported in [65], which is based on the multimode resonances of four rotationally symmetric bent metallic strips (Figure 1.12). The resistor loaded metallic strips on the lossy layer generates three resonant modes with the current passing through the two chip-resistors in separate modes causing energy dissipation. This absorber as depicted in Figure 1.12(c) achieves an ultra-wideband absorption of 127.9% (2.68 to 12.19 GHz).

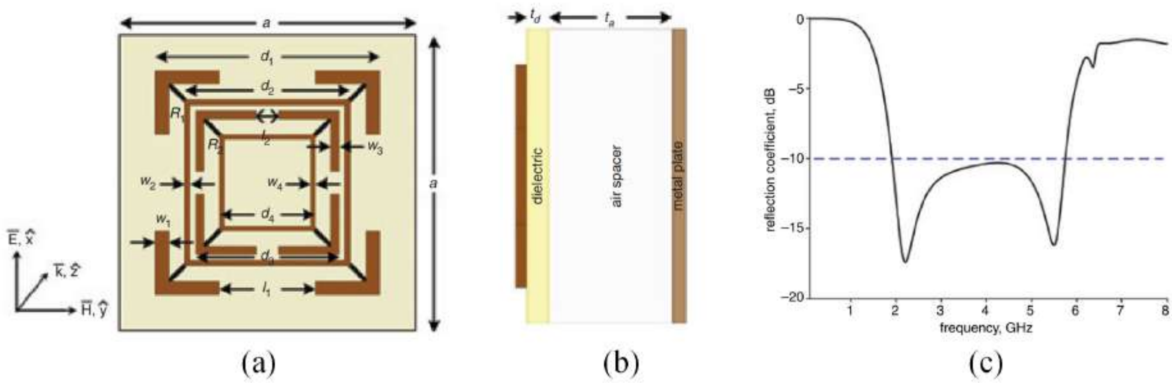

Figure 1.11: Broadband capacitive circuit absorber: (a) Top view, (b) side view, and (c) reflection coefficient. [64].

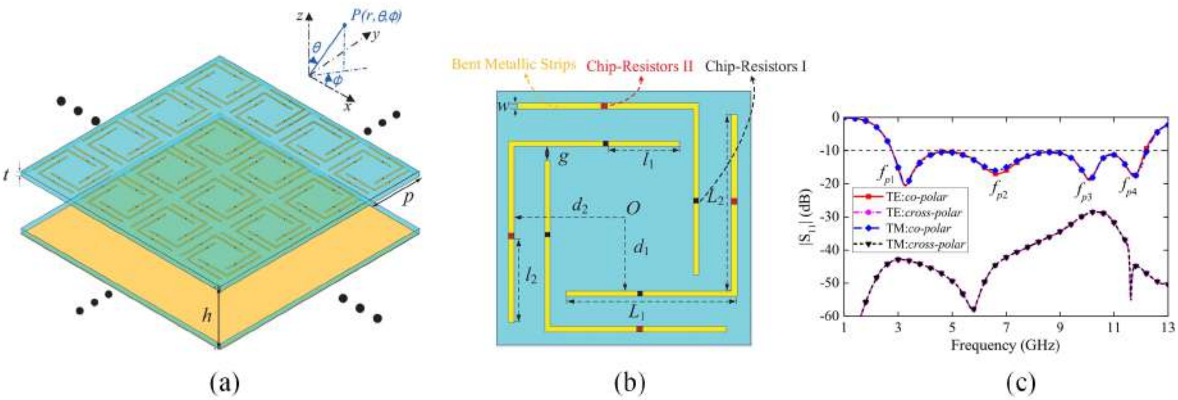

Figure 1.12: Multimode Resistor-Embedded broadband absorber: (a) Perspective view, (b) top view, and (c) reflection coefficients [65].

1.4 Frequency Selective Rasorber

The FSS based absorbers have been widely studied in the literature for its significant applications in the stealth technology and shielding. However, the absorber suffers from the limitation of causing total communication blockade of a system with which they are integrated [66, 67]. To overcome this zero communication drawback, a new type of structures have been developed by combining a FSS absorber with a bandpass FSS. The new structure is termed as frequency selective rasorber (FSR) or absorptive frequency selective transmission (AFST) structure or simply rasorber [68]. The term 'rasorber' is basically the combination of two words 'radome' and 'absorber'. The FSR have gained huge popularity in the recent years due to its performance of guaranteeing both transmission and absorption. A general schematic describing the FSR design is shown in Figure 1.13. The FSR design typically involves the combination of resistive layer with the bandpass FSS layer. The resistive layer realizes the absorption phenomenon of the incident wave in one band while the bandpass layer leads to the transmission in the desired passband. However, the combination of resistive and bandpass layers follows a certain methodology ensuring that the occurrence of desired transmission band does not affect the absorption.

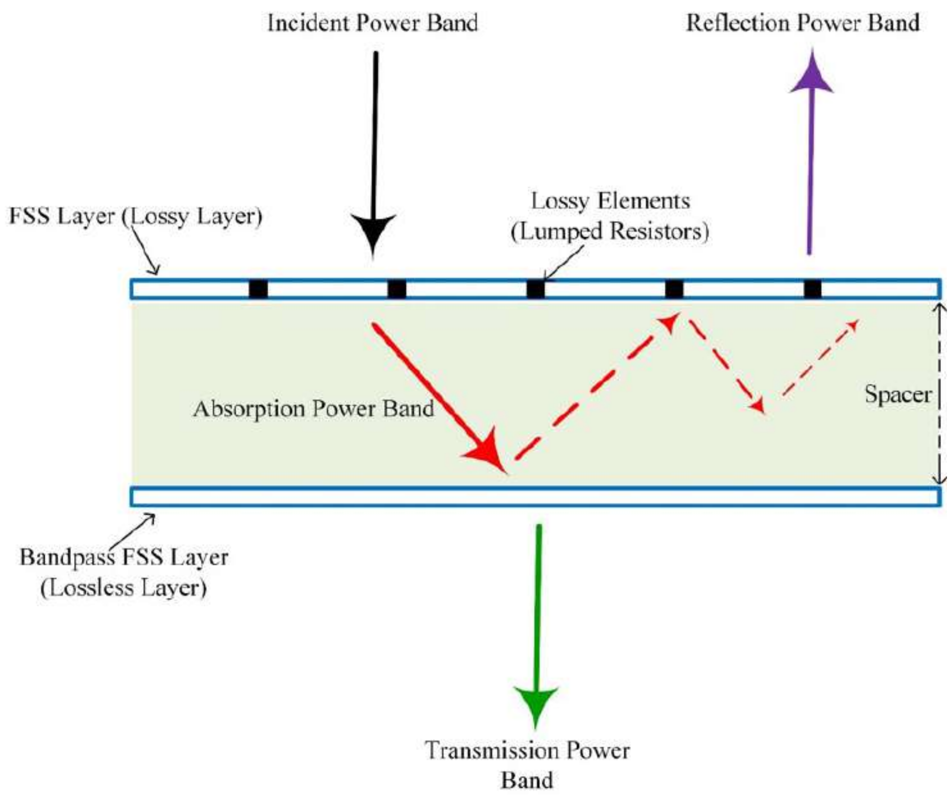

Figure 1.13: Schematic representation depicting the working of the general frequency selective rasorber.

FSRs offer significant application in the stealth technology for enhancing the secrecy of the target in the absorption while maintaining the required communication in the transmission band. Radar cross section (RCS) which quantifies the detectability parameter of the target should have a minimum value for enhancing its secrecy factor. The FSR having a transmission band corresponding to operating frequency of the radiating system can be suitably applied as a radome for realizing a system with low out-of-band RCS. Many such low RCS systems have been studied in the literature. The FSR is also known as absorptive frequency selective transmission (AFST) structure, while the band notched absorbers are known as AFSR (absorptive frequency selective reflection) structures [69]. In the case of AFSR structure the reflection band is required along with the single or multiple absorption bands [70]−[75]. The AFSR structure is applied as substrate for the radiating system having the operating band coinciding with the reflection band of AFSR structure, thus realizing a low out-of-band RCS system.

1.5 Literature Survey on the Frequency Selective Rasorbers

In recent years, studies on the designs of FSR have gained significant popularity. With the advancement of time, several works on improving the performance of FSR have been reported. According to the response realized, the FSRs have been broadly classified into various categories. This classification mainly includes FSR with lower transmission and upper absorption band (T-A) [76]−[81], lower absorption and higher transmission band (A-T) [82]−[90], transmission frequency positioned between the two absorption bands (A-T-A) [91]−[107], multiple absorptions and multiple transmission bands in an alternate form (A-T-A-T) [108]−[110] and so on [111]. In this section some of the recently reported works on these different types of FSRs are discussed sequentially.

1.5.1 T-A FSR

One of the earlier rasorber capable of realizing a lower transmission band and upper absorption band was reported in [76]. The structure as shown in Figure 1.14(a) [76], is realized by placing a resistive FSS layer on top of the interdigitated Jerusalem cross element based bandpass FSS layer. The reported work in [76], realizes a transmission band at 4.6 GHz with the upper absorption band from 10 to 18 GHz (Figure 1.14(b)). Subsequently, several other studies on T-A FSR were reported [77]−[81]. In [77], a dual-polarized T-A FSR (Figure 1.15) is designed with meander-line square loop printed on both the lossy and lossless layers. On the lossy layer the lumped resistors are loaded within the meander-line square loop. The FSR in [77] exhibits absorption band from 4.8 to 6.8 GHz, while the structure is almost transparent to the incident wave for frequencies below 1.54 GHz.

1.5.2 A-T FSR

Several design of FSR with lower absorption and upper transmission have been reported in the literature [82]−[90]. The A-T rasorber reported in [82] is realized by printing a parallel

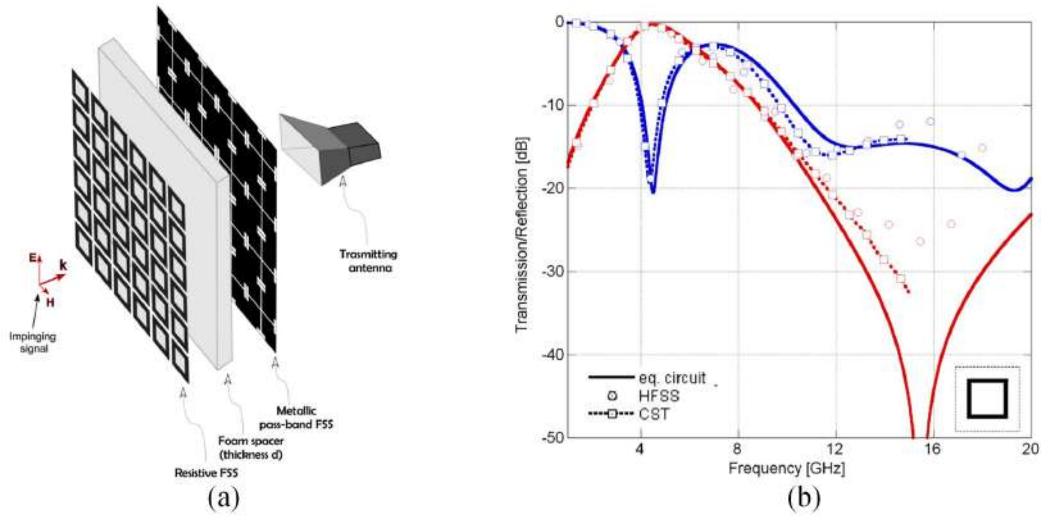

Figure 1.14: Frequency selective radome. (a) 3D representation, and (b) transmission/reflection response [76].

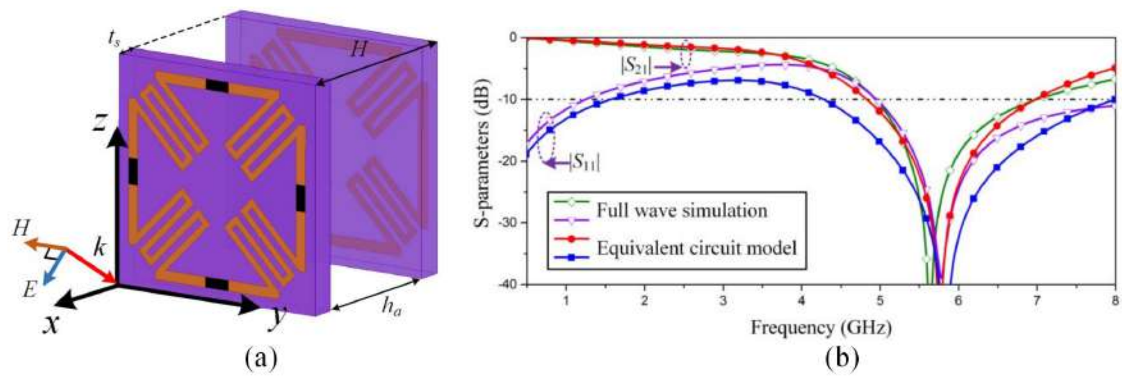

Figure 1.15: FSR based on meander-line square loop. (a) unit cell perspective view, and (b) full wave and equivalent circuit response [77].

LC resonator on the resistive layer (Figure 1.16). The rasorber provides a transmission at 10.2 GHz while a wide lower absorption band is exhibited from 3 to 9 GHz (Figure 1.16(b)).

A rasorber reported in [83] comprises of dipole-like and slot arrays in the resistive and lossless layers, respectively. The dipole-like elements printed on the two sided of resistive layer is connected by vias and is mounted with the lumped chip resistor as shown in Figure 1.17. The reported structure achieves a transmission at 5.6 GHz while the absorption band at lower side ranges from 2.8 to 5 GHz. The design in [83] is less complex with two lumped components per unit cell, however sensitive to polarization due to non-symmetry.

A miniaturized FSR design reported in [84] has a wide transmission band (8.3 to 11.07 GHz) above the absorption band (2.4 to 7.1 GHz). The design (Figure 1.18) comprises

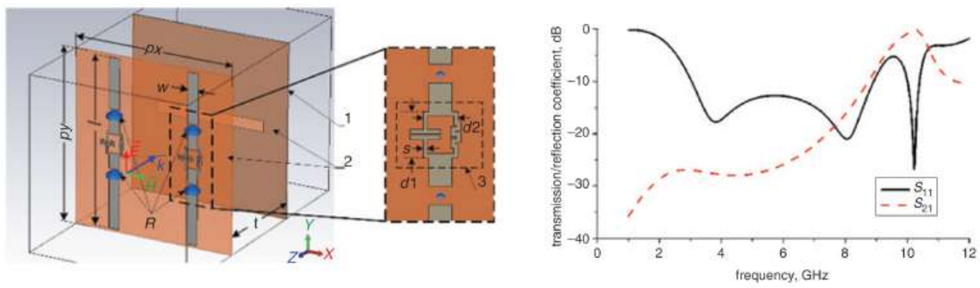

(a) (b)

Figure 1.16: FSR using parallel LC resonance. (a) unit cell perspective view, and (b) transmission/reflection response [82].

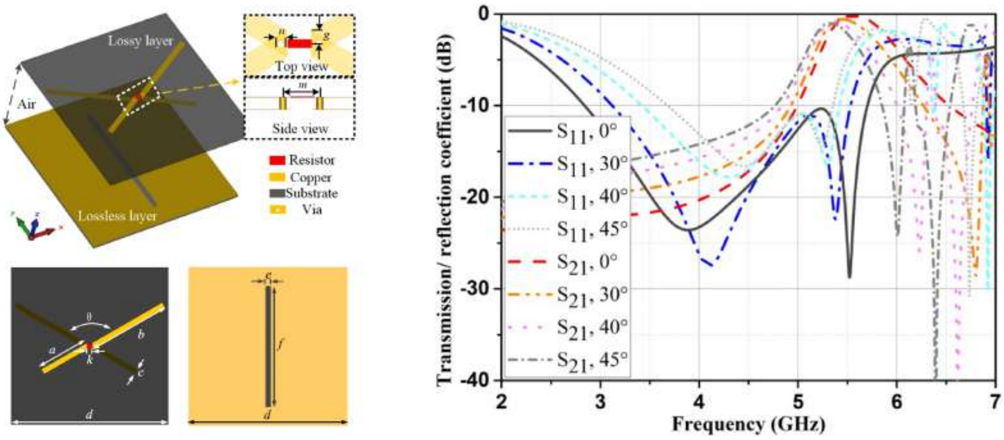

(a) (b)

Figure 1.17: FSR based on dipole arrays. (a) Unit cell schematic, and (b) transmission/reflection response [83].

of the high-inductance circular spiral resonator on the resistive layer and the associated parallel resonance achieves a wide higher transmission band while in the bandpass layer, a triple-layer hexagonal aperture are employed.

Next, a FSR [85] as shown in Figure 1.19, is designed using centrosymmetric bended-strip resonator which resonates at the transmssion band of the bandpass FSS realizing a higher passband. The transmission band of A-T rasorber in [85] is located at 12.76 GHz along with the absorption band lying within 6.10 to 10.98 GHz (Figure 1.19).

1.5.3 A-T-A FSR

Among other categories of FSR, the A-T-A type is more challenging to design, since due to the overlap of transmission and absorption bands, the performance at the transmission

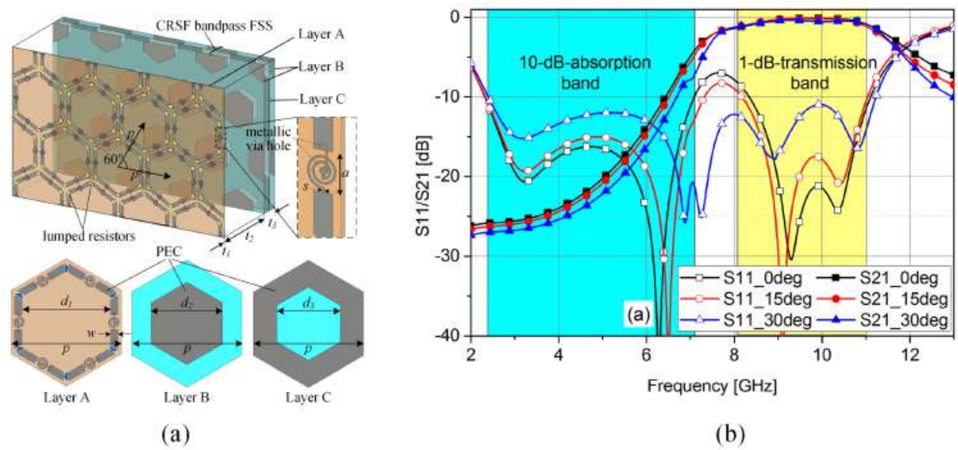

Figure 1.18: FSR using circular spiral resonator. (a) Unit cell representation, and (b) transmission/reflection response under various incident angles [84].

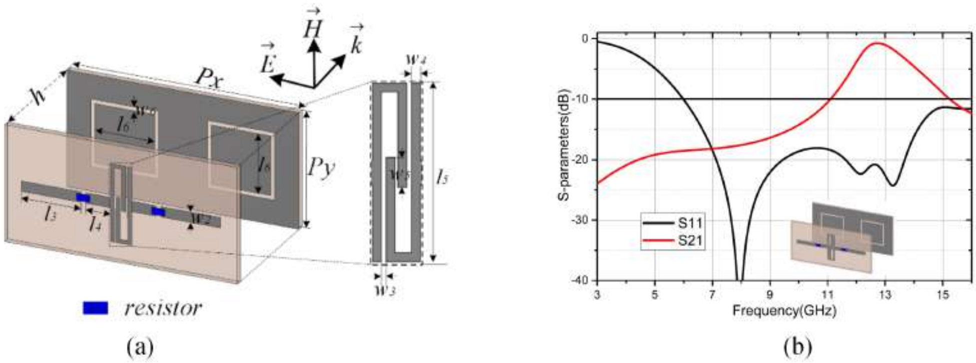

Figure 1.19: FSR using centrosymmetric bended-strip resonator. (a) Unit cell representation, and (b) transmission/reflection response [85].

band gets considerably degraded. In recent years, several A-T-A FSR designs have been reported [91]−[107] in the literature. The A-T-A FSR studied in [91] is a two-layer structure of resistive and bandpass layers (Figure 1.20). A notch resonator printed at the back side of the resistive layer provides a transmission pole corresponding to the bandpass layer. The rasorber achieves a transmission notch at 5.7 GHz while the lower and upper absorption bands are stretched from 2.6 to 5.2 GHz and 6.0 to 8.5 GHz, respectively.

In order to widen the absorption band, a rasorber designed using double lossy layer has been reported in [92] (Figure 1.21), where the two absorption bands correspond to each lossy layer and are independent of each other. With the use of one lossy layer the two absorption bands are lying between 2.3 to 4.5 GHz and 7.9 to 10.3 GHz while the transmission is at 6.3 GHz. However, by using two lossy layers the absorption bands get wider from 2.3 to 5.3 GHz and 7.8 to 14.6 GHz with the center transmission remaining

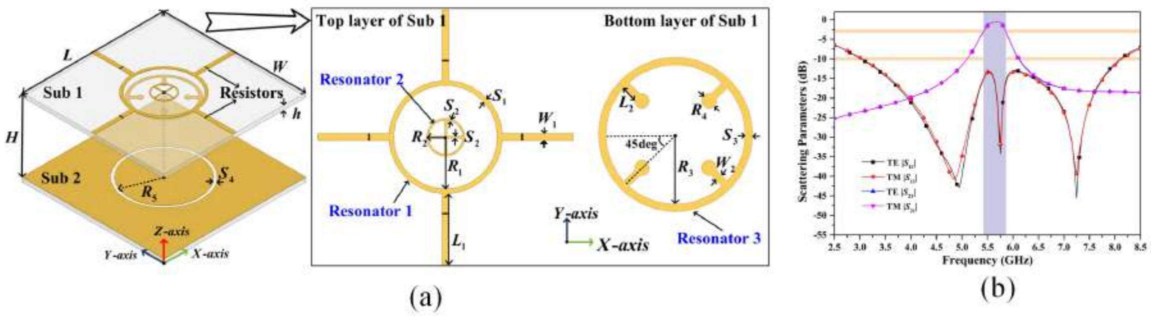

Figure 1.20: FSR based on notch resonator. (a) Unit cell representation, and (b) transmission/reflection response [91].

the same (Figure 1.21(b)).

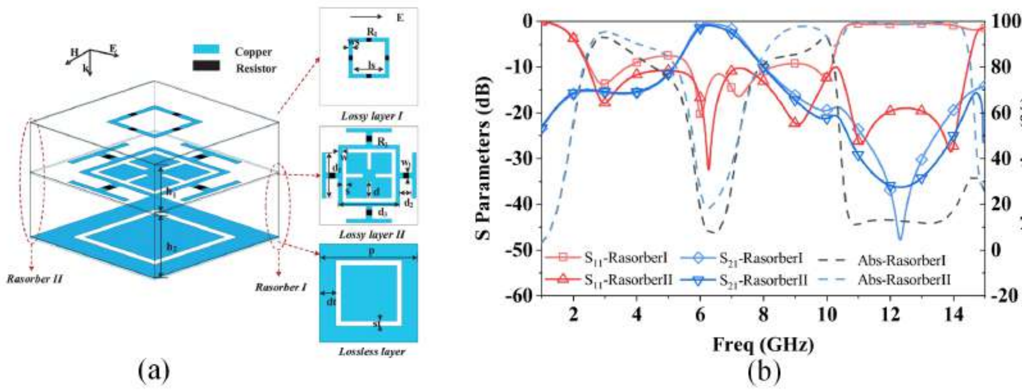

Figure 1.21: FSR based on double lossy layer. (a) Unit cell representation, and (b) transmission/reflection/absorptivity response [92].

A FSR designed using the equivalent circuit model is reported in [93] which consists of lossy and lossless layer as shown in Figure 1.22. The lossy layer consists of the Jerusalem element along with parallel resonance element at the center while the lossless layer consists of multilayer bandpass FSS for realizing a highly selective and wide transmission band. The transmission band is obtained from 7.9 to 9.0 GHz while the two adjacent absorption bands are from 3.3 to 7.1 GHz and 9.4 to 12.0 GHz.

In order to meet the demand of the systems operating at two different frequencies for two polarization, an FSR has been reported in [94] exhibiting anisotropic transmission bands for the two polarizations. The FSR as shown in Figure 1.23 consists of split circular resonator with metallic strips at the top resistive layer while the bottom bandpass layer consists of two types of slots associated with the two polarizations. The rasorber realizes a transmission at 10.40 GHz and absorption bands lying between 6.26 to 9.58 GHz and

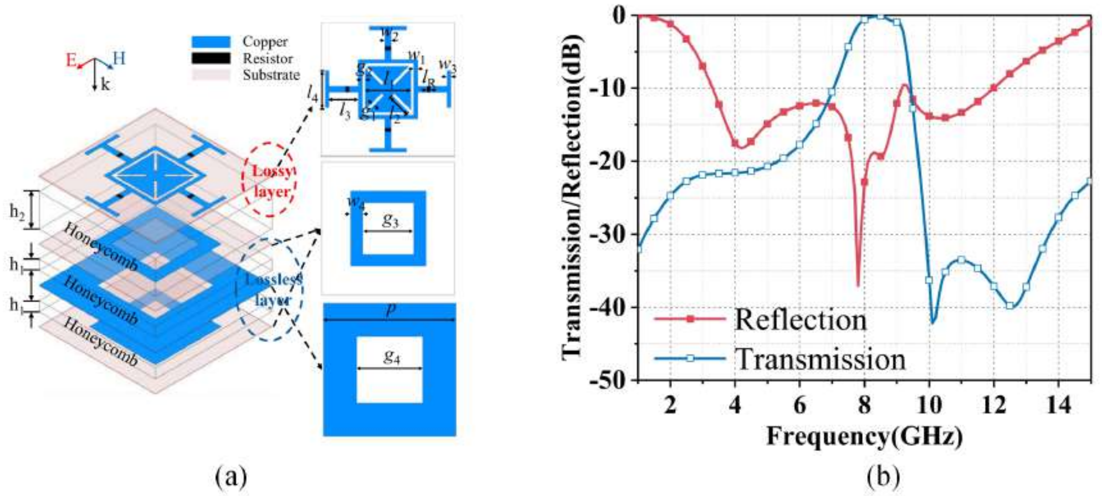

Figure 1.22: FSR based on low-profile bandpass filter. (a) Unit cell representation, and (b) transmission/reflection response [93].

11.46 to 14.06 GHz for the TE incident wave. For the TM incident wave, the transmission gets shifted to 11.40 GHz, with the absorption obtained in the frequency range of 6.35 to 10.42 GHz and 12.69 to 14.64 GHz.

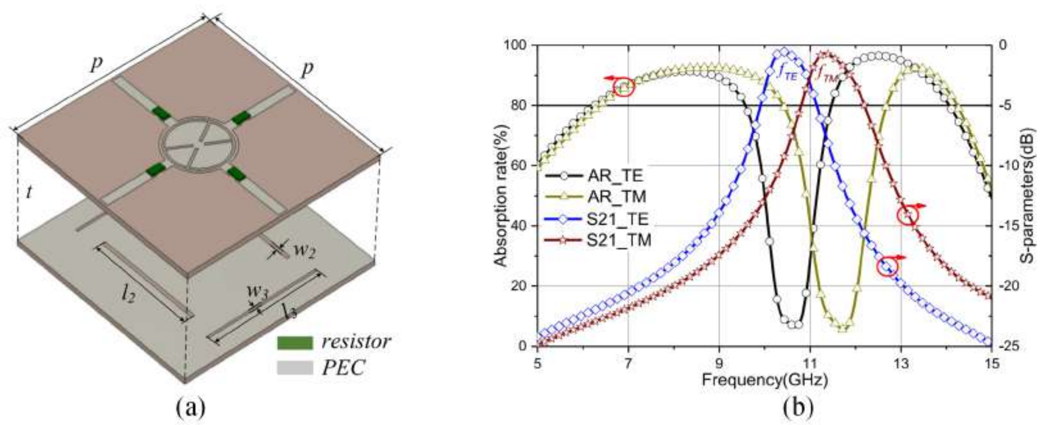

Figure 1.23: FSR with anisotropic transmission bands. (a) Unit cell representation, and (b) transmission/reflection/absorption response [94].

Recently A-T-A FSR based on resistive cross dipoles with electric field coupled resonators has been reported in [95]. The rasorber as showm in Figure 1.24, is designed on a single 6.5 mm thick substrate with the bottom bandpass layer printed on the other side of the substrate. The FSR exhibits transmission at 6.01 GHz and absorption bands ranging from 2.95 to 5.65 GHz and 7.4 to 9.24 GHz. Furthermore, the angular stability up to 50^o is obtained.

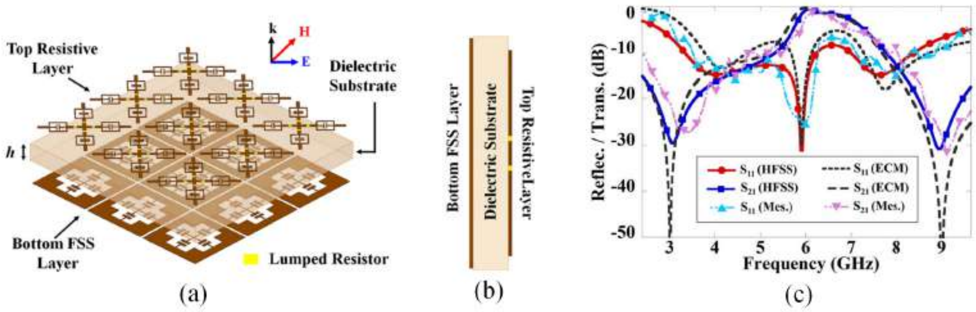

Figure 1.24: FSR based on based on resistive cross dipoles and electric field coupled resonator. (a) Unit cell representation, (b) side view, and (b) transmission/reflection response [95].

1.5.4 A-T-A-T FSR

With the advancement in time, studies on the development of dual transmissive rasorbers have been carried out. Several FSRs with A-T-A-T characteristics have been reported in the literature [108]−[110]. An FSR exhibiting dual transmission bands along with two absorption band is reported in [108] where the lumped-resistor-loaded metallic dipole with a dual-resonance structure is inserted in the center of the resistive layer (Figure 1.25). The bandpass FSS is a combination of two simple slots with different shapes etched adjacent to each other. The FSR realizes dual transmission at 7.7 and 12.6 GHz while the absorption bands are from 4.02 to 6.27 GHz and 8.21 to 12.02 GHz (Figure 1.25(b)).

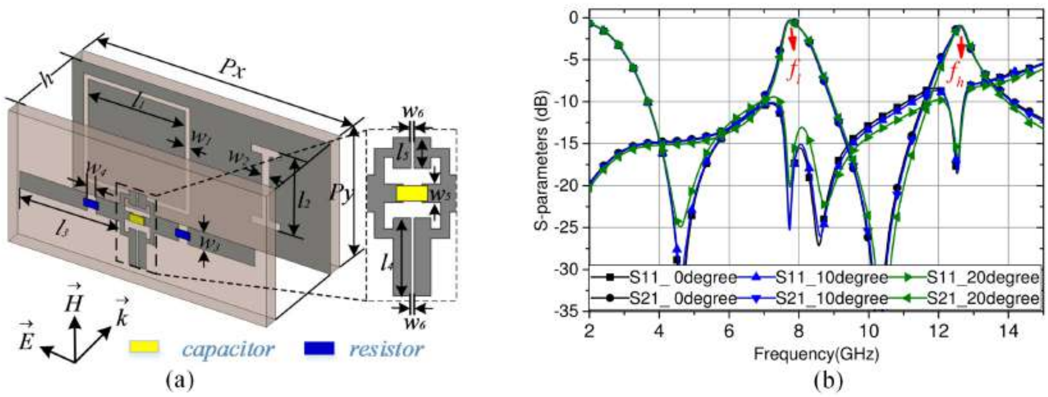

Figure 1.25: Dual transmission FSR with lumped-resistor-loaded metallic dipole. (a) Unit cell representation, and (b) transmission/reflection response under various angles [108].

A dual-polarized FSR having hexagonal shaped unit cell (Figure 1.26) has been reported in [109]. The lossy layer comprises of center loop loaded resistors along with three folded loops for generating the three transmission poles. The FSR attains the two transmissions at 6.1 and 10.1 GHz with the two absorption bands from 3.30 to 4.97 GHz and

7.42 to 9.03 GHz.

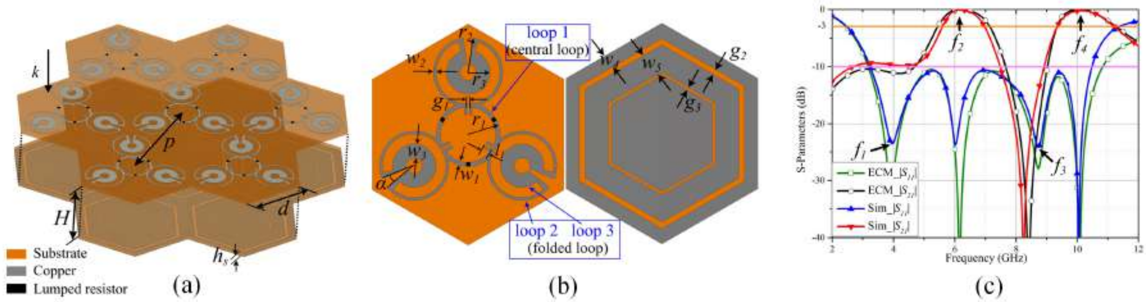

Figure 1.26: Dual transmission FSR. (a) Perspective view, (a) unit cell representation, and (b) transmission/reflection response [109].

Further in [110], another A-T-A-T FSR with the independently controlled dual transmission is reported. The lossy layer is designed using four square rings along with two stubs which is capable of realizing dual transmission pole and the corresponding frequencies can be controlled independently by separately varying the length of stubs (Figure 1.27). The rasorber in [110] realizes two passbands at 8.0 and 11.9 GHz within the -10 dB reflection band from 5.0 to 12.8 GHz.

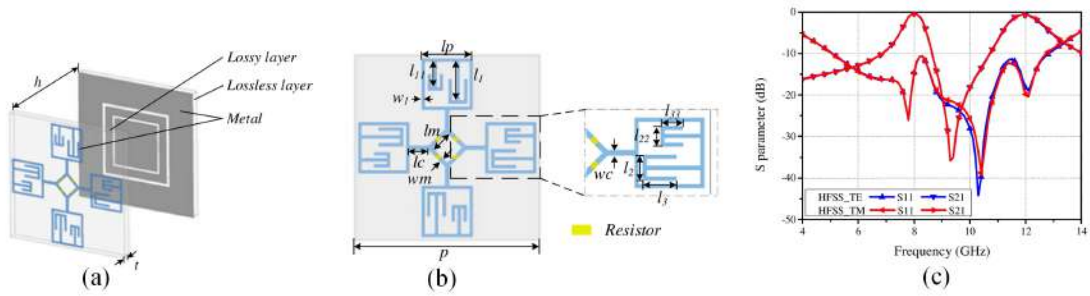

Figure 1.27: Dual transmission FSR with square rings and stubs. (a) Perspective view, (b) Unit cell top layer, and (b) transmission/reflection response [110].

1.6 RCS Reduction Based on FSR

In recent years, the studies involving the development of radiating systems with low radar cross-section (RCS) have gained a great deal of attention. RCS which quantifies the detectability parameter of the target should have the minimum value for enhancing the secrecy factor of the target in stealth technology. Thus, the RCS of the radiating system employed in the stealth technology is of key consideration. In the literature, several approaches for the realization of low RCS radiating systems have been reported [112]−[136].

Some of these reported techniques include geometrical shaping of antennas [112]−[115], applying radar absorbing materials [116]−[121], utilization of polarization converter structures [122],[124], and usage of surfaces involving artificial magnetic conductor [125]−[126]. However, in the reported techniques several shortcomings like poor radiation performance, narrow RCS reduction bandwidth and angle based low RCS are also accompanied.

The study reported in [127] involves the realization of low RCS antenna by integrating with the AFST structure. The AFST structure (Figure 1.28) designed using pairs of circular slot resonator and metallic strips achieves a middle transmission band (at 8.9 GHz)in the vertical polarization while only absorption exists in the horizontal polarization. The patch antenna designed at 8.9 GHz within the bottom layer of AFST structure shows more than 10 dB RCS reduction in the horizontal and vertical polarizations outside the operating frequency of antenna (Figure 1.28(f) and 1.28(g)).

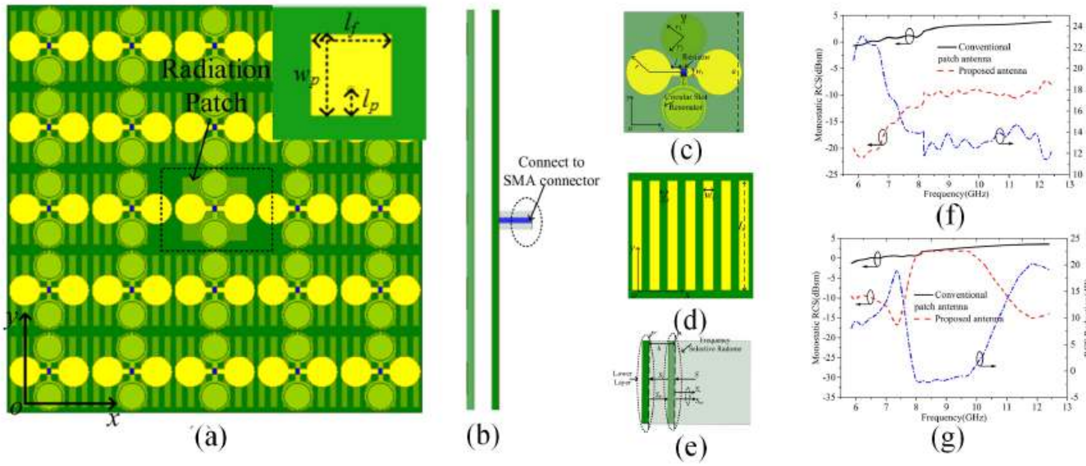

Figure 1.28: Low RCS antenna co-designed with AFST structure. (a) Overall structure, (b) side view, (c) unit view of top layer, (d) top view of lower layer, (e) explanation schematic of the proposed antenna, (f) monostatic RCS in horizontal polarization, and (g) monostatic RCS in vertical polarization [127].

A low RCS antenna designed using AFSR structure (band-notch absorber) is reported in [128]. The AFSR structure realizes a reflection notch in vertical polarization while wide absorption occurs in the horizontal polarization. The dipole antenna with operating frequency overlaping with the reflection notch of AFSR is mounted over the AFSR structure (as shown in Figure 1.29 (a)). The integrated antenna achieves the out-of-band RCS reduction of more than 10 dB in both the vertical and horizontal polarizations (Figure 1.29(b) and 1.29(c)).

The study in [129] reports the design of 3D AFSR structure with reflection notch and

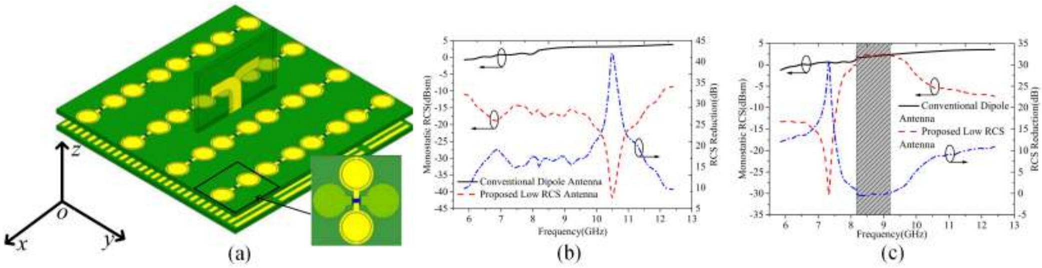

Figure 1.29: Low RCS antenna co-designed with AFSR structure. (a) Overall structure, (f) monostatic RCS in horizontal polarization, and (g) monostatic polarization in vertical polarization [128].

two-sided absorption band. Further, a monopole antenna placed over the the 3D AFSR structure (Figure 1.30) shows a wide RCS reduction in the band outside its operating frequency with the -10 dB RCS reduction bandwidth of 64.7% and 41%.

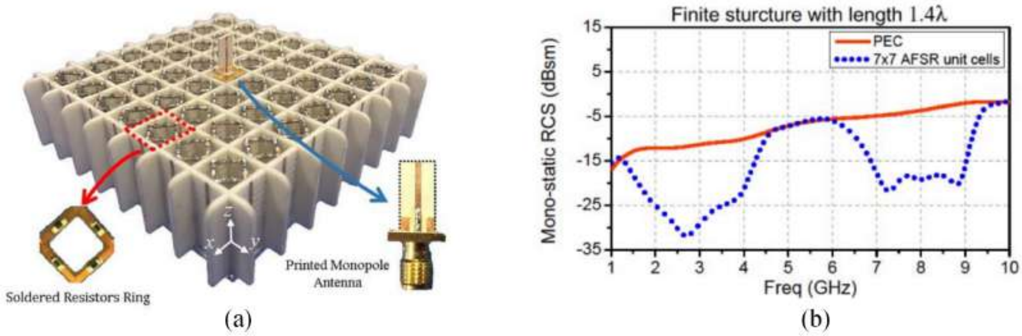

Figure 1.30: Low RCS antenna co-designed with 3D AFSR structure. (a) Overall structure, and (b) comparative monostatic RCS [129].

1.7 Motivation and Scope of Thesis

In the modern global world, the progress in communication technologies is unending. Electromagnetic wave propagation is the backbone behind wireless communication systems. With the advancing technologies, studies on selectively controlling EM propagation became a huge field of interest among researchers. Among them, the absorption of the EM wave is a significant requirement in the defense application for enhancing the secrecy of the target by reducing its corresponding RCS. Moreover, the EM absorption is also an important requirement in shielding and electromagnetic interference (EMI) reduction applications.

The unique feature of FSS based absorbers lies in its thin, lightweight and frequency selective properties over the conventional absorbers, which makes them easy to use and handle in the stealth technology. The FSS absorbers are generally narrowband, however with the multi-layer concept of circuit analog absorber using lossy components they can be designed for broadband absorption as well.

However, due to the limitation of communication blockade in FSS absorbers and the demand for frequency selective communication along with the absorption, there has been a growing interest towards the design of FSR. The FSR (also known as AFST structure) combines the bandpass application of FSS with the absorption for getting frequency selective absorption and transmission based on the requirement.

Although numerous single-layer designs are reported in the literature [44]−[58] from achieving single to higher multiple narrowband absorptions, however studies on designing the rasorbers for the single-layer narrowband absorptions are rarely reported. The FSR commonly reported are multi-layer structures exhibiting broadband absorptions. There lies a scope for upgrading the single-layer multi-band absorbers to narrowband rasorbers. The first motivation of this thesis is the development of thin, single-layer rasorber exhibiting narrowband absorptions along with transmission bands. The initial part of the thesis has been dedicated to the studies involving the development of multiple absorptions and multiple transmission FSR having thin and flexible structure and also suitable for the conformal applications.

FSR which is typically a multi-layer structure has been categorized depending upon the relative position of absorption and transmission bands. Among them, FSRs with T-A, A-T, T-A-T, A-T-A, A-T-A-T so on are commonly discussed configurations. In recent literature, ample works have been reported associated with the different designs of these FSRs for enhancing various performance parameters. The A-T FSR reported in [83, 85] have non-symmetric designs making it sensitive to the incoming polarization. The FSRs reported [84, 86] are dual-polarized structure with relatively wider absorption bandwidth. However, the FSR structure in [84, 86] consists of 4 layers and also the quantity of lumped components employed per unit is more (6 and 8). As such, there exists a scope for improving the A-T FSR design such that absorption is wider with less lumped components and reduced layers along with the design being polarization-insensitive. This thesis proposes the design for A-T rasorber and attempts to improve the said performances. The dual transmission rasorber with T-A-T response has not been reported in the literature so far. A detailed design strategy for realizing T-A-T FSR is studied in this thesis.

The A-T-A FSR exhibiting a transmission band between two absorption bands is the most suitable candidate in the application of out-of-band RCS and interference reduction. The A-T-A types are more challenging to design, since due to the overlap of transmission and absorption bands, the insertion loss at the transmission band gets considerably degraded. For the effective shielding and interference reduction of the radiating systems operating in a narrowband of frequency, the selectivity at the transmission band must be high. The selectivity represents the steepness of the transmission notch, and the corresponding Q factor measures it. The reported A-T-A FSRs [91]−[107] do not have sharp selectivity within the transmission band, making them less suitable candidates for narrowband applications of shieling and RCS/EMI reduction. This thesis deals with the objective to design a compact polarization-insensitive A-T-A FSR with a high-Q factor in the transmission band for low RCS radome applications. Further, in this thesis the study is extended to designing a dual transmission A-T-A-T FSR with superior performance over the reported works [108]−[110] in terms of absorption band, polarization-insensitivity, compactness and angular stabilty.

The absorptive frequency-selective reflection (AFSR) type structure are the band notched absorbers having reflection band along with one-/two-sided absorption bands. The AFSR type structure can be used as ground layer for the radiation system and leads to out-of-band RCS reduction [69]. Several studies on the AFSR structures have been reported in the literature [70]−[75]. In [128], a dipole antenna is studied with a single-polarization AFSR structure realizing a reduction in out-of-band RCS. Low RCS monopole and dipole antennas have been studied in [129], by integrating with a 3-D AFSR structure. The AFSR structure exhibiting polarization-insensitive behavior can have a suitable application for RCS reduction of the radiating system operating in dual polarization. This thesis presents the integration strategy of a dual-polarized crossed dipole antenna with a polarization-insensitive AFSR structure for achieving RCS reduction.

Polarization-Insensitive rasorber/absorber designs studied in the thesis are outlined below:

1. Narrowband flat/flexible FSR on a single layer substrate.

2. A-T/T-A-T rasorbers with improved performances.

3. Highly selective A-T-A/ A-T-A-T FSRs

4. Low RCS radiation system co-designed with A-T-A FSR.

5. Low RCS dual-polarized radiation system co-designed with AFSR Structure.

1.8 Organization of Thesis

The thesis has been presented in nine chapters. A brief overview of the frequency selective rasorber is discussed in **chapter 1**. Starting from EM absorption, the chapters continue to discuss frequency selective surface based absorbers/rasorber and the state-of-art designs. The motivation behind the work done in the thesis and the outcome are also laid down subsequently.

In **chapter 2**, a frequency selective surface (FSS) based T-A-T rasorber has been proposed by combining the designs of the split-ring absorber and dual bandpass FSS on the front and backside of single layer 0.8 mm thick substrate. The proposed rasorber exhibits a narrowband resonant absorption between the dual transmission bands.

Chapter 3 discusses flexible frequency selective surface (FSS) based A-T-T-A (2T2A)/ A-T-A-T-A (2T3A) rasorbers exhibiting dual/triple absorption bands along with dual-band transmission. The proposed rasorbers are designed by combining the individual designs of dual-/triple-band resonant absorber and dual bandpass FSS on the two sides of a flexible substrate. Also, the performance of the rasorbers is also studied for conformal behaviour with 120^o, 150^o, and 180^o degrees of curvatures.

In **chapter 4**, a A-T FSR is proposed where a transmission band at a higher frequency is achieved besides the lower broadband absorption. The FSR is designed by first studying and then combining the individual designs of the broadband absorber and bandpass frequency selective surface (FSS).

In **chapter 5**, a compact T-A-T type FSR is proposed with dual transmission bands located at the two sides of a broad absorption band. The proposed FSR is a two-layer structure designed by combining the Jerusalem cross based dual bandpass frequency selective surface (FSS) with a broadband resistive square loop absorber, such that both the absorption and transmission characteristics are retained.

In **Chapter 6**, a novel design of compact frequency-selective rasorber exhibiting absorption–transmission–absorption characteristics and having high passband selectivity has been proposed. The transmission frequency is realized by printing a Minkowski fractal-shaped resonator with a high-Q factor on the resistive layer, which provides a transmission pole at the frequency corresponding to the passband of a double-cross-slot-shaped bandpass layer. Further, in the chapter, a low radar cross-section antenna is realized by integrating a patch antenna with the proposed FSR, which achieves an average out-of-band monostatic/bistatic radar cross-section (RCS) reduction, while maintaining the other antenna parameters.

In **chapter 7**, a novel design strategy for realizing a compact A-T-A-T type frequency selective rasorber (FSR) is presented. A resonator with cross-loop slot in the Minkowski fractal (MF) design is studied and incorporated within the top resistive layer of the square loop broadband absorber. The proposed FSR design realizes two transmission windows with the adjacent absorption bands.

Chapter 8 proposes a novel strategy for realizing a reduction in radar cross-section (RCS) of dual-polarized crossed dipole antenna. A compact and polarization-insensitive absorptive frequency-selective reflection (AFSR) structure is proposed and then integrated with a dual-polarized crossed dipole antenna for achieving monostatic as well as bistatic RCS reduction as compared to the conventional reflector backed counterpart.

Finally, **chapter 9** discusses the conclusion and future scope of the works done in this thesis.

1.9 Outcome of Thesis

The chapterwise outcome of the research work presented in the thesis is summarized in Table 1.1.

Table 1.1: Chapterwise summary of Proposed Polarization-Insensitive Rasorber/Absorber Designs

Absorption	Chapter No.	Rasorber Type	Achieved Parameters
Narrowband	2	T-A-T	Single Layer; Absorption: 6.2 GHz; B.W= 110 MHz (1.75 %) Transmission 1: 3.1 GHz; I.L = 0.6 dB Transmission 2: 8.4 GHz; I.L = 1.2 dB
	3	A-T-T-A (2T2A),A-T-A-T-A (2T3A)	Single Layer; Flexible; Conformal Response Tested up to 180^o curvature angle. **2T2A:** A- 6.4 and 14.7 GHz; T- 9.6 and 13.4 GHz **2T3A:** A- 6.6,11.1 and 14.7 GHz: T- 9.6 and 13.4 GHz
Broadband	4	A-T	Absorption: 3.1−8.7 GHz (94.91%) Transmission: 11.4 GHz; I.L = 0.7 dB
	5	T-A-T	Absorption: 3.6−7.4 GHz (69.09%) Transmission 1: 2.1 GHz; I.L =1.4 dB Transmission 2: 8.8 GHz; I.L = 1.5 dB
	6	A-T-A	Absorption 1: 3.4−7.5 GHz (75.22%) 80% Absorption 2: 9.2−10.8 GHz; 16% Transmission: 8.4 GHz; I.L = 0.7 dB **FSR + Patch Antenna:** Average Monostatic RCS Reduction = 11.92 dB (Lower Band) and 5.04 dB (Upper Band) Average Bistatic RCS Reduction = 77% (Lower Band) and 60% (Upper Band)
	7	A-T-A-T	Absorption 1: 5.2−10.1 GHz (64.05%) Absorption 2: 10.7−14.4 GHz; (29.48%) Transmission 1: 10.4 GHz; I.L = 1.9 dB Transmission 2: 15.2 GHz; I.L = 0.9 dB
	8	AFSR	Absorption 1: 4.2−7.0 GHz (50%) Absorption 2: 9.2−11.5 GHz (22.2%) Reflection: 8.2 GHz Attenuation = 1.5 dB **AFSR + Crossed Dipole:** Average Monostatic RCS Reduction = 12 dB Average Bistatic RCS Reduction = 80%

A: Absorption; T: Transmission; B.W: Bandwidth; I.L: Insertion Loss

Chapter 2

Single Layer Dual-Band Transmissive Rasorber

In this chapter, a thin T-A-T type rasorber designed on a single substrate layer is proposed. The rasorber exhibits dual transmissive property along with the narrow absorption band. The proposed T-A-T rasorber possess a polarization-insensitive nature due to its symmetric structure. The rasorber consists of a resonant FSS absorber and a dual-bandpass FSS printed on the front and back of a single dielectric substrate, respectively. The working principle of the rasorber is analyzed using an equivalent circuit model. In order to validate the results, a 21 x 21 array of the proposed rasorber unit cell is fabricated and measurements are carried out.

2.1 Design and Analysis of the Rasorber

The unit cell schematic of the proposed rasorber is shown in Figure 2.1. It consists of a single layer of dielectric substrate with metal printed design on its front and back side. The front side consists of a metallic split-ring structure while the back side has two concentric ring slots etched within fully metallic copper. The proposed rasorber is printed on both sides of FR-4 dielectric substrate, having dielectric permittivity (ϵ_r) = 4.3, dielectric loss tangent ($tan\delta$) = 0.025 and $35\mu m$ thick copper layer. The optimized parameters are given as: $p = 20$, $r = 6.6$, $w = 3.2$, $g = 1$, $r_1 = 4$, $r_2 = 8.5$, $w_1 = 0.8$, $w_2 = 0.8$ and $t = 0.8$ (all dimensions are in mm).

The design of the proposed rasorber constitutes of three steps. In step-1, a split ring

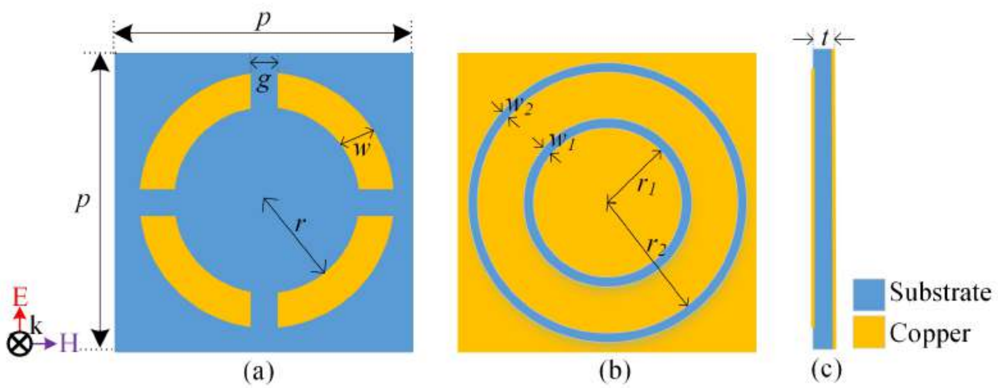

Figure 2.1: Unit cell schematic of the proposed FSS based rasorber. (a) Front, (b) back, and (c) side views.

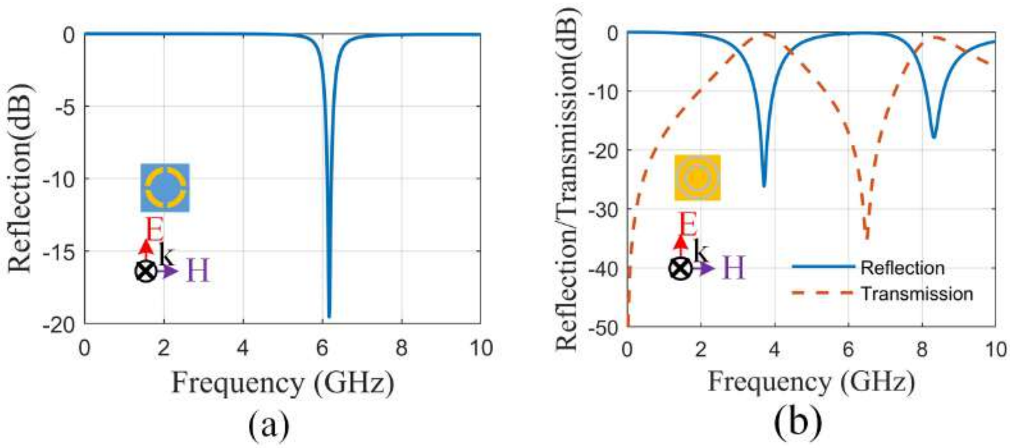

Figure 2.2: Simulated reflection/transmission coefficients. (a) Resonant FSS Absorber (Step-1), (b) Bandpass FSS (Step-2).

resonator in the front and full copper plate on the backside is analyzed, which yields a narrow-band absorption at the resonating frequency as shown in Figure 2.2(a). In step-2, a dual bandpass FSS, designed by etching two concentric rings within the metallic sheet and other side completely etched, is analyzed as shown in Figure 2.2(b). The parameters of the design in two steps are optimized in such a way that for the absorption frequency of step-1, the bandpass FSS of step-2 should have maximum reflection. The objective is to make the bandpass FSS act as a complete metallic ground at the absorption frequency. Now in step-3, the metallic ground of the split ring absorber is replaced by the bandpass absorber.

An equivalent circuit model (ECM) of the proposed rasorber is shown in Figure 2.3, which is obtained by combining the corresponding LC models of front and back structure of the rasorber.

The series $L_{\mathrm{F}}-C_{\mathrm{F}}$ circuit corresponds the inductance and capacitance of the front-side

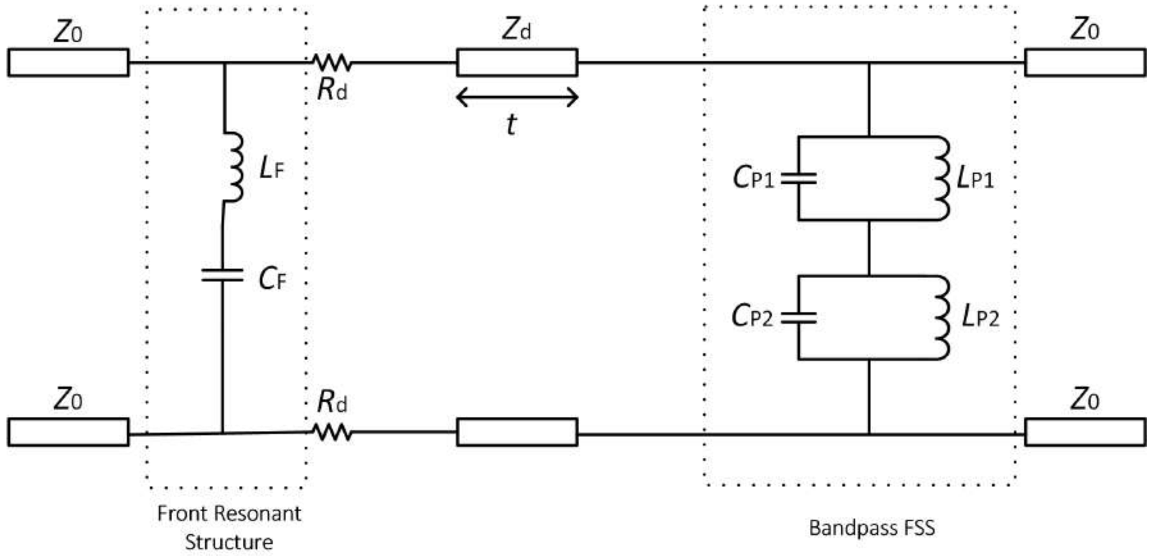

Figure 2.3: Equivalent circuit model of the proposed FSS based rasorber

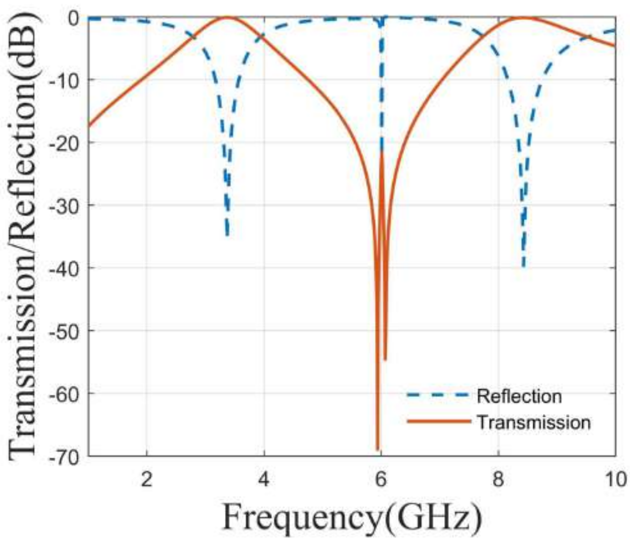

Figure 2.4: Simulated reflection and transmission coefficients of the equivalent circuit model

split-ring structure. The dielectric substrate is modelled using a lossy transmission line of length equal to the substrate thickness and having the characteristic impedance of Z_d given by,

$$Z_{\mathrm{d}} = \frac{Z_0}{\sqrt{\epsilon_r}} \tag{2.1}$$

where Z_0 is the characteristic impedance of free space. R_{d} represents the equivalent resistance due to dielectric loss of the substrate [137]. The propagation constant β is given as $\beta = \beta_0\sqrt{\mu_r\epsilon_r}$ (μ_r and ϵ_r are the relative permeability and permittivity of the dielectric substrate, respectively). The back-side dual-band FSS is achieved by the cas-

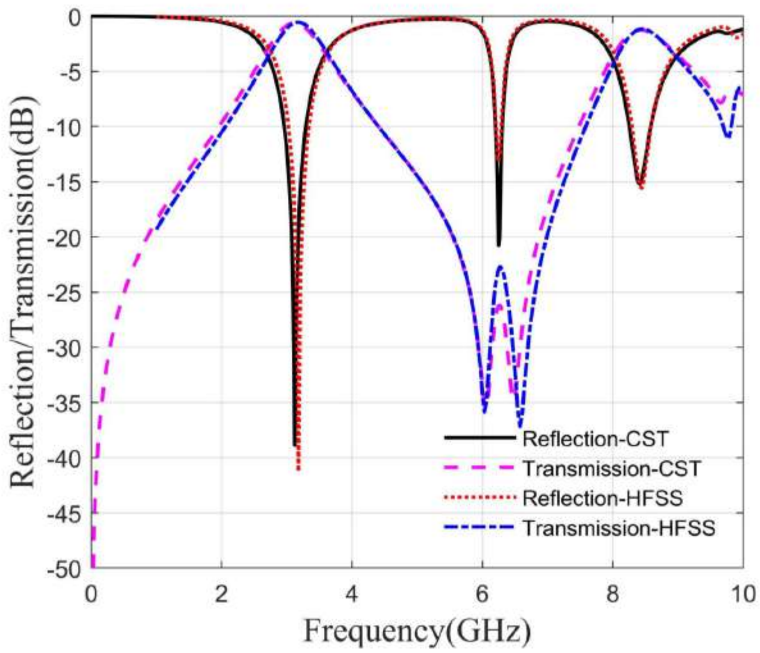

Figure 2.5: Simulated reflection and transmission of the proposed FSS based rasorber

caded arrangement of parallel $L_{\mathrm{P1}} - C_{\mathrm{P1}}$ and parallel $L_{\mathrm{P2}} - C_{\mathrm{P2}}$, having dual resonance frequencies.

The overall ABCD parameters of the ECM can be obtained by the cascaded matrix multiplication given as,

$$\begin{bmatrix} A & B \\ C & D \end{bmatrix} = \begin{bmatrix} 1 & 0 \\ 1/Z_{\mathrm{F}} & 1 \end{bmatrix} \times \begin{bmatrix} 1 & R_{\mathrm{d}} \\ 0 & 1 \end{bmatrix} \times \begin{bmatrix} \cos\beta t & \mathrm{j} Z_d \sin\beta t \\ \mathrm{j}\sin\beta t / Z_{\mathrm{d}} & \cos\beta t \end{bmatrix} \times \begin{bmatrix} 1 & 0 \\ 1/Z_{\mathrm{P}} & 1 \end{bmatrix} \tag{2.2}$$

where Z_{F}, Z_{P} represents impedances of front resonant structure and back side dual-pass FSS respectively. Z_{F} and Z_{P} are calculated as,

$$Z_{\mathrm{F}} = \mathrm{j}\left(\omega L_{\mathrm{F}} - \frac{1}{\omega C_{\mathrm{F}}}\right) \tag{2.3}$$

$$Z_{\mathrm{P}} = \mathrm{j}\left(\frac{\omega L_{\mathrm{P1}}}{1 - \omega^2 L_{\mathrm{P1}} C_{\mathrm{P1}}} + \frac{\omega L_{\mathrm{P2}}}{1 - \omega^2 L_{\mathrm{P2}} C_{\mathrm{P2}}}\right). \tag{2.4}$$

The S-parameters are calculated from the ABCD parameters using the conversion formula

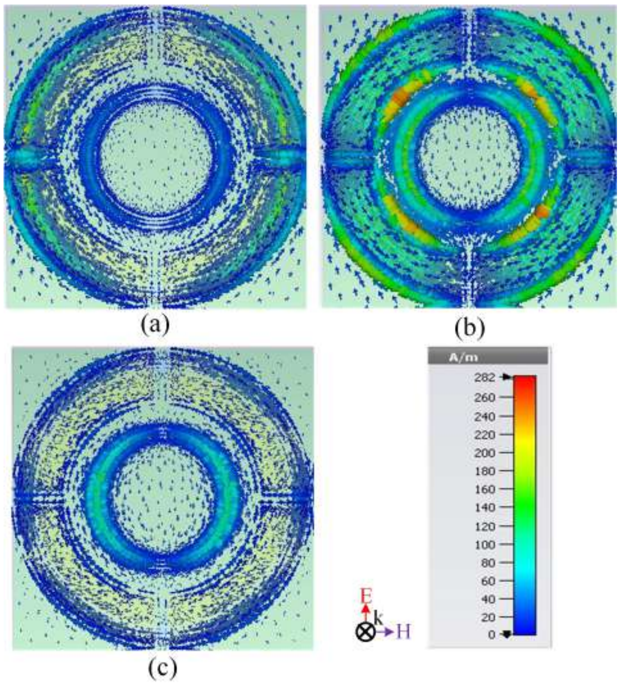

Figure 2.6: Surface current distribution of the proposed rasorber. (a) At 3.1 GHz, (b) At 6.2 GHz, (c) At 8.4 GHz.

given as,

$$S_{11} = \frac{A+B/Z_0-CZ_0-D}{A+B/Z_0+CZ_0+D} \tag{2.5}$$

$$S_{21} = \frac{2}{A+B/Z_0+CZ_0+D}. \tag{2.6}$$

The absorptivity is thus calculated as,

$$A(\omega) = 1 - |S_{11}|^2 - |S_{21}|^2. \tag{2.7}$$

The ECM of the proposed rasorber is simulated using Keysight ADS software. The simulated transmission and reflection parameters of the ECM are depicted in Figure 2.4. The optimized values of the circuit elements are given as: $L_\mathrm{F} = 51.63$ nH, $C_\mathrm{F} = 0.0133$ pF, $L_\mathrm{P1} = 3.0$ nH, $C_\mathrm{P1} = 0.7$ pF, $L_\mathrm{P2} = 0.8$ nH, $C_\mathrm{P2} = 0.437$ pF, $R_\mathrm{d} = 4.7$ Ω. It can be observed from the simulated plots in Figure 2.4, that the front resonant $L_F - C_F$ model causes the resonance at around 6.2 GHz such that both transmission and reflection coefficients are below -10 dB which leads to absorption at that frequency. Also, the transmission at around 3.1 GHz and 8.4 GHz is due the resonance in $L_\mathrm{P1} - C_\mathrm{P1}$ and $L_\mathrm{P2} - C_\mathrm{P2}$ models respectively.

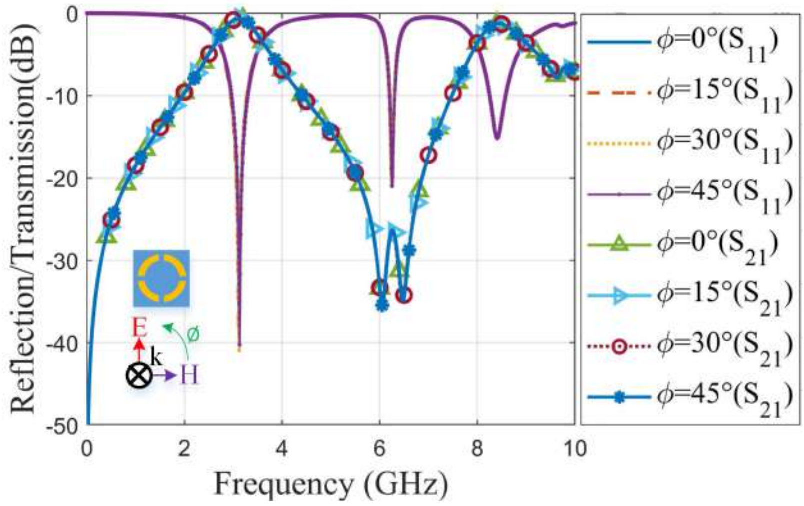

Figure 2.7: Simulated reflection and transmission response of the proposed FSS based rasorber under various polarization angles

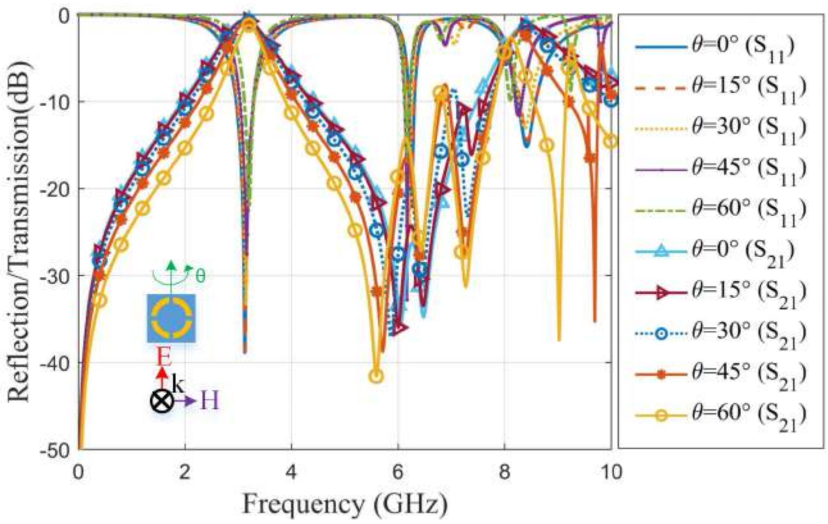

Figure 2.8: Simulated reflection and transmission response of the proposed FSS based rasorber under various incident angles

The resulting FSS structure is analyzed in the electromagnetic simulation software, CST Microwave Studio and Ansys HFSS. Figure 2.5 shows the simulated reflection and transmission parameters of the proposed FSS based rasorber under normal incidence. The proposed FSS based rasorber exhibits the combination of narrow-band absorption and two transmission bands. The transmission windows are obtained at around 3.1 GHz and 8.4 GHz with insertion loss of around 0.6 dB and 1.2 dB, respectively. The transmission bands at 3.1 GHz and 8.4 GHz possess -10 dB bandwidth from 2.95−3.3 GHz (11.20%) and 8.29−8.63 GHz (4.01%), respectively. The absorption band is around 6.2 GHz in which both the reflection and transmission is below -10 dB. The absorption band obtained

Table 2.1: Performance parameters at various incident angles

Incidence angle (θ)	Insertion loss @3.1 GHz	Absorption @6.2 GHz	Insertion loss @8.4 GHz
0^o	0.62 dB	98.91%	1.24 dB
15^o	0.64 dB	99.0%	1.35 dB
30^o	0.73 dB	98.63%	1.53 dB

is narrow with -10 dB bandwidth from 6.21−6.32 GHz (1.75%). The operating principle of the rasorber can be further analyzed by the simulated surface current distributions at the three resonant frequencies as shown in the Figure 2.6. At 3.1 GHz, the currents are concentrated along the edges of outer ring slot, which provides the transmission band at that frequency. The current concentration gets shifted along the inner ring slot at the frequency of 8.4 GHz and corresponds the transmission band. For the absorption frequency at around 6.2 GHz, the currents are mainly concentrated along the edges of the front split-ring structure.

The proposed FSS based rasorber possess four-fold symmetry and the response parameters are independent of polarization angle of the incident electromagnetic wave. The polarization independence of the proposed FSS rasorber is shown by the simulated reflection and transmission parameters for various polarization angles in Figure 2.7. The proposed structure is also analysed under oblique incidence with various angle of incidence as shown in Figure 2.8. The angular stability of the proposed rasorber can be studied by examining the insertion loss at the transmission bands centered at 3.1 and 8.4 GHz and absorbance at the absorption band centered at 6.2 GHz for the different oblique incidence angles. The performance parameters of the proposed absorber for $\theta = 0$, 15 and 30 degrees are presented in Table 2.1. In the proposed study, the acceptable range of insertion loss at each transmission frequency is considered to be within 1.5 dB, which gets exceeded for incidence angle greater than 30^o at 8.4 GHz. Thus, it can be indicated that the proposed rasorber exhibits an acceptable response up to 30^o of incidence angle.

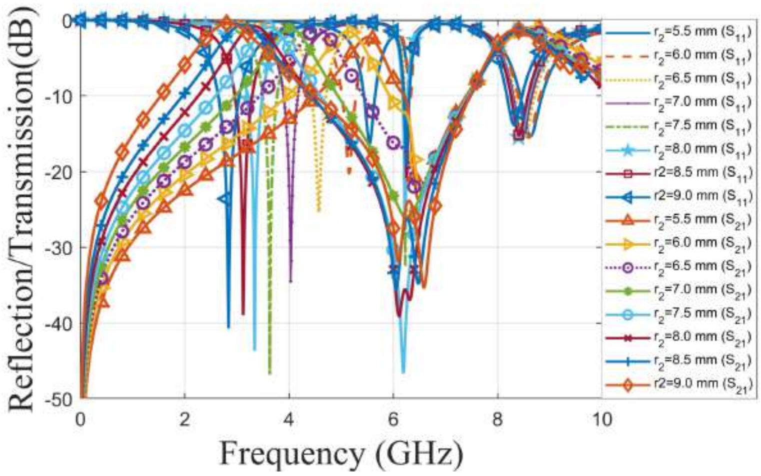

Figure 2.9: Simulated reflection and transmission coefficients with the variations in r_2 at $r_1 = 4.0$ mm

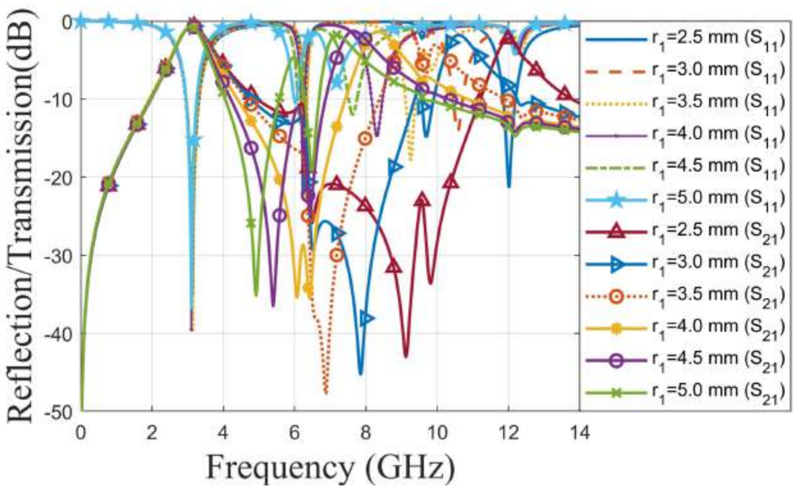

Figure 2.10: Simulated reflection and transmission coefficients with the variations in r_1 at $r_2 = 8.5$ mm

2.2 Effects of the Design Parameters on the Performance of Rasorber

The proposed rasorber exhibits two transmission bands and a narrow absorption frequency in between them. The rasorber can be characterised by the insertion losses at two passbands, absorptivity at the absorption band and relative spacing between the passbands and the absorption band. In order to study the effect of rasorber design parameters on the relative spacing of absorption and transmission bands, transition ratios $\mathrm{TR_l}$ and $\mathrm{TR_u}$ are defined as below.

$$\mathrm{TR_l} = \frac{f_{\mathrm{tl}}}{f_{\mathrm{a}}} \tag{2.8}$$

Table 2.2: Variation of parameters with r_2 keeping $r_1 = 4.0$ mm

r_2 (mm)	I.L @ $f_{tl}(GHz)$	f_a (GHz) (Absorption %)	I.L @ f_{tu}(GHz)	TR_l	TR_u
9.0	0.43 dB@2.8	6.2 (98.56%)	1.35 dB@8.4	0.45	1.35
8.5	0.61 dB@3.1	6.2 (98.91%)	1.24 dB@8.4	0.5	1.35
8.0	0.78 dB@3.3	6.2 (99.44%)	1.23 dB@8.4	0.53	1.35
7.5	0.93 dB@3.6	6.2 (99.92%)	1.19 dB@8.4	0.58	1.35
7.0	1.06 dB@4.0	6.2 (99.43%)	1.15 dB@8.4	0.64	1.35
6.5	1.19 dB@4.5	6.2 (95.77%)	1.22 dB@8.4	0.72	1.35
6.0	1.46 dB@5.1	6.2 (75.02%)	1.30 dB@8.4	0.82	1.35
5.5	2.24 dB@ 5.5	6.2 (72.42%)	1.27 dB@8.4	0.88	1.35

$$\mathrm{TR_u} = \frac{f_{\mathrm{tu}}}{f_{\mathrm{a}}} \tag{2.9}$$

where f_a is the absorption frequency, f_{tl} is lower transmission frequency and f_{tu} is upper transmission frequency. From the surface current distribution plots in Figure 2.6, it has been studied that f_{tl} can be primarily controlled by r_2 (radius of outer ring slot) while r_1 (radius of inner ring slot) determines f_{tu}. A study is carried out on the variation of TR_l with change in value of r_2, keeping r_1 fixed. In the similar manner, keeping r_2 fixed, change in value of TR_u by varying r_1 can also be studied. Figure 2.9 shows the parametric sweep with respect to r_2, keeping r_1 constant at 4.0 mm. Similarly, Figure 2.10 shows the parametric sweep with respect to r_1, keeping r_2 constant at 8.5 mm. The observations from plots of Figure 2.9 and Figure 2.10 are arranged in Table 2.2 and Table 2.3, respectively.

It can be observed from the Table 2.2, that decreasing the radius of outer slot from $r_2 = 9.0$ mm to $r_2 = 5.5$ mm, the lower transmission frequency f_{tl} increases from 2.8 GHz to 5.5 GHz. Similarly, from Table 2.3 it is notable that for decreasing value of inner slot from $r_1 = 5.0$ mm to $r_1 = 2.5$ mm, the upper transmission frequency f_{tu} is increased upto 12.0 GHz.

In accordance with the observations made from Table 2.2 and Table 2.3, an optimum range of each f_{tl} and f_{tu} is defined. From Table 2.2, for decreasing value of r_2, the corresponding value of lower transmission frequency f_{tl} goes on increasing, whereas the upper transmission frequency f_{tu} is nearly fixed. However, the absorption at 6.2 GHz remains significant upto f_{tl} reaching the value of 4.5 GHz. In this study, significant

Table 2.3: Variation of parameters with r_1 keeping $r_2 = 8.5$ mm

r_1 (mm)	I.L @ $f_{\mathrm{tl}}(GHz)$	f_{a} (GHz) (Absorption)	I.L @ f_{tu}(GHz)	$\mathrm{TR_l}$	$\mathrm{TR_u}$
5.0	0.65 dB@3.1	6.2 (48.80%)	1.54 dB@6.5	0.5	1.04
4.5	0.62 dB@3.1	6.2 (86.13%)	1.18 dB@7.7	0.5	1.24
4.0	0.61 dB@3.1	6.2 (98.91%)	1.24 dB@8.4	0.5	1.35
3.5	0.58 dB@3.1	6.2 (96.02%)	1.84 dB@9.2	0.5	1.46
3.0	0.58 dB@3.1	6.2 (93.75%)	1.79 dB@10.5	0.5	1.69
2.5	0.58 dB@3.1	6.2 (89.02%)	2.23 dB@12.0	0.5	1.93

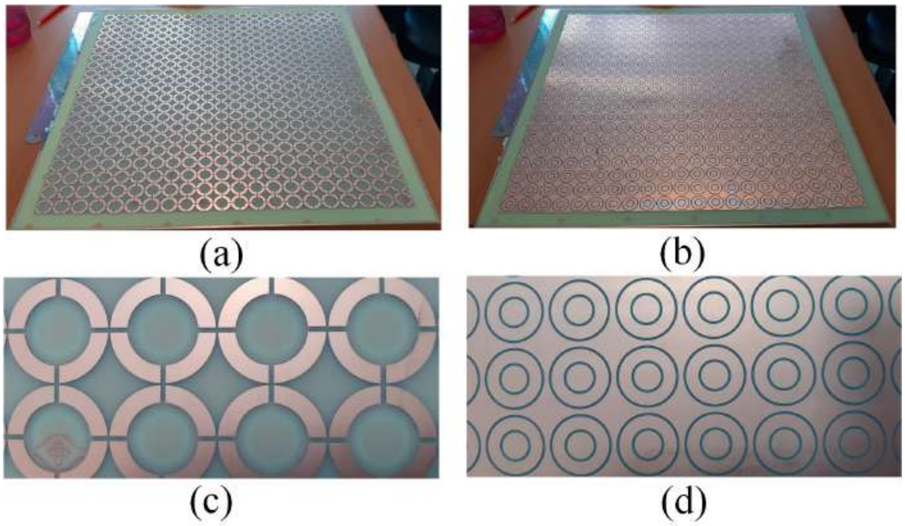

Figure 2.11: Photograph of the fabricated prototype. (a) Front side, (b) back side, (c) zoomed front side, and (d) zoomed back side.

absorption is designated for absorption above 90% and the insertion loss at transmission is maintained within 2 dB. Thus the upper and lower limit of f_{tl} is given as,

$$f_{\mathrm{tl(min)}} \simeq 2.8 \text{ GHz} = 0.45 f_{\mathrm{a}} \tag{2.10}$$

$$f_{\mathrm{tl(max)}} \simeq 4.5 \text{ GHz} = 0.72 f_{\mathrm{a}} \tag{2.11}$$

where f_{a} is frequency of absorption. Further, from Table 2.3, f_{tl} is almost constant at 3.1 GHz and f_{tu} goes on increasing with the decreasing value of r_1. Upto $f_{\mathrm{tu}} = 10.5$ GHz, a significant absorpton is obtained at around 6.2 GHz. Thus for f_{tl} constant at 3.1 GHz, the lower and upper limit of f_{tu} is given below.

$$f_{\mathrm{tu(min)}} \simeq 8.4 \text{ GHz} = 1.35 f_{\mathrm{a}} \tag{2.12}$$

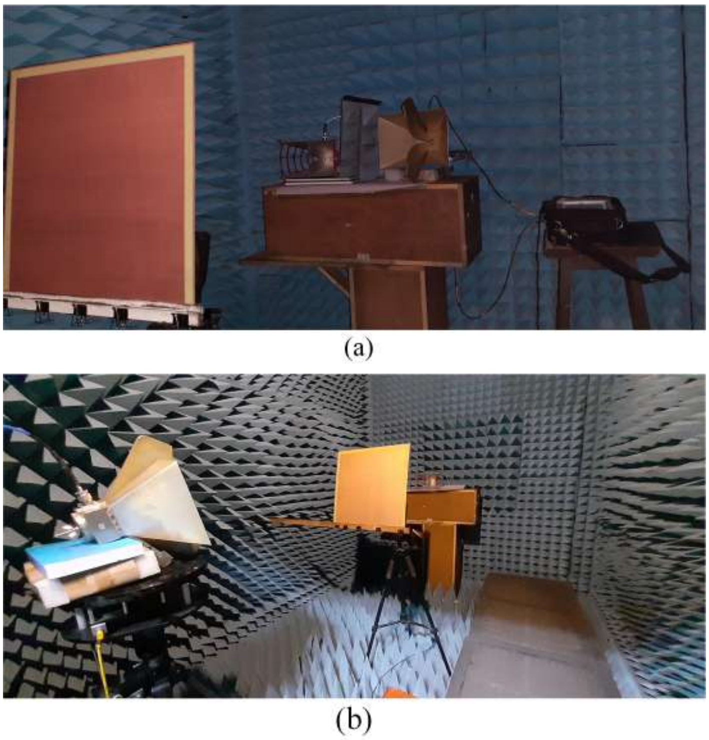

Figure 2.12: Experimental setup for measurements. (a) Reflection, and (b) transmission coefficients

$$f_{\text{tu(max)}} \simeq 10.5 \text{ GHz} = 1.69 f_{\text{a}} \tag{2.13}$$

Hence, the optimum range of f_{tl} and f_{tu}, with f_{a} kept constant at 6.2 GHz is given as follows.

$$f_{\text{tl}} \simeq 0.45 f_{\text{a}} \quad to \quad 0.72 f_{\text{a}} \tag{2.14}$$

$$f_{\text{tu}} \simeq 1.35 f_{\text{a}} \quad to \quad 1.69 f_{\text{a}} \tag{2.15}$$

In the proposed design of rasorber, TR_{l} can be varied from 0.72 to 0.45 by changing r_2 from 6.5 mm to 9 mm, keeping r_1 fixed at 4.0 mm. Similarly, variation of r_1 from 3.0 mm to 4.0 mm, keeping r_2 fixed at 8.5 mm results in change of TR_{u} between 1.69 to 1.35. Thus the relative spacing between lower/upper transmission and absorption bands can be controlled by judicious choice of r_1 and r_2.

2.3 Fabrication and Measurements

An experimental verification of the simulated results are done by carrying out measurements on fabricated prototype of the proposed FSS based rasorber. An array of 21 x 21

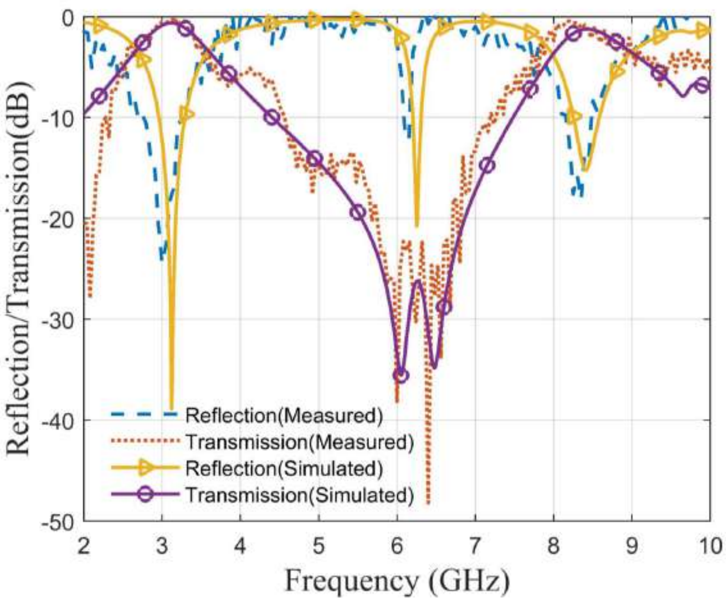

Figure 2.13: Comparison between simulated and measured reflection/transmission coefficients

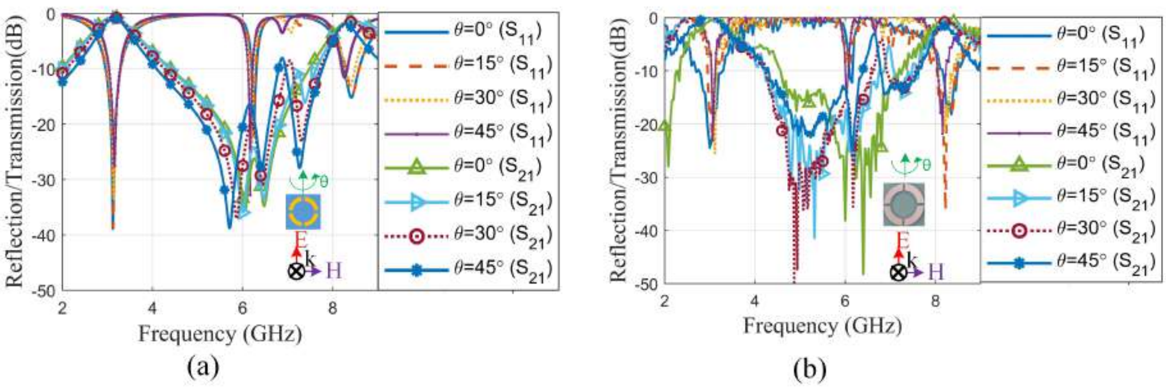

Figure 2.14: Reflection and transmission response of the proposed rasorber under various incident angles. (a) Simulated, and (b) measured.

rasorber unit cells is fabricated on a 0.8 mm thick FR-4 substrate. The photograph of the fabricated rasorber with overall size of 460 x 460 mm is depicted in Figure 2.11.

The measurement of the fabricated prototype is carried out in the anechoic chamber facility at CARE, IIT Delhi, using free space measurement technique. A pair of wide-band horn antenna connected with a portable Anritsu MS2028C vector network analyzer is used for reflection (S_{11}) and transmission (S_{21}) measurements. The experimental setups for measurements are shown in Figure 2.12. The measurement process includes the reference measurements for both reflection and transmission. In case of reflection, the measurements are first carried out on a perfect reflecting metallic sheet, which acts as a reference measurement. Afterwards, the metallic sheet is replaced by the fabricated

Table 2.4: Performance comparison of proposed FSS based rasorber.

Ref.	Absorption	Transmission with I.L	Thickness	Unit Cell Size	polarization
[77]	Broadband (4.8−6.81 GHz)	I.L <1dB @<1.5GHz	$0.04\lambda_L$ (2-layers)	0.0432 λ_L	Dual-Polarised
[91]	Broadband (2.6−5.25, 6.05−8.5 GHz),	0.48 dB @ 5.7 GHz	$0.134\lambda_L$ (2-layers)	$0.234\lambda_L$	Dual-Polarised
[108]	Broadband (4.02− 6.27, 8.21−12.02 GHz)	2.30dB @7.20GHz, 1.69dB @13.05GHz	$0.107\lambda_L$ (2-layers)	$0.2412\lambda_L$ x $0.1206\lambda_L$	Polarization-Sensitive
This Work	Narrowband @6.2GHz	0.6dB @ 3.1GHz, 1.2dB @ 8.4GHz	$0.00789\lambda_L$ (1-layer)	$0.197\lambda_L$	Polarization-Insensitive

prototype structure and measurements are carried out. The effective reflection coefficient is obtained by calculating the difference between the measured reflection coefficients of metallic sheet and fabricated prototype. For transmission, the reference measurement involves the direct path measurement between the two horn antennas. The effective transmission coefficient is the difference between the measured transmission coefficients of direct path and the fabricated prototype. The measured results plotted in comparison with the simulated results are shown in Figure 2.13, from which a reasonable agreement between the two is concluded.

Further, the measurements are carried out on the fabricated structure for various incident angles. The measured and simulated responses for multiple oblique incidence are shown in Figure 2.14, whereby an acceptable agreement between the two is achieved.

The comparison of the proposed FSS based rasorber with the previously reported rasorbers are shown in Table 2.4. The proposed rasorber is polarization-insensitive, single layer thin structure compared with other reported rasorbers [77, 91, 108]. The proposed rasorber also possess better insertion loss at two transmission bands in comparison with the other rasorbers reported in [77, 108].

2.4 Conclusion

In this chapter, a single-layer T-A-T rasorber is proposed exhibiting a narrowband absorption at 6.2 GHz between the two transmission bands at 3.1 and 8.4 GHz. The design is realized by combining the resonant absorber and dual bandpass FSS on the two sides of a single substrate layer. An ECM is studied for explaining the working of the proposed rasorber. An optimum range of lower and upper transmission bands is determined with respect to the center absorption frequency by tuning the bandpass FSS parameters. A prototype of the rasorber is fabricated and experimental validation is obtained.

Chapter 3

Single-Layered Flexible Multi-Band Rasorbers

In the previous chapter, a T-A-T type rasorber with a single narrowband absorption between two transmission bands has been designed on a single 0.8 mm thick substrate. The proposed T-A-T rasorber exhibits a single absorption band and is not thin enough for conformal applications. Now in this chapter, A-T-T-A / A-T-A-T-A type rasorber designs are proposed on a 0.25 mm thick flexible substrate. An A-T-T-A rasorber with dual-band transmission and dual-band absorption (2T2A) is obtained by combining the designs of a dual resonant FSS absorber and dual bandpass FSS on the two sides of a single dielectric substrate. Further, the rasorber structure is modified by an additional resonant structure for realizing A-T-A-T-A response, thus obtaining a rasorber with dual-band transmission and triple-band absorption (2T3A). The proposed rasorbers have desirable features like ultra-thin, polarization-insensitive, single-layered, and also exhibit conformal characteristics which makes the proposed structure more suited for practical applications.

3.1 Design and Analysis of the rasorber

A general theoretical understanding of a FSS based rasorber is represented by the schematic shown in Figure 3.1. The wave incident on a rasorber can be transmitted or reflected or absorbed depending upon its interaction with the structure at a particular frequency. In the transmission mode, the FSS rasorber selectively transmits the incident wave, whereas the reflections are minimized. However, the absorption mode occurs when both the trans-

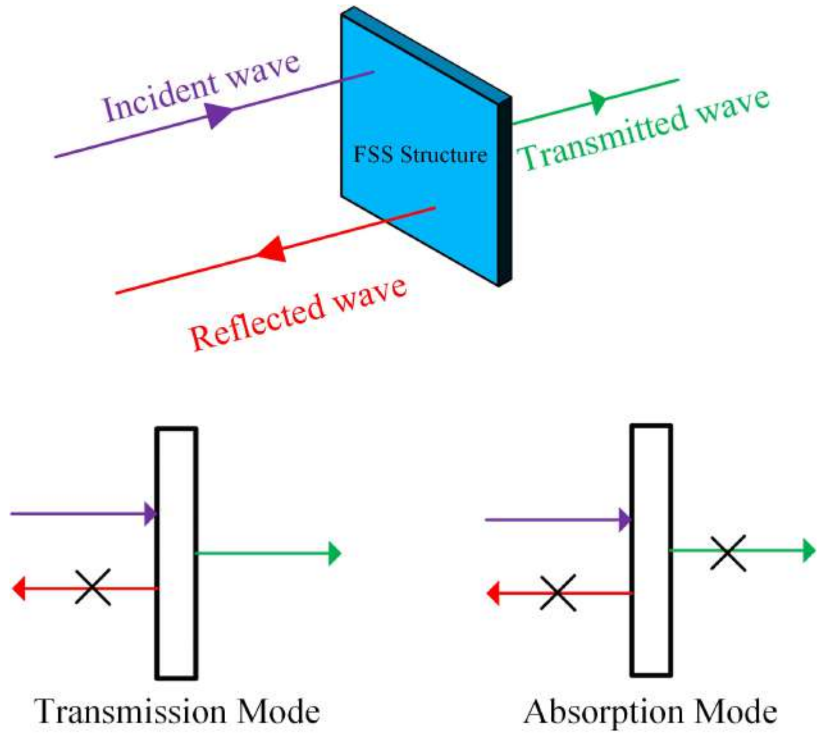

Figure 3.1: Schematic of a FSS based rasorber.

mission and reflection are minimum in a particular frequency band. This can be mathematically expressed by the following relation:

$$A = 1 - R - T$$

where A, R, and T are the absorption, reflection and transmission coefficients, respectively.

In the design for FSS based rasorber, the ground layer of the absorber is replaced by the bandpass FSS. However, the key point is that the bandpass FSS should act as a metallic reflecting surface at the absorbing frequencies, such that both the absorption and transmission characteristics are retained. Accordingly, the design approach for the FSS based rasorber involves the three-step process. In the first step, a dual bandpass FSS is studied. In the next step, the resonant absorption for various resonant structures are studied so as to appropriately locate the absorption frequencies with respect to the transmission bands of the bandpass FSS. In the last step, the absorption and bandpass FSS designs are combined on the two sides of a single substrate to realize the desired absorption and transmission characteristics. The proposed FSS based rasorber is designed on an ultra-thin flexible Taconic substrate of thickness (t) equal to 0.254 mm, dielectric constant (ϵ_r) of 2.2, loss tangent ($tan\delta$) equal to 0.0009, and the thickness of copper

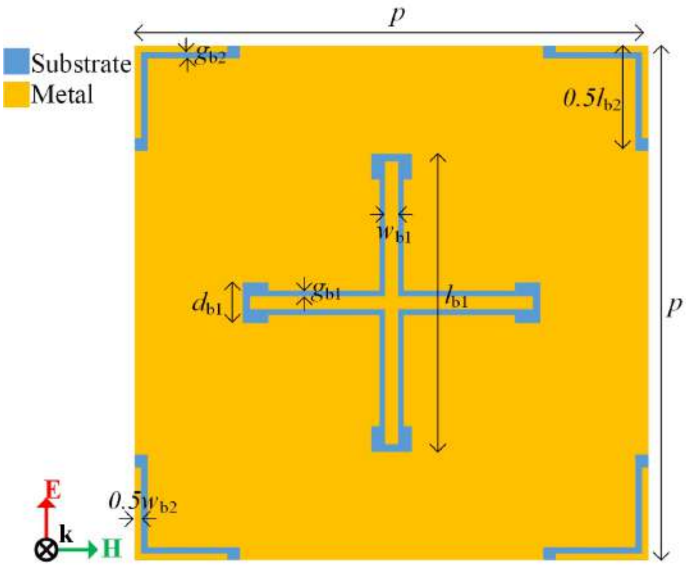

Figure 3.2: Unit cell schematic of the dual bandpass FSS. $p = 15$, $l_{b1} = 8.5$, $w_{b1} = 1$, $g_{b1} = 0.3$, $d_{b1} = 1$, $l_{b2} = 6.3$, $w_{b2} = 1$, $g_{b2} = 0.3$ (all dimensions are in mm).

plating equal to 0.035 mm.

3.1.1 Bandpass FSS

The unit cell schematic of the dual bandpass FSS is depicted in Figure 3.2. The unit cell consists of a cross-loop shaped slot etched at the center of the unit cell with length l_{b1}. Also, a quarter of cross-loop shaped slot with length l_{b2} is etched at each corner of the unit cell. The center and the corner loop slots give rise to the passband at their corresponding resonating frequencies. The simulated response of bandpass FSS shows dual transmission bands at 9.7 and 13.0 GHz as illustrated in Figure 3.3(a), where the transmission bands at 9.7 GHz and 13.0 GHz are due to the center loop slot and the corner loop slot, respectively. The design flow of the bandpass FSS is illustrated using Figure 3.3(b) and 3.3(c), where the simulated response for cross slot and cross-loop slot are shown, respectively. In the case of cross slot shaped bandpass FSS, the passband is obtained at around 14.3 GHz (Figure 3.3(b)). The passband is decreased from 14.3 to 9.7 GHz (Figure 3.3(c)) by inserting a metallic cross of width w_{b1} in between the cross shaped slot, thus modifying the slot shape from simple cross to cross-loop. The decrease in transmission frequency in the case of cross-loop shaped design can be attributed to the increased slot dimensions for cross-loop slot. Also, in the case of cross-loop shaped bandpass FSS, the transmission response has a higher selectivity and is steeper at the

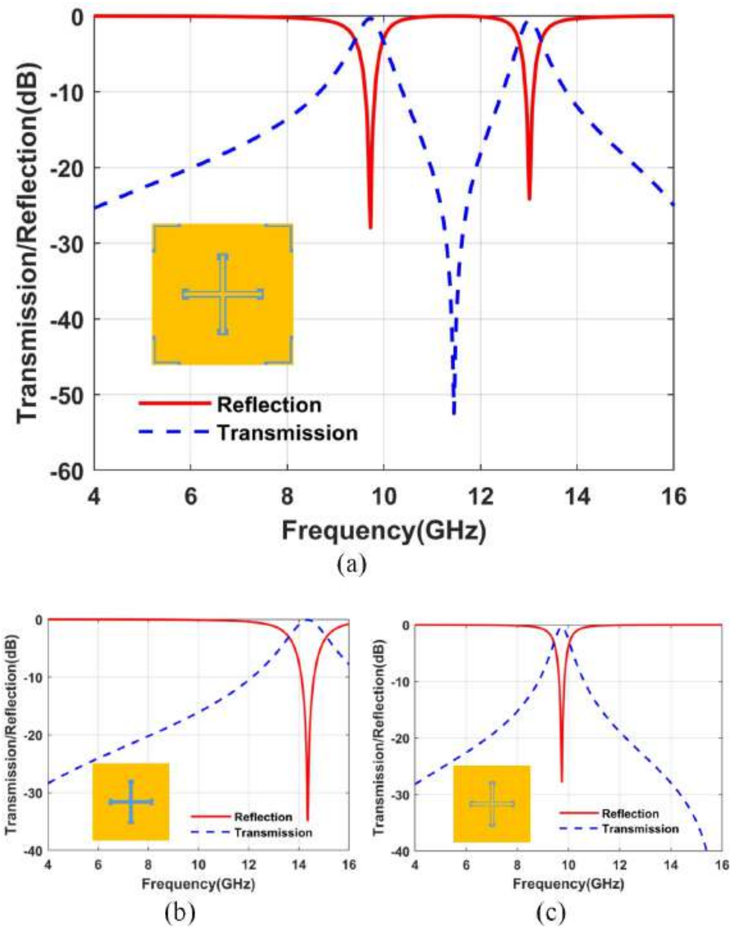

Figure 3.3: Simulated transmission and reflection coefficients of (a) dual bandpass FSS, (b) cross slot bandpass FSS, and (c) cross loop slot bandpass FSS.

passband in comparison with the simple cross shaped bandpass FSS. For rasorber design, the passband with higher selectivity is more preferred, so that bandpass FSS can be utilized as a reflective surface in the near adjacent bands. The addition of corner slots in the bandpass FSS results in an another passband at a higher frequency of 13.0 GHz. The dependence of the two passbands on its corresponding slots is further illustrated in Figure 3.4(a) and 3.4(b), where the response of the bandpass FSS with respect to the varying slot lengths l_{b1} and l_{b2} are provided, respectively. The variation of center cross-loop length l_{b1} from 7.5 mm to 9.5 mm, causes the lower passband to decreases from 10.9 to 8.9 GHz, respectively and a marginal shift in the upper passband frequency. Similarly, the variation of corner cross-loop length l_{b2} from 5.3 mm to 7.3 mm, decreases the higher passband from 15.2 to 11.2 GHz, while lower passband frequency remains unaltered.

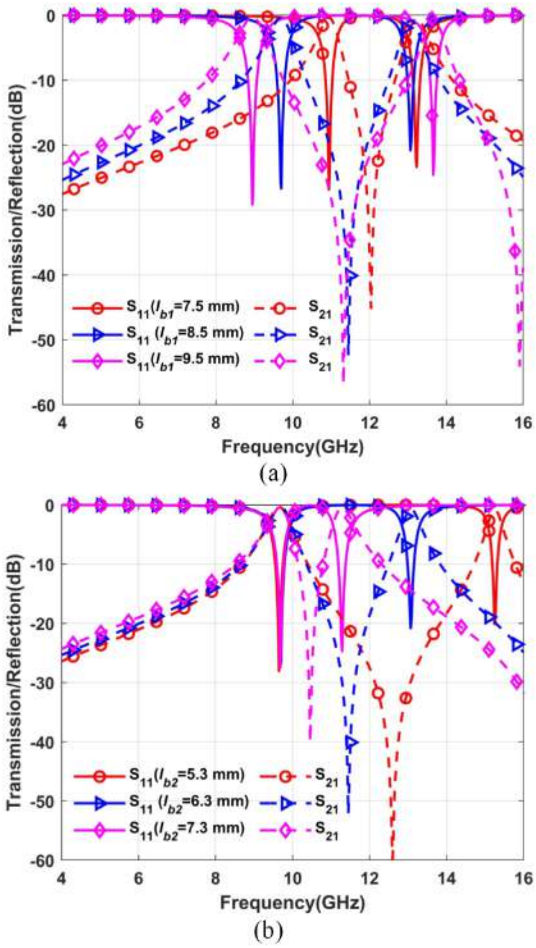

Figure 3.4: Simulated response of the dual bandpass FSS with varying (a) l_{b1}, and (b) l_{b2}.

3.1.2 FSS Absorber

The FSS absorber is designed in such a way that at the absorption frequencies, the bandpass FSS analyzed in the previous subsection acts as a maximum reflective surface. The unit cell schematic of the dual-band FSS absorber as shown in Figure 3.5, consists of a metallic ring resonator surrounding a metallic cross resonator printed on the front side of substrate while having a complete metallic cover on its other side. The inner and outer radii of the ring resonator are denoted by r_1 and $r_1 + w_1$, respectively. The length and width of the cross resonator are denoted by l_3 and w_3, respectively. The two resonators leads to the resonant absorption at two separate frequencies. The two resonant structures are selected such that its corresponding resonant frequencies are above and below the two passband frequencies obtained for the bandpass FSS in the previous subsection. The simulated reflection coefficient of the dual-band FSS absorber is shown in Figure 3.6, where the resonant absorption at two frequencies are obtained. The absorption

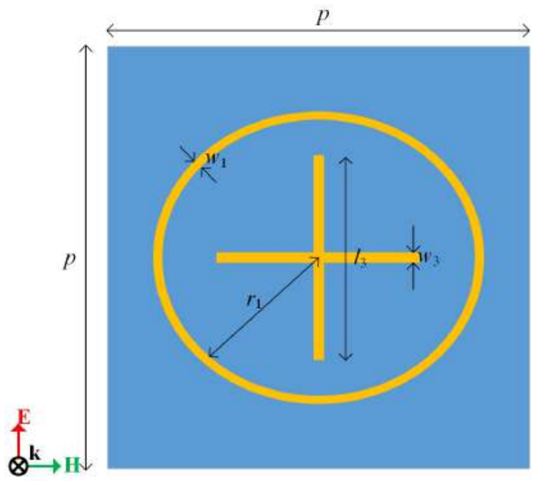

Figure 3.5: Unit cell schematic of the dual-band FSS absorber. p = 15, r_1 = 5.0, w_1 = 0.5, l_3 = 7.0, w_3 = 0.4 (all dimensions are in mm).

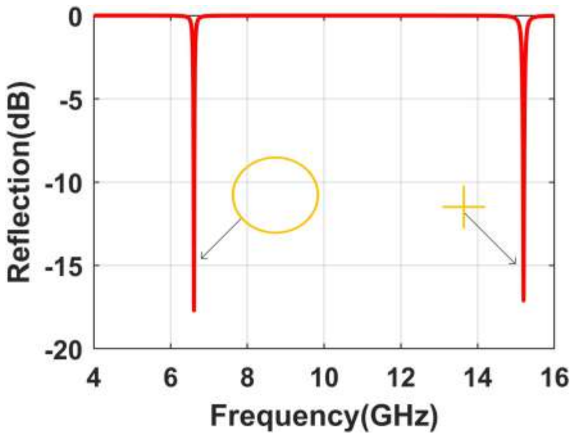

Figure 3.6: Simulated reflection coefficient of the dual-band FSS absorber.

at higher frequency of 15.1 GHz corresponds to the cross resonator while the ring resonator contributes to the absorption at 6.6 GHz. The two absorption frequencies achieved are located on the two sides of the dual passband frequencies of the bandpass FSS (9.7 and 13.0 GHz) studied in the previous subsection.

3.1.3 Proposed 2T2A and 2T3A rasorbers

The schematic of the proposed 2T2A rasorber is shown in Figure 3.7. The design of the proposed rasorber with dual-band absorption and dual-band transmission is accomplished by printing the individual designs of dual-band FSS absorber and dual bandpass FSS on the front and back sides of a 0.254 mm thick Diclad substrate, respectively. The front side of the rasorber unit cell consists of the printed metallic ring and cross resonators (Figure 3.7(b)). On the backside of rasorber, centre and corner cross loop slots are etched out

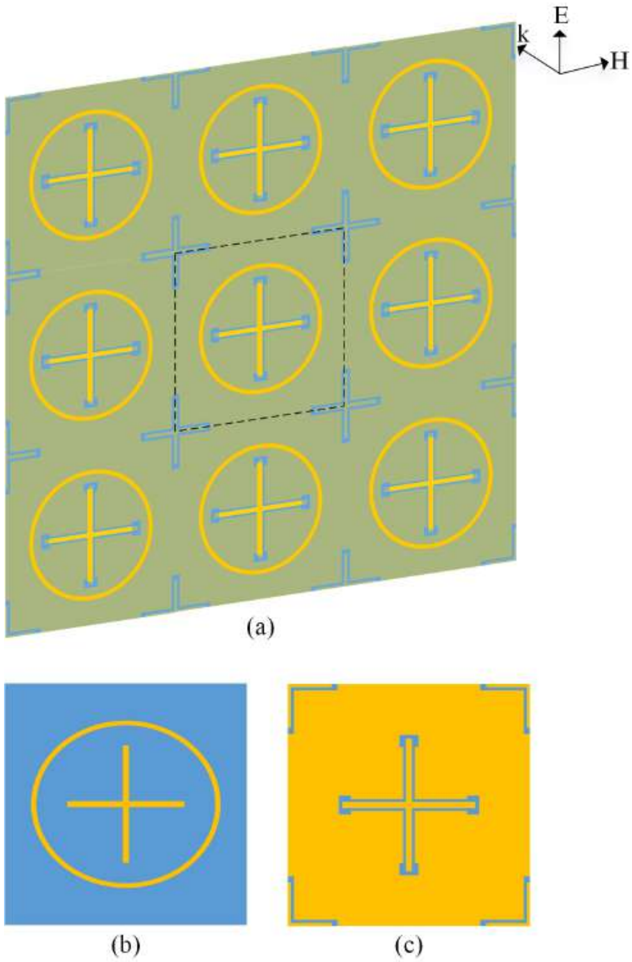

Figure 3.7: (a) Perspective view of the proposed 2T2A rasorber. (b) Front, and (c) back views of the unit cell of 2T2A rasorber.

within the metal plated substrate (Figure 3.7(c)). The proposed design of the rasorber is analyzed using CST EM Solver. The simulated transmission and reflection coefficients of the 2T2A rasorber are shown in Figure 3.8. Maximum absorption of 93.62% and 92.29% are obtained at the lower absorption frequency (f_{al}= 6.4 GHz) and the upper absorption frequency (f_{au}= 14.7 GHz), respectively. The lower transmission frequency (f_{tl}= 9.6 GHz) and the upper transmission frequency (f_{tu} = 13.4 GHz) exhibits a minimum insertion loss of 0.2 dB and 0.4 dB, respectively.

Further, it can be observed from Figure 3.8 that between the two transmission bands at 9.6 and 13.4 GHz, there occurs a reflective band within which the transmission dip occurs. This reflective band between the two transmission bands is utilized for achieving another absorption band. The proposed 2T2A rasorber, is modified to obtain the third absorption band in between the two transmission bands, thus leading to two transmission and three absorption (2T3A) bands. The front view of the modified unit cell for obtaining

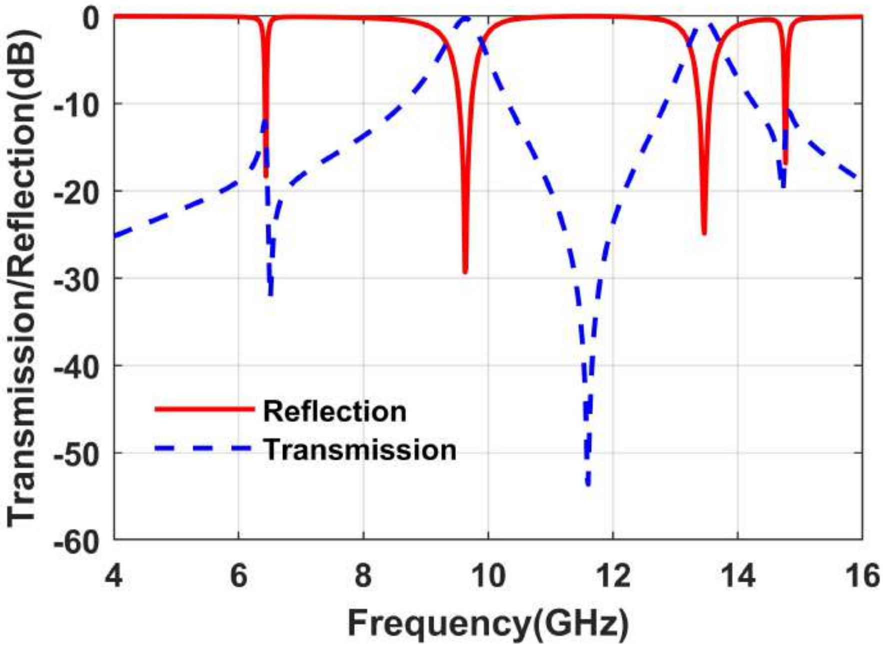

Figure 3.8: Simulated reflection and transmission coefficients of the proposed 2T2A rasorber.

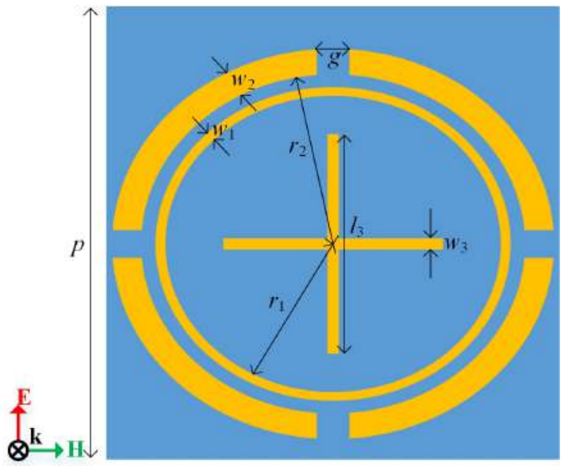

Figure 3.9: Front view of the unit cell of the proposed 2T3A rasorber. $p = 15$, $r_1 = 5.0$, $w_1 = 0.5$, $l_3 = 7.0$, $w_3 = 0.4$, $r_2 = 5.9$, $w_2 = 0.9$, $g = 0.8$ (all dimensions are in mm).

dual transmission and triple absorption bands is shown in Figure 3.9, which consists of an additional split-ring resonator along with the ring and cross resonators. The split-ring has an inner and outer radii of r_2 and $r_2 + w_2$, respectively. The gap dimensions of the split-ring are denoted by g. The split-ring resonator is capable of achieving a resonance at the desired frequency between the two transmission bands. The perspective view of the 2T3A rasorber is shown in Figure 3.10. The simulated reflection and transmission coefficients for the 2T3A rasorber are shown in Figure 3.11. A middle absorption frequency (f_{am}) in between the two transmission bands is achieved in addition to the lower and upper

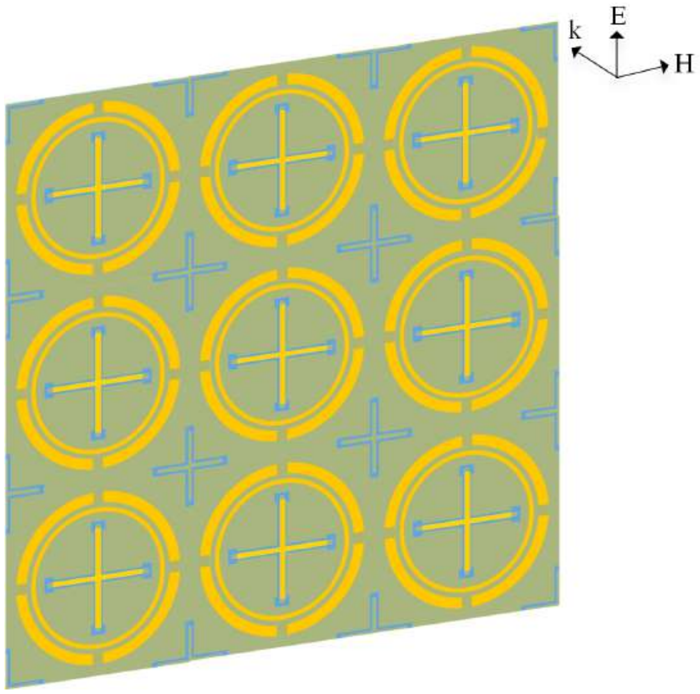

Figure 3.10: Perspective view of the proposed 2T3A rasorber.

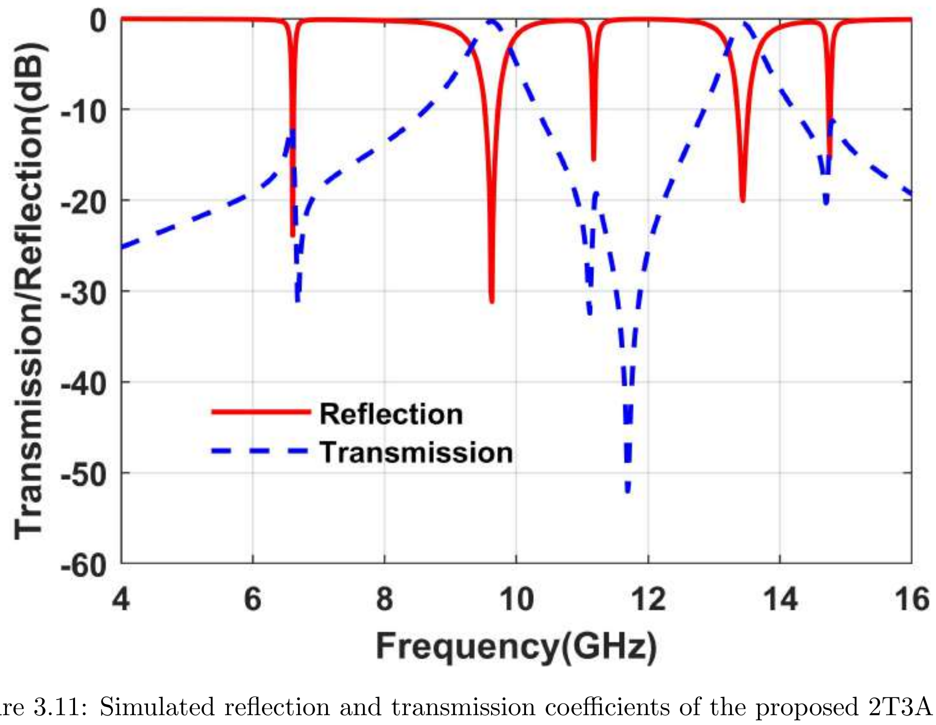

Figure 3.11: Simulated reflection and transmission coefficients of the proposed 2T3A rasorber.

absorption frequencies. The three absorption frequencies in the proposed 2T3A rasorber are obtained at 6.6 GHz, 11.1 GHz and 14.7 GHz with the absorption peaks of 94.00%, 96.81% and 91.91%, respectively. The transmission bands for 2T3A rasorber are at 9.6 and 13.4 GHz, with the minimum insertion loss of 0.3 dB and 0.5 dB, respectively.

The working of the proposed rasorber can be explained by the electric field / surface

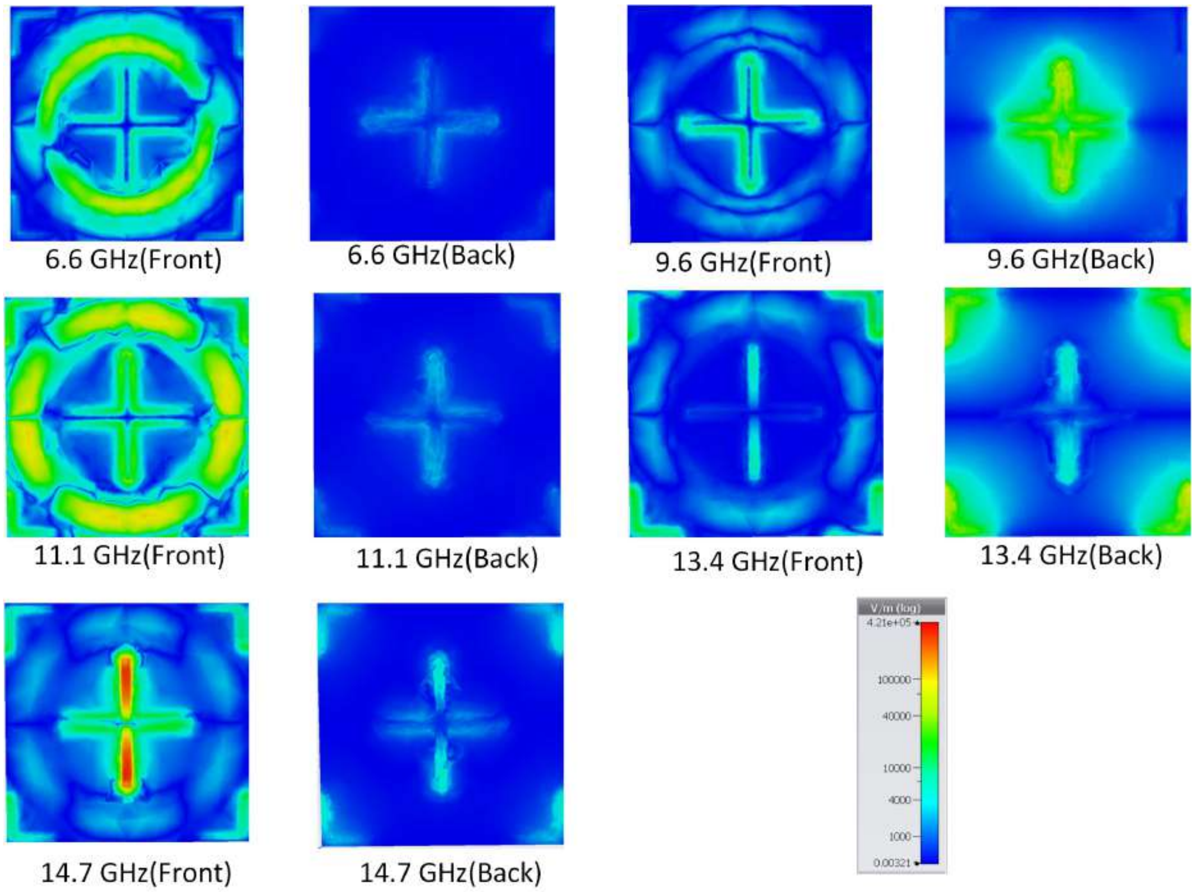

Figure 3.12: Electric field distribution of the proposed 2T3A rasorber.

current distributions and the corresponding equivalent circuit model (ECM). The scalar electric field intensity (volts/meter) on the front and back sides for the proposed 2T3A rasorber at different frequencies of interest (6.6, 9.6, 11.1, 13.4 and 14.7 GHz) are shown in Figure 3.12. At the absorption frequencies of 6.6, 11.1 and 14.7 GHz, the electric field is strongly concentrated on the front side of circular ring, split-ring and cross resonators, respectively. Relatively, lesser concentration of field is observed on the back side of each resonator at the absorption frequencies. The strong concentration of fields shows that there is no reflection and no transmission, leading to absorption of incident EM wave.

The absorption and transmission phenomenon can further be explained by the analysis of surface current and the associated ECM model. The surface current distributions at the absorption and transmission frequencies for the 2T3A rasorber are shown in Figure 3.13. An equivalent circuit model (ECM) for both 2T2A and 2T3A rasorbers are presented in Figure 3.14. The metallic resonators at the front side is modelled using a series networks whereas, the slot resonators are represented by the parallel LC network. The addition of split-ring in the 2T3A rasorber is model by an additional $L_3 - C_3$ network (Figure

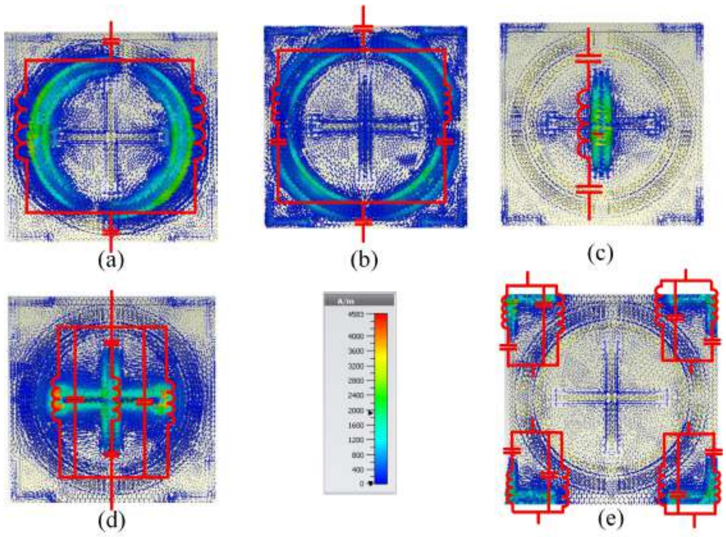

Figure 3.13: Surface current distribution of the proposed 2T3A rasorber (a) 6.6 GHz, (b) 11.1 GHz, (c) 14.7 GHz, (d) 9.6 GHz, and (e) 13.4 GHz.

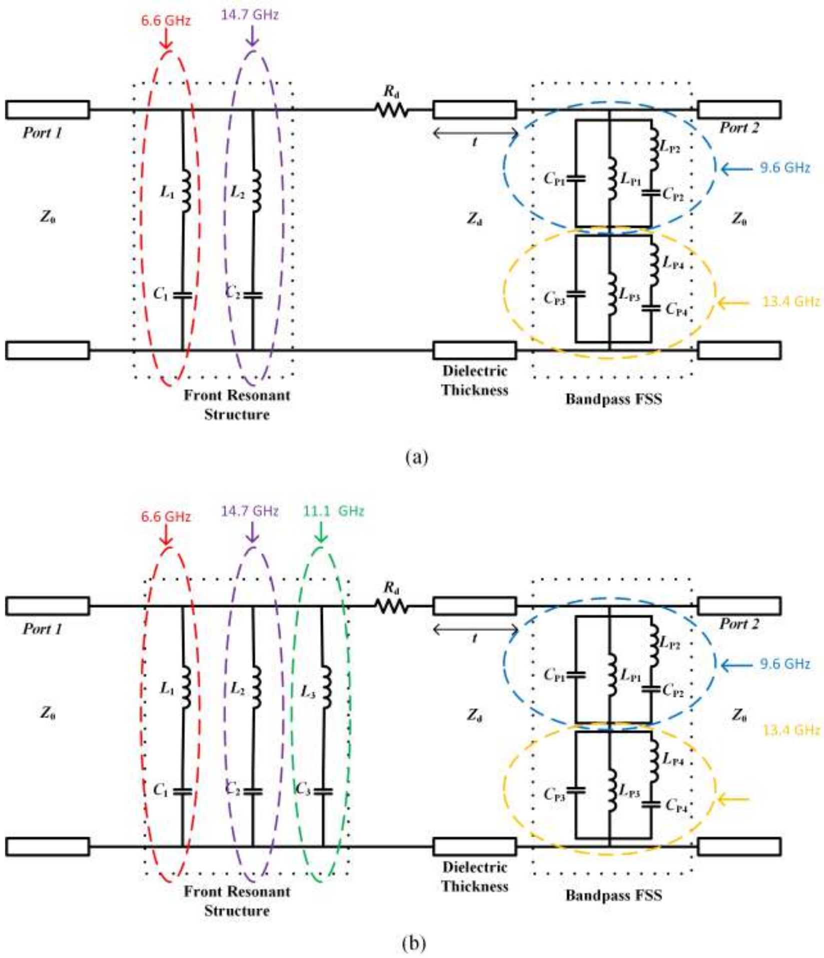

Figure 3.14: ECM of the proposed (a) 2T2A, and (b) 2T3A rasorbers (L_1 = 91.827 nH, L_2 = 15.260 nH, L_3 = 25.553 nH, C_1 = 0.006 pF, C_2 = 0.007 pF, C_3= 0.007 pF, R_d = 1.791 Ω, Z_d = 254.173 Ω, L_{P1} = 0.145 nH, C_{P1} = 0.100 pF, L_{P2} = 0.180 nH, C_{P2} = 0.850 pF, L_{P3} = 0.120 nH, C_{P3} = 0.010 pF, L_{P4} = 0.311 nH, C_{P4} = 0.315 pF).

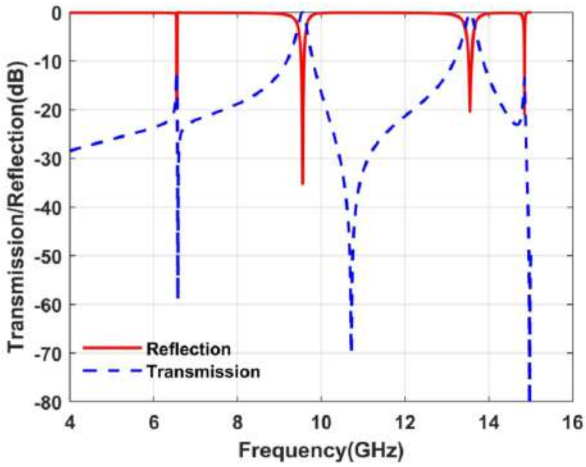

(a)

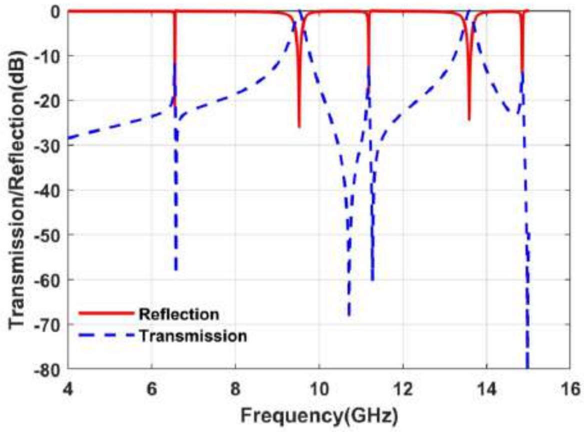

(b)

Figure 3.15: Simulated response for ECM of the proposed (a) 2T2A, and (b) 2T3A rasorbers.

3.14(b)).

At 6.6 GHz (lower absorption frequency), the surface currents are concentrated along the circular ring resonator (Figure 3.13(a)). Due to the induced time varying current, an inductive effect gets generated along the metallic ring patch, while the inter-element spacing leads to the capacitance effect. This inductor-capacitor arrangement can be reduced to a simple series LC network (L_1 and C_1 in Figure 3.14) at that particular frequency. At 11.1 GHz (middle absorption frequency) the surface currents are concentrated along the split-ring resonator on the front side of the structure Figure 3.13(b). Due to the spilt-gap in the resonator an additional capacitor exists in the corresponding LC network. Thus, the equivalent network contributed by split ring resonator can be reduced to series LC network (L_3 and C_3 in Figure 3.14) shown in the ECM. The currents at the higher absorption frequency of 14.7 GHz are concentrated along the metallic cross patch at the center of the structure thus leading to the corresponding series LC response as shown in

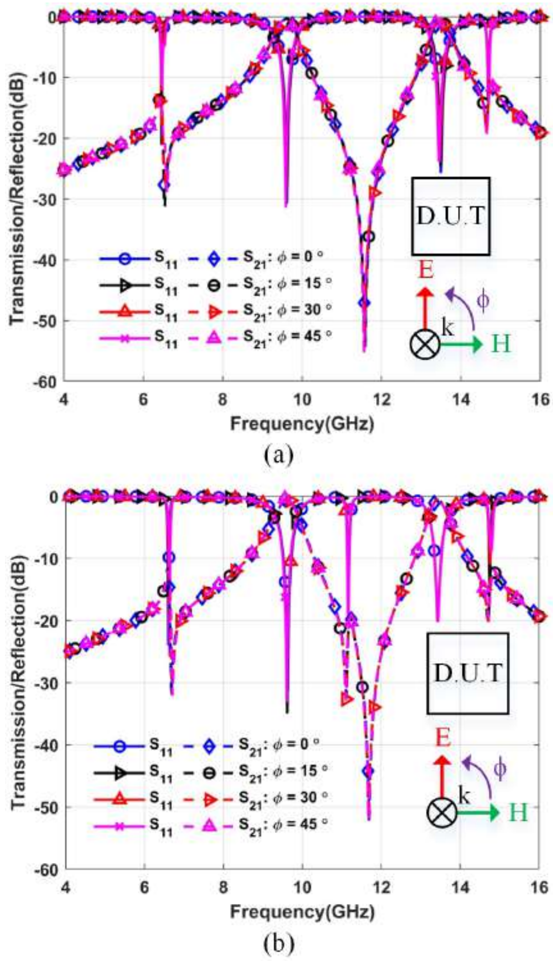

Figure 3.16: Simulated response under various polarization angles for the proposed (a) 2T2A, and (b) 2T3A rasorbers.

Figure 3.13(c). The equivalent network contributed by the metallic cross patch is also a series LC network (L_2 and C_2 in Figure 3.14).

For the transmission frequencies at 9.6 and 13.4 GHz, it can be observed that the electric field intensity is concentrated along the edges of the center and corner cross loop slots, respectively on the back side of the structure (Figure 3.13). In contrast to the absorption frequencies, relatively less concentration of fields is observed on the metallic resonators printed on the front side of substrate. Due to the higher concentration of electric fields along the edges of the slot, the transmission occurs at the corresponding resonant frequency while the reflections are minimized.

The surface current intensity at transmission frequencies of 9.6 and 13.4 GHz are induced at the edges of the center and corner cross loop slot, respectively at the backside of the structure in accordance with the incident electric field. The inductance and capacitance effect due to the induced surface current at 9.6 and 13.4 GHz is modelled using the

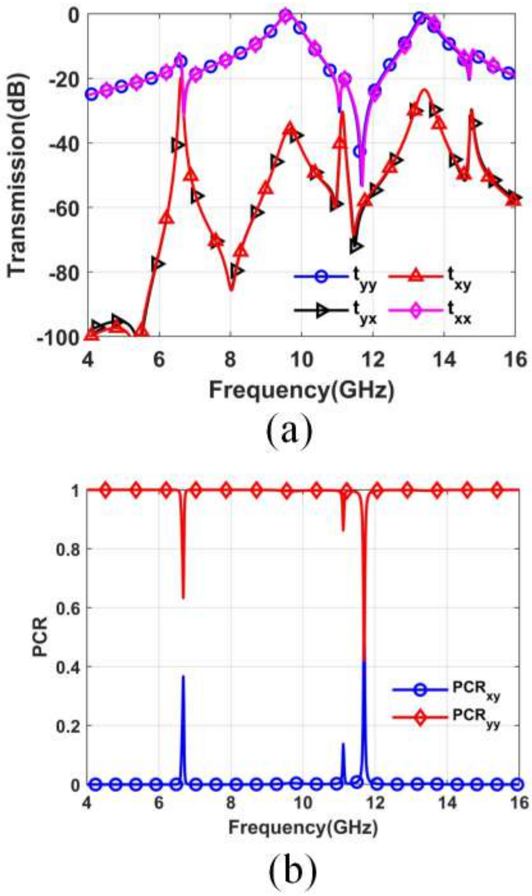

Figure 3.17: (a) Co- and cross-polarization transmission response, and (b) PCR of the proposed 2T3A rasorber.

LC network shown in Figure 3.13(d) and 3.13(e), respectively. The networks corresponding to 9.6 GHz and 13.4 GHz can be reduced to the parallel LC arrangement (L_{P1}, L_{P2}, C_{P1}, C_{P2} at 9.6 GHz and L_{P3}, L_{P4}, C_{P3}, C_{P4} at 13.4 GHz in Figure 3.14).

The dielectric thickness is modelled using a transmission line of length equal to the substrate thickness t and the characteristics impedance Z_d given by

$$Z_d = \frac{Z_0}{\sqrt{\epsilon_r}} \tag{3.1}$$

where Z_0 is the characteristic impedance of free space. R_d models the equivalent resistance due to the dielectric loss of substrate [137]. The overall ABCD parameters of the ECM can be obtained by the cascaded matrix multiplication given as:

$$\begin{bmatrix} A & B \\ C & D \end{bmatrix} = \begin{bmatrix} 1 & 0 \\ Y_{\mathrm{F}} & 1 \end{bmatrix} \times \begin{bmatrix} 1 & R_{\mathrm{d}} \\ 0 & 1 \end{bmatrix} \times \begin{bmatrix} \cos\beta t & \mathrm{j} Z_d \sin\beta t \\ \mathrm{j}\sin\beta t / Z_{\mathrm{d}} & \cos\beta t \end{bmatrix}$$

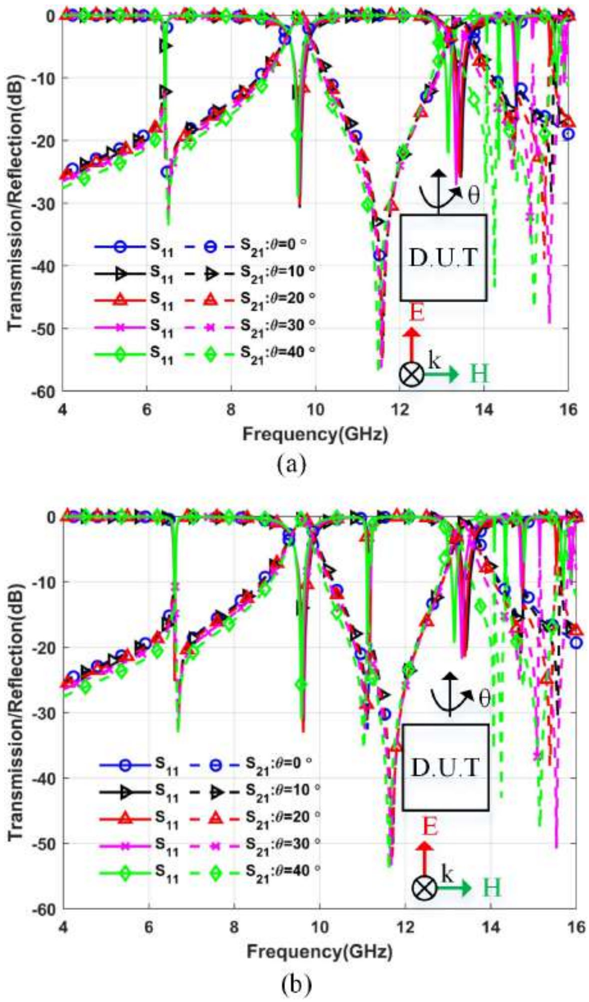

Figure 3.18: Simulated response under various incident angles for the proposed (a) 2T2A, and (b) 2T3A rasorbers.

$$\times \begin{bmatrix} 1 & 0 \\ Y_{\mathrm{P}} & 1 \end{bmatrix} \tag{3.2}$$

where Y_{F}, Y_{P} represents admittance of front resonant structure and dual bandpass FSS at the back side of substrate, respectively. Also, the propagation constant β is given as $\beta = \beta_0\sqrt{\mu_r\epsilon_r}$ (μ_r and ϵ_r are the relative permeability and permittivity of the dielectric substrate, respectively).

The S-parameters of the ECM are calculated from the ABCD parameters using the conversion formula given as follows:

$$S_{11} = \frac{A+B/Z_0-CZ_0-D}{A+B/Z_0+CZ_0+D} \tag{3.3}$$

$$S_{21} = \frac{2}{A+B/Z_0+CZ_0+D}. \tag{3.4}$$

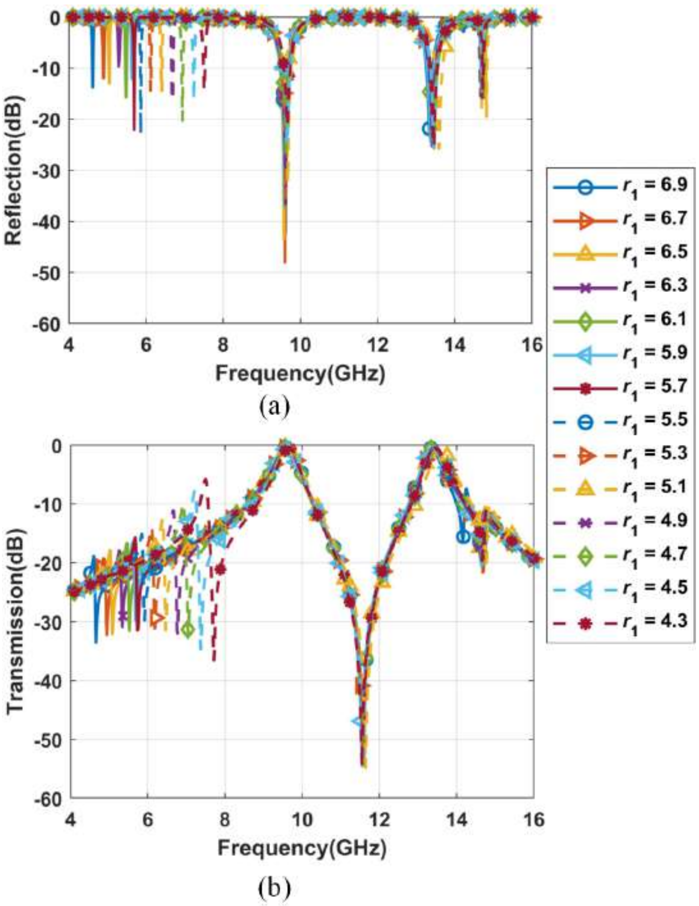

Figure 3.19: Simulated reflection and transmission coefficients of the proposed 2T2A rasorber for varying r_1 (in mm).

The absorptivity, $A(\omega)$ can be calculated from S-parameters obtained in equation (3.3) and (3.4) using the formula given below.

$$A(\omega) = 1 - |S_{11}|^2 - |S_{21}|^2. \tag{3.5}$$

The ECM of the proposed 2T2A and 2T3A rasorbers are analyzed using Keysight ADS simulator. The simulated transmission and reflection coefficients for the proposed rasorbers are shown in Figure 3.15. The simulation response for ECM of 2T2A rasorber shown in Figure 3.15(a), achieves dual resonant absorption at 6.5 and 14.8 GHz, along with dual passband at 9.5 and 13.5 GHz. The additional resonant network in the ECM of 2T3A rasorber achieves a third resonant absorption at 11.1 GHz as depicted in Figure 3.15(b).

The proposed 2T2A and 2T3A rasorbers are analyzed under various polarization angles of the incident EM wave as shown in Figure 3.16. For both the 2T2A and 2T3A

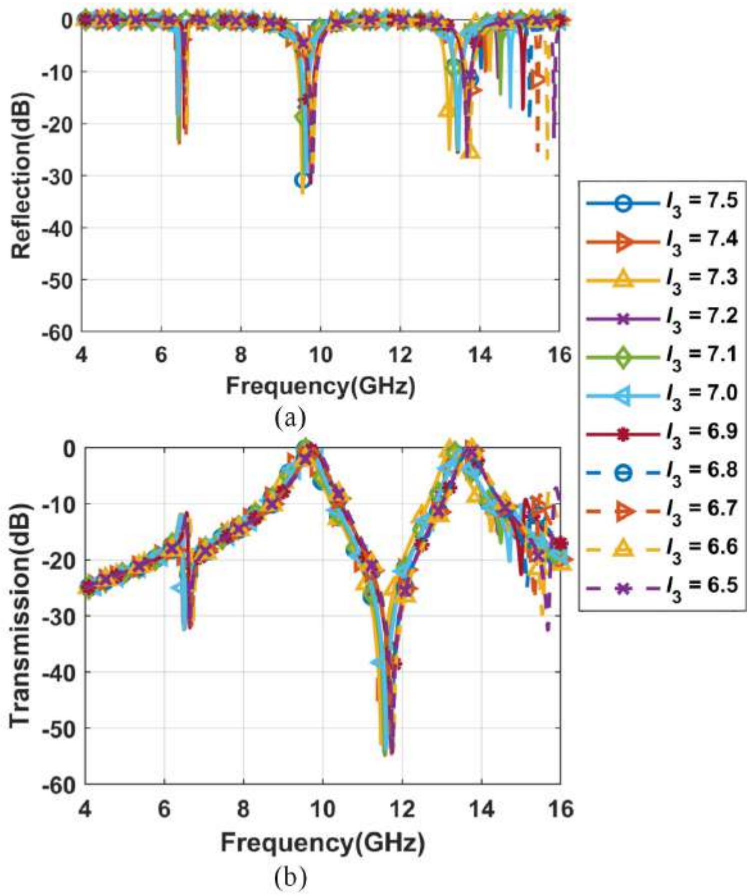

Figure 3.20: Simulated reflection and transmission coefficients of the proposed 2T2A rasorber for varying l_3 (in mm).

rasorbers, the simulated transmission and reflection coefficients remain unaltered for different polarization angle, thereby verifying the polarization-independent behavior of the proposed rasorber.

The polarization characteristics of the proposed 2T3A rasorber are analyzed by studying the cross-polarized (t_{ij}) transmission coefficients with respect to their co-polarized (t_{ii}) counterpart. The co- and cross-polarization transmission response for the x-polarized or y-polarized incident wave for 2T3A rasorber is shown in Figure 3.17(a). The cross-polarized transmission coefficient (t_{yx} or t_{xy}) for the x-polarized or y-polarized incident wave is negligible as compared to the co-polarized transmission coefficient (t_{xx} or t_{yy}), which suggests that the transmitted wave has the same polarization as that of the incident wave. Thus, the proposed transmissive rasorber structures do not affect the polarization of the incident EM wave. The polarization conversion ratio (PCR) [36] plot for the proposed 2T3A rasorber is provided in the Figure 3.17(b). It can be observed that PCR_{yy} is close to 1, while PCR_{xy} is close to 0 at the two transmission frequencies, which further verifies that

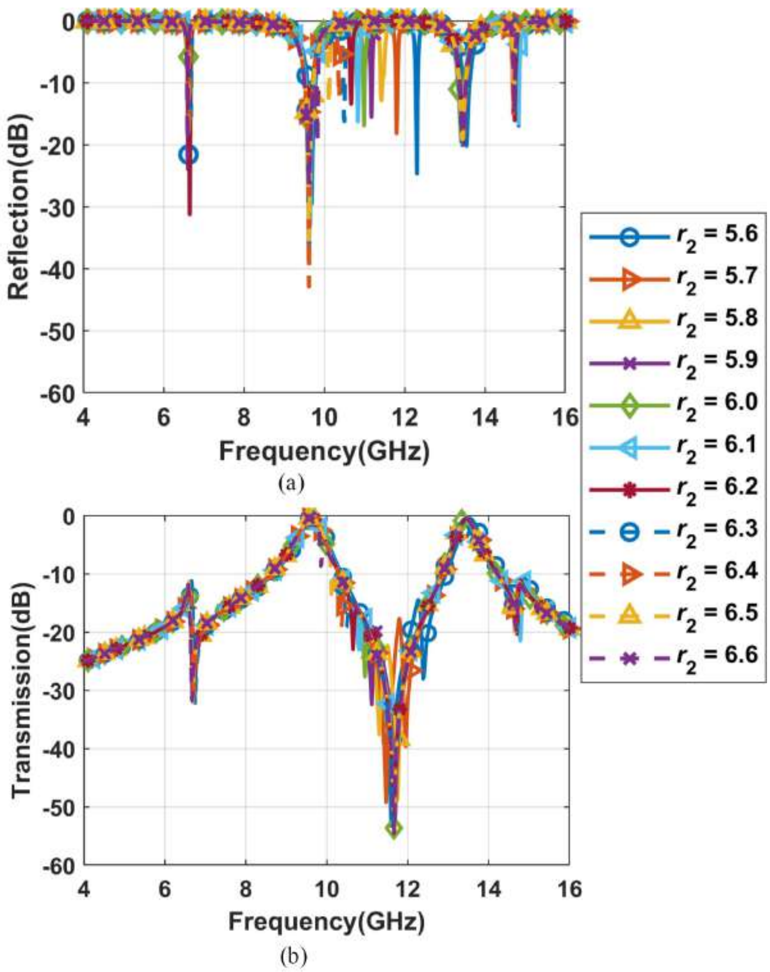

Figure 3.21: Simulated reflection and transmission coefficients of the proposed 2T3A rasorber for varying r_2 (in mm).

no polarization conversion takes place in the proposed rasorber structure.

The oblique incidence response of the proposed rasorbers is studied under various angle of incidence for TE polarization as shown in Figure 3.18. In both 2T2A and 2T3A rasorbers, an acceptable response for the reflection and transmission coefficients are maintained up to 40° of incident angle, within which the acceptable transmission and absorption at the corresponding frequencies are maintained. Beyond 40° of incident angle, the absorption at only 14.7 GHz gets considerably degraded, even though the performance at other frequencies of interest are maintained up to 60° of incident angle, thus limiting the overall angular stability of the proposed rasorber to 40°.

Table 3.1: Performance parameters of 2T2A rasorber with varying r_1

r_1 (mm)	f_{a1} (GHz) (Ab)	f_{t1} (GHz) (I.L)	f_{tu} (GHz) (I.L)	f_{au} (GHz) (Ab%)
6.9	4.61 (94.64%)	9.61 (0.32 dB)	13.35 (0.53 dB)	14.69 (93.10%)
6.7	4.89 (92.27%)	9.60 (0.28 dB)	13.38 (0.49 dB)	14.74 (92.89%)
6.5	5.05 (94.05%)	9.57 (0.30 dB)	13.42 (0.49 dB)	14.69 (93.33%)
6.3	5.29 (97.70%)	9.60 (0.32 dB)	13.38 (0.50 dB)	14.71 (93.60%)
6.1	5.48 (94.75%)	9.60 (0.30 dB)	13.38 (0.47 dB)	14.76 (92.44%)
5.9	5.64 (92.40%)	9.58 (0.33 dB)	13.36 (0.47 dB)	14.69 (90.84%)
5.7	5.69 (97.32%)	9.61 (0.28 dB)	13.42 (0.49 dB)	14.71 (91.36%)
5.5	5.86 (97.11%)	9.60 (0.31 dB)	13.41 (0.47 dB)	14.69 (91.00%)
5.3	6.12 (92.84%)	9.61 (0.27 dB)	13.42 (0.47 dB)	14.71 (92.71%)
5.1	6.41 (92.57%)	9.67 (0.28 dB)	13.59 (0.45 dB)	14.82 (92.36%)
4.9	6.69 (92.13%)	9.61 (0.28 dB)	13.42 (0.49 dB)	14.67 (92.70%)
4.7	6.94 (91.61%)	9.63 (0.30 dB)	13.46 (0.47 dB)	14.69 (92.74%)
4.5	7.23 (81.45%)	9.65 (0.30 dB)	13.45 (0.46 dB)	14.71 (90.56%)
4.3	7.51 (71.67%)	9.65 (0.36 dB)	13.46 (0.50 dB)	14.72 (91.92%)

Ab: Absorption; I.L: Insertion loss; f_{al}: Lower absorption frequency; f_{tl}: Lower transmission frequency; f_{tu}: Upper transmission frequency; f_{au}: Upper absorption frequency.

3.2 Parametric Studies on the Proposed Rasorbers

In the proposed 2T2A rasorber, resonant absorption occurring at the two sides of the dual passband corresponds to the ring and the cross metallic resonators printed on the front side of the substrate. The lower absorption frequency is associated with the ring resonator while the upper absorption frequency is associated with the cross resonator. A parametric analysis is carried out on the proposed 2T2A rasorber with respect to the dimensions of the ring and cross resonators, keeping the bandpass dimensions constant such that a frequency range is obtained within which the lower and upper absorption frequency can be tuned in the proposed design.

Table 3.2: Performance parameters of 2T2A rasorber with varying l_3

l_3 (mm)	f_{al} (GHz) (Ab)	f_{t1} (GHz) (I.L)	f_{tu} (GHz) (I.L)	f_{au} (GHz) (Ab%)
7.5	6.45 (91.25%)	9.56 (0.29 dB)	13.43 (0.51 dB)	14.02 (78.79%)
7.4	6.45 (94.48%)	9.56 (0.28 dB)	13.45 (0.47 dB)	14.13 (82.98%)
7.3	6.42 (92.57%)	9.54 (0.28 dB)	13.22 (0.51 dB)	14.25 (85.90%)
7.2	6.41 (92.97%)	9.60 (0.38 dB)	13.43 (0.47 dB)	14.46 (88.74%)
7.1	6.42 (94.52%)	9.58 (0.30 dB)	13.43 (0.48 dB)	14.51 (92.29%)
7.0	6.43 (93.62%)	9.63 (0.29 dB)	13.46 (0.48 dB)	14.76 (92.29%)
6.9	6.57 (93.29%)	9.75 (0.27 dB)	13.69 (0.43 dB)	15.07 (90.61%)
6.8	6.57 (92.35%)	9.77 (0.27 dB)	13.67 (0.43 dB)	15.24 (89.62%)
6.7	6.62 (94.17%)	9.75 (0.30 dB)	13.70 (0.42 dB)	15.45 (88.02%)
6.6	6.64 (93.00%)	9.79 (0.28 dB)	13.74 (0.41 dB)	15.69 (83.80%)
6.5	6.57 (90.80%)	9.79 (0.27 dB)	13.67 (0.42 dB)	15.86 (82.55%)

Ab: Absorption; I.L: Insertion loss; f_{al}: Lower absorption frequency; f_{tl}: Lower transmission frequency; f_{tu}: Upper transmission frequency; f_{au}: Upper absorption frequency.

The reflection and transmission coefficients for varying values of r_1 while keeping other parameters constant, are shown in Figure 3.19. The variation in the performance parameters of the 2T2A rasorber with varying r_1 shown in Figure 3.19 has been arranged in Table 3.1. It can be observed from Table 3.1 that decreasing the value of r_1 from 6.9 mm to 4.3 mm increases the lower absorption frequency (f_{al}) from 4.61 GHz to 7.51 GHz while the other frequencies of interest (f_{tl}, f_{tu}, f_{au}) remains nearly the same with small variations. It can be observed that by increasing the value of f_{al} beyond 6.94 GHz the corresponding absorption reduces below 90%. Thus for retaining the absorption greater than 90% the range of lower absorption frequency f_{al} can be achieved from 4.61 to 6.94 GHz by changing the value of r_1 from 6.9 mm to 4.7 mm, respectively.

In another case the reflection and transmission coefficients corresponding to varying length of cross resonator l_3 keeping the other parameters constant, are depicted in Figure

Table 3.3: Performance parameters of 2T3A rasorber with varying r_2

r_2 (mm)	f_{al} (GHz) (Ab%)	f_{t1} (GHz) (I.L)	f_{am} (GHz) (Ab%)	f_{tu} (GHz) (I.L)	f_{au} (GHz) (Ab%)
5.6	6.62 (95.08%)	9.68 (0.29 dB)	12.30 (97.06%)	13.53 (0.49 dB)	14.84 (91.69%)
5.7	6.66 (93.01%)	9.61 (0.29 dB)	11.80 (96.55%)	13.44 (0.55 dB)	14.70 (91.89%)
5.8	6.67 (91.06%)	9.63 (0.29 dB)	11.42 (93.87%)	13.41 (0.63 dB)	14.74 (92.67%)
5.9	6.60 (94.00%)	9.63 (0.31 dB)	11.17 (96.81%)	13.43 (0.52 dB)	14.75 (91.91%)
6.0	6.64 (92.74%)	9.61 (0.28 dB)	10.98 (97.25%)	13.41 (0.58 dB)	14.74 (91.83%)
6.1	6.66 (93.58%)	9.64 (0.32 dB)	10.83 (96.94%)	13.42 (0.52 dB)	14.83 (92.83%)
6.2	6.64 (94.71%)	9.61 (0.28 dB)	10.66 (94.07%)	13.45 (0.50 dB)	14.74 (92.73%)
6.3	6.67 (91.26%)	9.61 (0.29 dB)	10.50 (95.53%)	13.42 (0.52 dB)	14.74 (91.02%)
6.4	6.63 (93.18%)	9.61 (0.30 dB)	10.37 (92.74%)	13.45 (0.52 dB)	14.69 (92.69%)
6.5	6.60 (92.45%)	9.61 (0.28 dB)	10.10 (87.54%)	13.44 (0.51 dB)	14.71 (92.22%)
6.6	6.59 (93.53%)	9.61 (0.34 dB)	9.82 (54.94%)	13.45 (0.56 dB)	14.72 (92.73%)

Ab: Absorption; I.L: Insertion loss; f_{al}: Lower absorption frequency; f_{tl}: Lower transmission frequency; f_{tu}: Upper transmission frequency; f_{am}: Middle absorption frequency; f_{au}: Upper absorption frequency.

3.20. The performance parameters at each frequency of interest for varying cross resonator length l_3 are illustrated in Table 3.2. The upper absorption frequency (f_{au}) increases from 14.02 to 15.86 GHz by decreasing the resonator length l_3 from 7.5 mm to 6.5 mm, respectively. Also, the performance at other frequencies of interest (f_{al}, f_{tl}, f_{tu}) remains nearly the same. However, for retaining the absorption greater than 90%, the upper absorption frequency f_{au} can slide from 14.51 GHz to 15.07 GHz by the decreasing the value of l_3 from 7.1 mm to 6.9 mm, respectively.

In the 2T3A rasorber design, the middle absorption frequency (f_{am}) corresponds to the resonance frequency of the split-ring resonator. Thus a range for f_{am} can be obtained by studying the parametric variation of split-ring radius r_2 on the corresponding absorption frequency. The reflection and transmission coefficients of the proposed 2T3A rasorber

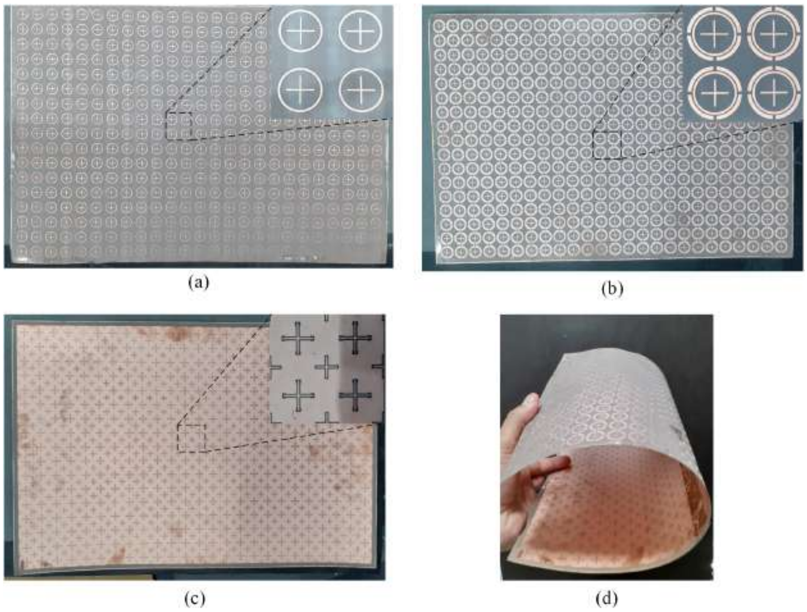

Figure 3.22: Photograph of the fabricated prototypes of the proposed rasorbers. (a) Front side of 2T2A rasorber, (b) front side of 2T3A rasorber, (c) back side of both 2T2A and 2T3A rasorbers, and (d) flexible view of 2T3A rasorber.

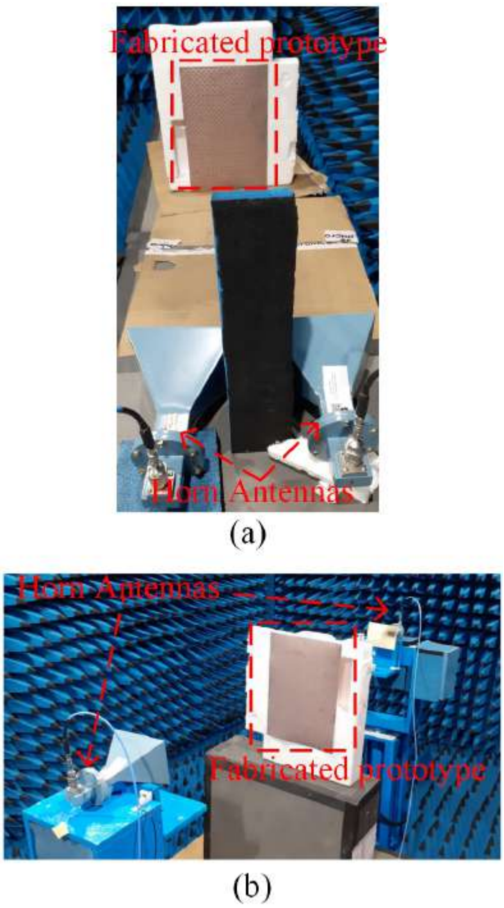

Figure 3.23: Photograph of the experimental setup for (a) reflection, and (b) transmission measurements.

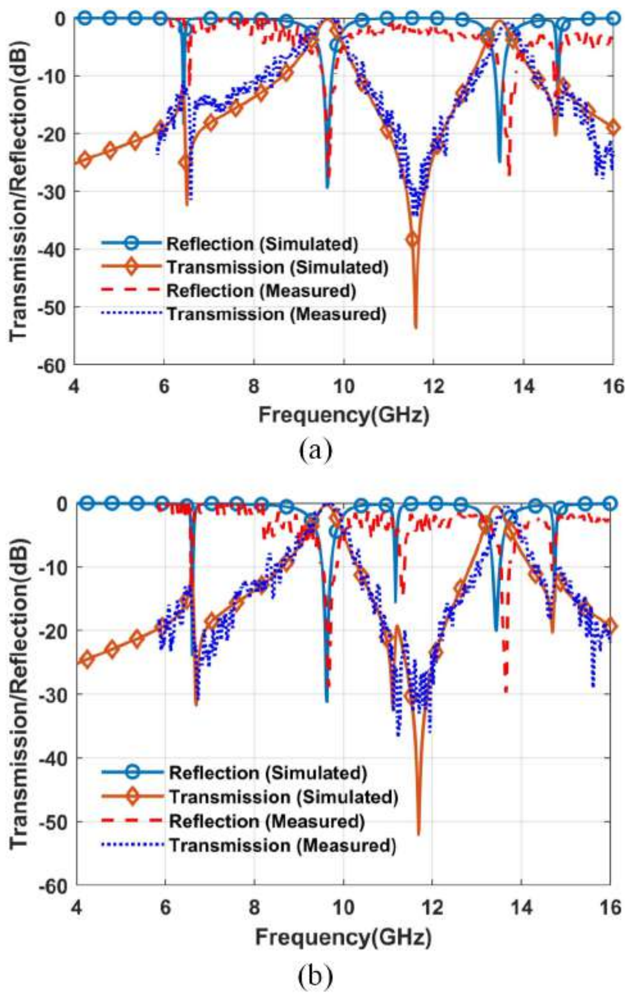

Figure 3.24: Simulated and measured reflection and transmission coefficients of the proposed (a) 2T2A, and (b) 2T3A rasorbers.

for the varying value of r_2 while keeping the other parameters constant, are depicted in Figure 3.21. The performance at each frequency of interest with respect to different values of r_2 has been provided in Table 3.3. It can be observed that by varying the radius of split-ring r_2 from 5.6 mm to 6.6 mm, the middle absorption frequency f_{am} decreases from 12.30 GHz to 9.82 GHz, respectively. However, below 10.37 GHz, the absorption reduces below 90%. As such an acceptable range of f_{am} can be defined from 12.30 GHz to 10.37 GHz which corresponds to value of r_2 from 5.6 mm to 6.4 mm, respectively.

3.3 Experimental Verification and Discussion

An experimental verification of the proposed 2T2A and 2T3A rasorbers are obtained by carrying out measurements on the fabricated prototype of each rasorber. An array consisting of 17 x 25 unit cells for each 2T2A and 2T3A rasorber are fabricated on a 0.254

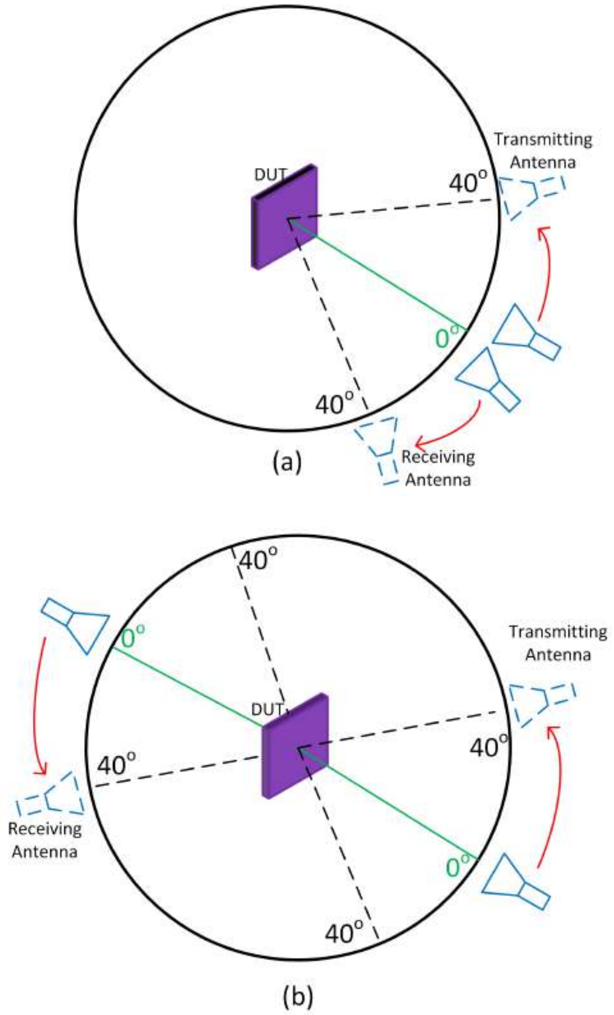

Figure 3.25: Schematic of the setups for the (a) reflection, and (b) transmission measurement of the proposed rasorber (DUT) under oblique incidence.

mm thick Taconic substrate having dielectric constant (ϵ_r) of 2.2 and loss tangent (tan δ) equal to 0.0009. The photograph of the fabricated prototype for both 2T2A and 2T3A rasorbers, with an overall dimensions of 265 mm x 385 mm are shown in Figure 3.22. The bandpass FSS design on the back side of substrate is same for both the proposed rasorbers as shown in Figure 3.22(c).

The measurement of the fabricated prototypes are carried out in an anechoic chamber using free space measurement technique. For carrying out measurements a pair of three different standard gain horn antennas connected with a Keysight PNA Network Analyzer N5224B, are sequentially used. The three different horn antennas used belongs to separate J(5.85−8.20 GHz), X(8.20−12.40 GHz) and Ku(12.40−18.0 GHz) frequency bands. The experimental setups for reflection and transmission measurements are shown in Figures 3.23(a) and 3.23(b), respectively. A reference measurement is initially carried out in both

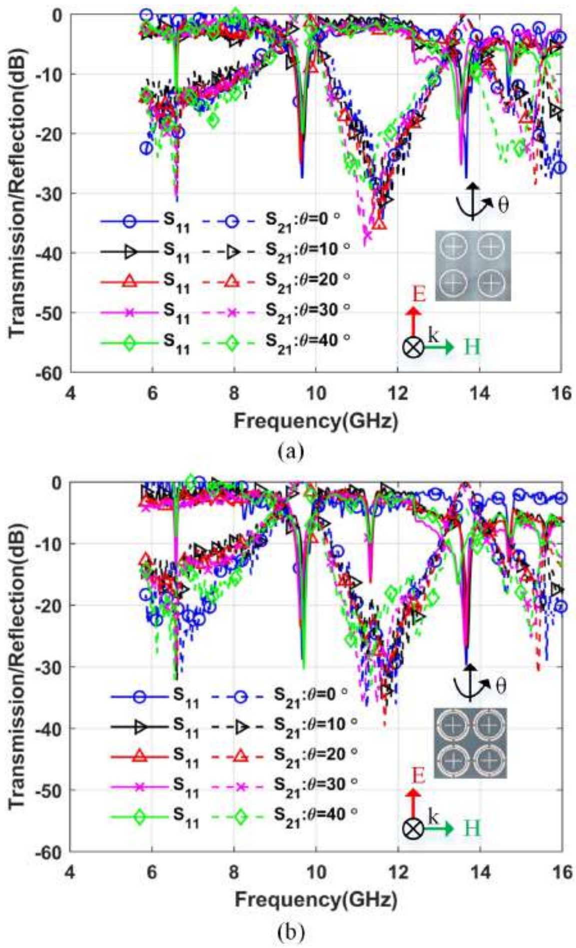

Figure 3.26: Measured reflection and transmission coefficients under oblique incident angles (TE polarized incident wave) for the proposed (a) 2T2A, and (b) 2T3A rasorbers.

the reflection and transmission setup, with which the measured results are then normalised for obtaining the effective reflection and transmission coefficients. In case of reflection, the reference measurement is the reflections obtained from a metallic sheet while for the other case of transmission, the direct free space path loss measurement between the two horn antennas provides the reference measurement. The comparison of simulated and measured reflection and transmission coefficients for both the 2T2A and 2T3A rasorbers are shown in Figure 3.24. A close agreement between the measured and simulated results for both the rasorber provides an experimental validation for the responses of the proposed rasorbers.

The performance of the proposed rasorbers has been verified experimentally under the oblique incident waves. The schematic of measurement setups for reflection and transmission coefficients for wave striking the rasorbers at oblique angles is shown in Figure 3.25. The rasorber structure (DUT: Device Under Test) is placed at the center of the

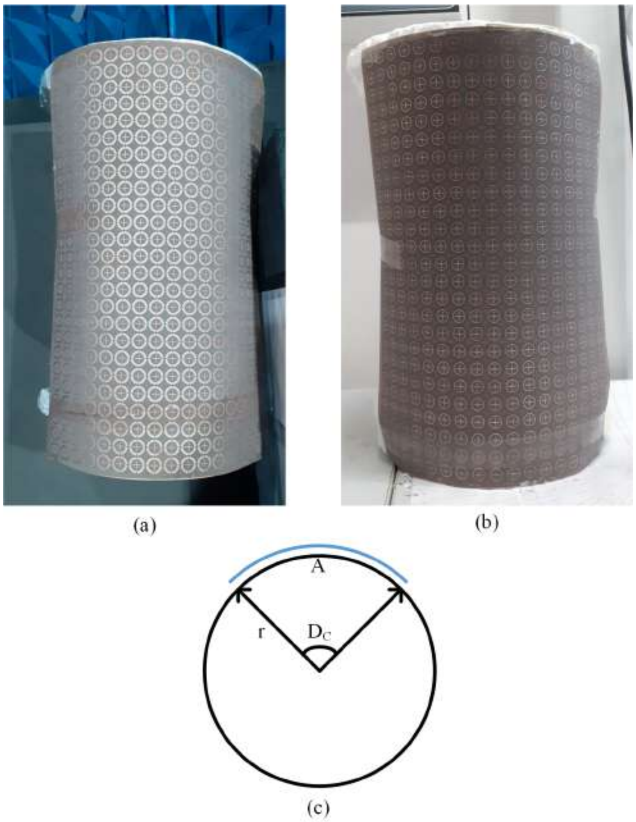

Figure 3.27: Photograph of the curved prototype of the proposed (a) 2T2A, and (b) 2T3A rasorbers. (c) Lateral schematic of the curved prototype with radius r, degree of curvature D_C and arc length A.

defined circular area. The path perpendicular to the surface is the normal incidence path (or the 0° line). For measurement at different oblique angles of incidence, the transmitting and the receiving antennas are moved along the circular path (either clockwise or anticlockwise) making the required oblique angles with the normal incidence path.

In case of reflection measurement, as depicted in Figure 3.25(a) the transmitting and receiving antennas are placed at the front side of the structure. In the normal incidence both the antennas are placed along the 0° line, while for the oblique incidence the transmitting and receiving antennas are moved in the anticlockwise (or clockwise) and clockwise (or anticlockwise) direction, respectively on the circular path making the necessary angle with the normal path. This measurement technique for the different angles is consistent with the basic theory of EM propagation i.e. angle of incidence is equal to angle of reflection.

For transmission coefficient measurement, the transmitting antenna is placed at the front side of the structure, while the receiving antenna is placed at the back side of the structure (Figure 3.25(b)). For the normal incidence both the antennas are placed along the 0° line, while for the oblique incidence, the transmitting and the receiving antennas are

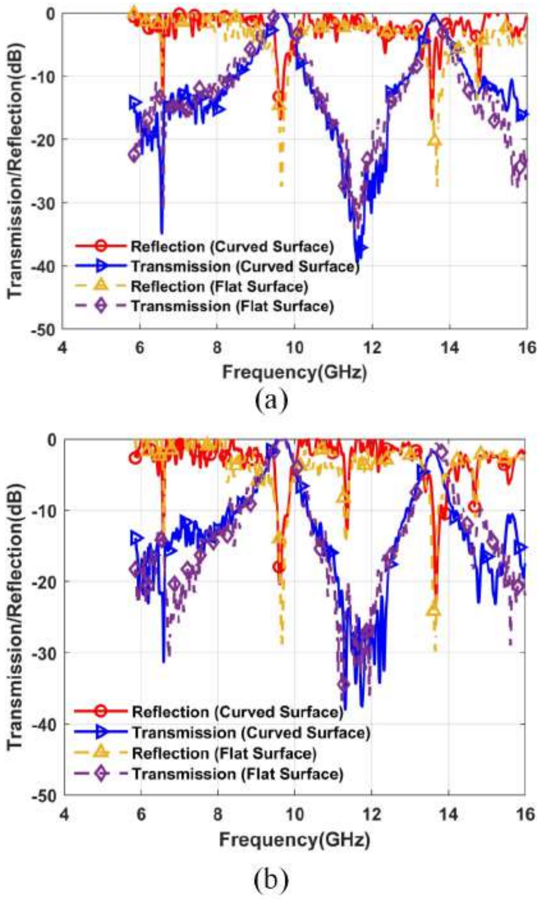

Figure 3.28: Comparison of the measured reflection and transmission coefficients for flat and curved surface with degree of curvature (D_C) = 120° for the proposed (a) 2T2A, and (b) 2T3A rasorbers under the normal TE incidence.

moved along the circular path in the same direction i.e. either clockwise or anticlockwise, making the required oblique angle with the normal incidence path.

The measured reflection and transmission coefficients of the rasorber prototypes carried out under oblique incidence for TE polarization is provided in Figure 3.26, and the angular stability up to 40° is experimentally verified.

In order to verify the flexible behavior of the proposed rasorber, reflection and transmission measurements for TE polarized incident wave are also carried out for the curved surface. The fabricated prototype is pasted on a cylindrical foam based structure, with the curvature given along the narrower side and the degree of curvature equal to 120°. The radius r of the cylindrical foam based structure is 126.5 mm, which is calculated using the formulae $r = \frac{180A}{\pi D_C}$, where A is the arc length and D_C is the degree of curvature. The narrower side of structure having length of 265 mm is the arc length A. The photograph of the curved structure for both 2T2A and 2T3A rasorbers are shown in Figure 3.27. The reference measurement for reflection is obtained by the metal sheet pasted on

Table 3.4: Performance Comparison of proposed FSS based rasorber with earlier reported multi/wide-band absorbers/rasorbers

Ref.	Absorption	Transmission / Min. Insertion loss	Thick	Size	N.O.L	L.E	Polarization	Con.
[48]	Dual-band (16.6 and 24.4 GHz)	-Nil-	$0.022\lambda_0$	$0.076\lambda_0^2$	1	No	Insensitive	No
[49]	Penta-band (9.9, 10.4, 10.9, 11.7 and 13.2 GHz)	-Nil-	$0.026\lambda_0$	$0.146\lambda_0^2$	1	No	Sensitive	No
[47]	Triple-band (4.1, 6.6, 9.9 GHz)	-Nil-	$0.007\lambda_0$	$0.038\lambda_0$	1	No	Insensitive	Yes
[108]	Wide band (4.0−6.2 GHz, 8.2−12.0) GHz	Dual-band (7.2 GHz / 2.3 dB and 13.0 GHz / 1.69 dB)	$0.107\lambda_0$	$0.029\lambda_0^2$	2	Yes	Sensitive	No
[111]	Wide band (1.6−2.9 GHz, 3.8−4.7 GHz, 5.3−6.9 GHz)	Dual-band (3.5 GHz / 0.25 dB and 4.9 GHz / 0.1 dB)	$0.076\lambda_0$	$0.021\lambda_0^2$	2	Yes	Dual	No
[78]	Wide band (3.8−10.8 GHz)	Low pass (< 860 MHz) / (< 1 dB)	$0.140\lambda_0$	$0.048\lambda_0^2$	2	Yes	Dual	No
[96]	Wide band (1.5−4.6 GHz, 9.2−13.7 GHz)	6.5 GHz / 0.67 dB	$0.171\lambda_0$	$0.010\lambda_0^2$	4	Yes	Dual	No
[92]	Wide band (2.3−5.3 GHz, 7.8−14.6 GHz)	6.3 GHz / 0.78 dB	$0.111\lambda_0$	$0.023\lambda_0^2$	3	Yes	Dual	No
[97]	Wide band (2.5−4.6 GHz, 7.7−12.0 GHz)	6.0 GHz / 0.27 dB	$0.075\lambda_0$	$0.010\lambda_0^2$	2	Yes	Dual	No
	Wide-band (2.9−5.6 GHz, 7.4−9.2 GHz)	Single-band (6.0 GHz / 0.38 dB)	$0.0639\lambda_0$	$0.038\lambda_0^2$	1	Yes	Dual	No
[95]	Wide-band (3.1−5.0 GHz, 6.4−8.3 GHz)	Single-band (5.8 GHz / 0.45 dB)	$0.0878\lambda_0$	$0.042\lambda_0^2$	1	Yes	Dual	No
	Wide-band (3.2−6.4 GHz, 8.3−10.5 GHz)	Single-band (7.7 GHz / 0.25 dB)	$0.0987\lambda_0$	$0.045\lambda_0^2$	2	Yes	Dual	Yes
This	**Dual-band (6.4 and 14.7 GHz)**	**Dual-band (9.6 GHz / 0.29 dB and 13.4 GHz / 0.48 dB)**	$\mathbf{0.0054\lambda_0}$	$\mathbf{0.101\lambda_0^2}$	**1**	**No**	**Insensitive**	**Yes**
work	**Triple-band (6.6, 11.1 and 14.7 GHz)**	**Dual-band (9.6 GHz / 0.31 dB and 13.4 GHz / 0.52 dB)**	$\mathbf{0.0055\lambda_0}$	$\mathbf{0.108\lambda_0^2}$	**1**	**No**	**Insensitive**	**Yes**

λ_0= free space wavelength at the lowest frequency of interest, Con. = Conformal, L.E = Lumped Elements, N.O.L = No. of Layers.

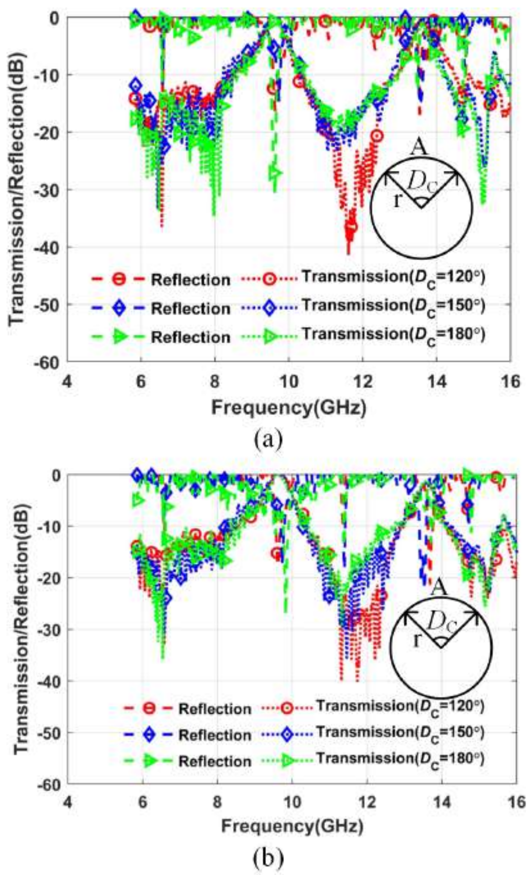

Figure 3.29: Comparison of the measured reflection and transmission coefficients for curved surface with various degree of curvature (D_C) for the proposed (a) 2T2A, and (b) 2T3A rasorbers under the normal TE incidence.

the same cylindrical foam. The measured reflection and transmission coefficients of the curved structure in comparison with the measured results of the flat structure for both the 2T2A and 2T3A rasorbers are shown in Figure 3.28. A close agreement between the measured results of curved and flat structures, verifies the conformal behavior of the proposed rasorbers.

The conformal behavior of the proposed structures is further studied by increasing the degree of curvature D_C to 150° and 180° for each curved structure. For obtaining the degree of curvature D_C equal to 150° and 180°, the structures are pasted on cylindrical foam having radius r equal to 101.2 mm and 84.3 mm, respectively. Figure 3.29 compares the measured response of the curved 2T2A and 2T3A rasorber prototypes at various degrees of curvature D_C. An acceptable response at each frequency of interest even upto 180° degree of curvature confirms the enhanced conformality of the proposed structures.

The comparison of the performance of the proposed ultra-thin, conformal rasorbers with the previously reported multi-band absorbers/wide-band rasorbers is presented in

Table 3.4. The proposed rasorbers possess the superior performance of exhibiting dual transmission band along with the dual/triple absorptions as compared to the reported multi-band absorbers in [48],[49],[47]. In comparison with the wide absorptive rasorber reported in [108, 111, 78, 96, 92, 95, 97] the proposed rasorber is an ultra-thin, conformal, single-layer structure with multiple narrow band absorptions and does not require any mounted lumped elements. Furthermore, the proposed rasorber is also a flexible structure and the measured results verifies the conformal characteristics up to 180° curvature angle.

3.4 Conclusion

In this chapter, a single-layer flexible (A-T-T-A/A-T-A-T-A)rasorbers is proposed exhibiting dual transmission along with dual/triple absorption bands. The design for dual bandpass FSS is studied and combined with dual-band resonant absorber in such a way that at the absorption frequencies the bandpass FSS possess maximum possible reflection, thus realizing a 2T2A rasorber where the two resonant absorption (f_{al} = 6.4 GHz and f_{au} = 14.7 GHz) are located on the two sides of dual transmission bands (f_{tl} = 9.6 GHz and f_{tu} = 13.4 GHz). Further, the structure is modified to 2T3A rasorber in which an additional resonant absorption (f_{am} = 11.1 GHz) is obtained in between the two transmission bands. A prototype of the proposed rasorbers consisting of 17 x 25 unit cells are fabricated and the results are experimentally verified. Further, the conformal property of the proposed rasorbers is experimentally verified by carrying out measurements on the curved prototypes with multiple curvature angles.

Chapter 4

A-T FSR Using Modified Double Cross Slot Bandpass Layer

In the previous two chapters, thin single-layer designs for rasorbers having narrowband absorptions were presented. From the current chapter onwards, the work will focus on the designs of rasorbers with broadband absorption. Unlike narrowband rasorber, the designs for the broadband rasorbers are a multi-layered structures with mounted lossy lumped components. In this chapter, a polarization-insensitive A-T FSR has been proposed in which the two phenomenon of broadband absorption and bandpass transmission are first individually studied and then combined to obtain the desired A-T performance. In the proposed FSR, a broad absorption band, along with a transmission band at a higher frequency is achieved. The proposed FSR exhibits an angular stability up to 30^o of incident angle. The working of FSR is analyzed using an equivalent circuit model (ECM). A prototype of the proposed FSR is fabricated and validated experimentally.

4.1 Design and Analysis of the FSR

The FSR is typically a multi-layered structure comprising of a lossy and a lossless layer. The design of FSR is realized by combining the two separate applications of FSS viz. broadband absorption and frequency selective bandpass transmission. The design for FSR is accomplished by replacing the grounded layer of absorber with a bandpass FSS, such that within the absorption band, the bandpass FSS should act as a complete metallic ground. Accordingly, the design of FSR constitutes of three broad steps. In the first step,

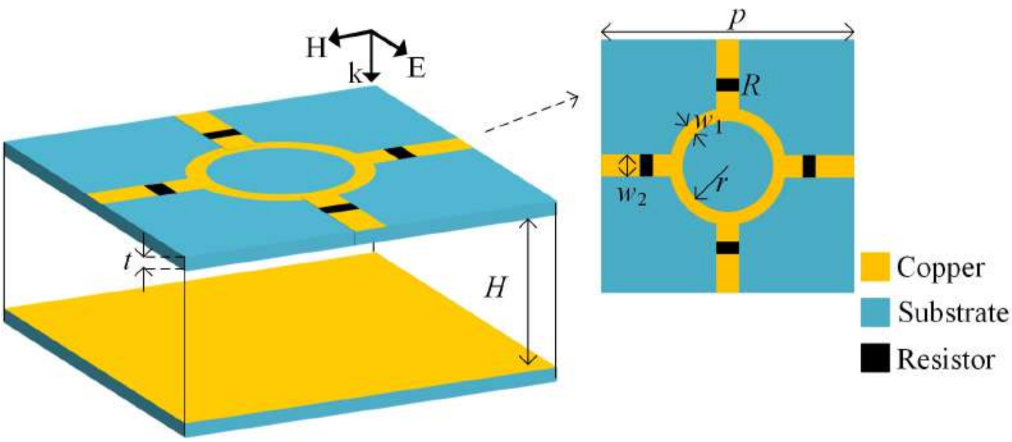

Figure 4.1: Unit cell schematic of the broadband absorber.

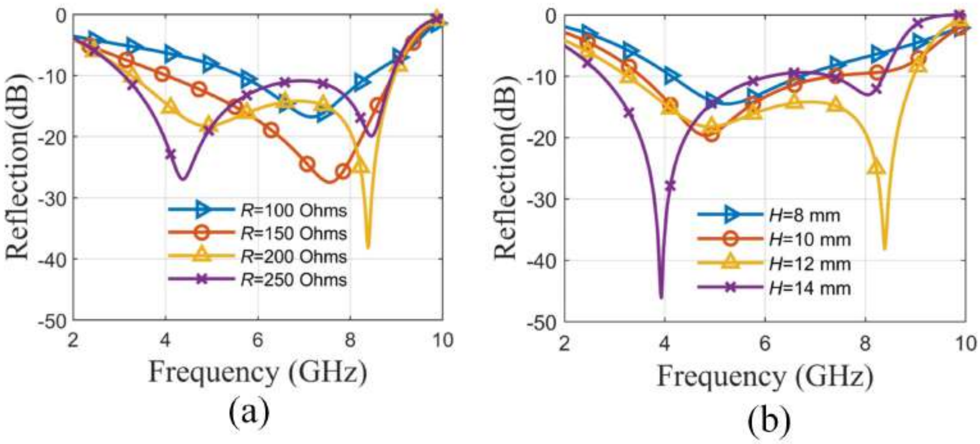

Figure 4.2: Simulated reflection coefficient of broadband absorber with varying, (a) R, and (b) H.

a broadband absorber is studied wherein a broad absorption within the required band is obtained. The next step is associated with designing and improving the performance by changing various parameters of bandpass FSS. In the third and final step, the designs of the previous steps are combined and parameters are optimized to obtain the required FSR.

4.1.1 Analysis of the Broadband Absorber

The unit cell of broadband absorber consists of two layers printed on a 0.8 mm thick FR-4 substrate having dielectric permittivity ϵ_r= 4.4, and loss tangent (tan δ= 0.02). The unit cell schematic of the broadband absorber is shown in Figure 4.1. In the front side of top layer of the absorber, a circular cross resonator is printed while the back side of the top layer is completely etched. Chip resistors R are mounted within the gaps of circular cross resonator. A copper laminated substrate in the bottom layer acts as a ground. Between the two layers, an air spacer of thickness H is maintained. The unit cell of the broadband absorber is simulated using CST electromagnetic solver and the reflection responses obtained corresponding to different values of R and H are shown in Figure 4.2. The optimum value of R for better reflection bandwidth is obtained at 200 ohms. Similarly, the optimum value of H is 12 mm which corresponds to $\lambda/4$ at the centre frequency of absorption band. The other optimized parameters are given as: $p = 20$, $r = 5$, $w_1 = 0.5$, $w_2 = 1$, and $t = 0.8$ (all dimensions are in mm). The broadband absorption is achieved from around 3.2 to 8.9 GHz, within which the reflection coefficient for the incident EM wave is below -10 dB.

4.1.2 Analysis of the Bandpass FSS

In order to achieve a higher transmission band in comparison with the broadband absorption obtained in the previous subsection, a bandpass FSS is designed such that its unit cell dimensions are matched with the unit cell dimensions of the circular cross shaped broadband absorber. The unit cell of bandpass FSS as depicted in Figure 4.3(a), is designed by etching a double cross slot (DCS) within the metal laminated substrate. The slot etched within a metal plated unit cell corresponds to the bandpass filtering of incident EM wave at a particular resonant frequency. The bandpass frequency is inversely dependent upon the dimensions of DCS, such that for decreasing length of slot, the transmission frequency increases. Figure 4.3(b) depicts the simulated response of bandpass FSS for varying slot length l_b. The transmission frequency of the bandpass FSS is required to be maintained at a higher frequency in such a way that for the lower absorption band of 3.2–8.9 GHz, the bandpass FSS acts as a reflective metallic ground. It is noticeable from Figure 4.3(b), that reducing the slot size increases the transmission frequency. However, as the size of double cross slot decreases, the corresponding insertion loss at the increased transmission frequency also increases. In other words, for obtaining higher transmission frequency the slot length is reduced, and with the reduced slot length, the density of slot within the unit cell is also reduced and this leads to the degradation of insertion loss at the higher transmission frequency. As such it is evident that for better performance parameters at the resonant frequency, the resonant slot should be in comparable size with respect to the unit cell size.

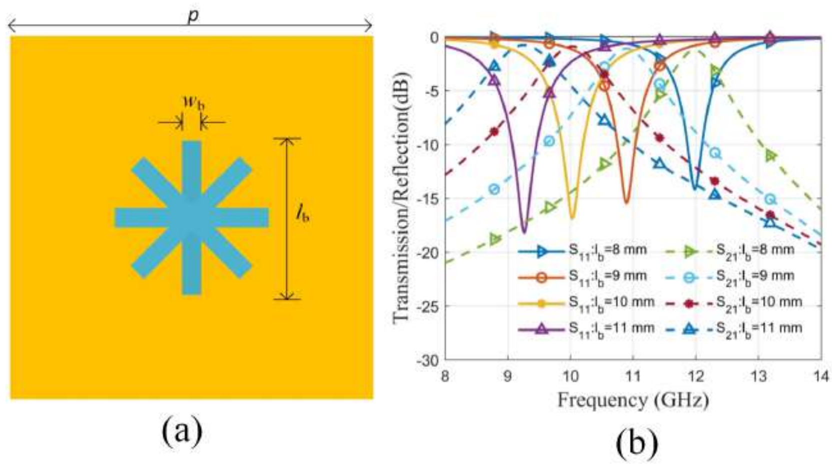

Figure 4.3: DCS shaped bandpass frequency selective surface. (a) Unit cell schematic, and (b) simulated response.

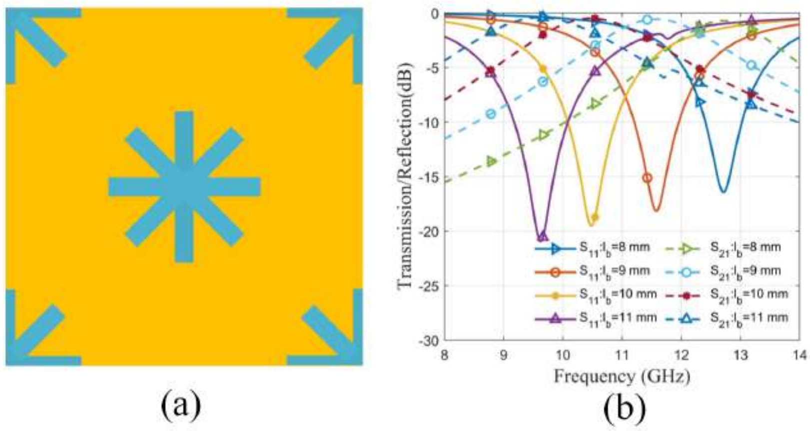

Figure 4.4: MDCS shaped bandpass frequency selective surface. (a) Unit cell schematic, and (b) simulated response.

In order to improve the performance parameters of bandpass FSS at higher frequencies, the bandpass FSS is modified and the density of resonant slot is increased within a unit cell. The increased density of slot is accomplished by replicating a quarter of DCS at each corner of the unit cell as shown in Figure 4.4(a). The simulated response for the MDCS type bandpass FSS for varying l_b is shown in Figure 4.4(b). In the modified double cross slot (MDCS) shaped bandpass FSS, additional slots change the overall capacitance and inductance of the structure due to which transmission frequency at each slot size increases. However, besides the increase in resonant frequency, the insertion loss and also the -10 dB reflection bandwidth at the transmission window of MDCS structure is considerably improved.

For better understanding, the various parameters of the DCS and MDCS type band-

Table 4.1: Performance Comparison of DCS and MDCS type bandpass FSS with l_b = 9 mm.

Structure	Transmission frequency f_T	Minimum Insertion Loss	-10 dB Reflection Bandwidth
DCS	10.9 GHz	1.82 dB	157 MHz
MDCS	11.56 GHz	0.56 dB	752 MHz

pass FSS for a fixed slot length l_b= 9 mm are represented in Table 4.1. It is observed that MDCS type bandpass FSS exhibits wider transmission band with reduced insertion loss in comparison with the DCS type bandpass FSS. The other optimized parameters are: p = 20 mm, w_b = 1.2 mm, l_b = 9 mm.

4.1.3 Analysis of the Proposed FSR

The proposed FSR, as shown in Figure 4.5, is designed by replacing the ground substrate of broadband absorber with the MDCS shaped bandpass FSS. The bandpass FSS acts as a reflective metallic ground for the absorption band, with the transmission occurring in the relatively upper band. The resultant structure is analyzed to obtain the simulated transmission and reflection coefficients depicted in Figure 4.6. The simulated response of the proposed FSR exhibits a transmission band at around 11.46 GHz along with the broadband absorption from around 3.1 to 8.7 GHz. Within the absorption band, both the transmission and the reflection coefficients are less than -10 dB. The proposed FSR exhibits the minimum insertion loss of 0.7 dB within the transmission band, with -10 dB bandwidth of around 520 MHz (4.53%).

In order to further validate the absorption phenomenon, the proposed FSR is also studied for the cross-polarized effect. The simulated transmission and reflection coefficients of the proposed FSR under the cross-polarization are shown in Figure 4.7. The negligible response of the proposed FSR under the cross-polarization rules out the possibility of polarization conversion thereby validating the absorption phenomenon.

The response of the proposed FSR under various polarization angles of the incident EM wave is shown in Figure 4.8. It can be seen that both the reflection and transmission coefficients remain unaltered with the increase in polarization angle from 0^o to 45^o. Thus, symmetricity in the proposed design leads to polarization independent behaviour.

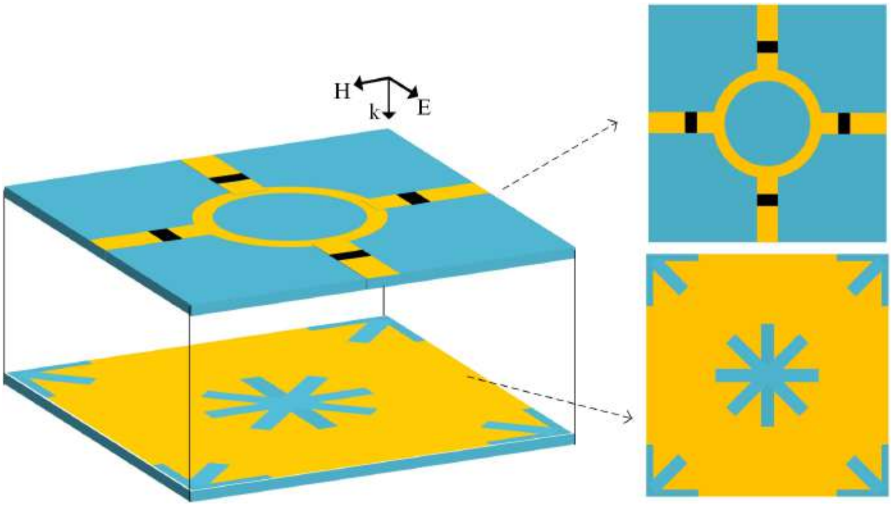

Figure 4.5: Unit cell schematic of the proposed FSR.

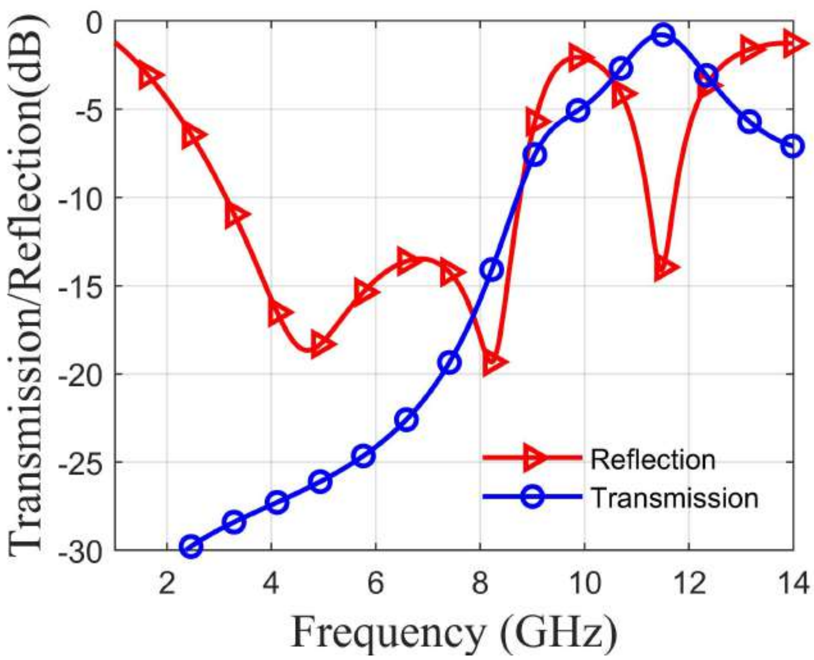

Figure 4.6: Simulated reflection and transmission coefficients of the proposed FSR.

The angular stability of the proposed structure is evaluated by the simulated response for the various angle of incidence as shown in Figure 4.9. The reflection coefficient for the proposed FSR is shifted above the -10 dB level once the incidence angle is exceeded above 30^o, thereby diminishing the absorptivity. Thus, the acceptable response of proposed FSR is attained up to 30^o of incident angle beyond which the performance is degraded.

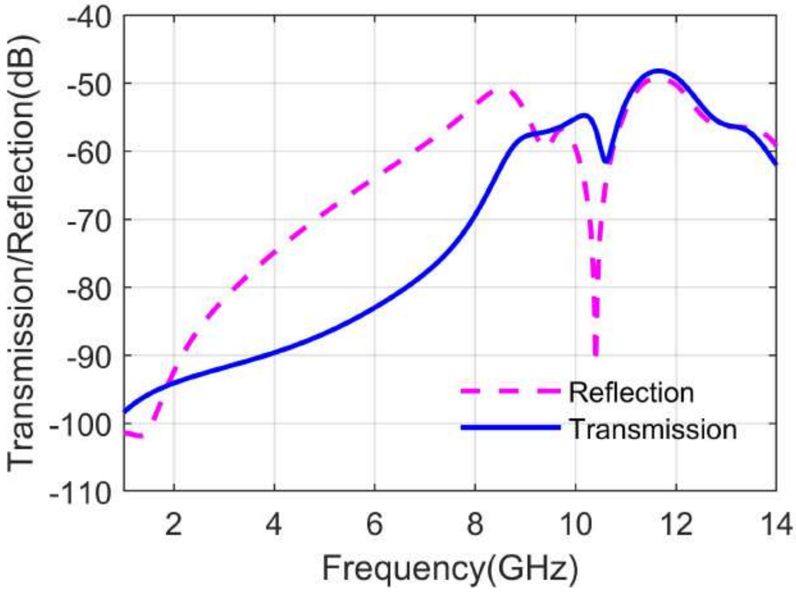

Figure 4.7: Transmission and reflection coefficients of the proposed FSR under cross-polarization.

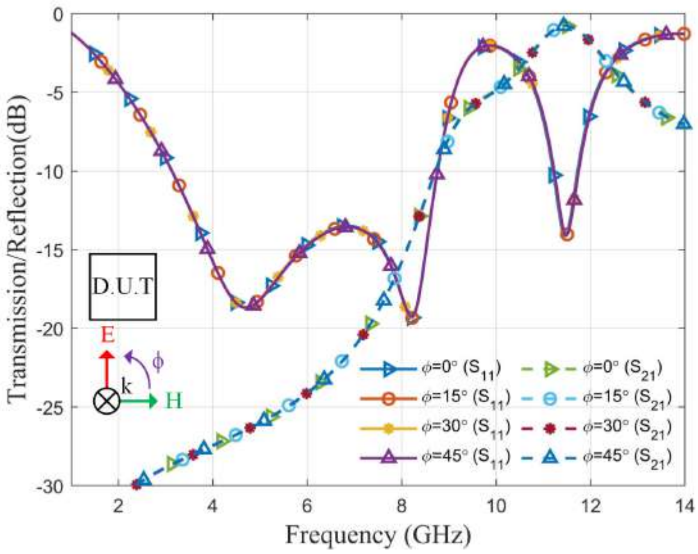

Figure 4.8: Simulated response of the proposed FSR with varying polarization angles.

4.2 Equivalent Circuit Analysis

In order to understand the working principle of the proposed FSR, an ECM of the proposed FSR is illustrated in Figure 4.10, in which the respective ECMs of broadband absorber and bandpass FSS are cascaded. The top resistive layer consists of a parallel L_1 and C_1 which models the central circular resonant structure. The series arrangement of R and L_0 models the outer rectangular strip along with the mounted lumped resistor. For the bandpass layer, the centre and the corner slots of bandpass FSS in the bottom layer are modelled by series combination of parallel $L_{P1} - C_{P1}$ and $L_{P2} - C_{P2}$ resonators. The

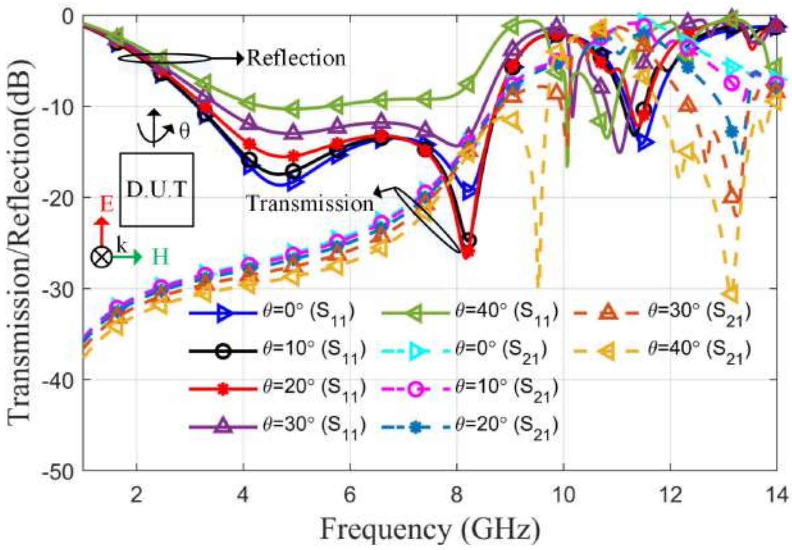

Figure 4.9: Simulated response of the proposed FSR with varying incident angles.

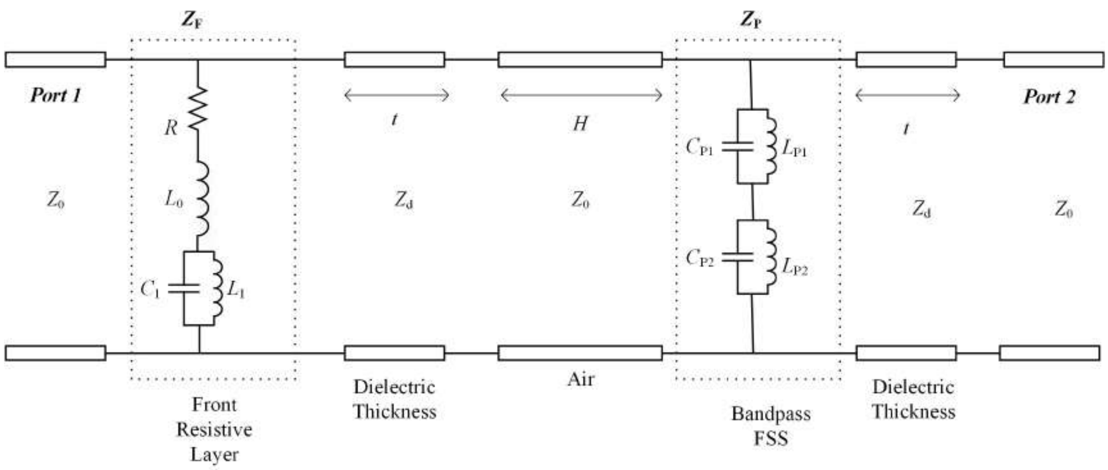

Figure 4.10: Equivalent circuit model of the proposed FSR.

dielectric substrate thickness of the top and bottom layer is represented using a transmission line model with length equal to substrate thickness t and characteristic impedance $Z_d = z_0/\sqrt{\epsilon_r}$, where Z_0 is the characteristic impedance of free space. Another transmission line section with characteristic impedance Z_0 and length H, models the air gap between the two layers. The ABCD parameters of the ECM is obtained by the cascaded matrix multiplication as given below:

$$\begin{bmatrix} A & B \\ C & D \end{bmatrix} = \begin{bmatrix} 1 & 0 \\ 1/Z_{\mathrm{F}} & 1 \end{bmatrix} \times \begin{bmatrix} \cos\beta t & \mathrm{j}Z_d \sin\beta t \\ \mathrm{j}\sin\beta t/Z_{\mathrm{d}} & \cos\beta t \end{bmatrix} \times$$

$$\begin{bmatrix} \cos\beta_0 H & \mathrm{j}Z_0 \sin\beta_0 H \\ \mathrm{j}\sin\beta_0 H/Z_0 & \cos\beta_0 H \end{bmatrix} \times \begin{bmatrix} \cos\beta t & \mathrm{j}Z_d \sin\beta t \\ \mathrm{j}\sin\beta t/Z_{\mathrm{d}} & \cos\beta t \end{bmatrix} \times \begin{bmatrix} 1 & 0 \\ 1/Z_{\mathrm{P}} & 1 \end{bmatrix} \quad (4.1)$$

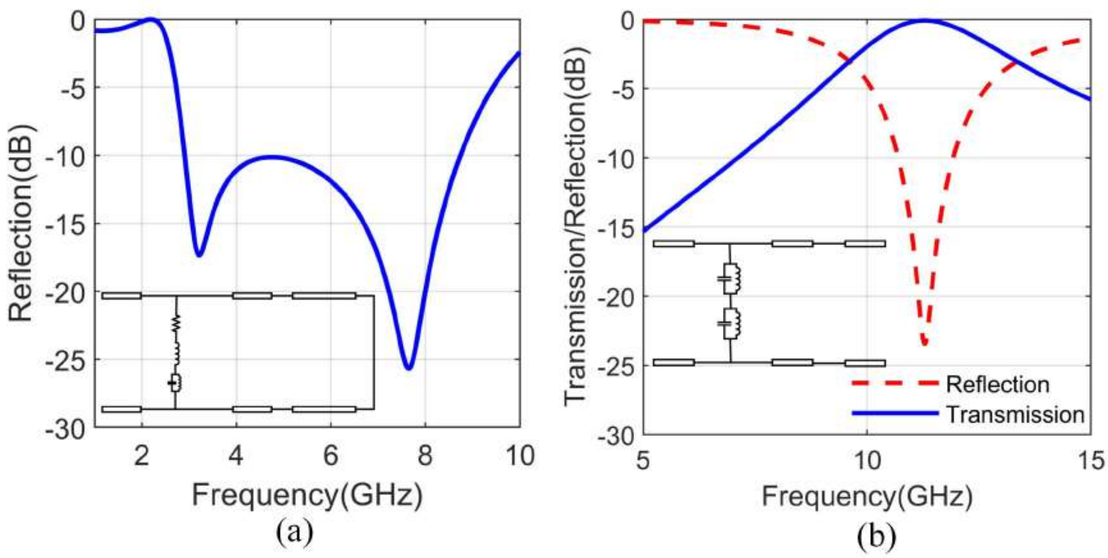

Figure 4.11: Simulated response of equivalent circuit model, (a) broadband absorber, and (b) bandpass FSS.

Here $\beta = \beta_0\sqrt{\mu_r\epsilon_r}$ where β_0 is the propagation constant of free space and Z_F and Z_P are resultant impedances of the front resistive layer and the bandpass FSS layer, respectively and are given by the following expressions:

$$Z_{\mathrm{F}} = R + \mathrm{j}\omega\left(L_0 + \frac{L_1}{1-\omega^2 L_1 C_1}\right) \tag{4.2}$$

$$Z_{\mathrm{P}} = \mathrm{j}\left(\frac{\omega L_{\mathrm{P1}}}{1-\omega^2 L_{\mathrm{P1}} C_{\mathrm{P1}}} + \frac{\omega L_{\mathrm{P2}}}{1-\omega^2 L_{\mathrm{P2}} C_{\mathrm{P2}}}\right). \tag{4.3}$$

The S-parameters are calculated for obtaining the reflection S_{11} and transmission S_{21} coefficients, from the following conversion formula:

$$S_{11} = \frac{A+B/Z_0-CZ_0-D}{A+B/Z_0+CZ_0+D} \tag{4.4}$$

$$S_{21} = \frac{2}{A+B/Z_0+CZ_0+D}. \tag{4.5}$$

The absorptivity is calculated as following:

$$A(\omega) = 1 - |S_{11}|^2 - |S_{21}|^2. \tag{4.6}$$

The ECM of the proposed FSR is simulated using Keysight ADS electromagnetic

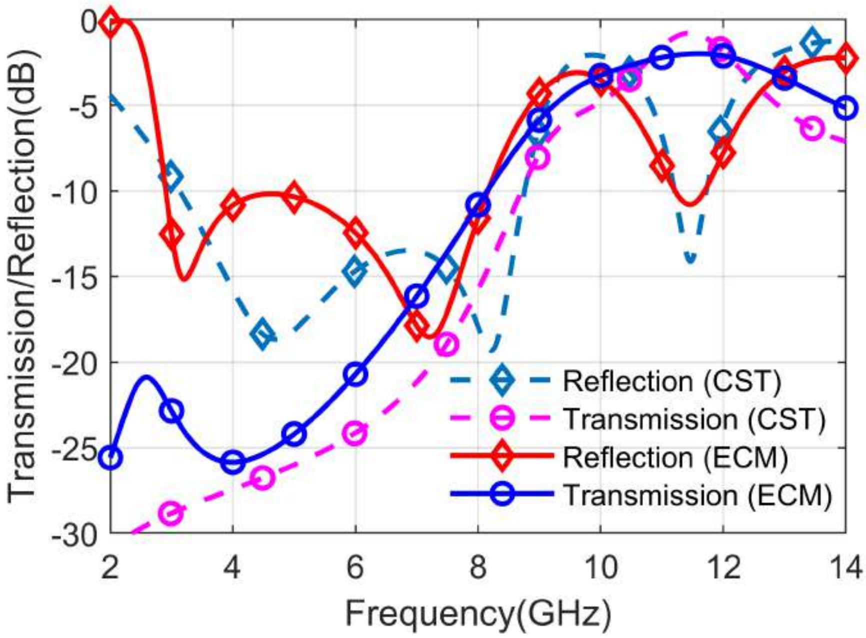

Figure 4.12: Comparison of the reflection and transmission response of the ECM and full wave simulation of the proposed FSR.

simulator. Figure 4.11(a) and Figure 4.11(b) depict the simulated response of ECM for broadband absorber and bandpass FSS, respectively. The ECM corresponding to broadband absorber is a single-port network that consists of only a front resistive layer with another port grounded. The optimized values for each circuit element are given as: L_0 = 17.4 nH, L_1 = 5.14 nH,C_1 = 0.302 pF, L_{P1} = 0.414 nH,C_{P1} = 0.432 pF, L_{P2} = 0.414 nH, C_{P2} = 0.432 pF, R = 200 Ω, Z_d = 179.72 Ω, Z_0 = 377 Ω. The simulated response of the ECM in comparison with the CST simulation results for the proposed FSR is shown in Figure 4.12. A close resemblance of the absorption band (2.7–8.8 GHz) and transmission band (11.4 GHz) is achieved, in comparison with the response obtained for the proposed FSR.

4.3 Effect of Bandpass FSS on the Performance of FSR

The proposed FSR exhibits a higher transmission band at around 11.46 GHz with respect to the lower absorption band (3.1–8.7 GHz). The performance of the FSR can be examined by defining a transition rate TR, which quantifies the rate of transition between absorption and transmission. The TR is defined as the ratio of transmission to absorption frequency

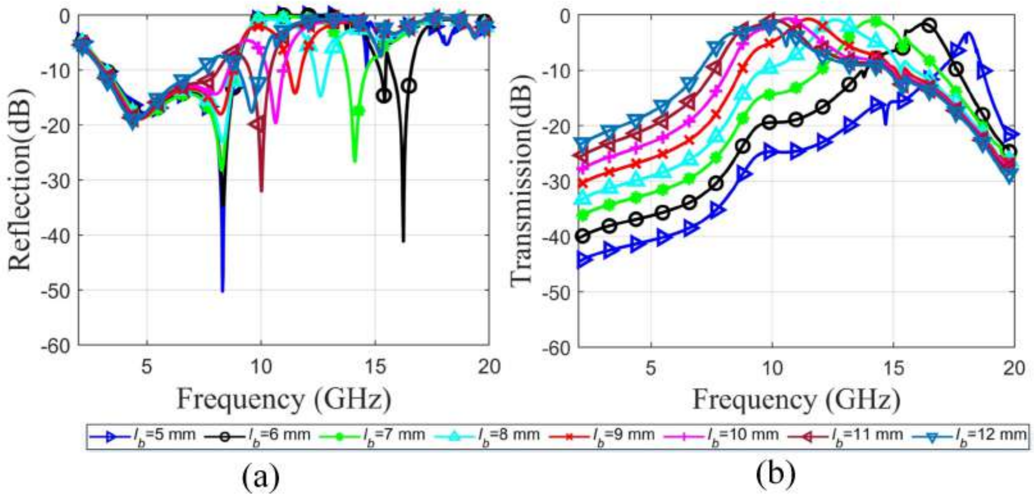

Figure 4.13: Simulated response of the proposed FSR with slot length l_b. (a) Reflection, and (b) transmission coefficients

given below,

$$TR = \frac{f_T}{f_a} \tag{4.7}$$

where f_T is the transmission frequency and f_a is the maximum absorption frequency. The higher transmission band occurs due to the bandpass FSS layer, therefore the range of the higher transmission band can be tuned by varying the design parameters of the bandpass FSS. In order to determine the range within which the higher transmission band can be achieved for the proposed FSR, a study is carried out where the variation in transmission frequency is analyzed by varying the slot dimension of the bandpass FSS layer. Figure 4.13 depicts the parametric analysis of the proposed FSR with respect to the slot length l_b. The transmission frequency above the transmission band is lowered by the increasing l_b. The various effects on the performance parameters of the proposed FSR due to varying l_b, observed from the Figure 4.13 are presented in Table 4.2.

From Table 4.2, it is observed that for the increasing slot length l_b from 5 mm to 12 mm, f_T decreases from 18.1 GHz to 9.6 GHz with the variation in TR ranging from 2.03 to 1.39. The insertion loss at f_T decreases as l_b is varied from 5 mm to 10 mm, and then increases for the value of l_b greater than 10 mm. Further, as the f_T is lowered to 9.6 GHz, the absorption band is also reduced substantially to 3.0–6.9 GHz. Thus, for obtaining an acceptable range of f_T, within which the corresponding insertion loss is below 2.0 dB and also the lower absorption band is maintained nearly same, the slot parameters can

Table 4.2: Variation of performance parameters with varying l_b.

l_b (mm)	Transmission frequency f_T	Insertion Loss @ f_T GHz	Absorption	TR
5	18.1 GHz	3.25 dB	3.2–8.9 GHz	2.03
6	16.2 GHz	1.56 dB	3.2–8.9 GHz	1.82
7	14.1 GHz	1.04 dB	3.2–8.8 GHz	1.60
8	12.6 GHz	0.85 dB	3.1–8.8 GHz	1.43
9	11.4 GHz	0.74 dB	3.1–8.7 GHz	1.31
10	10.6 GHz	0.68 dB	3.0–8.1 GHz	1.30
11	10.0 GHz	1.04 dB	3.0–7.5 GHz	1.33
12	9.6 GHz	2.07 dB	3.0–6.9 GHz	1.39

be varied from $l_b = 6$ mm to $l_b = 10$ mm. Thus the corresponding range of f_T can be achieved as follows:

$$10.6GHz \leq f_t \leq 16.2GHz \tag{4.8}$$

The TR is achieved as 1.30 and 1.82 for $f_T = 10.6$ and 16.2 GHz, respectively. Hence, in the proposed FSR the higher transmission frequency can be tuned from 10.6 to 16.2 GHz by varying the bandpass FSS parameter l_b from 10 to 6 mm, respectively.

4.4 Experimental Verification

In order to validate the response of the proposed FSR, a 13 x 14 unit cell array for both the layers of the proposed structure are fabricated. Chip resistors having 200 Ω resistance (CRCW0603200RFKEA from VISHAY36) are soldered on front side of the top layer. The photograph of fabricated prototype with overall dimensions of 260 mm x 280 mm is shown in Figure 4.14. Air gap between the two fabricated substrates is maintained using plastic spacer standoff (Figure 4.14(d)).

The measurement on the fabricated prototype is carried out using free space measurement technique. Combination of S/C/J/X band horn antennas, connected with Keysight PNA Network Analyzer N5224B, are sequentially used for carrying out the transmission and reflection measurements in their respective frequency band. The experimental setup for each transmission and reflection measurements are given in Figure 4.15. For reflection measurements, a PEC sheet is used for the reference measurement which is then replaced

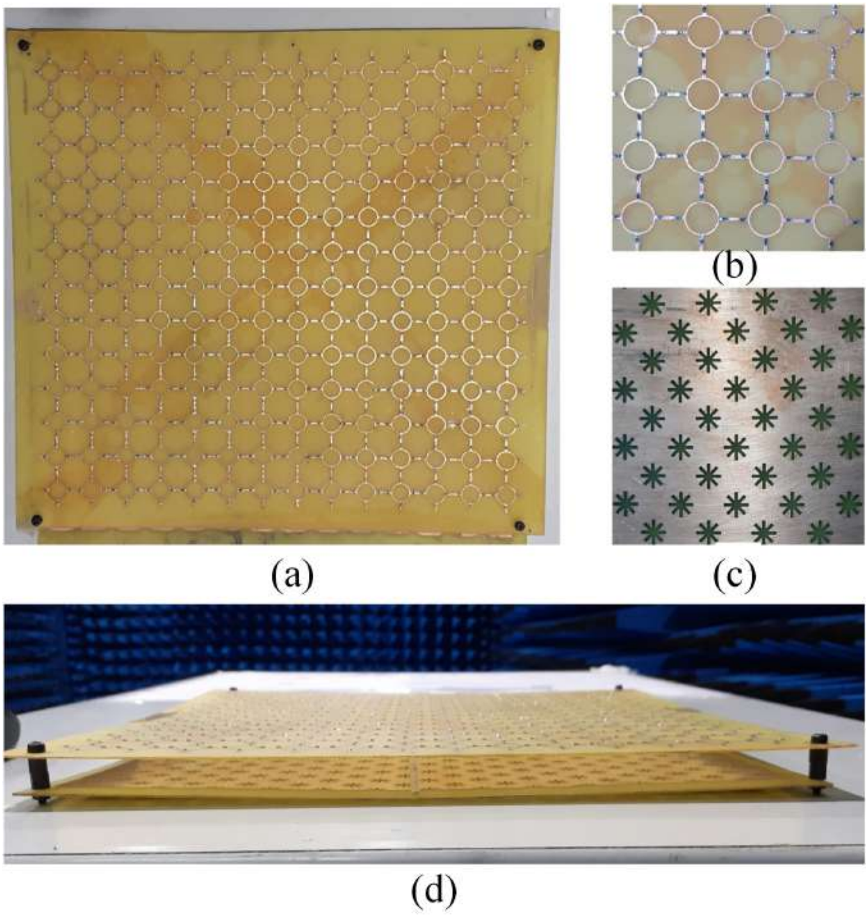

Figure 4.14: Fabricated prototype of the proposed FSR. (a) Top layer, (b) enlarged view of top layer, (c) enlarged view of bottom layer, and (d) side view.

by the fabricated prototype to obtain the reflection coefficient. In case of transmission, reference measurement involves the direct path measurement between the two horn antennas. The effective transmission coefficient is then obtained by the difference of measured reflection coefficient of direct path and the fabricated prototype. The measured transmission and reflection response obtained in comparison with simulated results are shown in Figure 4.16, whereby a reasonable agreement is observed.

A relative performance comparison of the proposed A-T FSR with the earlier reported A-T FSR [83]-[86] is given in Table 4.3. The proposed FSR exhibits polarisation insensitive response, wider absorption band in comparison with the previously reported FSRs in [83, 85, 86]. Also, the proposed FSR is a 2-layer structure with less lumped elements in comparison with the reported FSRs in [84, 86].

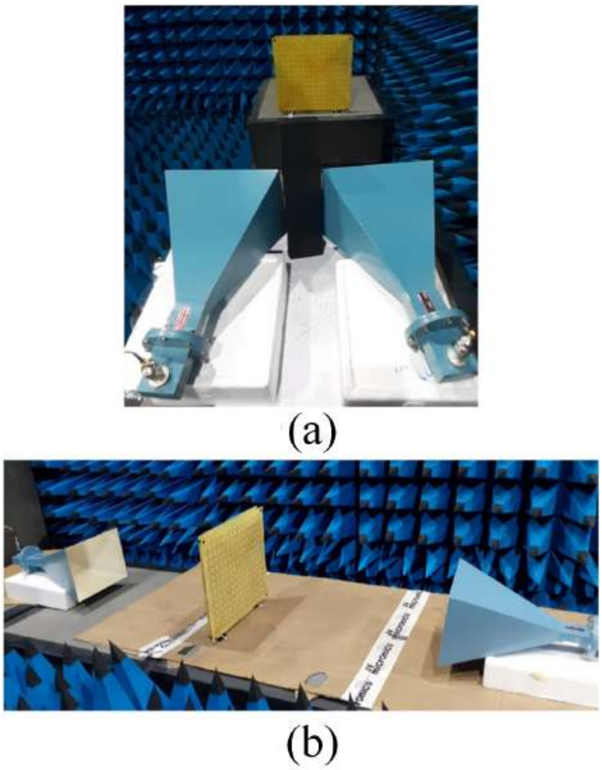

Figure 4.15: Measurement setup. (a) Reflection, and (b) transmission measurement.

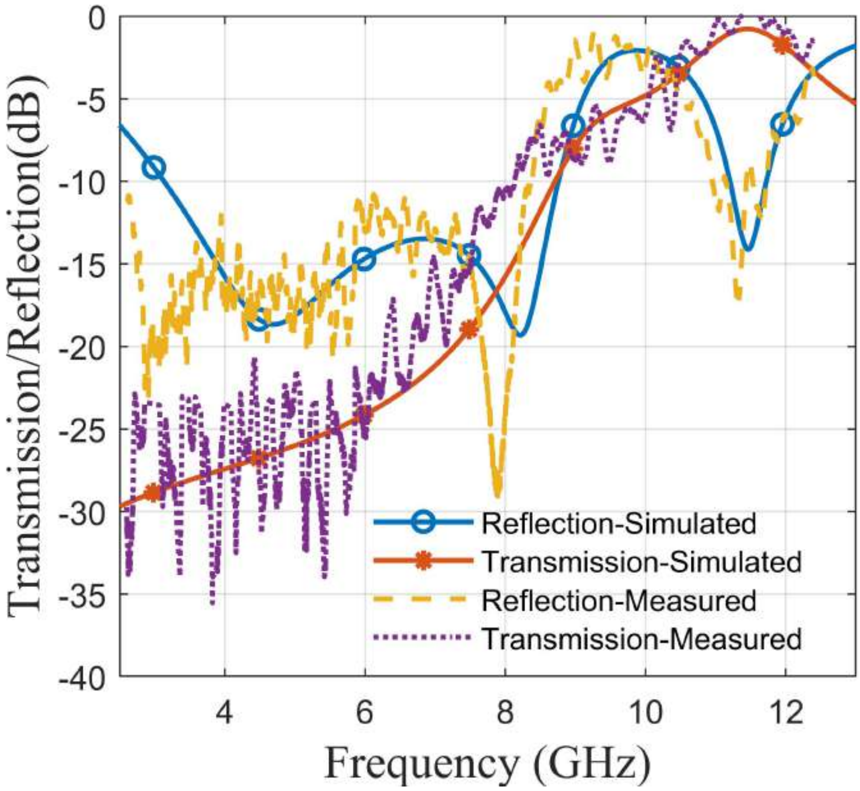

Figure 4.16: Simulated and measured response of the proposed FSR.

Table 4.3: Performance comparison of proposed A-T FSR.

Ref.	f_T/ Minimum I.L	Absorption	No. of Layers	Lumped elements per unit cell	Size	Thickness	Polarization
[83]	5.6 GHz / 0.2 dB	2.8–5.0 GHz (56.41 %)	2	1	$0.28\lambda_L$	$0.122\lambda_L$	Sensitive
[85]	12.76 GHz / 0.65 dB	6.10–10.98 GHz (57.14 %)	2	2	$0.366\lambda_L$ x $0.183\lambda_L$	$0.122\lambda_L$	Sensitive
[84]	10 GHz / 0.5 dB	2.4–7.1 GHz (98.94 %)	4	6	$0.096\lambda_L$	$0.12\lambda_L$	Dual-Polarized
[86]	6.1 GHz / 0.37 dB	1.6–4.3 GHz (91.5 %)	4	8	$0.16\lambda_L$	$0.158\lambda_L$	Dual-Polarized
This work	11.4 GHz / 0.7 dB	3.1–8.7 GHz (94.91%)	2	4	$0.206\lambda_L$	$0.14\lambda_L$	Insensitive

f_T is Transmission frequency; λ_L is free space wavelength at lowest frequency of -10 dB reflection; I.L is the insertion loss.

4.5 Conclusion

This chapter presents a design of FSR having wideband absorption and a relatively higher transmission band (A-T). The FSR structure is a two-layer design consisting of resistive and bandpass layers. The proposed FSR achieves a broad absorption band ranging from 3.1 to 8.7 GHz with absorptivity greater than 80% and a higher transmission band at 11.46 GHz with insertion loss of 0.7 dB and -10 dB reflection bandwidth of 520 MHz (11.206 to 11.726 GHz). An ECM corresponding to the proposed rasorber design is studied for explaining the working principle. A parametric study is carried out for determining the optimum range within which the higher transmission band can be varied. A prototype of the proposed FSR structure is fabricated and experimental validation of simulated results is obtained.

Chapter 5

T-A-T FSR

In the previous chapter, A-T FSR with a broad absorption band and higher transmission band has been studied. Now in this chapter, a study is presented for realizing dual transmission T-A-T type FSR. A dual bandpass FSS is combined with the broadband absorber in such a way that a broad absorption is achieved between the two transmission bands. The proposed FSR is a two-layered compact structure and can be a suitable candidate for RCS reduction of a dual-band radiating systems. The working of the proposed FSR is analyzed using an equivalent circuit model (ECM). A prototype of the proposed FSR is fabricated and the corresponding measurements are carried out. A good agreement is obtained between simulated and measured results, thus providing an experimental validation for the performance of the proposed FSR.

5.1 Design and Analysis of FSR

The design of a FSR generally consists of a two-layer arrangement of the lossy and lossless layers. The lossy layer consisting of elements like lumped resistors give rise to the broadband absorption, while the lossless layer acting as a bandpass FSS, yields the corresponding transmission bands. In the design of FSR, the dual bandpass FSS is first studied, followed by the analysis of the broadband absorber whose dimensions are synchronized with the dimensions of the bandpass FSS, besides that the absorption band lies between the two transmission bands. The bandpass FSS yielding the transmission bands should act as a reflective layer for the absorption band. The bandpass FSS replaces the ground layer of the broadband absorber to arrive at the design of the FSR.

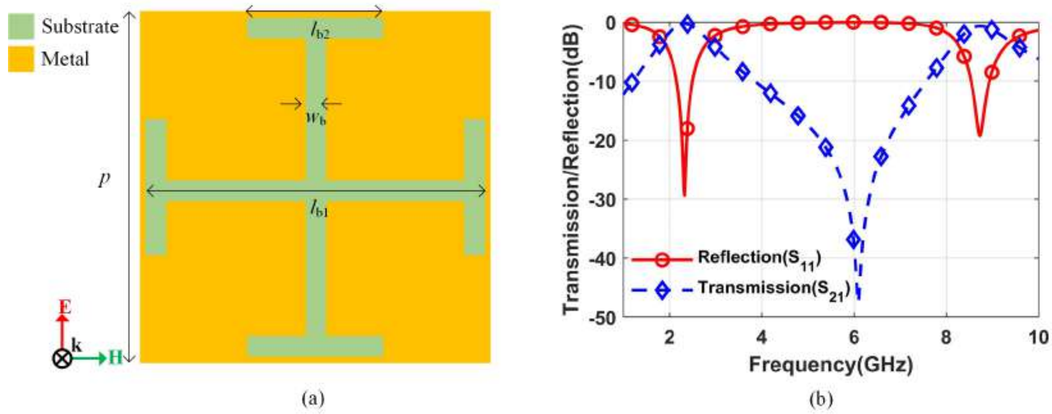

Figure 5.1: Jerusalem shaped bandpass FSS. (a) Unit cell schematic, and (b) simulated reflection and transmission coefficients.

5.1.1 Bandpass FSS

The unit cell schematic of the bandpass FSS is shown in Figure 5.1(a) where a Jerusalem cross shaped slot is etched within the metal layered substrate. A 0.8 mm thick FR-4 substrate having dielectric permittivity (ϵ_r) of 4.4, loss tangent (tanδ) equal to 0.02, and metal thickness of 0.035 mm is employed in the design. The Jerusalem cross shaped bandpass FSS is obtained by etching a perpendicular rectangular slot of length l_{b2} at each end of the cross slot having length l_{b1}. The unit cell of the bandpass FSS is simulated using CST electromagnetic solver. The optimized values of the various parameters are given as: $p = 25$, $l_{b1} = 24$, $l_{b2} = 12$, $w_b = 1.3$ (All dimensions are in mm).

The simulated reflection and transmission coefficients of the bandpass FSS are depicted in Figure 5.1(b), from which dual transmission bands are observed at 2.3 and 8.7 GHz. The rectangular slot with length l_{b2} at each end of the cross slot gives rise to the transmission at the higher frequency while the center cross slot with length l_{b1} is associated with the transmission band at the lower frequency. Figures 5.2(a) and 5.2(b), depict the response of the bandpass FSS with respect to varying l_{b1} and l_{b2}. It can be noticed from Figure 5.2(a), that increasing the value of l_{b1} from 20 to 24 mm leads to decrease in the lower transmission frequency (f_{tl}) from 3.1 to 2.3 GHz, respectively while the upper transmission frequency (f_{tu}) remains nearly the same. Similarly, the dependence of f_{tu} on l_{b2} can be observed from Figure 5.2(b) where the increasing value of l_{b2} from 10 to 14 mm causes the f_{tu} to decrease from 10.0 to 7.7 GHz, respectively while the lower transmission frequency remains nearly the same.

Further, it can be observed from Figure 5.1(b) that between the two transmissions

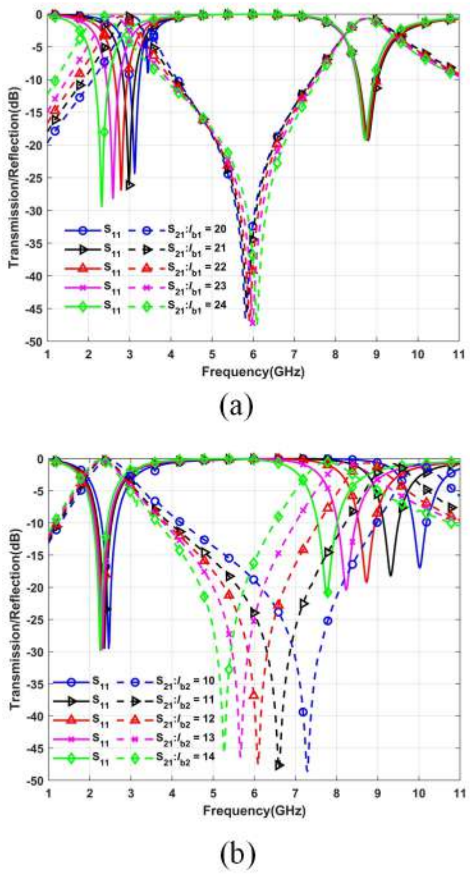

Figure 5.2: Simulated reflection and transmission coefficients of bandpass FSS with varying (a) l_{b1} (in mm), and (b) l_{b2} (in mm)

bands, within the frequency band of 3.8 to 7.5 GHz, the transmission coefficient dips below -10 dB with the reflection coefficient close to 0 dB. Within this frequency range the bandpass FSS can be utilized as a complete reflecting surface.

5.1.2 Broadband Absorber

The broadband absorber is a two-layer design consisting of the resistive and ground layers. The broadband absorber is designed such that its absorption band exists within the two transmission frequencies of the bandpass FSS studied in the previous subsection. Also, the size of the unit cell of the broadband absorber is kept same as that of the bandpass FSS. The unit cell schematic of the broadband absorber is shown in Figure 5.3, which is a two-layer structure of resistive and ground layers, designed using a 0.8 mm thick FR-4 substrate ($\epsilon_r = 4.4$, tan$\delta = 0.02$) with an air spacer of height H separating the two layers. The top layer consists of the resistive square loop having length l and thickness w. The lumped resistors with resistance R are mounted in between the gaps (gap-length = g) of

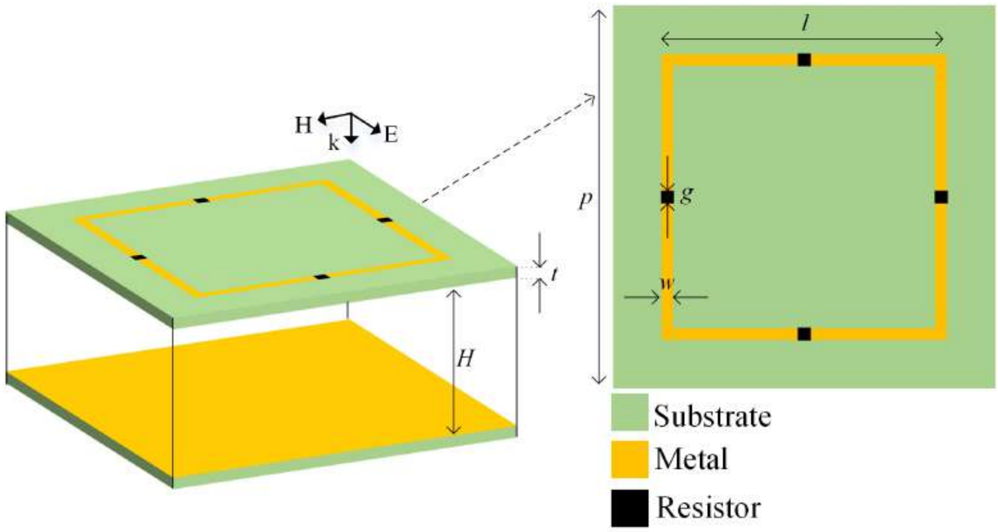

Figure 5.3: Unit cell schematic of the broadband absorber.

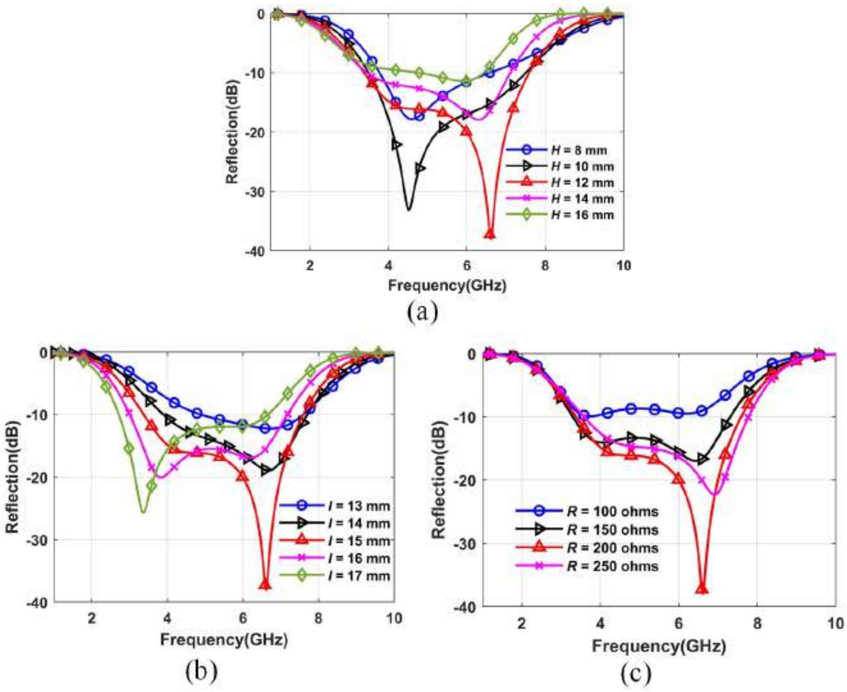

Figure 5.4: Reflection coefficient of broadband absorber with varying (a) H, (b) l, and (c) R

the metallic square loop. The simulated reflection coefficients of the broadband absorber with respect to various parameters viz. H, l, R are provided in Figure 5.4. The optimum values of the various parameters are given as: $R = 200\ \Omega$, $p = 25$, $l = 15$, $w = 0.5$, $t = 0.8$, $H = 12$ (All dimensions are in mm). For the optimum value of each parameter, the structure achieves a broad absorption in the range of 3.3 GHz to 7.5 GHz, within which the reflection coefficient is below -10 dB.

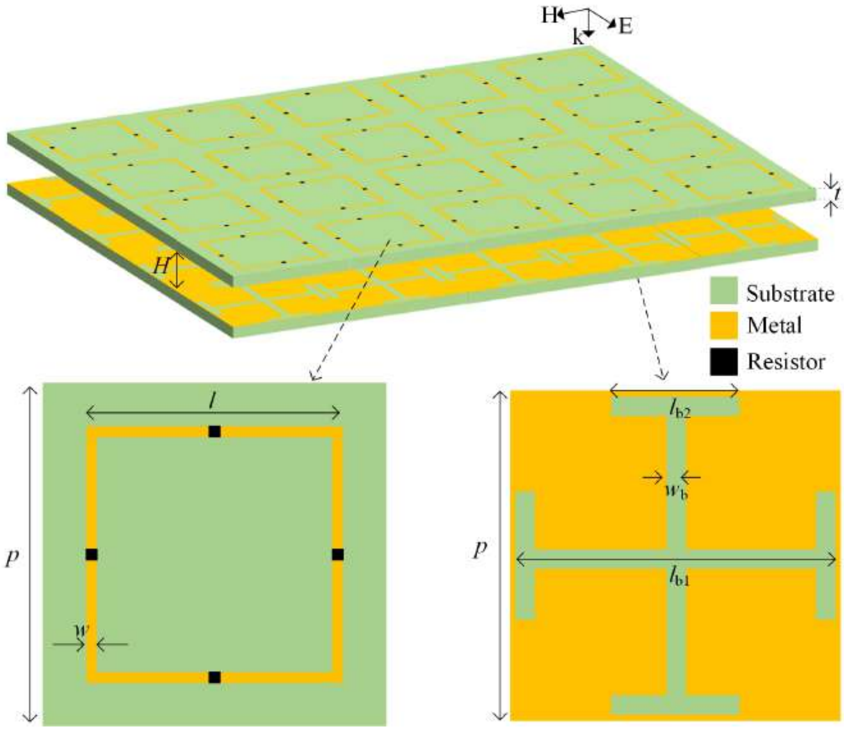

Figure 5.5: Schematic of the proposed FSR.

5.1.3 Proposed FSR

The proposed FSR as shown in Figure 5.5 is designed by replacing the ground layer of the broadband absorber by the Jerusalem shaped bandpass FSS. The resultant structure is analyzed to obtain the simulated transmission and reflection coefficient as provided in Figure 5.6. The proposed FSR exhibits dual transmission bands having the center frequencies at 2.1 and 8.8 GHz. At the lower transmission frequency of 2.1 GHz, the minimum insertion loss of 1.4 dB is obtained within the -10 dB reflection bandwidth of around 443 MHz (1.972–2.415 GHz). At the higher transmission frequency of 8.8 GHz, the minimum insertion loss of 1.5 dB is achieved within the -10 dB reflection bandwidth of around 496 MHz (8.579–9.075 GHz). In between the two transmission bands, a broad absorption is achieved ranging from 3.6 to 7.4 GHz (69.09%), within which both the transmission and reflection coefficients of the proposed FSR are below -10 dB. The corresponding absorption curve of the proposed FSR is depicted in Figure 5.7.

The proposed FSR is analyzed for the different polarization angles of the incident wave, as shown in Figure 5.8. The reflection and transmission coefficients of the proposed FSR remains unchanged with respect to the polarization angles of the incident wave from 0^o to 45^o. Thus the proposed FSR exhibits the polarization-insensitive behavior.

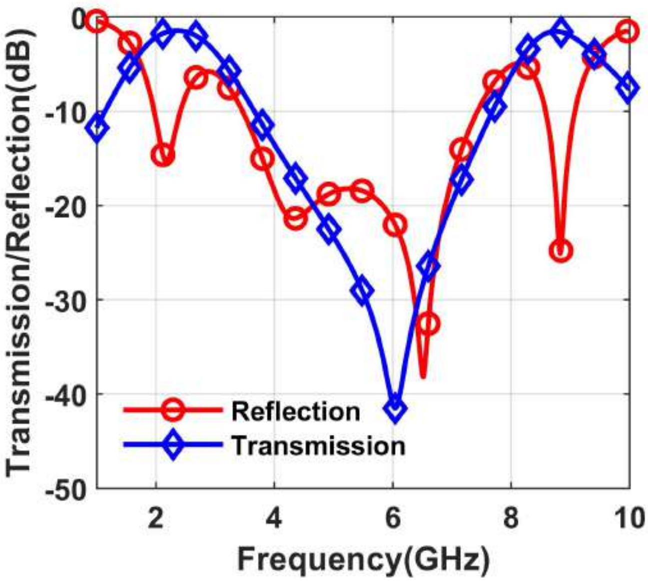

Figure 5.6: Simulated reflection and transmission coefficients of the proposed FSR.

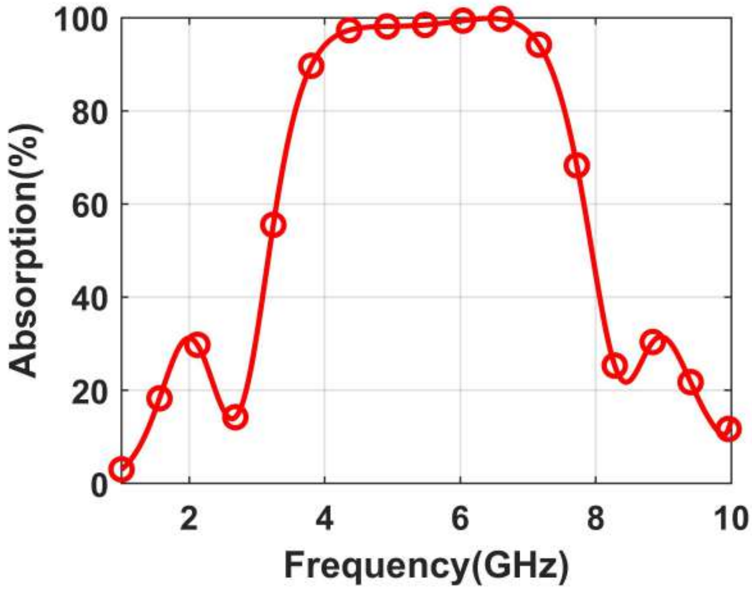

Figure 5.7: Absorption curve of the proposed FSR.

The response of the proposed FSR under oblique incidence for the TE polarized wave is also studied. The reflection and transmission coefficients of the proposed FSR for various angle of incidence from 0^o to 40^o are shown in Figure 5.9. It can be observed that by increasing the incident angle, the insertion loss at the two transmission frequencies gets increased. The increase of loss at the upper transmission frequency is more as compared to the lower transmission frequency. Up to 40^o of incident angle the insertion loss at the upper transmission band remains within 3 dB and increasing the incident angle further leads to the loss beyond 3 dB. Thus, the proposed FSR exhibits an acceptable performance

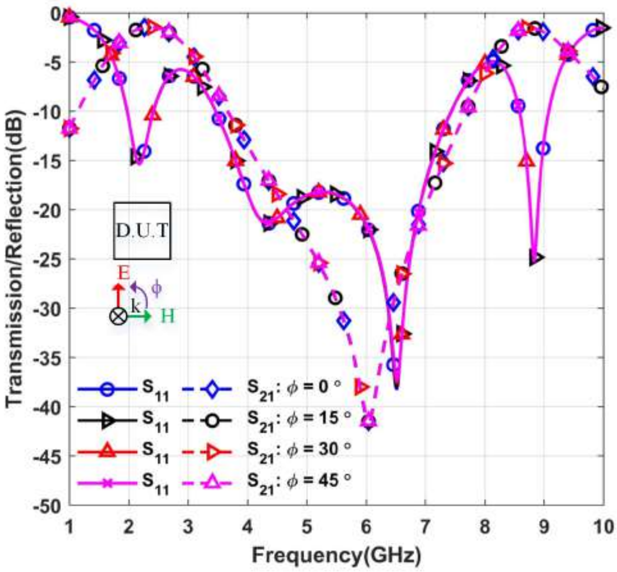

Figure 5.8: Simulated reflection and transmission coefficients of the proposed FSR under various polarization angle of the incident wave.

up to 40^o of incident angle.

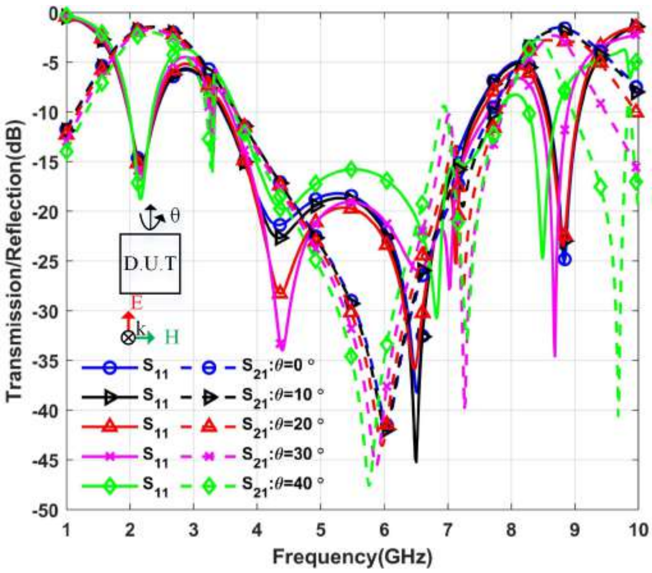

Figure 5.9: Simulated reflection and transmission coefficients of the proposed FSR under different incident angles for a TE polarized wave.

5.2 Equivalent Circuit Model

The working principle of the proposed FSR can be perceived by analyzing an equivalent circuit model (ECM). The ECM of the proposed FSR as shown in Figure 5.10 is a two-port network consisting of circuit models for the resistive and bandpass FSS layers. The resistive square loop on the front layer is modelled using a series $R - L_1 - C_1$ network.

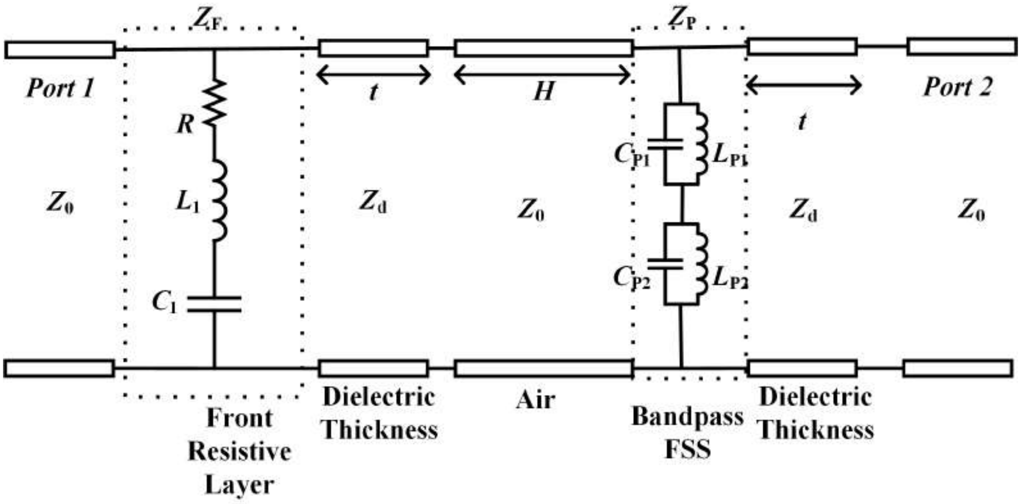

Figure 5.10: ECM of the proposed FSR.

The dual bandpass layer at the back is modelled using the series arrangement of parallel L_{P1}–C_{P1} and L_{P2}–C_{P2} resonators. The air gap between the two layer is modelled using a transmission line with characteristics impedance equal to the free space impedance Z_0. The substrate thickness is also modelled using a transmission line of length equal to substrate thickness t and characteristic impedance Z_d, where $Z_d = Z_0 \,/\sqrt{\epsilon_r}$. The input and the output ports of the ECM are terminated with the free space impedances. The overall ABCD parameters of the ECM can be obtained by the cascaded multiplication of the individual ABCD parameters as shown in equation below.

$$\begin{bmatrix} A & B \\ C & D \end{bmatrix} = \begin{bmatrix} 1 & 0 \\ 1/Z_{\mathrm{F}} & 1 \end{bmatrix} \times \begin{bmatrix} \cos\beta t & \mathrm{j}Z_d \sin\beta t \\ \mathrm{j}\sin\beta t/Z_{\mathrm{d}} & \cos\beta t \end{bmatrix} \times$$
$$\begin{bmatrix} \cos\beta_0 H & \mathrm{j}Z_0 \sin\beta_0 H \\ \mathrm{j}\sin\beta_0 H/Z_0 & \cos\beta_0 H \end{bmatrix} \times \begin{bmatrix} \cos\beta t & \mathrm{j}Z_d \sin\beta t \\ \mathrm{j}\sin\beta t/Z_{\mathrm{d}} & \cos\beta t \end{bmatrix} \times \begin{bmatrix} 1 & 0 \\ 1/Z_{\mathrm{P}} & 1 \end{bmatrix} \quad (5.1)$$

In equation (5.1), $\beta = \beta_0\sqrt{\mu_r\epsilon_r}$ represents the propagation constant of the dielectric substrate (μ_r and ϵ_r are the relative permeability and relative permittivity of the dielectric substrate), where β_0 is the free space propagation constant. Z_F and Z_P represents the equivalent impedances of the resistive and the bandpass FSS layers, respectively. The resultant expression of Z_F and Z_P are given in the equations (5.2) and (5.3).

$$Z_{\mathrm{F}} = R + \mathrm{j}\left(\omega L_1 - \frac{1}{\omega C_1}\right) \quad (5.2)$$

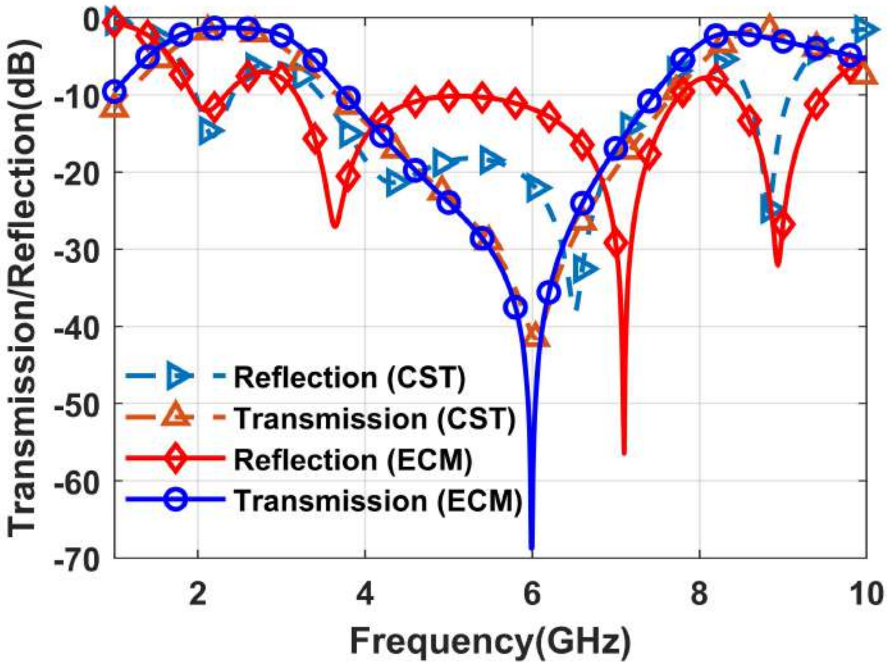

Figure 5.11: Comparison of the reflection and transmission coefficients for the proposed FSR and its corresponding ECM.

$$Z_{\mathrm{P}} = \mathrm{j}\left(\frac{\omega L_{\mathrm{P1}}}{1-\omega^2 L_{\mathrm{P1}} C_{\mathrm{P1}}} + \frac{\omega L_{\mathrm{P2}}}{1-\omega^2 L_{\mathrm{P2}} C_{\mathrm{P2}}}\right). \tag{5.3}$$

The S-parameters are calculated from the ABCD parameters for obtaining the reflection (S_{11}) and transmission (S_{21}) coefficients, using the conversion formula provided in equations (5.4) and (5.5).

$$S_{11} = \frac{A+B/Z_0-CZ_0-D}{A+B/Z_0+CZ_0+D} \tag{5.4}$$

$$S_{21} = \frac{2}{A+B/Z_0+CZ_0+D}. \tag{5.5}$$

The absorptivity is calculated from the S-parameter using the formula given in equation (5.6).

$$A(\omega) = 1 - |S_{11}|^2 - |S_{21}|^2. \tag{5.6}$$

The ECM of the proposed FSR is analyzed for the corresponding S-parameters using the Keysight ADS simulator. The optimum values for each circuit element in the ECM are provided as: $R = 200\ \Omega$, $L_1 = 8.96$ nH, $C_1 = 0.11$ pF, $L_{P1} = 0.69$ nH, $C_{P1} = 0.49$ pF, $L_{P2} = 7.15$ nH, $C_{P2} = 0.62$ nH, $Z_0 = 377\ \Omega$, $Z_d = 179.72\ \Omega$. The simulated reflection and transmission coefficients of the ECM along with the CST full-wave simulation of the proposed FSR are shown in Figure 5.11. The simulated response of the ECM achieves dual transmission bands at 2.1 and 8.9 GHz, along with the in-between absorption band from 3.1 to 7.4 GHz, which are in close agreement with the response obtained for the proposed FSR.

5.3 Effect of Parametric Variations on the Performance of Proposed FSR

The proposed FSR exhibits dual-transmission characteristics with a broad absorption band existing between the two transmission bands. The relative spacing between the transmission and absorption bands can be tuned by the corresponding variation of the bandpass FSS parameters. In order to study the effect of parametric variation on the relative spacing between the transmission and absorption bands, transition ratios are defined as given in equations (5.7) and (5.8).

$$TR_l = \frac{f_{tl}}{f_a} \tag{5.7}$$

$$TR_u = \frac{f_{tu}}{f_a} \tag{5.8}$$

In the above equations, TR_l and TR_u denotes the transition ratios for the lower and upper bands, respectively. Also, f_{tl} and f_{tu} are the center frequencies of the lower and upper transmission bands, respectively, while f_a is the center frequency of the absorption band.

Parametric studies are carried out on the proposed FSR to determine the range of the transition ratios. The lower transmission band corresponds to the cross slot (length l_{b1}) of the Jerusalem cross based bandpass FSS while the upper transmission band is dependent on the rectangular slots (length l_{b2}) at the end of each cross slot. Thus, two parametric analysis are carried out on the proposed FSR with respect to the values of l_{b1} and l_{b2}.

Figure 5.12 shows the reflection and transmission coefficients of the FSR with respect to the variation in the value of l_{b1} from 25 mm to 20 mm, while keeping the other parameters fixed. For better understanding, the performance of FSR corresponding to each value of l_{b1} is presented in Table 5.1. It can be observed from Table 5.1, that for l_{b1}

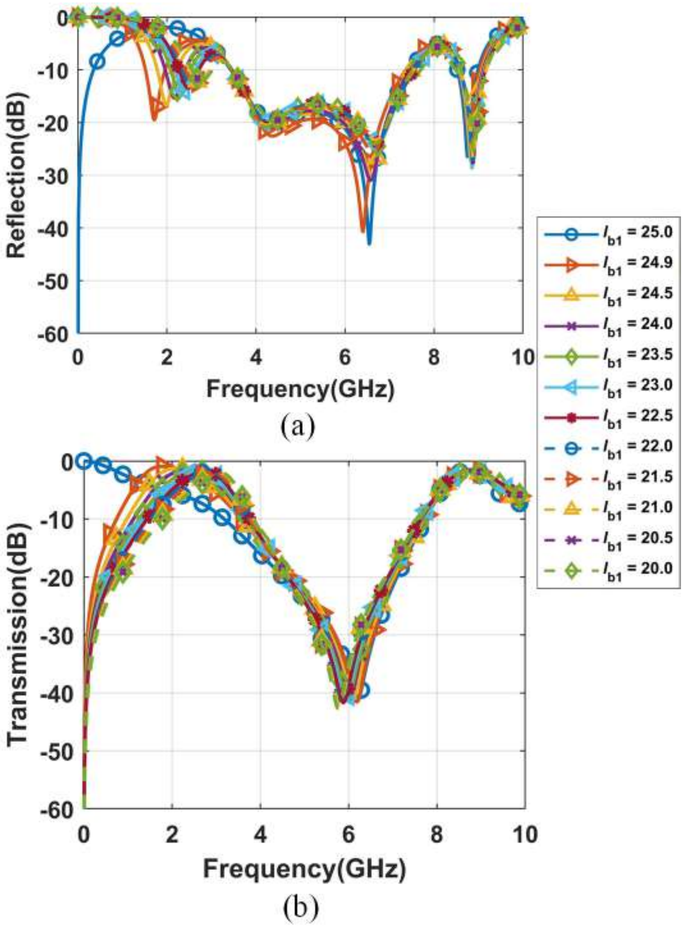

Figure 5.12: Simulated response of the proposed FSR for varying l_{b1} (in mm). (a) Reflection, and (b) transmission coefficients.

equal to the unit cell dimension (25.0 mm), the lower transmission frequency f_{tl} does not exist. However, decreasing l_{b1} from 24.9 mm to 20 mm, the value to f_{tl} increases from 1.71 to 2.85 GHz, respectively, while the absorption band (absorption > 80 %) and upper transmission frequency f_{tu} (Insertion loss < 2 dB) remains nearly the same with some minor variations. It can also be observed that the increase in f_{tl} leads to the increase in the corresponding insertion loss and beyond f_{tl} = 2.61 GHz (for l_{b1} = 21.5 mm), the insertion loss exceeds 2 dB. Maintaining the insertion loss within 2 dB, f_{tl} can be varied from 1.71 to 2.61 GHz by decreasing l_{b1} from 24.9 mm to 21.5 mm, respectively. Thus, the minimum and maximum limits of f_{tl} with respect to the corresponding center frequency of absorption (f_a) are provided in equations (5.9) and (5.10).

$$f_{tl(min)} = 1.71\,GHz = 0.31 f_a \tag{5.9}$$

$$f_{tl(max)} = 2.61\,GHz = 0.46 f_a \tag{5.10}$$

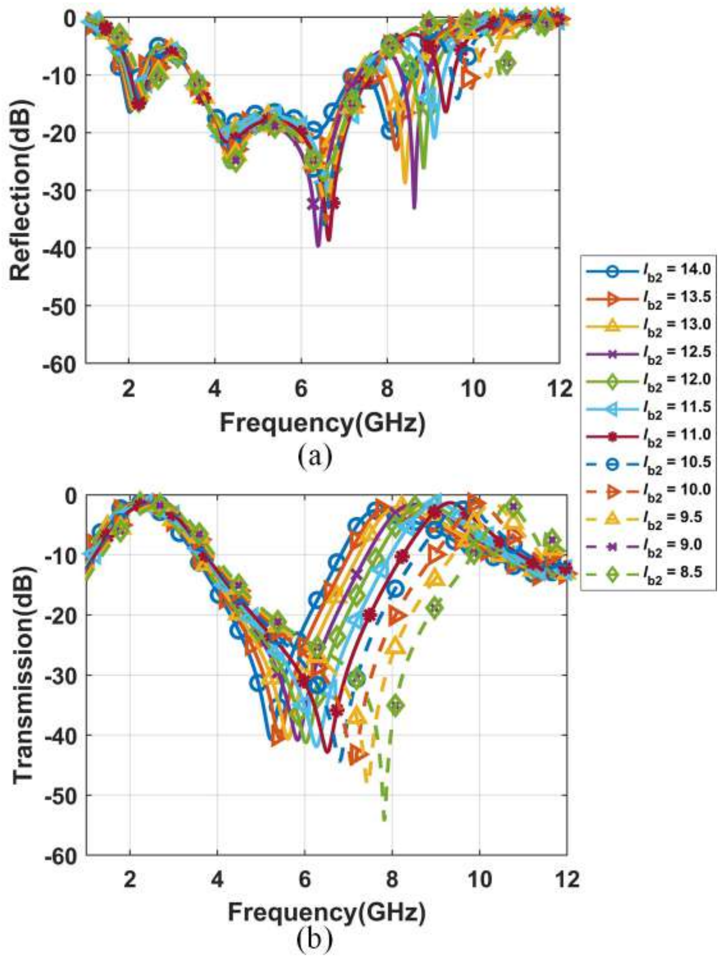

Figure 5.13: Simulated response of the proposed FSR for varying l_{b2} (in mm). (a) Reflection, and (b) transmission coefficients.

Further, the reflection and transmission coefficients of the FSR for l_{b2} varying from 14 mm to 8.5 mm with other parameters constant are shown in Figure 5.13. The performance of FSR for the different values of l_{b2} is arranged in Table 5.2. Decreasing the values of l_{b2} from 14 mm to 9.0 mm causes the upper transmission frequency f_{tu} to increase from 8.05 to 10.65 GHz, respectively, while the absorption band and lower transmission frequency f_{tl} remains nearly the same with some minor variations. Beyond $f_{tu} = 10.65$ GHz, reflection coefficient increases above -10 dB, making the transmission insignificant. Therefore, maintaining the insertion loss within 2 dB, f_{tu} can be varied from 8.62 to 10.65 GHz by decreasing l_{b2} from 12.5 to 9.0 mm, respectively.

The minimum and maximum limit of f_{tu} with respect to corresponding center frequency of absorption (f_a) are mentioned in equations (5.11) and (5.12).

$$f_{tu(min)} = 8.62\, GHz = 1.56 f_a \tag{5.11}$$

Table 5.1: Performance parameters of the FSR with varying l_{b1}.

l_{b1} (mm)	f_{tl} (GHz)	Minimum I.L in f_{tl} band	Absorption / (f_a) (GHz)	f_{tu} (GHz)	Minimum I.L in f_{tu} band	T_{Rl}	T_{Ru}
25.0	- Nil-	-Nil-	3.43–7.45 / (5.44)	8.74	1.67 dB	-	1.60
24.9	1.71	0.93 dB	3.56–7.36 / (5.46)	8.79	1.50 dB	0.31	1.60
24.5	1.98	1.25 dB	3.61–7.49 / (5.55)	8.81	1.66 dB	0.35	1.58
24.0	2.16	1.45 dB	3.67–7.47 / (5.57)	8.85	1.57 dB	0.38	1.58
23.5	2.29	1.61 dB	3.68–7.55 / (5.61)	8.85	1.76 dB	0.40	1.57
23.0	2.38	1.70 dB	3.72–7.55 / (5.63)	8.85	1.76 dB	0.42	1.57
22.5	2.47	1.78 dB	3.74–7.54 / (5.64)	8.87	1.73 dB	0.43	1.57
22.0	2.54	1.86 dB	3.75–7.54 / (5.64)	8.88	1.72 dB	0.45	1.57
21.5	2.61	1.93 dB	3.76–7.50 / (5.63)	8.86	1.66 dB	0.46	1.57
21.0	2.71	2.06 dB	3.83–7.54 / (5.68)	8.88	1.74 dB	0.47	1.56
20.5	2.79	2.15 dB	3.84–7.53 / (5.68)	8.89	1.69 dB	0.49	1.56
20.0	2.85	2.24 dB	3.86–7.53 / (5.69)	8.90	1.66 dB	0.50	1.56

Note: f_{tl} is the center frequency of the lower transmission band; f_a is the center frequency of the broad absorption band; f_{tu} is the center frequency of the upper transmission band; I.L is the insertion loss at the transmission band.

$$f_{tu(max)} = 10.65\, GHz = 1.86 f_a \tag{5.12}$$

The optimum range for the lower and upper transmission frequencies of the proposed FSR with respect to absorption frequency are given in equations (5.13) and (5.14).

$$f_{tl} = 0.31 f_a \ to \ 0.46 f_a \tag{5.13}$$

$$f_{tu} = 1.56 f_a \ to \ 1.86 f_a \tag{5.14}$$

Table 5.2: Performance parameters of the FSR with varying l_{b2}.

l_{b2} (mm)	f_{tl} (GHz)	Minimum I.L in f_{tl} band	Absorption / (f_a) (GHz)	f_{tu} (GHz)	Minimum I.L in f_{tu} band	T_{Rl}	T_{Ru}
14.0	2.02	1.30	3.47–6.82 / (5.14)	8.05	2.61	0.39	1.56
13.5	2.06	1.34	3.54–7.01 / (5.46)	8.20	2.20	0.37	1.50
13.0	2.09	1.38	3.59–7.22 / (5.27)	8.41	2.06	0.39	1.59
12.5	2.14	1.40	3.67–7.33 / (5.50)	8.62	1.57	0.38	1.56
12.0	2.16	1.45	3.67–7.47 / (5.57)	8.85	1.57	0.38	1.58
11.5	2.19	1.52	3.68–7.57 / (5.62)	9.09	1.48	0.38	1.61
11.0	2.23	1.53	3.72–7.56 / (5.64)	9.36	1.33	0.39	1.65
10.5	2.29	1.57	3.78–7.51 / (5.64)	9.62	1.22	0.40	1.70
10.0	2.35	1.62	3.83–7.55 / (5.69)	9.95	1.27	0.41	1.74
9.5	2.40	1.67	3.88–7.55 / (5.71)	10.35	1.63	0.42	1.81
9.0	2.45	1.72	3.92–7.53 / (5.72)	10.65	1.52	0.42	1.86
8.5	2.47	1.78	3.94–7.65 / (5.79)	-	-	0.42	-

Note: f_{tl} is the center frequency of the lower transmission band; f_a is the center frequency of the broad absorption band; f_{tu} is the center frequency of the upper transmission band; I.L is the insertion loss at the transmission band.

5.4 Experimental Verification and Discussion

A prototype of the proposed FSR consisting of an array of 10 x 10 unit cells, for the resistive and bandpass layers is fabricated. The photograph of the prototype with overall dimension of 250 mm x 250 mm is shown in Figure 5.14. An Air gap of 12 mm between the two layers is maintained using plastic spacer standoff (Figure 5.14(a). In the resistive layer, chip resistors having 200 Ω resistance from VISHAY (CRCW0603200RFKEA), are mounted in between the gaps of metallic square ring as shown in Figure 5.14(b). The measurement on the fabricated prototype is carried out using free space measurement

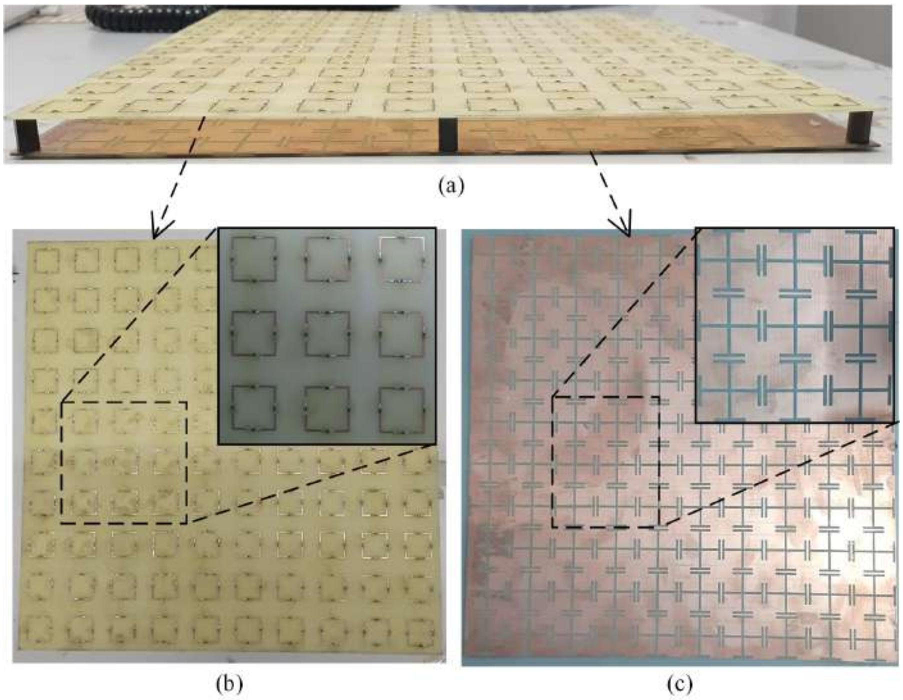

Figure 5.14: Photograph of the fabricated prototype. (a) Side view, (b) top, and (c) bottom layers.

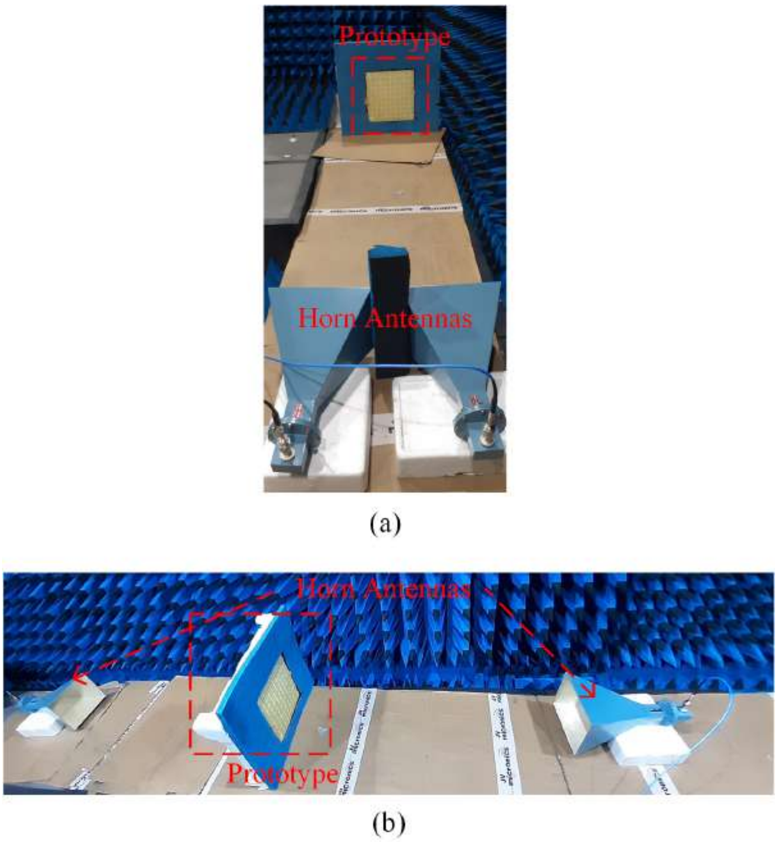

Figure 5.15: Measurement setups for (a) reflection, and (b) transmission coefficients.

technique wherein a pair of standard gain horn antennas connected with the two ports of a Keysight Vector Network Analyzer (N5224B) is used. The measurement setup for

Table 5.3: Performance comparison of the proposed FSR

Reference	A/T Location	Transmission band / I.L	Absorption band	Size	Thickness	Polarization
[77]	T-A	1.5 GHz/ 1.5 dB	4.95-7.0 GHz (34.3%)	$0.001{\lambda_L}^2$	$0.0432\lambda_L$	Dual
[98]	A-T	10 GHz / 0.2dB	3-9 GHz (100 %)	$0.072{\lambda_L}^2$	$0.12\lambda_L$	Dual
[91]	A-T-A	5.7 GHz / 0.48 dB	2.60-5.25 GHz (67.51 %) and 6.05-8.50 GHz (33.67 %)	$0.054{\lambda_L}^2$	$0.134\lambda_L$	Dual
[99]	A-T-A	6 GHz / 0.5 dB	2.18-4.43 GHz (68.07 %) and 7.55-9.98 GHz (27.72 %)	$0.019{\lambda_L}^2$	$0.078\lambda_L$	Insensitive
[108]	A-T-A-T	7.2 GHz/ 2.30 dB and 13.05 GHz / 1.69 dB	4.02-6.27 GHz (43.73 %) and 8.21-12.02 GHz (37.66 %)	$0.029{\lambda_L}^2$	$0.107\lambda_L$	Sensitive
This Work	T-A-T	2.1 GHz / 1.5 dB and 8.8 GHz /1.5 dB	3.6-7.4 GHz (69.09 %)	$0.026{\lambda_L}^2$	$0.09\lambda_L$	Insensitive

Note: A is the absorption band; T is the transmission band; λ_L denotes the free space wavelength corresponding to the lowest frequency of -10 dB reflection; I.L is the insertion loss at the transmission band.

both transmission and reflection are depicted in Figure 5.15. In the reflection measurement, a PEC sheet is used for the reference measurement which is then replaced by the fabricated FSR prototype and the effective reflection coefficient is determined. For transmission measurement, the reference case involves the direct path measurement between the two horn antennas. The measured transmission and reflection coefficients obtained in comparison with the simulated response is shown in Figure 5.16, where a close agreement between the two is achieved, thereby validating the response of the proposed FSR.

A relative performance comparison of the proposed T-A-T FSR with the earlier reported FSRs is presented in Table 5.3. The proposed FSR is a thin, polarization-insensitive and exhibits dual transmission property as compared to the reported FSRs [77, 98, 91, 99, 108].

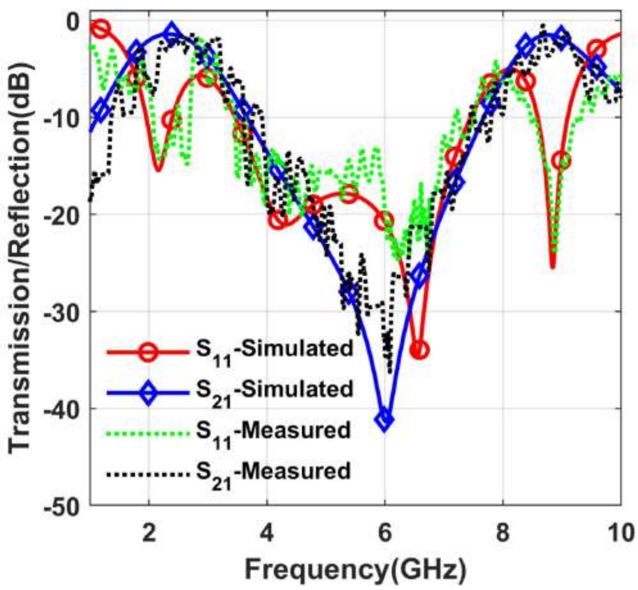

Figure 5.16: Simulated and measured reflection and transmission coefficients of the proposed FSR.

5.5 Conclusion

In this chapter, a dual transmission and polarization-insensitive T-A-T type rasorber is proposed. The design is realized by combining the square loop based broadband absorber with the dual bandpass FSS such that a broad absorption (3.6 to 7.4 GHz) is achieved between the two transmission bands (2.1 and 8.8 GHz). An ECM explains the working of proposed FSR. A tunable range of transmission frequencies corresponding to the bandpass FSS parameters is determined with respect to the center absorption frequency. A prototype consisting of 10 x 10 FSR unit cells is fabricated and the experimental validation of the performance of the FSR is obtained.

Chapter 6

A-T-A FSR for Low RCS Radiating System

In the previous two chapters, designs of A-T and T-A-T FSRs have been discussed. However, for achieving low out-of-band RCS of radiating systems, the A-T-A type FSR with transmission and two-sided absorption bands are more suitable. In this chapter, the objective is to design a compact, polarization-insensitive A-T-A rasorber with a high Q-factor in the transmission band for shielding and RCS reduction of a narrowband radiating system. Further, as an application of shielding a narrow band radiator, the proposed high-Q A-T-A FSR is used as radome on top of a patch antenna with an operating frequency same as the rasorber's transmission frequency. The co-design of the proposed A-T-A FSR with the narrow band patch antenna experimentally verifies the RCS reduction in out-of-band while maintaining the in-band characteristics.

6.1 Proposed A-T-A FSR

The FSR is commonly a two-layered design consisting of a resistive layer at the top while the bandpass FSS forms the bottom layer of the structure. The resistive layer mounted with the lossy components leads to the absorption of the incident electromagnetic (EM) wave, whereas the bandpass layer provides the necessary transmission. For realizing the FSR with A-T-A (absorption-transmission-absorption) response, the transmission band associated with the bandpass FSS must be located within the absorption band. However, the insertion loss is much higher at the desired transmission band due to overlap with the absorption band. An additional resonator printed on the lossy layer provides the desired transmission, thereby suppressing the absorption in that particular band.

The proposed FSR is printed on a 0.8 mm thick Rogers Kappa substrate (dielectric constant (ϵ_r) of 4.3, loss tangent (tanδ) equal to 0.005, and the thickness of copper plating equal to 35 μm). The steps involved in the design of the proposed FSR are summarized below:

1. In the first step, a study on broadband absorber is carried out to achieve an absorption within a wide frequency range.
2. The bandpass FSS is studied for achieving the desired transmission frequency.
3. The bandpass FSS substitutes the ground layer of the broadband absorber.
4. An MF-shaped resonator with a high-Q factor is co-designed with the lossy layer, which provides the resonant transmission at the desired frequency.
5. A further modification of the lossy layer improves the performance of the FSR at a higher absorption band.

6.1.1 Design and Analysis

The unit cell geometry of the FSS based broadband absorber is shown in Figure 6.1, involving a two-layered design of resistive and ground layers. As depicted in Figure 6.1(b), the resistive layer consists of a printed metallic square loop attached by a rectangular strip at the four sides. The lumped chip resistors having 200Ω resistance are mounted within the gap of the rectangular strips. The structure is analyzed using the CST microwave studio. The resistive and the ground layers are placed at a distance of $\lambda/4$ (λ corresponding to the center frequency of the desired absorption band). As depicted in Figure 6.1(c), the reflection coefficient is below -10 dB in the frequency band of 4.2 to 12.7 GHz. Thus, 90% absorption can be obtained in the operating band of 4.2 to 12.7 GHz.

The bandpass FSS, as shown in Figure 6.2(a), is studied by etching a double-cross-slot (DCS) within the metal-coated substrate. The simulated response, as shown in Figure 6.2(b) depicts a transmission band around 8.3 GHz. The metallic ground layer of the broadband absorber is substituted with the bandpass FSS, as shown in Figure 6.3(a).

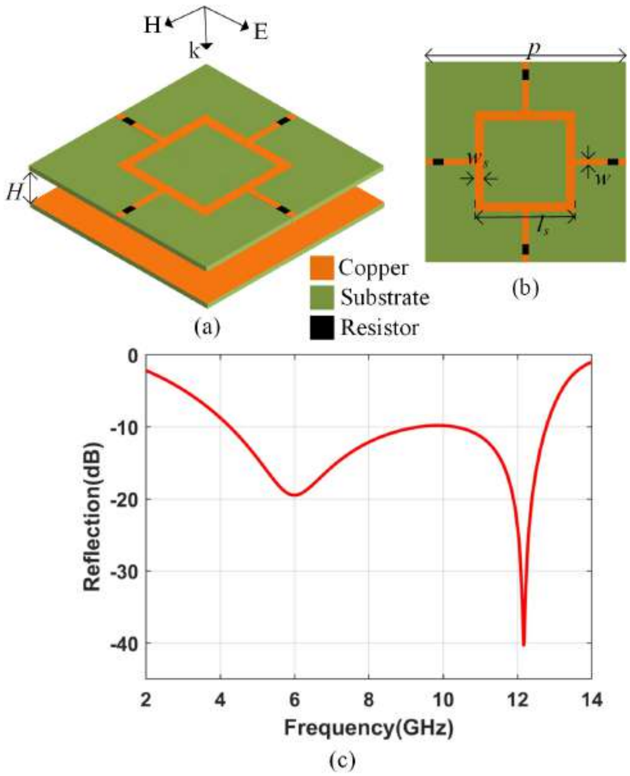

Figure 6.1: (a) Perspective, (b) front view of the unit cell geometry, and (c) simulated reflection coefficient of the broadband absorber. p = 15, w = 0.5, w_s = 0.8, l_s = 7.1, H=8 (all dimensions are in mm).

The response of the broadband absorber in combination with the bandpass FSS is shown in Figure 6.3(b). It can be observed that the insertion loss at the transmission frequency of bandpass FSS is quite high (more than 5 dB) which signifies a poor transmission. The higher reflections greater than -10 dB, further leads to weak transmission. The higher loss at the transmission frequency occurs due to overlapping with the absorption band in which the mounted lossy elements contribute to the losses.

To mitigate the losses at the transmission frequency, an MF-shaped resonator with higher transmission selectivity is added within the square loop resistive resonator, as shown in Figure 6.4. A cross loop slot is etched within the MF-shaped resonator. The shape and design of the resonator are appropriately chosen to achieve the desired transmission pole within the absorption band. The resonance frequency of the MF-shaped structure should coincide with the desired transmission frequency. The currents at the resonance get concentrated along the slots of the MF-shaped resonator thereby preventing the surface currents from flowing through the lumped components, thus reducing the associated losses. This can be explained by studying the surface current distribution at the transmission frequency for the two cases, as shown in Figure 6.5. In the case of the resis-

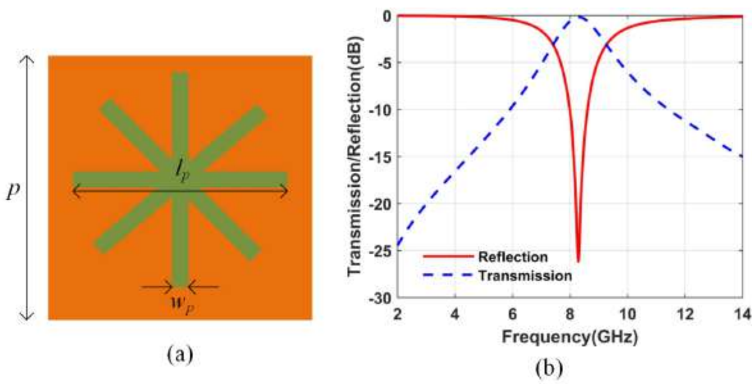

Figure 6.2: (a) Front view of unit cell geometry, and (b) simulated reflection/transmission coefficients of the bandpass FSS. $p = 15$, $l_p = 12$, $w_p = 0.6$ (all dimensions are in mm).

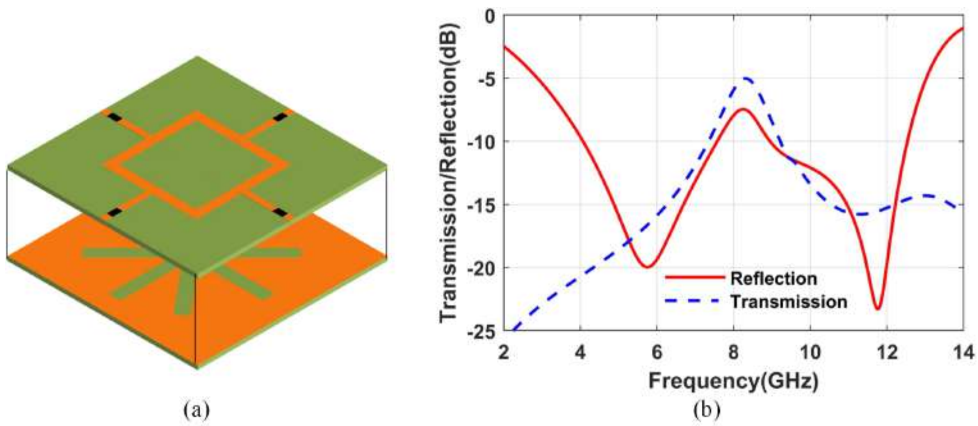

Figure 6.3: (a) Perspective view of the unit cell geometry, and (b) simulated reflection/transmission coefficients of the square loop resistive layer in combination with the bandpass FSS layer. .

tive layer without the MF-shaped resonator at center, the surface currents at the required transmission frequency are concentrated on the rectangular strip (Figure 6.5(a)), due to which a dominating current passes through the lumped resistor causing significant losses. However, as shown in Figure 6.5(b), by inserting the MF-shaped resonator, the resonating currents at the transmission frequency get concentrated along the resonator slots. The current through the lumped elements gets considerably reduced thereby decreasing the associated ohmic losses.

To further understand the effect of the MF resonator, the simulation response for only the front resistive layer with the MF resonator is provided in Figure 6.6. At the desired resonant frequency of 8.3 GHz, the insertion loss is reduced, and a typical transmission is realized.

In the proposed FSR, the MF resonator, which includes a resistive layer, is combined with the bandpass FSS. The full-wave simulation results of the proposed FSR is shown in Figure 6.7. A transmission notch is achieved at 8.4 GHz within a broad absorption band.

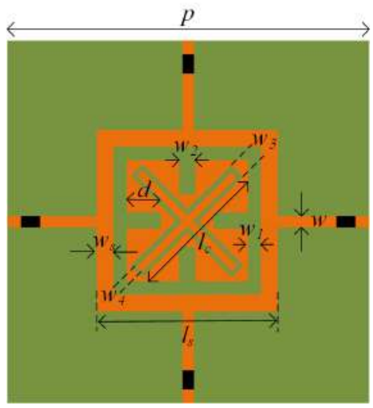

Figure 6.4: Front view of the unit cell with MF shaped resonator. $p = 15$, $w = 0.5$, $w_s = 0.8$, $l_s = 7.1$, $w_1 = 0.3$, $w_2 = 0.3$, $l_c = 5.8$, $w_3 = 0.6$, $w_4 = 0.2$, $d = 1.6$ (all dimensions are in mm).

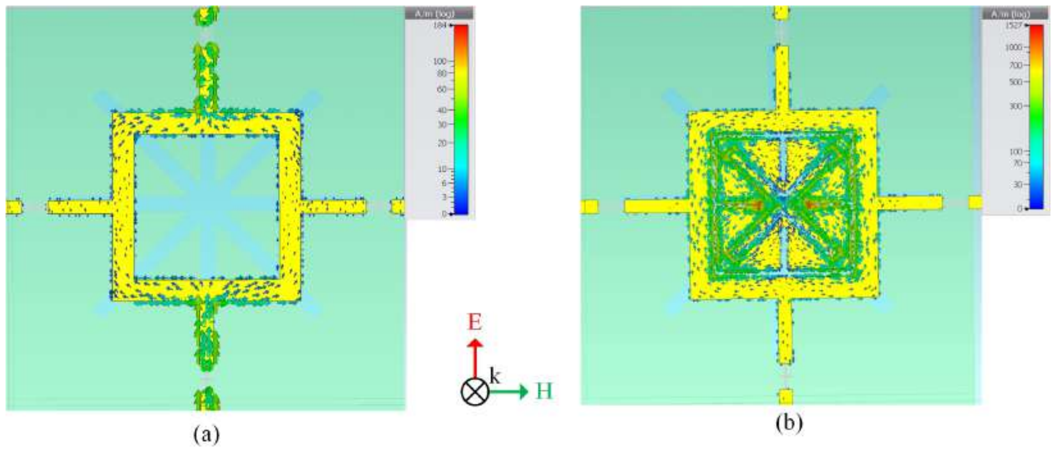

Figure 6.5: The surface current distribution of the resistive layer at 8.3 GHz, (a) without, and (b) with MF resonator.

However, as noticed in Figure 6.7, the reflection coefficient in the upper absorption band is slightly above -10 dB, due to which the absorptivity gets degraded at the upper absorption band. Further, in the proposed FSR design, the metallic square loop printed on the resistive layer is diagonally trimmed at its four corners, as depicted in Figure 6.8. The effect of this corner trimmed square loop can be observed in Figure 6.9, wherein the reflection coefficient at the upper absorption band is reduced below -10 dB. As such, the absorption performance in the upper band is improved by the corner trimming of the front square loop.

The proposed A-T-A FSR achieves a transmission notch at 8.4 GHz, with the absorption bands on both sides. The 80% lower absorption bandwidth is from 3.4 to 7.5 GHz (75.22%), while the upper absorption bandwidth ranges from 9.2 to 10.8 GHz (16%). The minimum insertion loss achieved at the transmission frequency (8.45 GHz) is 0.7 dB. The 3 dB bandwidth at the transmission band ranges from 8.17 to 8.69 GHz. For the proposed

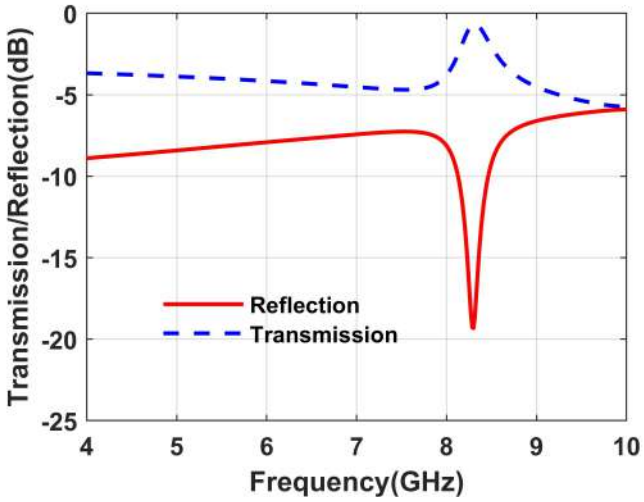

Figure 6.6: Simulated coefficients for the front resistive layer only with MF resonator.

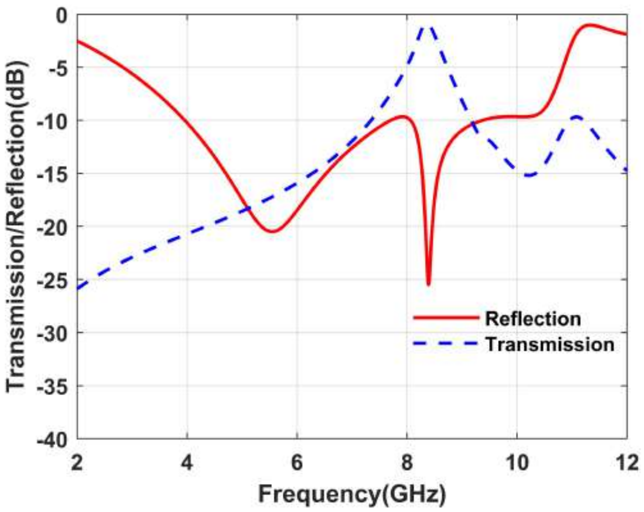

Figure 6.7: Simulated transmission and reflection coefficients of the proposed FSR

FSR structure Q factor at the passband is 16.25. which is the measure of selectivity and is quantitatively defined by the ratio of center frequency to bandwidth.

The proposed FSR is further analyzed with respect to various polarization angles of the incident EM wave. The simulated response of the proposed FSR under different polarization angles is shown in Figure 6.10(a). It is observed that the corresponding transmission and reflection coefficients remain unaltered in response to different polarization angles of the incident EM wave. As such, the proposed FSR, in accordance with its four-fold symmetry, exhibits a polarization-insensitive behavior.

The proposed FSR structure is also analyzed under the oblique incidence. Figure 6.10(b) depicts the response of the proposed FSR for the angle of incidence up to 40^o. The increase in incidence angle results in the decrease in absorptivity for the lower and

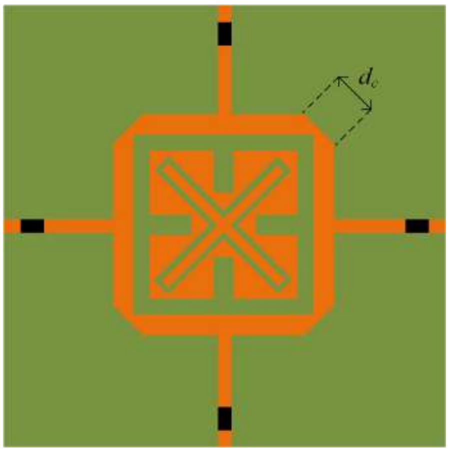

Figure 6.8: Front view of the proposed FSR unit cell with corner trimmed square loop.

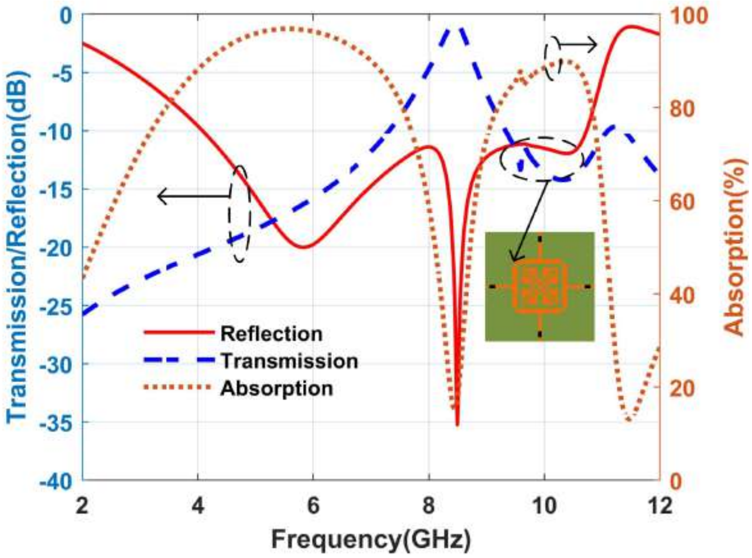

Figure 6.9: Simulated response of the proposed FSR with corner trimmed square loop.

upper absorption bands, while the effect on the transmission band is comparably less. However, up to 40^o of incidence angle, the absorption on the two sides of the transmission band remains within the acceptable limit. Thus, the proposed FSR possesses angular stability up to 40^o.

6.1.2 Equivalent Circuit Model

The functioning of the proposed FSR is further analyzed based on the corresponding equivalent circuit model (ECM). The FSR structure's incident wave leads to the generation of surface currents. Due to these surface currents on the metallic designs, inductive and capacitive effects get induced which can be modeled by the corresponding inductors and capacitors, respectively. An ECM analogous to the proposed FSR is provided in

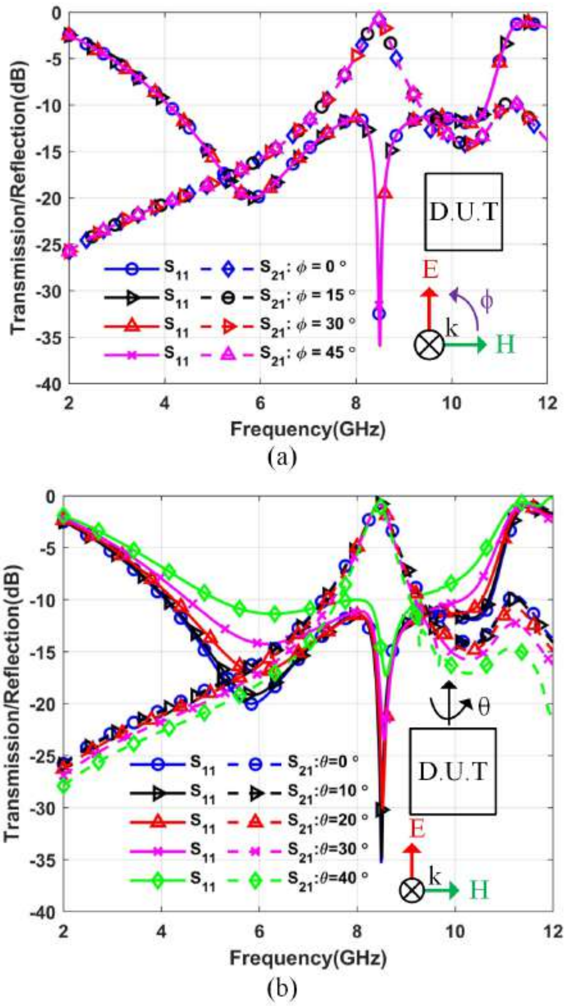

Figure 6.10: Simulated transmission and reflection coefficients of the proposed FSR under various (a) polarization, and (b) incidence angles.

Figure 6.11, in which the corresponding equivalent models of resistive layer, a dielectric substrate, air gap, and bandpass layer have been cascaded.

The parallel $R-C_0$ circuit models the mounted lumped resistance and the corresponding gap capacitance. Inductor L_1 models the inductance of the rectangular strip on the two sides of the edge trimmed square loop resonator. The parallel $L_2 - C_2$ arrangement is associated with the square loop-shaped metallic resonator. The MF-shaped resonator consisting of cross-loop slot is modeled using the parallel combination of series $L_3 - C_3$ and $L_4 - C_4$. The inter capacitance between the square loop and MF-shaped resonator is modeled using C_1. The double cross-slot-shaped bandpass layer is modeled using a parallel $L_P - C_P$ circuit. The air gap maintained between the two layers is represented using the transmission line model with free space characteristic impedance Z_0 and length H. The thickness of the top and bottom dielectric layers can be characterized using a

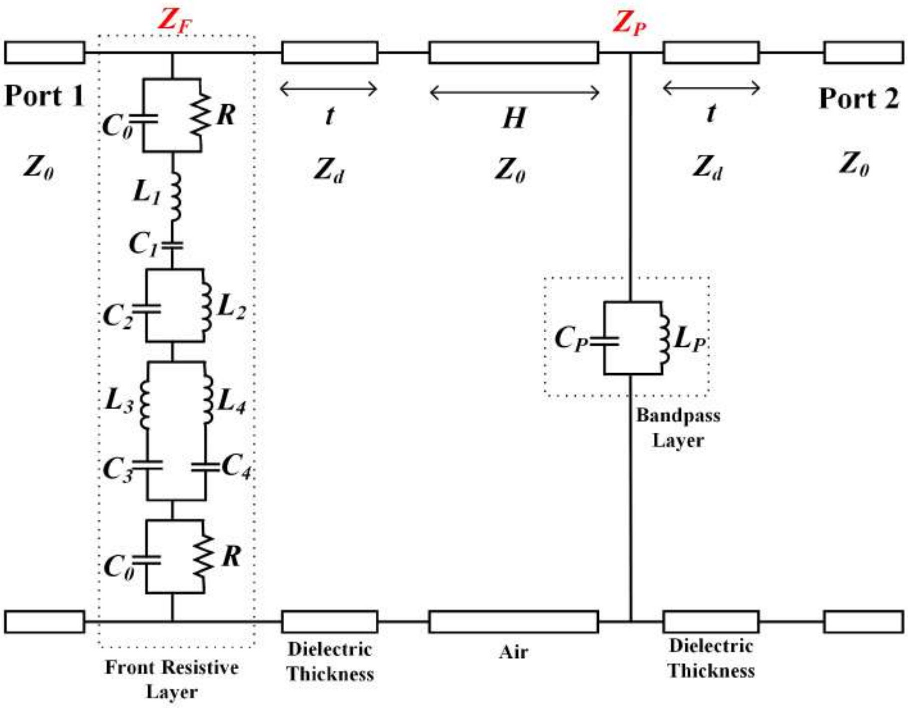

Figure 6.11: ECM corresponding to the proposed FSR (R= 200Ω, C_0 = 0.036085 pF, C_1 = 0.187 pF, L_1 = 2.45 nH, L_2 = 0.53 nH, C_2 = 0.338 pF, L_3 = 0.33 nH, C_3 = 0.401 pF, L_4 = 1.085 nH, C_4 = 0.65 pF, L_P = 0.7 nH, C_P = 0.5 pF, Z_d = 181 Ω, t = 0.8 mm, Z_0 = 377 Ω).

transmission line model with characteristic impedance $Z_d = Z_0/\sqrt{\epsilon_r}$ and length equivalent to the thickness of substrates (t). The overall circuit is a two-port network matched to the free space at both ports.

The ABCD parameters for the ECM can be calculated by the sequential multiplication of individual ABCD parameters corresponding to each layer given by the following equation:

$$\begin{bmatrix} A & B \\ C & D \end{bmatrix} = \begin{bmatrix} 1 & 0 \\ 1/Z_\mathrm{F} & 1 \end{bmatrix} \times \begin{bmatrix} \cos\beta t & \mathrm{j}Z_d \sin\beta t \\ \mathrm{j}\sin\beta t/Z_\mathrm{d} & \cos\beta t \end{bmatrix} \times$$
$$\begin{bmatrix} \cos\beta_0 H & \mathrm{j}Z_0 \sin\beta_0 H \\ \mathrm{j}\sin\beta_0 H/Z_0 & \cos\beta_0 H \end{bmatrix} \times \begin{bmatrix} \cos\beta t & \mathrm{j}Z_d \sin\beta t \\ \mathrm{j}\sin\beta t/Z_\mathrm{d} & \cos\beta t \end{bmatrix} \times$$
$$\begin{bmatrix} 1 & 0 \\ 1/Z_\mathrm{P} & 1 \end{bmatrix} \quad (6.1)$$

where β represents the propagation constant calculated as $\beta = \beta_0\sqrt{\mu_r\epsilon_r}$ (μ_r and ϵ_r are the relative permeability and permittivity of the dielectric substrate, respectively). The

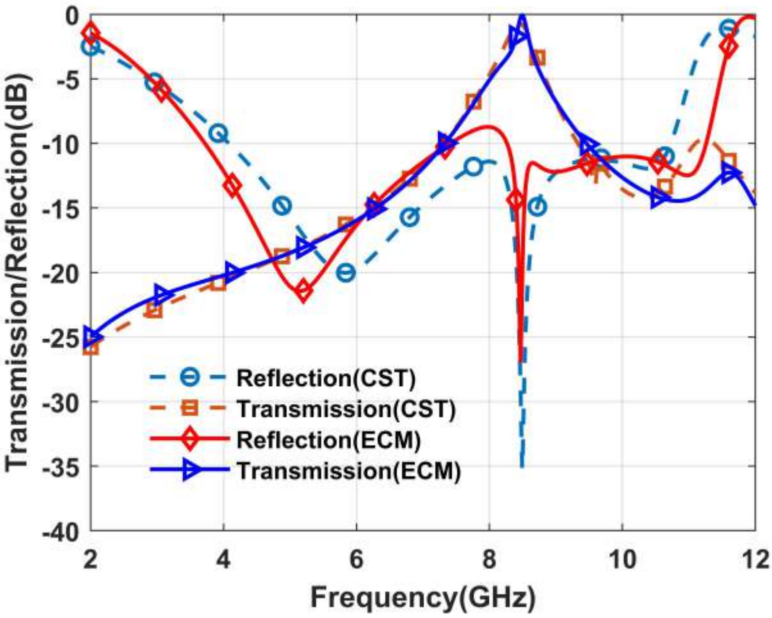

Figure 6.12: Simulated transmission and reflection coefficients of the ECM and full-wave simulation of the proposed FSR.

Z_F and Z_P denoting the impedance of the top resistive layer and bottom bandpass FSS are given by (6.2) and (6.3).

$$Z_F = \frac{2R}{1-\omega^2 R^2 (C_0)^2} + j\left\{\omega L_1 - \frac{1}{\omega C_1} - \frac{2R^2\omega C_0}{1-\omega^2 R^2(C_0)^2} + \frac{\omega L_2}{1-\omega^2 C_2 L_2} - \frac{(1-\omega^2 L_3 C_3)(1-\omega^2 L_4 C_4)}{\omega C_3 + \omega C_4 - \omega^3 L_3 C_3 C_4 - \omega^3 L_4 C_3 C_4}\right\} \tag{6.2}$$

$$Z_P = \frac{j\omega L_P}{1-\omega^2 L_P C_P} \tag{6.3}$$

The S-parameters associated with the ECM are calculated from ABCD parameters using the following conversion formula:

$$S_{11} = \frac{A+B/Z_0-CZ_0-D}{A+B/Z_0+CZ_0+D} \tag{6.4}$$

$$S_{21} = \frac{2}{A+B/Z_0+CZ_0+D}. \tag{6.5}$$

The absorptivity $A(\omega)$ can subsequently be calculated from S-parameters obtained in (4) and (5) using (6).

$$A(\omega) = 1 - |S_{11}|^2 - |S_{21}|^2. \tag{6.6}$$

The ECM corresponding to the proposed FSR is analyzed in a Keysight ADS Simula-

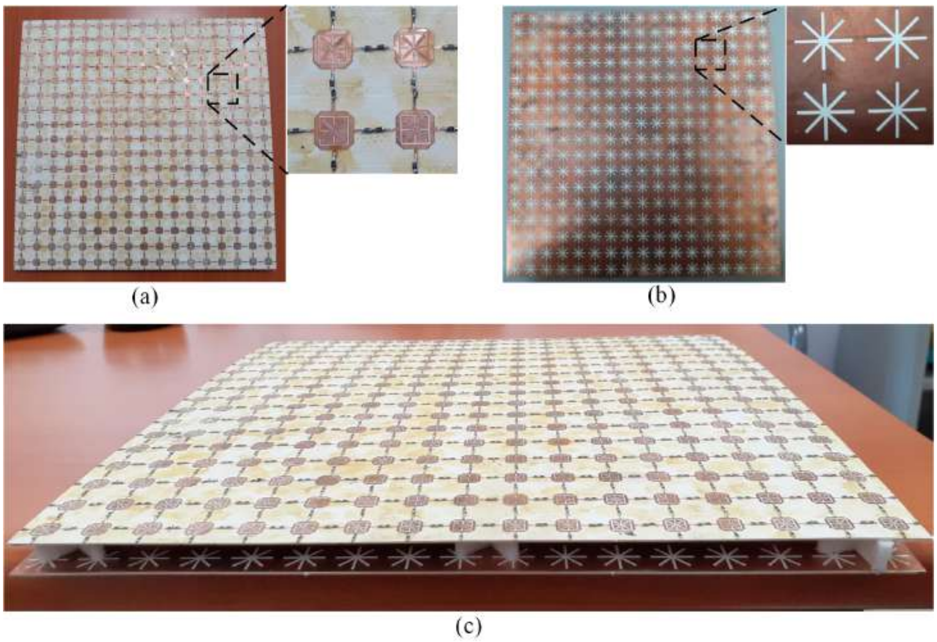

Figure 6.13: Photographs of the fabricated prototype of the proposed FSR: (a) top layer, (b) bottom layer, and (c) side view.

tor. The simulated S-parameters of the ECM in comparison with the full-wave simulation of the proposed FSR are provided in Figure 6.12. It can be observed that the simulated reflection and transmission coefficients of ECM closely follow the A-T-A characteristics of the proposed rasorber, with the center transmission frequency at 8.4 GHz having absorption bands on both sides. Thus, the working of the proposed FSR is explained by studying the corresponding ECM.

6.2 Experimental Measurement of the proposed FSR and Discussions

Experimental validation for the features of the proposed FSR is obtained by carrying out measurements on the fabricated prototype of the proposed FSR. A prototype consisting of 17 x 17 units cells of the proposed FSR is fabricated using a 0.8 mm thick Rogers Kappa substrate having a dielectric constant (ϵ_r) of 4.3, loss tangent (tanδ) equal to 0.005. The photographs of the fabricated prototype having an overall dimension of 255 mm x 255 mm are provided in Fig 6.13. The resistive layer consisting of mounted chip resistors (CRCW0603200RFKEA from VISHAY) having 200Ω resistance is provided in Figure 6.13(a). The bandpass FSS layer having DCS type etching is shown in Figure 6.13(b).

Table 6.1: Proposed A-T-A FSR in comparison with the recently reported A-T-A rasorbers

Ref.	Passband (I.L)	Q-factor	Operating Bandwidth (GHz)	Lower Absorption B.W (GHz)	Upper Absorption B.W(GHz)	Thickness	No. of Layers	Unit Cell Size	Polarization	Angular Stability	RCS Reduction Verified
[91]	5.7 GHz (0.48 dB)	12.95	2.6−8.5 (106.3%)	2.6−5.25 (67.5%)	6.05−8.5 (33.7%)	15.524 mm ($0.15\lambda_L$)	2	27 mm x 27 mm ($0.075\lambda_L^2$)	Dual	35^o	No
[100]	5 GHz (0.35 dB)	7.35	2.7−8.4 (102.7%)	2.76−4.40 GHz (45.81%)	5.64−8.42 (39.5%)	11 mm ($0.101\lambda_L$)	2	14 mm Hexagon ($0.037\lambda_L^2$)	Dual	30^o	No
[111]	3.63 GHz (0.14 dB)	6.36	1.9−6.82 (112.8%)	1.9−2.74 (57.7%)	4.04−6.82 (51.1%)	13 mm ($0.082\lambda_L$)	2	25 mm x 25 mm ($0.024\lambda_L^2$)	Dual	40^o	No
[96]	6.5 GHz (0.67 dB)	DNG	1.5−13.7 (160.5%)	1.5−4.6 (101.63%)	9.2−13.7 (39.3%)	32 mm ($0.16\ \lambda_L$)	4	20 mm x 20 mm ($0.01\lambda_L^2$)	Dual	DNG	No
[95]	6.01 GHz (0.38 dB)	DNG	2.95−9.24 (103.1%)	2.95−5.65 (62.7%)	7.4−9.24 (22.1%)	6.5 mm ($0.063\lambda_L$)	2	20 mm x 20 mm ($0.038\lambda_L^2$)	Dual	50^o	No
[101]	6.6 GHz (0.44 dB)	6.05	2.89−8.85 (101.5 %)	2.89−5.59 (63.8%)	8.79−8.85 (6.03%)	10.17 mm ($0.097\lambda_L$)	4	20 mm x 20 mm ($0.037\lambda_L^2$)	Dual	45^o	No
[102]	8.7 GHz (1 dB)	3.28	– (116.2 %)	– (63.51%)	– (31.84%)	9.802 mm ($0.113\lambda_L$)	4	10 mm x 10 mm ($0.014\lambda_L^2$)	Dual	45^o	No
[94]	10.4 GHz (0.52 dB)	DNG	6.26−14.06 (76.77 %)	6.26−9.58 (41.91%)	11.46−14.06 (20.37%)	6.016 mm ($0.125\lambda_L$)	2	18 mm x 18 mm ($0.141\lambda_L^2$)	Dual	30^o	No
[93]	7.9−9.0 GHz (1 dB)	7.68	3.3−12.0 113.72 %)	3.3−7.1 (73.07%)	9.4−12.0 (24.29%)	10.45 mm ($0.01\lambda_L$)	4	18 mm x 18 mm ($0.031\lambda_L^2$)	Dual	20^o	No
[92]	6.3 GHz (0.78 dB)	DNG	2.5−14.6 (141.52%)	2.3−5.3 (78.94%)	7.8−14.6 (60.71%)	13.85 mm ($0.111\lambda_L$)	3	20 mm x 20 mm ($0.023\lambda_L^2$)	DNG	DNG	No
[103]	10.28 GHz (0.47 dB)	DNG	3.06−19.26 (145.2%)	DNG	DNG	11.93 mm ($0.122\lambda_L$)	3	9 mm x 18 mm ($0.016\lambda_L^2$)	Single	30^o	No
[104]	8−12.5 GHz (2 dB)	DNG	1.5−21.8 (174%)	1.5−3.6 (82.35%)	15.2−21.8 (35.67%)	23 mm ($0.126\lambda_L$)	3	60 mm x 60 mm ($0.09\lambda_L^2$)	Dual	45^o	No
This Work	**8.4 GHz (0.7 dB)**	**16.25**	**3.4−10.8 (104.2%)**	**3.4−7.5 (75.22%)**	**9.2−10.8 (16%)**	**9.6 mm ($0.108\lambda_L$)**	**2**	**15 mm x 15 mm ($0.028\lambda_L^2$)**	**Insensitive**	40^o	**Yes**

λ_l= free space wavelength for the lowest absorption frequency, DNG = Data not given.

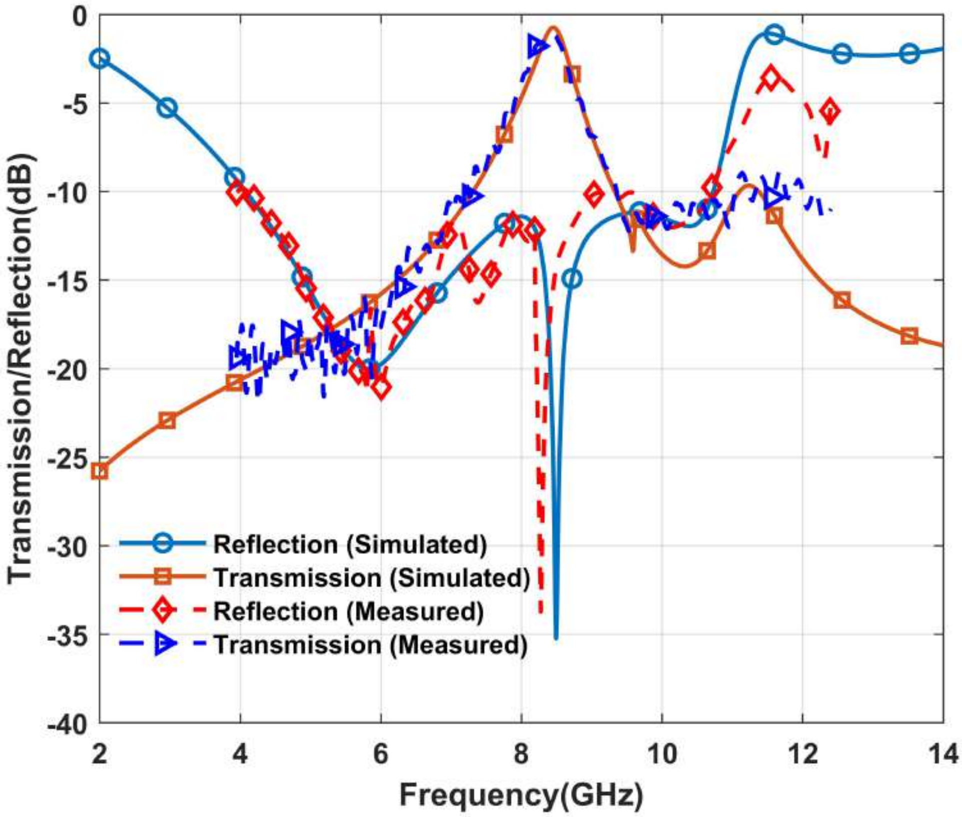

Figure 6.14: Measured transmission and reflection coefficients of the fabricated 17 x 17 array of FSR prototype compared with the simulated results.

The two-layer arrangement of the proposed FSR using the plastic spacers between the resistive and bandpass layers is shown in Figure 6.13(c).

The free space measurements are carried out separately for C(3.95 to 5.85 GHz), J(5.85 to 8.20 GHz), and X(8.20 to 12.4 GHz) bands using the corresponding standard gain horn antennas for each of the bands. The S-parameters are measured using the Keysight PNA Network Analyzer N5224B. For the reflection measurement, the time domain application of the PNA is utilized in which a single horn antenna measures the reflection coefficient of the fabricated structure using the time gating technique. The reflection and transmission coefficients are measured with their respective references. The metallic reflecting surface is taken as a reference for the reflection measurements. In contrast, the measurement corresponding to the direct path between the two horn antennas is considered a reference for transmission. The measured transmission and reflection coefficients compared to the simulated results are provided in Figure 6.14. A close agreement between the measured and simulated results is observed, which experimentally validates the performance of the proposed FSR.

In Table 6.1, the performance of the proposed A-T-A FSR is compared with the recently reported A-T-A FSRs in the literature. The novelty and performance of the proposed FSR over the recently reported A-T-A FSRs are listed as follows:

1. The Q-factor at the transmission band, which quantitatively measures selectivity, is higher in the proposed FSR among all the reported FSRs [91]−[96], [100]−[104], [111]. The higher selectivity of the proposed FSR makes it the most suitable candidate for shielding and EMI reduction of the narrowband radiating systems over all the reported FSRs.

2. The proposed structure provides better absorption bandwidth of 75.22% in the lower band as compared to the FSR designs reported in [91, 93, 94, 95, 100, 101, 102, 111] and 16% in the upper band over the design studied in [101].

3. The proposed FSR is a 2-layer structure which makes the proposed design less complex as compared to the reported 4-layer [93, 96, 101, 102] and 3-layer [92, 103, 104] FSR designs.

4. The unit cell size of the proposed FSR is more compact as compared to the reported works [91, 93, 94, 95, 100, 101, 104].

5. The thickness of the proposed FSR is lesser than the reported FSRs [91, 92, 94, 96, 102, 103, 104].

6. The proposed FSR, as a radome, is experimentally verified for the RCS reduction of the narrowband patch antenna (discussed in the next section), which emphasizes the upper hand of the proposed work over the reported works [91]−[96], [100]−[104], [111].

6.3 Low RCS Antenna Co-designed With proposed FSR

This section discusses the proposed A-T-A rasorber integrated with a narrowband patch antenna to realize a low out-of-band RCS radiating system. The patch antenna is designed on a 0.762 mm thick Rogers Diclad substrate ($\epsilon_r = 2.2$, $\tan\delta = 0.0009$) such

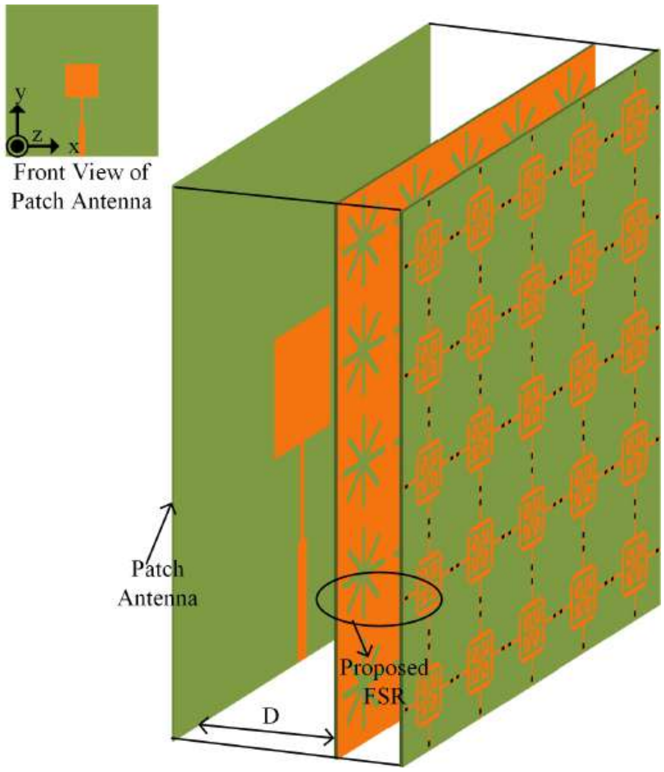

Figure 6.15: Schematic of the FSR integrated patch antenna. D=18 mm.

that its operating frequency coincides with the transmission frequency of the proposed FSR. The ground dimensions of the patch antenna are chosen to be 75 mm x 75 mm, which corresponds to the dimension of a 5 x 5 array of the proposed FSR unit cell. The schematic shown in Figure 6.15 represents the arrangement in which an array of 5 x 5 FSR unit cells is placed as a superstrate above the patch antenna at a distance close to $\lambda/2$ at the antenna's operating frequency. A study on RCS, including the other antenna parameters, is carried out for the FSR integrated antenna compared to the conventional antenna. The fabricated prototype of the FSR integrated antenna is shown in Figure 6.16, which consists of an array of 5 x 5 unit cell of FSR placed as a superstrate over the patch antenna.

The simulated and measured S_{11} of both conventional and FSR integrated antenna along with the corresponding gains are shown in Figure 6.17. The operating frequency for both the conventional and FSR integrated antennas lies around 8.4 GHz. The gain of the FSR integrated antenna at 8.4 GHz is 6.072 dBi which is slightly lesser than that of the conventional antenna (6.854 dBi). The simulated and measured radiation patterns of conventional and FSR integrated antennas at 8.4 GHz in both xz and yz planes are depicted in Figure 6.18. The FSR integrated radiation pattern remains nearly stable

Figure 6.16: Fabricated prototype photograph of the FSR integrated patch antenna.

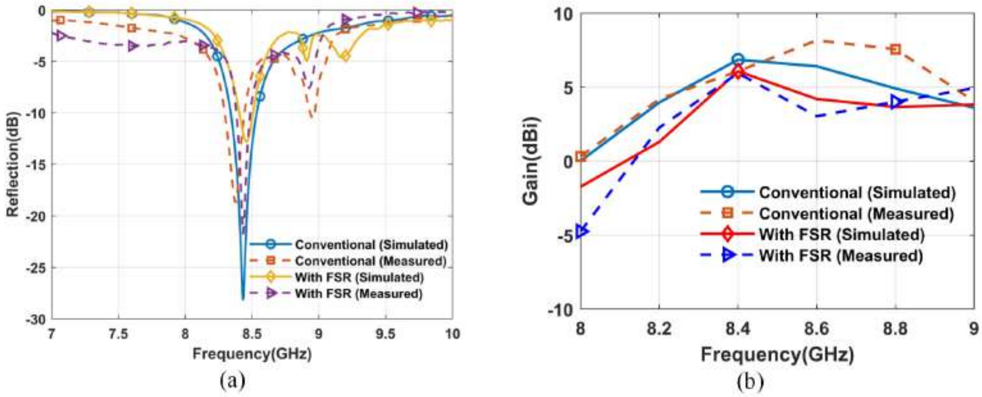

Figure 6.17: (a) Reflection coefficient, and (b) gain of the patch antenna.

compared to the conventional antenna.

6.3.1 Mono-static RCS Measurement

The RCS measurements on the fabricated prototypes of both conventional and FSR integrated antennas are carried out. In the case of mono-static RCS, the the transmitter and the receiver are located at the same position. The time domain gating application of the Keysight PNA Network Analyzer N5224B is utilized for the mono-static RCS measurement. A single horn antenna acts as both the transmitter and receiver. The general equation of the RCS is given by equation (6.7) [138].

$$RCS = \frac{P_r}{P_t} . \frac{(4\pi)^3 R^4}{G_t G_r \lambda^2} = K . \frac{P_r}{P_t} \tag{6.7}$$

where P_r and P_t are the received and transmitted powers, respectively. G_r and G_t are the gain of reflecting and transmitting antennas, respectively. R is the range to target, and

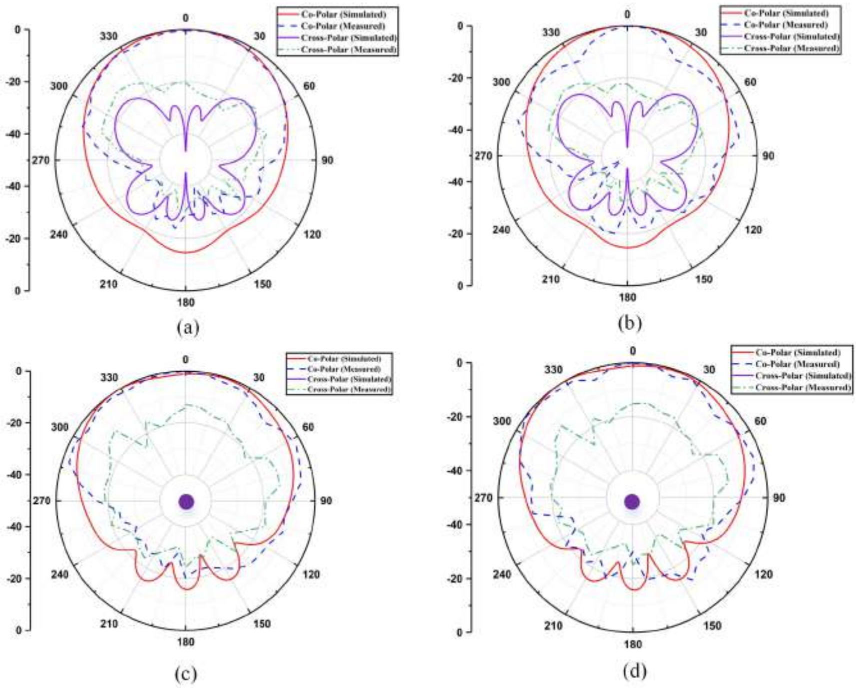

Figure 6.18: The radiation patterns of the patch antenna. (a) xz plane (without FSR). (b) xz plane (with FSR). (c) yz plane (without FSR). (d) yz plane (with FSR)

λ is the corresponding wavelength.

The mono-static RCS measurements of the FSR integrated antenna and conventional antenna are carried out in reference to a standard square PEC (size is the same as the cross-section of the ground plane of the antenna). The comparison of mono-static RCS of the FSR co-designed with the antenna, and the conventional antenna is shown in Figure 6.19. It can be observed that the mono-static RCS of the FSR integrated antenna is reduced in the out-of-band frequencies as compared to the conventional antenna. In contrast, the mono-static RCS remains the same around the antenna's operating frequency for both FSR co-designed with antenna and conventional antenna. In the lower band, the maximum RCS reduction is 23 dB at 5.1 GHz, while in the upper band, the maximum RCS reduction achieved is 10 dB at 10.9 GHz. The average RCS reduction of 11.92 dB and 5.04 dB is achieved in the lower (4−7.5 GHz) and upper (9.2−10.8 GHz) frequency bands, respectively, for the FSR co-integrated with the antenna.

6.3.2 Bi-static Measurement

In the case of bi-static RCS measurement, the receiving and the transmitting horn antennas are placed at different locations. The setup for the measurement of bi-static RCS

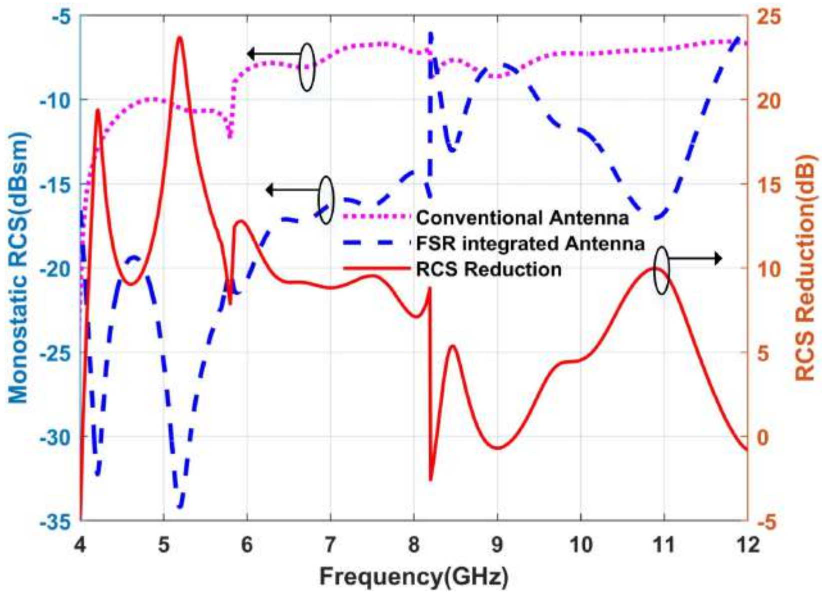

Figure 6.19: Monostatic RCS of the FSR integrated antenna compared to the conventional patch antenna.

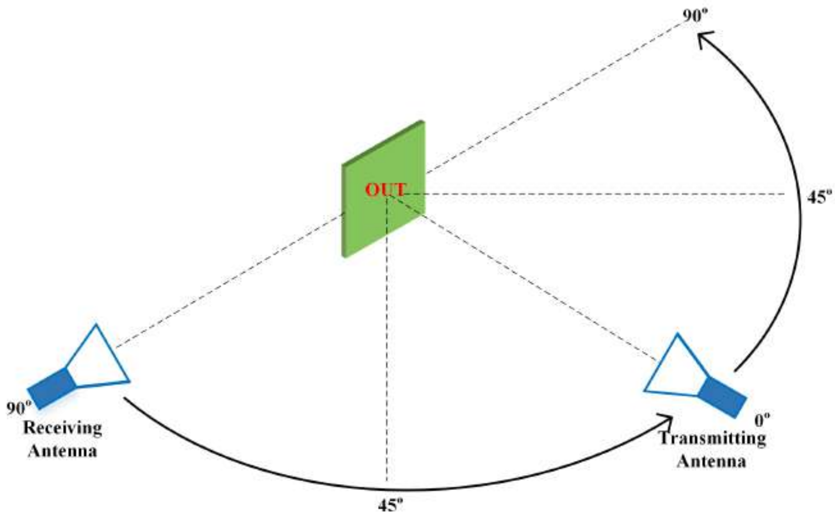

Figure 6.20: Schematic for the bistatic measurement setup.

is shown in Figure 6.20, where the transmitting horn antenna is kept stationary, and the incident wave falls in the normal direction to the object under test (OUT), while the receiving antenna is placed at a far-field distance R from the OUT. The receiving horn antenna is moved in a circular path from 0^o to 90^o at 10^o steps in either clockwise or anticlockwise direction. The transmission coefficient at each step is measured using PNA. The scattered field $E_{sca}(f, \phi)$ at each angle is defined by the following equation [139]:

$$E_{sca}(f, \phi) = S_{21,O}(f, \phi) - S_{21,FS}(f, \phi) \tag{6.8}$$

where $S_{21,O}$ and $S_{21,FS}$ is the transmission coefficient between the transmitter and

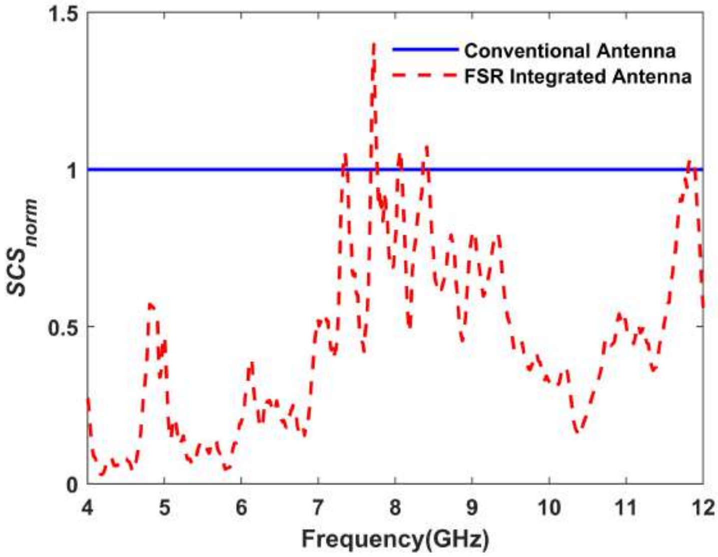

Figure 6.21: Normalized total bi-static RCS of the FSR integrated antenna with reference to the conventional antenna.

receiver horn antennas for the object and free space, respectively. The normalized total radar cross-section $RCS_{t,norm}$ of the FSR integrated antenna is determined by the integration of scattered fields intensities as given by the eq. 9 [139]:

$$RCS_{t,norm} = \frac{\int |E_{sca,FSRA}(f,\phi)|^2 d\phi}{\int |E_{sca,CA}(f,\phi)|^2 d\phi} \tag{6.9}$$

where $E_{sca,FSRA}$ and $E_{sca,CA}$ are the scattered fields of the FSR integrated and conventional antenna, respectively.

The $RCS_{t,norm}$ of the FSR integrated antenna with respect to the conventional antenna is shown in Figure 6.21. A significant reduction in the $RCS_{t,norm}$ of the FSR co-designed with antenna is observed with respect to the conventional antenna. The minimum $RCS_{t,norm}$ are obtained as 0.02 at 4.1 GHz and 0.15 at 10.4 GHz. It can be inferred that 98% (at 4.1 GHz) and 85% (at 10.4 GHz) reduction in total bistatic RCS is achieved for the proposed FSR co-designed antenna with respect to the conventional antenna. The average bi-static $RCS_{t,norm}$ is observed as 0.23 and 0.40 in the lower (4−7.5 GHz) and upper (9.2−10.8 GHz) absorption bands, respectively. Accordingly, the average total bi-static RCS reduction of 77% and 60% are achieved in the lower and upper absorption bands, respectively.

The performance comparison of the FSR integrated antenna provided with recently reported radome based low RCS antennas is given in Table 6.2. The performance of the

Table 6.2: Performance Comparison of the proposed FSR integrated antenna with the recently reported radome type low RCS antennas

Ref.	Operating Frequency	Size	Thick	No. of layers	Lumped element per unit cell	RCS reduction band	Max. mono-static RCS reduction	Average mono-static RCS reduction	Measured average total bi-static RCS reduction
[130]	10 GHz	1.8λ x 1.8λ	0.2λ	2	6	5.1−9.5 GHz and 13.2−16.2 GHz	20 dB	–	–
[131]	5 GHz	1.8λ x 1.8λ	0.225λ	4	3	–	–	11 dB	–
[132]	10 GHz	2.2λ x 2.2λ	0.8λ	5	12	6−18 GHz	11.8 dB	—	–
[133]	7.5 GHz	1.5λ x 1.5λ	0.8λ	4	8	5−5.33 GHz and 9−13.4 GHz	–	–	–
[134]	10 GHz	10.6λ x 10.6λ	0.5λ	2	2	2.9−7.6 GHz and 13.6−17.9 GHz	20 dB	–	–
This Work	8.4 GHz	**2.10λ x 2.10λ**	**0.7λ**	3	4	**4−7.5 GHz and 9.2−10.8 GHz**	**23 dB at 5.1 GHz**	**11.92 dB (4−7.5 GHz)/ 5.04 dB (9.2−10.8 GHz)**	**77% (4−7.5 GHz)/ 60% (9.2−10.8 GHz)**

λ= wavelength at the operating frequency of the antenna.

FSR integrated antenna can be enlisted as:

1. The proposed FSR integrated antenna has a more compact size than the reported designs in [132, 134]. Furthermore, the proposed FSR is electrically thinner than the structures studied in [132, 133].

2. The complexity of the proposed FSR integrated antenna is lesser than antennas reported in [131, 132] (in terms of lesser number of substrate layers dedicated) and [130, 132, 133] (in terms of lesser lumped components employed per unit cell).

3. In contrast to the reported works [130]−[134], the average total bi-static RCS reduction (77% from 4-7.5 GHz and 60% from 9.2-10.8 GHz) is experimentally demon-

strated for the proposed FSR integrated antenna with reference to the conventional antenna.

6.4 Conclusion

This chapter presents a novel design technique for realizing an A-T-A type FSR using an MF based resonator and exhibiting higher selectivity (Q = 16.25) at the passband. The MF resonator with a cross-slot printed on the front side of the resistive layer provides a transmission pole at the frequency corresponding to the transmission frequency of the DCS based bandpass FSS, thus realizing a transmission window (at 8.4 GHz) within a broad absorption band (3.4−10.8 GHz). An ECM corresponding to the proposed FSR is analyzed for understanding the related working principle. A prototype with 17 x 17 proposed unit cells are fabricated, and the corresponding measurements provide the experimental validation of the proposed design. Further, the proposed FSR with a 5 x 5 unit cell is integrated with a patch antenna as a superstrate to realize a low RCS system. The FSR integrated antenna achieves an average mono-static RCS reduction of 11.92 dB and 5.04 dB in the lower (4−7.5 GHz) and upper (9.2−10.8 GHz) absorption bands, respectively, while maintaining the other antenna parameters. Further, the average normalized total RCS of 0.23 and 0.40 is achieved for the FSR integrated antenna with respect to the conventional antenna in the lower and upper absorption bands, respectively.

Chapter 7

A-T-A-T FSR using Minkowski Fractal Resonator

In the previous chapter, a novel design of A-T-A FSR based on the Minkowski Fractal (MF) resonator has been proposed which provides higher selectivity at the transmission band. However, a dual transmission FSR is required for the RCS and EMI interference reduction of a dual-band radiating system. In this chapter, a dual transmission FSR having absorption-transmission-absorption-transmission (A-T-A-T) response has been proposed by extending the investigation on the MF shaped resonator in realizing a dual-band transmission. The proposed MF shaped resonator printed within the square loop lossy layer provides dual transmission poles which in combination with cross slot shaped dual bandpass FSS achieves two passbands in X and Ku bands within a broad absorption bands.

7.1 Design of Proposed Rasorber

The geometric description for the proposed dual transmissive rasorber is represented in Figure 7.1. The proposed rasorber is a double-layered design comprising of top resistive lossy layer and bottom bandpass layer separated by an air gap of H. Rogers Kappa having thickness equal to 0.8 mm, dielectric constant ϵ_r of 4.3 and loss tangent of 0.005 is utilized for the proposed design. In the top resistive layer (Figure 7.1(a)) the square loop resistor loaded resonator is filled with a MF-shaped resonator. Within the MF-shaped resonator, a cross-loop slot is incorporated. The bottom bandpass layer (Figure 7.1(b)) constitutes of the cross-loop shaped slot located at center of the metal coated surface. Also, at the

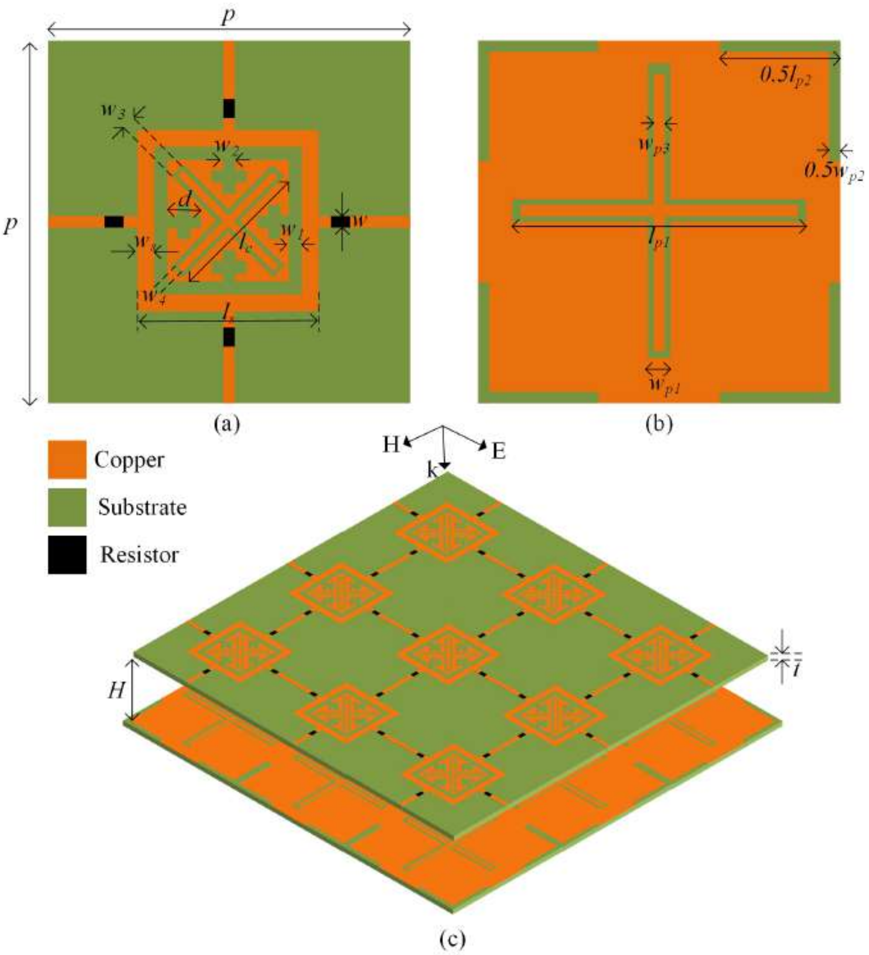

Figure 7.1: Schematic geometry of the proposed FSR unit cell. (a) Front resistive layer, (b) bandpass FSS, and (c) perspective view of 3 x 3 unit cell. p = 10, w = 0.5, w_s = 0.3, l_s = 4.6, w_1 = 0.2, w_2 = 0.2, l_c = 4.3, w_3 = 0.5, w_4 = 0.2, d = 1.2, l_{p1} = 6.1, l_{p2} = 6.2, w_{p1} = 0.8, w_{p2} = 0.4, w_{p3} = 0.4 (all dimensions are in mm).

four corners of the bandpass FSS a quarter of the cross slot is etched. A perspective view of a 3 x 3 proposed rasorber structure is represented in Figure 7.1(c).

The proposed design process for realization of the A-T-A-T FSR can be briefly summarised from the following steps:

1. Study of the square loop shaped broadband absorber.
2. Study of the cross slot shaped dual transmissive bandpass FSS.
3. Study on the design of the proposed MF-shaped resonator co-designed with the resistive layer for achieving two transmission poles corresponding to the dual bandpass FSS

The broadband absorber is studied with resistive layer consisting of the metallic square loop and lumped resistors mounted between the gaps of the metallic rectangular strips.

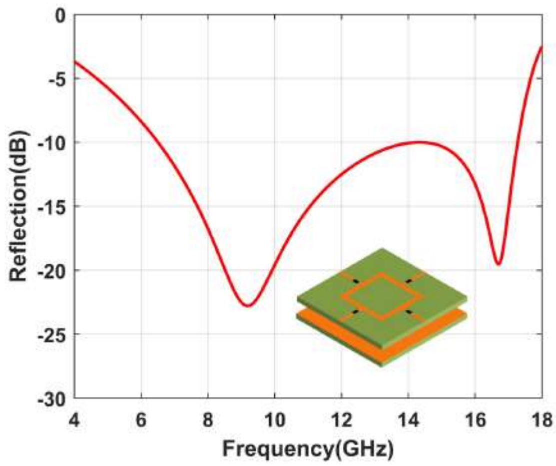

Figure 7.2: Reflection of the square loop based broadband absorber.

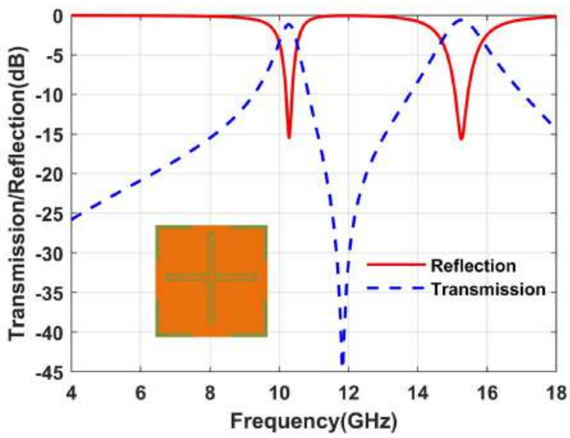

Figure 7.3: Transmission/reflection plots of the dual bandpass FSS.

The resistive layer separated with the ground layer at the distance of $\lambda/4$ achieves a broadband absorption. The reflection plot of the broadband absorber is provided in Figure 7.2, wherein the 90% absorption is achieved from 6.5 to 17.3 GHz.

For realizing two passbands, initially, a suitable design for dual-resonant bandpass FSS is studied separately. The bandpass FSS unit cell is realized by etching the cross-loop slot within the center of the metal laminated substrate. Also at the four corners of the unit cell, a quarter part of the cross slot is etched out. The associated simulated reflection and transmission response are shown in Figure 7.3 where from two transmission bands at 10.2 GHz and 15.2 GHz can be observed. The centered cross-loop slot leads to the transmission at 10.2 GHz while the fraction of cross slots etched at the four corners of the bandpass FSS corresponds to the upper transmission band at 15.2 GHz.

In order to attain the dual transmission bands within the broad absorption band, the bottom metallic layer in the absorber is interchanged with the designed bandpass

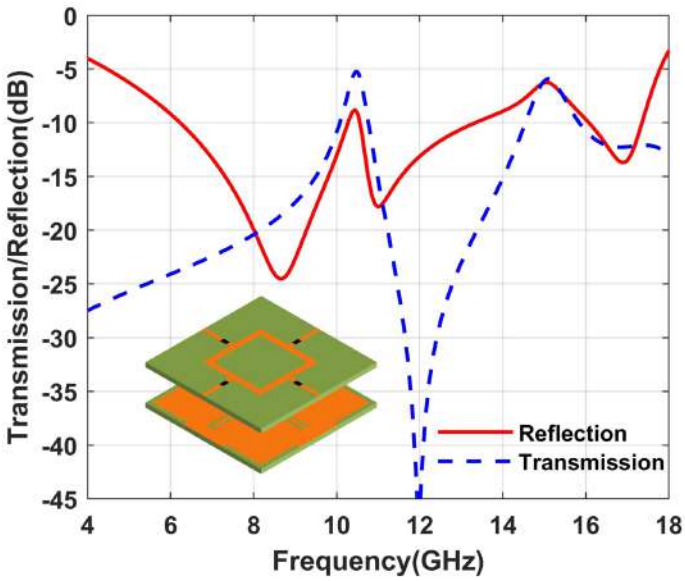

Figure 7.4: Transmission/reflection plots of the FSR without the MF-shaped resonator.

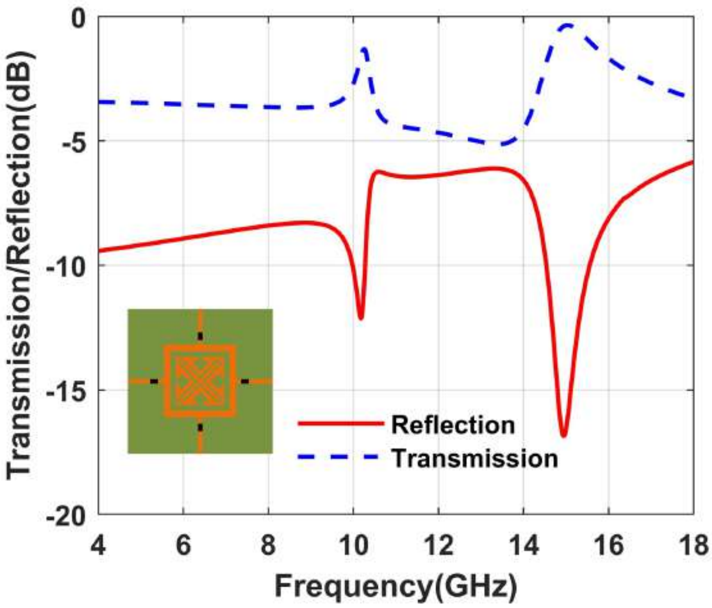

Figure 7.5: Transmission and reflection plots of the resistive layer with MF-shaped resonator.

FSS. The bottom bandpass FSS works as the ground layer for the absorber outside the transmission bands. However, as depicted from the transmission and reflection response in Figure 7.4, the insertion loss and reflection coefficient at the two desired transmission bands of 10.4 GHz and 15.2 GHz is quite high restricting the occurrence of desired transmission band. This is due to the ohmic loss caused by the lossy components mounted on resistive layer which prevents the realization of the two transmission bands at the frequency corresponding with the dual resonance of the bandpass FSS.

For achieving the desired dual transmissions, an MF-shaped resonator is thoroughly

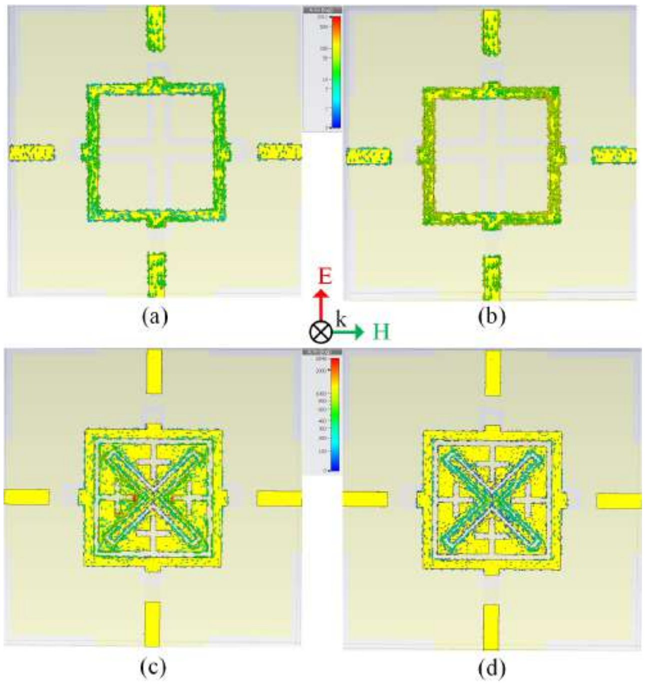

Figure 7.6: Surface currents at the resistive layer at, (a) 10.4 GHz (without MF resonator), (b) 15.2 GHz (without MF resonator), (c) 10.4 GHz (with MF resonator), (d) 15.2 GHz (with MF resonator).

studied and co-designed within the square loop resistive layer that realizes the transmission poles at the desired passbands. This can be understood from the simulated reflection and transmission plots of the single resistive top layer loaded with the MF-shaped resonator as shown in Figure 7.5. It can be observed that by incorporating the MF-shaped resonator with the resistive layer, the two transmission poles are achieved at around 10.4 GHz and 15.0 GHz. The addition of MF-shaped resonator in the resistive layer causes the resonance at the two frequencies (10.4 and 15.0 GHz), thereby reducing the ohmic loss at those particular frequencies. The working is further explained by analyzing the corresponding surface current distributions at the two resonant frequencies. It can be observed that currents on the top surface without MF-shaped resonator at the center are concentrated along the square loop and the outer rectangular strips (Figures 7.6(a) and 7.6(b)) due to which a significant amount of currents flows through the lumped lossy components, thus leading to ohmic losses at those frequencies. Now, from Figures 7.6(c) and 7.6(d), it can be observed that by the addition of MF resonator, the dominating currents gets concentrated with the edge of the MF resonator slots, thus preventing the current to flow through the lossy lumped components.

The transmission and reflection plots of the proposed MF-shaped based FSR are shown in Figure 7.7 from which the A-T-A-T responses can be observed. The lower absorption

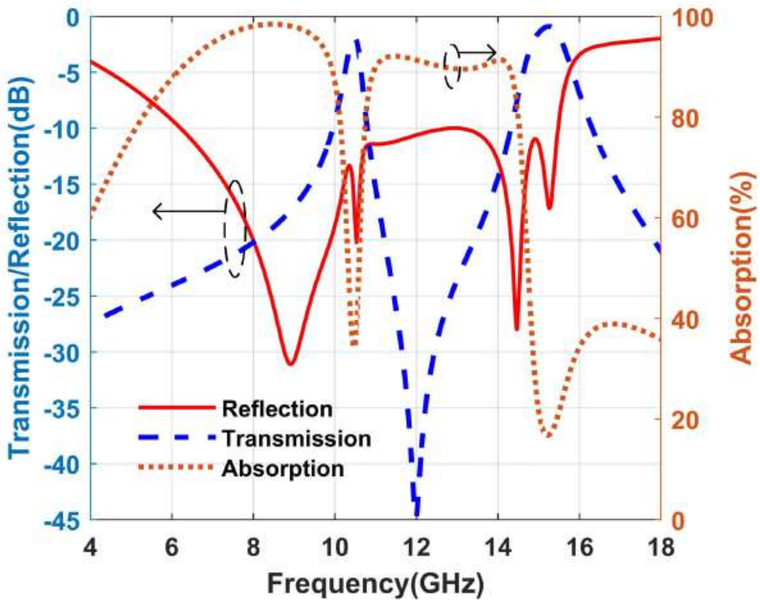

Figure 7.7: Transmission, reflection and absorption curves of the proposed MF resonator based A-T-A-T FSR.

band (80% absorption) is obtained from 5.2 to 10.1 GHz (64.05%) while the upper absorption band is from 10.7 to 14.4 GHz (29.48%). The transmission windows are achieved at 10.4 GHz and 15.2 GHz having the minimal insertion loss of 1.9 dB and 0.9 dB, respectively.

The response associated with the proposed A-T-A-T rasorber is studied under varying incident polarization angles. It can be depicted from Figure 7.8 that both reflection as well as transmission plots of the proposed structure remain constant with the varying incident polarization angles, thus leading to the polarization-independent behaviour of the proposed rasorber design. Further, the FSR design is also examined with respect to various oblique incidence. The plots in Figure 7.9 depict the responses of the proposed structure for the varying incidence angle. It can be observed that with the increase in incidence angle the lower absorption bandwidth gets reduced, while the upper absorption band along with the two transmission bands are nearly maintained. Thus, with respect to the lower absorption band, the angular stability up to 40^o is achieved.

7.2 Fabrication, Measurements and Discussions

Prototype of the proposed rasorber consisting of 15 x 15 array of the proposed unit cell are fabricated as shown in Figure 7.10. The top and the bottom layers fabricated on the

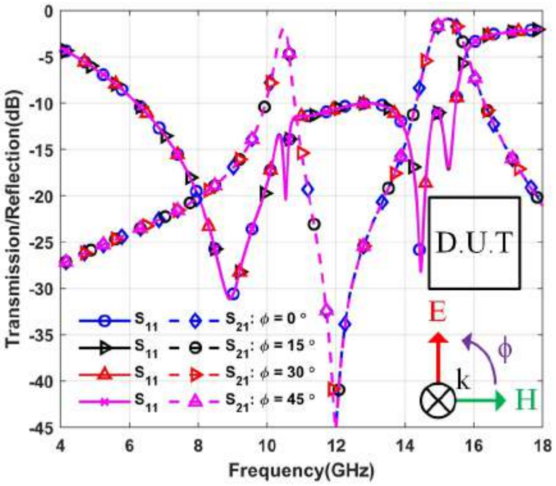

Figure 7.8: Transmission/reflection plots of the proposed FSR for various incident polarization angles.

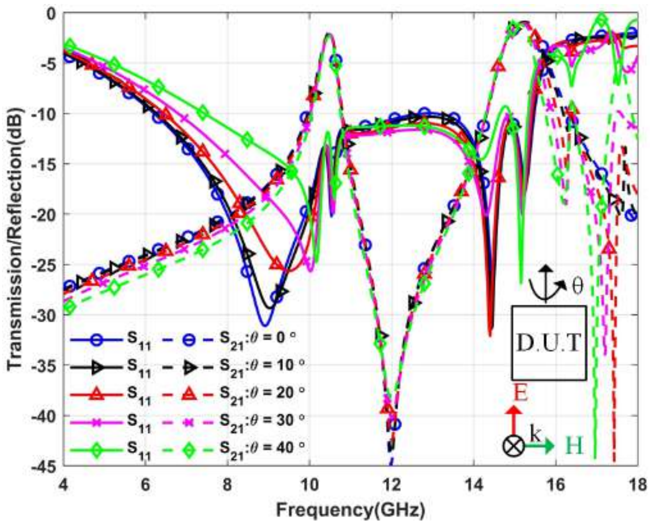

Figure 7.9: Transmission/reflection plots of the proposed FSR associated with various angle of incidence.

Rogers kappa substrate ($\epsilon_r = 4.3$, $tan\delta = 0.005$) are separated at the distance of 5 mm using the plastic spacers as shown from the photograph provided in Figure 7.10(a). On the top layer lumped chip resistor (CRCW0603200RFKEA from VISHAY) with a value of 200Ω are soldered within the gaps of rectangular strips (Figure 7.10(b)). The photograph of the bandpass FSS layer consisting of cross slots is provided in Figure 7.10(c). The fabricated structure with an overall dimension of 150 mm x 150 mm is loaded with 900 lumped chip resistors.

The fabricated prototype is analyzed using the free space measurement technique. Three standard gain horn antennas dedicated for J (5.85−8.20 GHz), X (8.20−12.40 GHz) and Ku (12.40−18.0 GHz) bands are sequentially used for carrying out the measurements on the Keysight performance network analyzer N5224B. The photograph depicting the measurement setup is shown in Figure 7.11. The reflection measurement is carried out

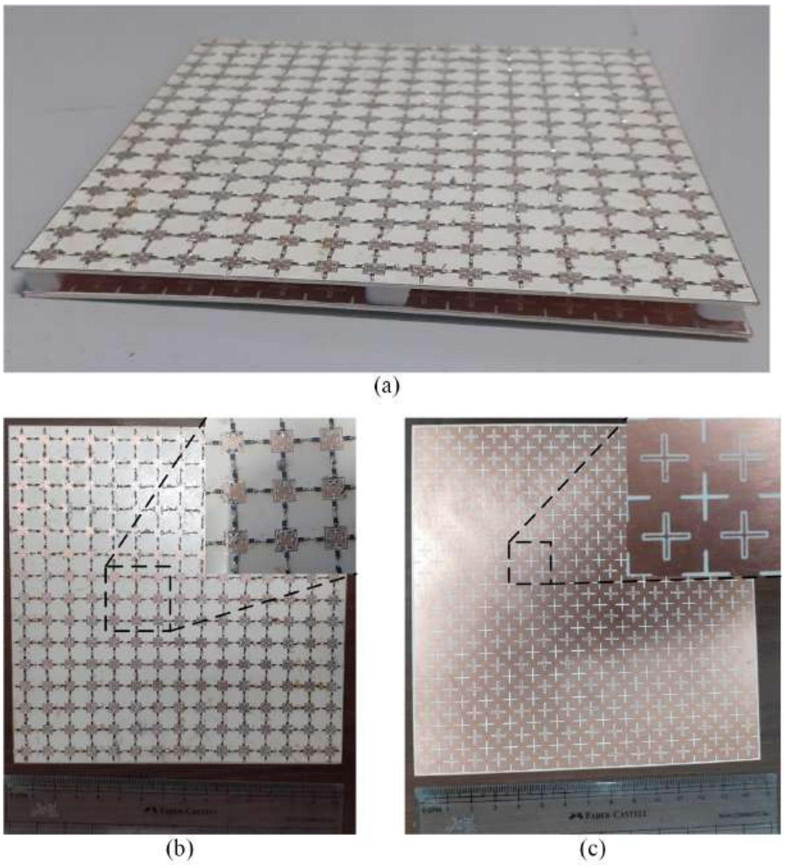

Figure 7.10: Photographs of fabricated prototype depicting (a) perspective view, (b) top layer, and (b) bottom layer.

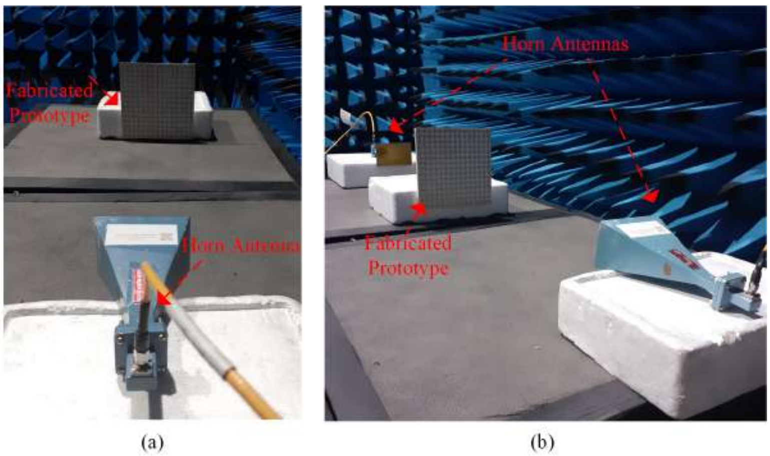

Figure 7.11: Setup for (a) reflection, and (b) transmission measurements.

using the time gating application of the PNA in which a single horn antenna measures the required reflection coefficient (Figure 7.11(a)). For the transmission measurement, the structure is placed between the two horn antennas connected with the two ports of the PNA (Figure 7.11(b)).

The measured transmission and reflection coefficients of the fabricated structure in

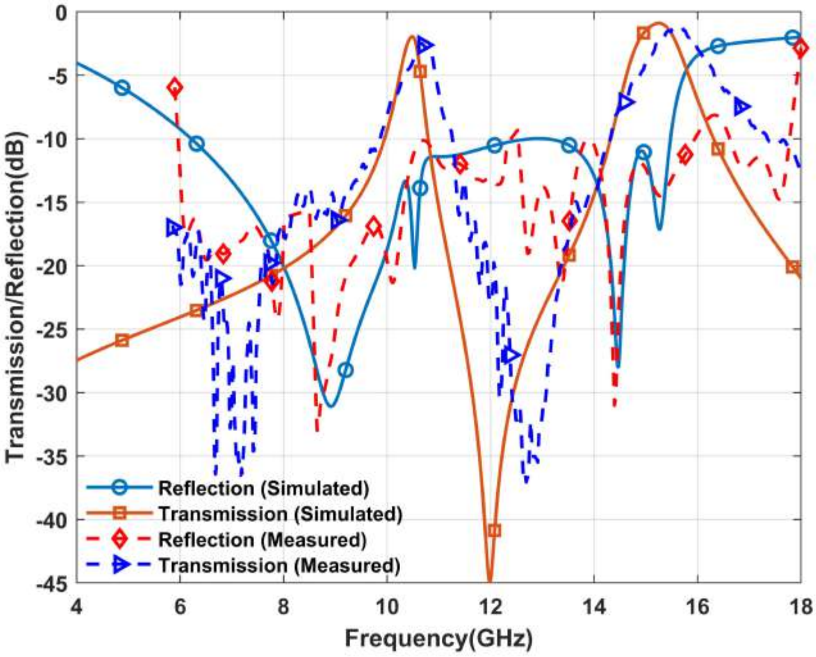

Figure 7.12: Measured reflection and transmission coefficients along with simulated responses.

comparison with the simulated results are shown in Figure 7.12. The acceptable resemblance between the measured and simulated results experimentally validates the working of the proposed A-T-A-T FSR. A slight discrepancy in the measured results is due to imperfect soldering and the limited size of the prototype.

A comparative performance analysis of the proposed FSR with the earlier reported A-T-A-T rasorbers is provided in Table 7.1. The performance exhibited by the proposed MF-shaped based FSR over the reported A-T-A-T rasorbers are summarized as:

1. The proposed FSR provides 64.05% lower absorption bandwidth which is wider than FSR reported in [108]−[109], and the upper absorption bandwidth is 29.48%, wider than [109]−[110].

2. The proposed design is thinner than the designs studied in [108]−[110] and compact than [110].

3. The proposed FSR has a symmetric design or polarization-independent as compared with design reported in [108].

4. The angular stablity up to 40^o is achieved which is higher than the reported structures in [108]−[110].

Table 7.1: Comparative analysis of the proposed rasorber with the reported A-T-A-T FSRs

Ref.	Passbands (I.L)	Lower absorption B.W (GHz)	Upper absorption B.W (GHz)	Thickness	Unit Cell Size	Polarization	Angular Stability
[108]	7.2 GHz (2.3 dB)/ 13.05 GHz (1.69 dB)	4.02−6.27 (43.73%)	8.21−12.02 (37.66%)	8 mm (0.107λ)	9 mm x 18 mm ($0.028\lambda^2$)	Single	20^o
[109]	6.1 GHz (0.06 dB)/ 10.1 GHz 0.2 dB)	3.3−4.97 (40.38%)	7.42−9.03 (19.57%)	9 mm (0.09λ)	8 mm hexagon ($0.020\lambda^2$)	Dual	30^o
[110]	8 GHz (0.39 dB)/ 11.9 GHz (0.64 dB)	4.5−7.3 (47.45%)	8.5−11 (25.64%)	7 mm (0.105λ)	15 mm x 15 mm ($0.05\lambda^2$)	Dual	30^o
This Work	10.4 GHz (1.9 dB)/ 15.2 GHz (0.9 dB)	5.2−10.1 (64.05%)	10.7−14.4 (29.48%)	5 mm (0.08λ)	10 mm x 10 mm ($0.029\lambda^2$)	Insensitive	40^o

λ calculated at lowest frequency of absorption.

7.3 Conclusion

In this chapter, a rasorber with A-T-A-T response is proposed having dual transmission and dual absorption bands. An MF-shaped resonator exhibiting dual transmission poles is studied and incorporated within the resistive layer of the broadband absorber which in combination with the bottom dual bandpass FSS realizes dual transmission band within the broad absorption band. The proposed rasorber attains two passbands at 10.4 and 15.2 GHz with the two absorption bands from 5.2 to 10 GHz and 10.7 to 14.4 GHz. Measurements carried on the fabricated 15 x 15 rasorber prototype experimentally validates the design.

Chapter 8

Low RCS Crossed Dipole Antenna Co-Designed with AFSR Structure

In chapters 2 to 7, designs for various categories of FSRs have been discussed. The FSR also known as AFST (absorptive frequency selective transmission) structure exhibits transmission band along with the absorption band and can be integrated as a radome for RCS reduction of a radiating system. The other way of achieving a low RCS radiating system is the use of a band-notched absorber also known as AFSR (absorptive frequency selective reflection) structure as a ground plane. The objective of this chapter is to study the integration strategy of a dual-polarized crossed dipole antenna with a polarization-insensitive AFSR structure for achieving RCS reduction. At first, a compact and polarization-insensitive AFSR structure is proposed by incorporating a bandstop ring resonator within a circular-cross shaped broadband absorber. A dual-polarized crossed dipole antenna is integrated with the AFSR structure in a novel and proficient manner such that the AFSR structure acts as a reflector at the antenna's operating frequency. The antenna integrated with the AFSR structure achieves the RCS reduction for both the TE and TM polarization of the incident wave in comparison with the conventional reflector back antenna.

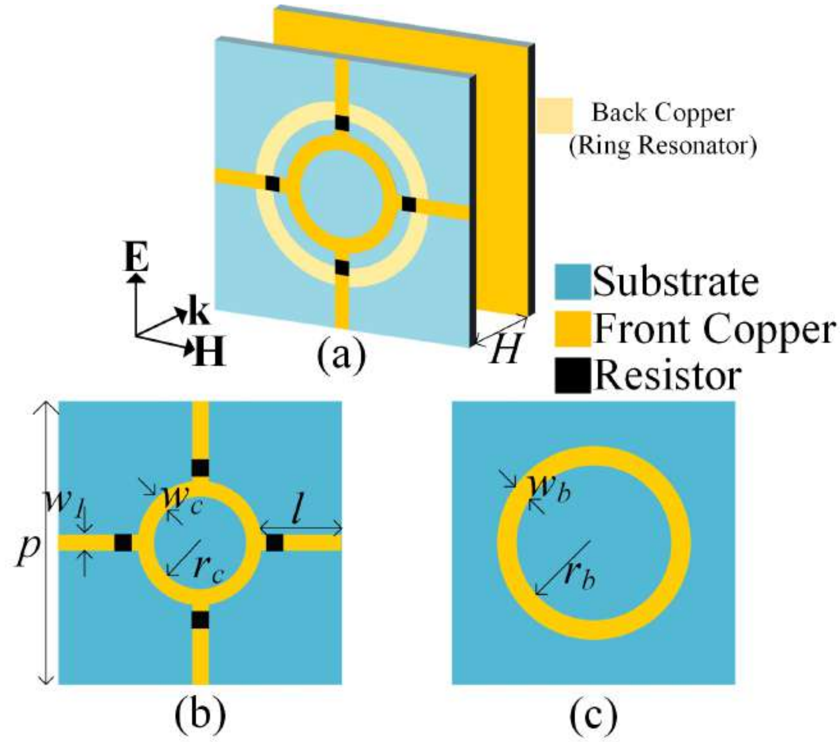

Figure 8.1: AFSR unit cell geometry, (a) perspective view, (b) front side, and (c) back side of top resistive layer. Dimensions (in mm): p = 15, r_c = 2.2, w_c = 1, r_b = 3.2,w_1 = 0.8, w_b = 0.6, l = 4.3, and H = 8.

8.1 AFSR Structure

8.1.1 Design and Analysis

The geometrical discription of the proposed unit cell for the ASFR structure is depicted in Figure 8.1, which is basically a two-layered combination comprising of resistive layer at top and ground layer at bottom and separated by distance H (Figure 8.1(a)). The design is printed on a 0.8 mm thick FR-4 substrate. The resistive layer comprises of a circular-cross shaped resonator on the front side in which the lumped chip resistors having resistance of 200 Ω are mounted within the four gaps of the rectangular strip (Figure 8.1(b)). On the backside of the resistive layer a metallic circular ring resonator is printed. The CST Microwave studio is used for analyzing the structure.

The resistive layer with circular-cross resonator and lumped chip resistors placed from the ground layer at a distance of $\lambda/4$ provides a broadband absorption for the incident EM wave as shown in Figure 8.2 and having 90% absorption bandwidth from 4.7 to 10.7 GHz. For obtaining a reflection notch in middle of the absorption band a metallic circular ring is printed on the backside of the resistive layer. This circular ring resonator acts as a bandstop FSS at the desired reflection notch of 8.2 GHz. It can be observed from Figure

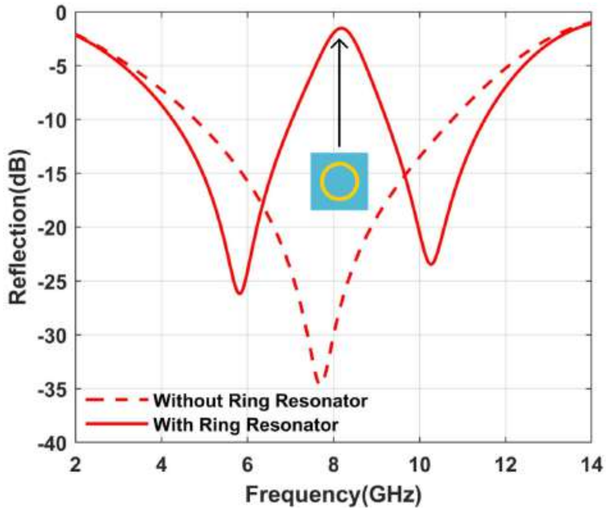

Figure 8.2: Simulated reflection coefficients of the AFSR structure and the broadband absorber.

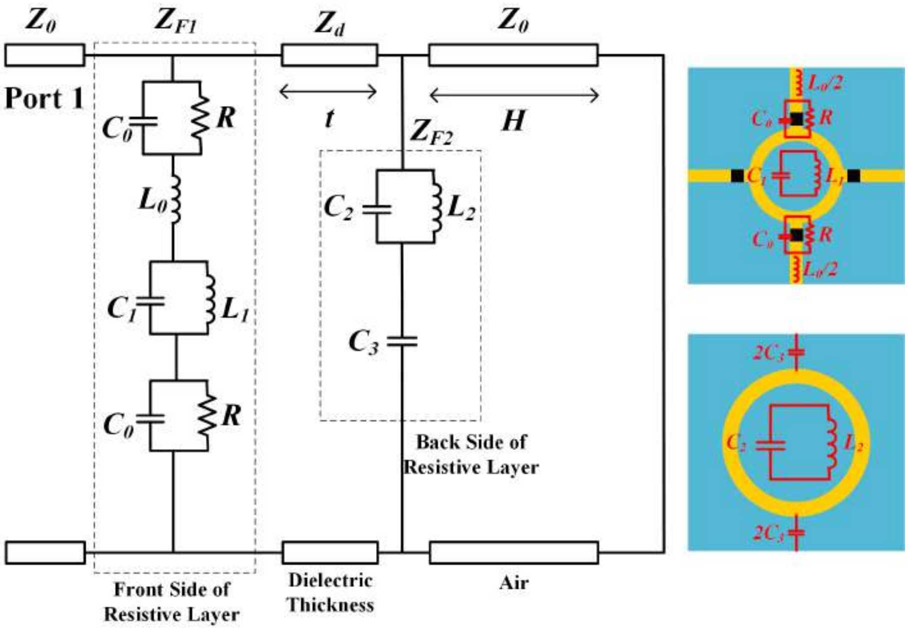

Figure 8.3: ECM of the proposed AFSR structure ($R = 200\Omega$, $C_0 = 0.051$ pF, $L_0 = 2.45$ nH, $C_1 = 0.0011$ pF, $L_1 = 3.185$ nH, $C_2 = 0.1$ fF, $L_2 = 39.305$ nH, $C_3 = 0.0091$ pF, $Z_d = 181\ \Omega$, $t = 0.8$ mm, $Z_0 = 377$ Ω).

8.2 that due to insertion of ring resonator at the back side of resistive layer the broad absorption band gets bifurcated into two absorption bands from 4.2 to 7.0 GHz and 9.2 to 11.5 GHz with a notch shaped reflection band at the center frequency of 8.2 GHz.

For understanding the working related to the proposed AFSR structure, a corresponding equivalent circuit model (ECM) is designed as shown in Figure 8.3. The ECM is a one-port network in which the corresponding models of front and back side resonators of the resistive layers are cascaded. For the circular-cross resonator at the front side, the lumped resistor and the associated gap capacitance is modelled by the parallel $R - C_0$

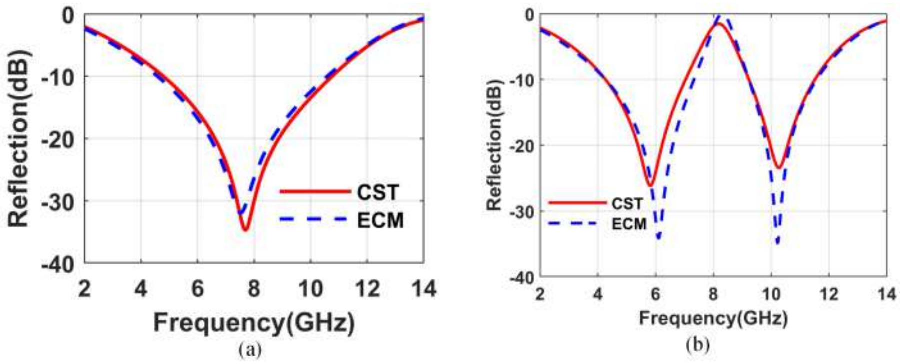

Figure 8.4: ECM response in comparison with the CST results. (a) Broadband absorber, and (b) AFSR structure.

combination. The inductance of the rectangular strip is modelled by inductor L_0 while the parallel $L_1 - C_1$ models the circular ring. At the backside of resistive layer, the circular ring is modelled by the parallel $L_2 - C_2$ while the inter-capacitance is represented by C_3. The thickness of the substrate is modelled by a transmission line having the characteristic impedance $Z_d = Z_0/\sqrt{\epsilon_r}$ (Z_0 denotes the impedance in free space) and length equivalent to the substrate thickness (t). The transmission line having characteristic impedance Z_0 and thickness H also models the air-gap between the resistive layer and the ground.

The Keysight ADS solver is used for analyzing the ECM of the proposed AFSR structure. The simulated reflection coefficient of the ECM compared with the full wave CST simulation is shown in Figure 8.4. The response of the ECM without the backside ring resonator model is shown in Figure 8.4(a), in which a broadband absorption is observed in close resemblence with the full wave simulation of the broadband absorber. The reflection of the ECM for AFSR is shown in Figure 8.4(b) in which the reflection notch at the center is achieved by the addition of corresponding model of the backside ring resonator. The close concurrence between the ECM and CST responses explains the working of the AFSR design.

The proposed AFSR structure is analyzed in response to multiple polarization angles associated with the incident EM wave as depicted in Figure 8.5(a). The consistent response of the design under various polarization angles determines the polarization-insensitive behavior of the AFSR structure. Furthermore, the AFSR structure is also analyzed corresponding to the oblique angle of incidence up to 50^o. The angular stability for the proposed structure exists up to 30^o beyond which the absorption bands gets degraded.

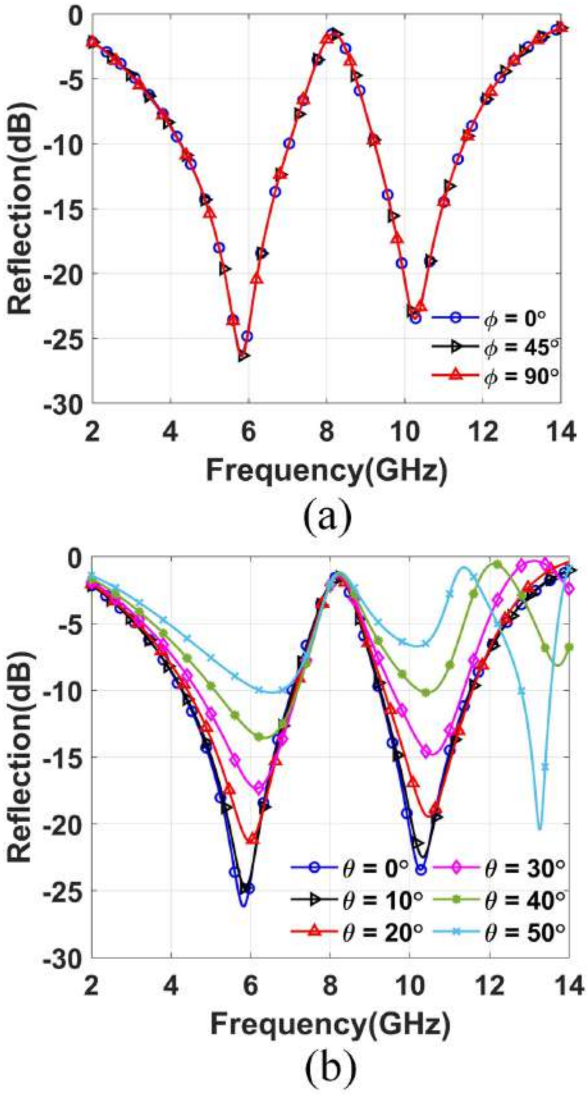

Figure 8.5: Simulated responses of the proposed AFSR structure with respect to different (a) polarization, and (b) incidence angle.

8.1.2 Fabrication and Measurements

For obtaining the experimental validation of the AFSR structure, a prototype consisting of 21 x 21 proposed unit cells are fabricated using a 0.8 mm thick FR-4 substrate ($\epsilon_r = 4.4, tan\delta = 0.02$). The photograph of the fabricated prototype having overall size of 315 mm x 315 mm is given in Figure 8.6. Lumped chip resistors with 200 Ω resistance (CRCW0603200RFKEA from VISHAY) are soldered within the gaps of the circular-cross resonators (Figure 8.6(a)). The metallic ring resonators are printed on the backside of the top resistive layer (Figure 8.6(b)). The resistive substrate is separated from the ground layer using a plastic spacers as presented in Figure 8.6(c).

The reflection measurements on the fabricated prototype is carried in an anechoic

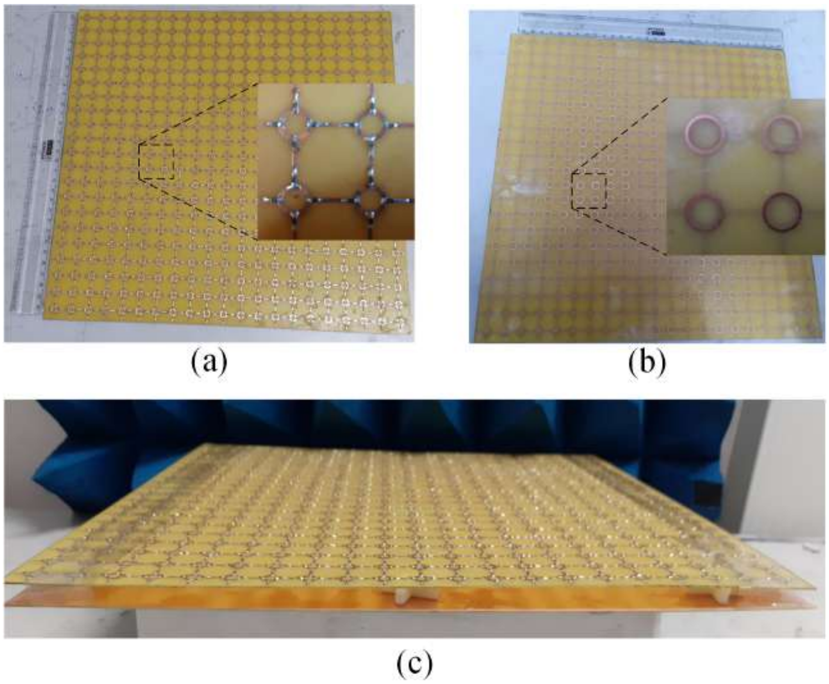

Figure 8.6: Photograph of the fabricated AFSR prototype. (a) Front, and (b) back side of the top layer. (c) Side view.

chamber using the free space technique with standard gain horn antennas of C, J and X bands in connection with the Keysight PNA N5224B. The measured reflection coefficient of the fabricated prototype in comparison with the simulated response is shown in Figure 8.7(a). The close resemblance achieved between the experimental and simulated responses validates the proposed design experimentally. Further, the polarization-independence of the proposed structure is also experimentally validated by measuring the response at various polarization angles as shown in Figure 8.7(b). The response of the proposed structure is measured under oblique incidence (Figure 8.7(c)) and the angular stability is experimentally validated up to 30^o, beyond which the absorptivity in the two bands gets degraded.

8.2 Low RCS Crossed dipole antenna

The design for the dual-polarized low RCS antenna utilizing the AFSR structure is proposed in this section. The AFSR structure exhibiting polarization-insensitive behavior is co-designed with the dual-polarized crossed dipole antenna. The crossed dipole antenna is designed having operating frequency around 8.2 GHz which corresponds to the reflection band associated with the proposed AFSR structure. A microstrip to broadside coupled

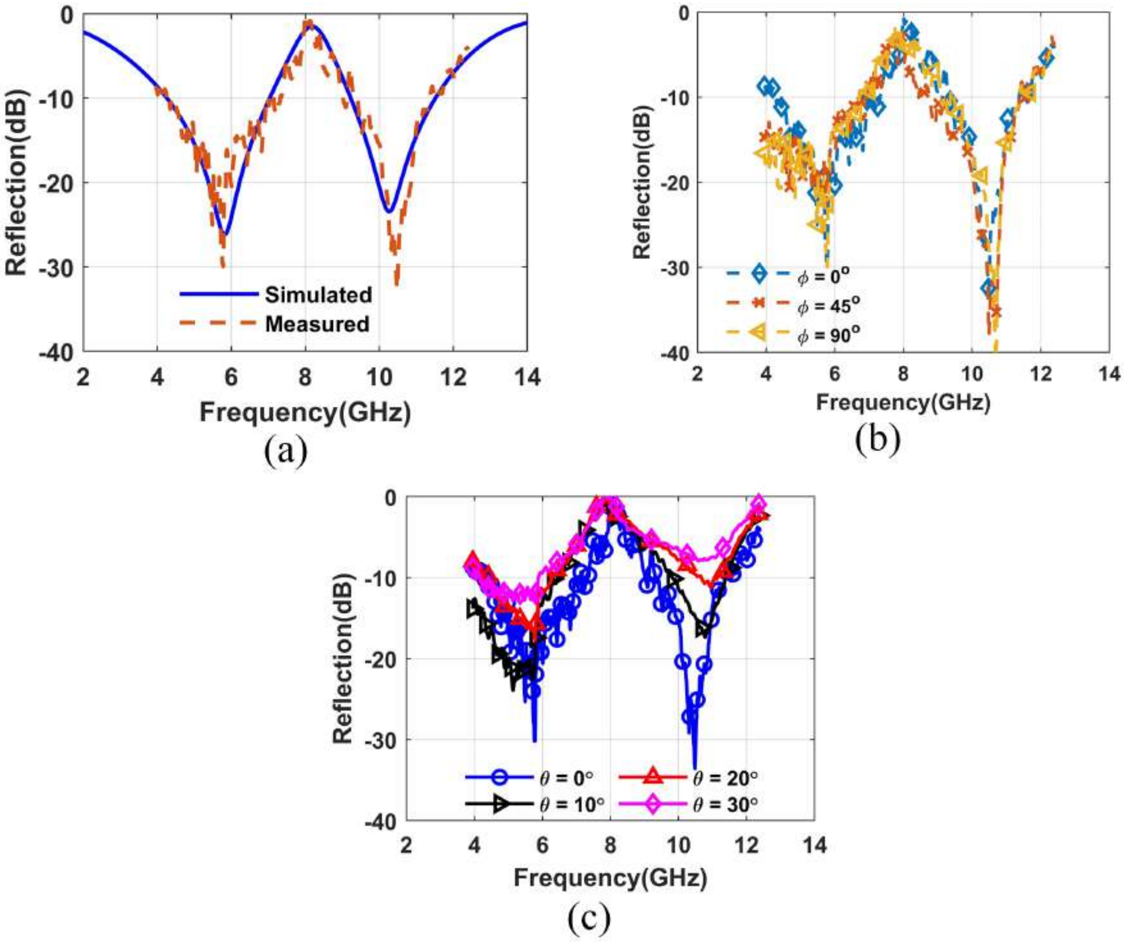

Figure 8.7: Measured reflection coefficients for the proposed AFSR structure (a) in comparison with the simulated result, (b) under different polarization, and (c) oblique incidence.

stripline transition feeds the crossed dipole [140] . The reference structure consists of a crossed dipole backed by a metallic reflector as shown in Figure 8.8(a). The dimension of the reflecting surface is taken to be equal with the size of 6 x 6 AFSR unit cell arrray (90 mm x 90 mm). In the design for AFSR integrated antenna, an array comprising of 6 x 6 unit cell is taken. On the resistive layer, a square portion with size of the order of the feed substrate is truncated at the center. The crossed dipole connected with the feed substrate as shown in Figure 8.8(b), is inserted within this square portion and connected with the ground layer of the AFSR structure. In other words the grounded reflector of the antenna is modified with the 6 x 6 AFSR structure. The photographs showing the fabricated prototypes for the crossed dipole antenna with both metallic reflector and AFSR structure are depicted in Figure 8.9.

The simulated and measured reflection coefficients (S_{11}) of the crossed dipole antenna with both reflector and AFSR structure are shown in Figure 8.10. The reflection of less

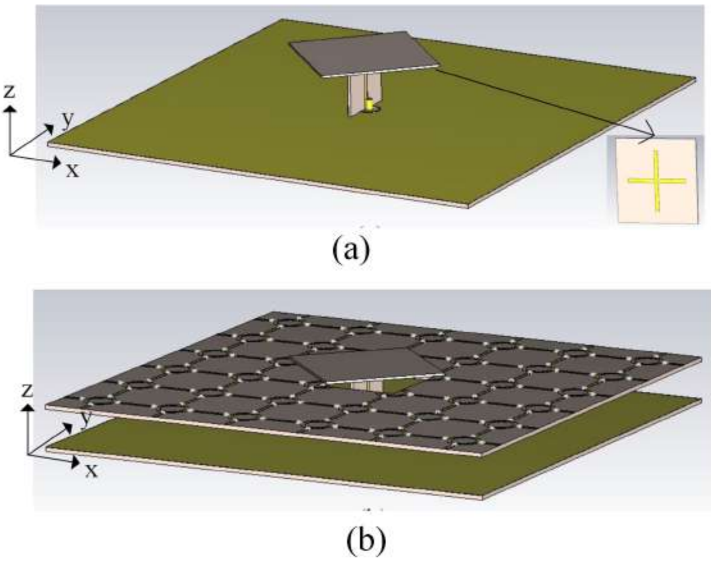

Figure 8.8: Schematic representation of the crossed dipole antenna with (a) reflector, and (b) AFSR structure.

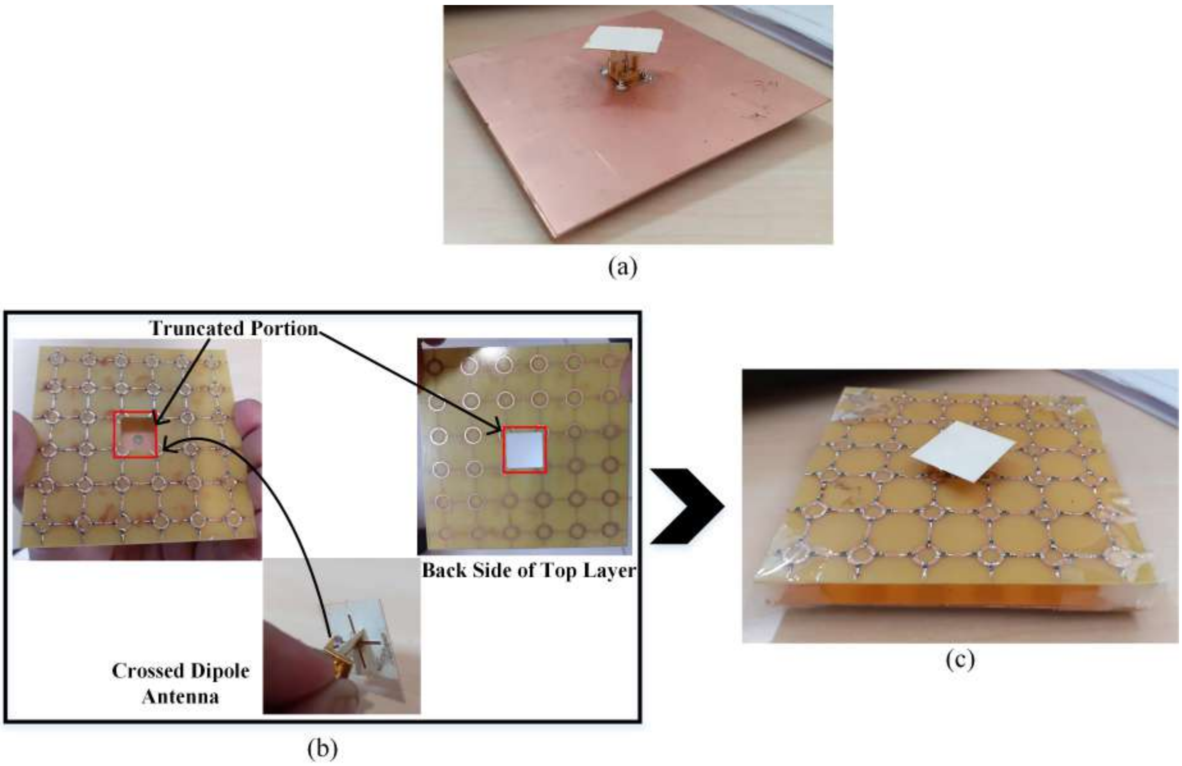

Figure 8.9: Photographs of the fabricated prototype of the crossed dipole antenna with (a) reflector, (b) truncated 6 x 6 structure and (c) final AFSR structure.

than -10 dB is observed at the operating frequency of 8.2 GHz for both the cases of reflector and ASFR backed antenna. At 8.2 GHz the gain of 5.52 dBi is observed for the AFSR backed antenna which is slightly less than the gain corresponding to reflector backed antenna (6.35 dBi). The simulated and measured radiation patterns of the crossed

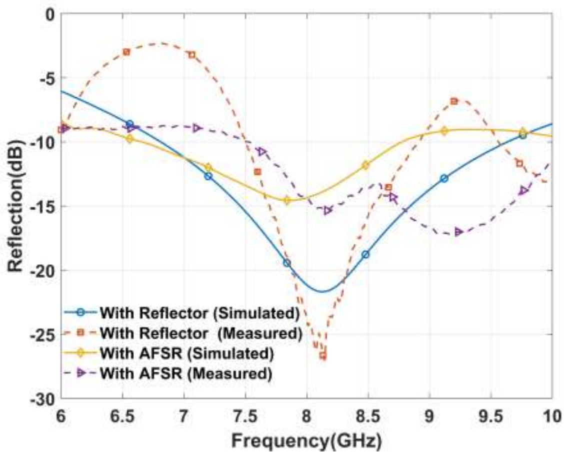

Figure 8.10: Reflection coefficient of the crossed dipole antenna.

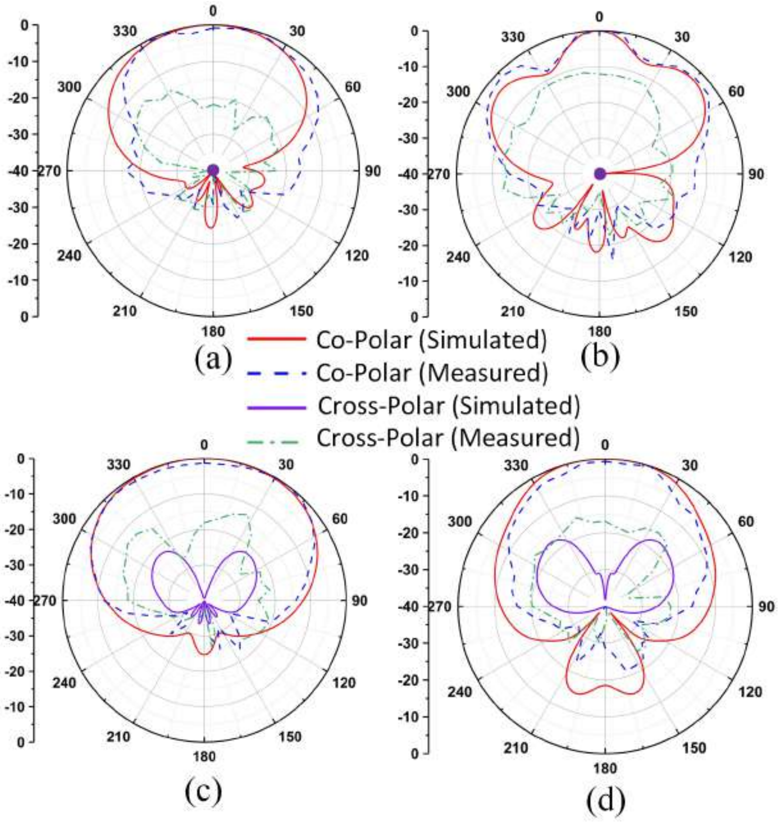

Figure 8.11: (Radiation pattern of the crossed dipole antenna at 8.2 GHz. (a) xz plane (with reflector). (b) xz plane (with AFSR). (c) yz plane (with reflector). (d) yz plane (with AFSR).

dipole antenna with both the reflector and AFSR backing in both the xz and yz planes are given in Figure 8.11. It can be examined that the radiation pattern of the AFSR backed antenna is nearly similar as compare to the reflector backed antenna.

8.2.1 Mono-static RCS Measurement

The radar cross section measurements are carried out for the fabricated structures involving both the reflector and AFSR backed crossed dipole antennas. The Keysight PNA N5224B featured with time domain gating application is employed for the mono-static RCS measurement using the same standard gain horn antenna for both transmitter and receiver. The RCS is defined from the general equation by (8.1).

$$RCS = \frac{P_r}{P_t} . \frac{(4\pi)^3 R^4}{G_t G_r \lambda^2} = K . \frac{P_r}{P_t} \tag{8.1}$$

The terms P_r and P_t in (8.1) denote the received and transmitted powers, respectively. The gains associated with reflecting and transmitting antennas are represented by G_r and G_t, respectively. The range to target is given by R, whereas λ gives the associated wavelength.

The mono-static RCS is measured in reference to a standard square PEC having same size as that of the grounded dimensions associated with antenna. The comparitive mono-static RCS of the metallic reflector and AFSR backed crossed dipole antenna for the TE and TM incident waves are shown in Figure 8.12. It is observable that as compared with the reflector backed antenna, the AFSR integrated antenna achieves a low RCS with the maximum reduction of 27.52 dB (at 10.6 GHz) and 38.01 dB (10.6 GHz) for the TE and TM incidence, respectively. The AFSR integrated antenna achieves an average reduction of 12.51 dB and 12.62 dB for the TE and TM incident waves, within the frequency band extending from 4.2 to 11.5 GHz, respectively as compared to the conventional metallic reflector backed antenna.

8.2.2 Bi-static Measurement

The bi-static RCS measurement involves the transmitter and receiver test antennas placed at different locations. In the bi-static measurement, as depicted by Figure 6.20 in chapter 6, the transmitting antenna is normal to the structure while the receiving horn antenna is moved from 0^o to 90^0 along the circular path at 10^o steps in either anticlockwise or clockwise direction. The $E_{sca}(f, \phi)$ denoting the scattered field for each step angle is defined by (8.2) [139].

Table 8.1: Comparative performance of the proposed AFSR integrated antenna with the recently reported Low RCS antennas

Ref.	Antenna Structure	Operating Frequency	Size	Lumped Elements in the structure	10 dB monostatic RCS bandwidth	Average Monostatic RCS reduction	Average Total Bistatic RCS reduction
[128]	Dipole + AFSR	8.7 GHz	3.65λ x 3.65λ	200	26% (Lower) and 16.7% (upper)	NA	NA
[129]	Monopole/Dipole + 3D AFSR	5.5 GHz	2.56λ x 1.54λ	196	64.7% (Lower) and 42.4% (upper)	NA	NA
[130]	Patch array antenna + AFST	10 GHz	7.2λ x 7.2λ	96	60.3% (Lower) and 20.4% (upper)	NA	NA
[134]	Patch antenna + Absorptive/Diffusive FSR	10 GHz	10.66λ x 10.66λ	512	90% (Lower) and 27.6% (upper)	NA	NA
[133]	Patch antenna + ASFT	7.5 GHz	1.5λ x 1.5λ	128	6.9% (Lower) and 39.3% (upper)	NA	NA
[135]	Slot array antenna + 3D AFST	6.15 GHz	1.96λ x 1.96λ	192	87.2% (Lower) and 45.8% (upper)	NA	NA
[136]	Cross-shaped Vivaldi antenna	1.8−6 GHz	0.58λ x 0.58λ	NA	NA	4.3 dB (TE) and 5 dB (TM)	NA
This Work	**Crossed dipole + AFSR**	**8.2 GHz**	**2.46λ x 2.46λ**	**144**	**38.59% (Lower-TE)/42.9% (Lower-TM) and 30.75% (upper-TE), 27% (Upper-TM)**	**12.51 dB (TE) and 12.62 dB (TM)**	**80 % (TE and TM)**

λ= wavelength at the operating frequency of antenna.

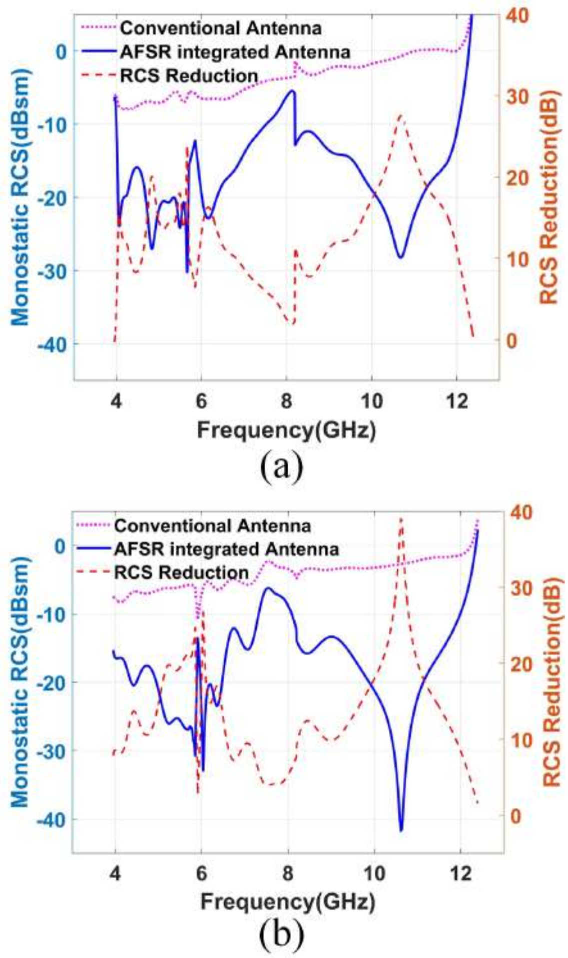

Figure 8.12: Mono-static RCS of the AFSR integrated antenna in comparison with the conventional reflector based antenna for (a) TE, and (b) TM incident wave.

$$E_{sca}(f,\phi) = S_{21,O}(f,\phi) - S_{21,FS}(f,\phi) \tag{8.2}$$

where the transmission coefficients between the two horn antennas corresponding to the object and free space are represented by $S_{21,O}$ and $S_{21,FS}$, respectively. The normalized total radar cross section $RCS_{t,norm}$ of the AFSR integrated antenna is calculated by the integrating scattered fields intensities as given in (8.3) [139]:

$$RCS_{t,norm} = \frac{\int |E_{sca,AFSRA}(f,\phi)|^2 d\phi}{\int |E_{sca,RA}(f,\phi)|^2 d\phi} \tag{8.3}$$

where $E_{sca,AFSRA}$ and $E_{sca,RA}$ are the scattered fields of the AFSR based and conventional reflector antennas, respectively.

The measured $RCS_{t,norm}$ for the AFSR combined crossed dipole antenna in reference with the metal reflector based antenna is provided in Figure 8.13. It is noticed that with

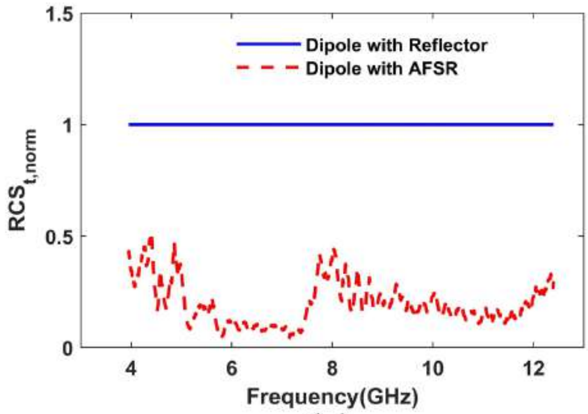

(a)

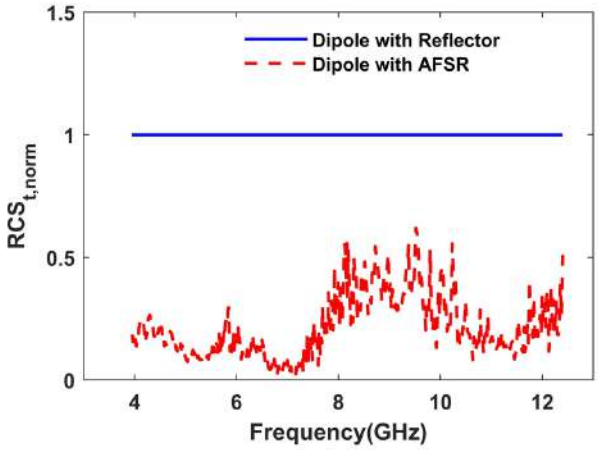

(b)

Figure 8.13: Normalised total bi-static RCS of the AFSR integrated antenna with reference to the conventional reflector based antenna for (a) TE, and (b) TM incident wave.

respect to the reflector based antenna, the AFSR structure based crossed dipole antenna achieves a significant reduction in the normalized total RCS. In the entire operating frequency band of 4.2 to 11.5 GHz, the average value of normalized RCS obtained is around 0.197 and 0.198 for the TE and TM incident wave, respectively which signifies a total RCS reduction of around 80.24% for both the TE and TM incidence, relative to the conventional reflector based crossed dipole antenna.

Table 8.1 presents the proposed AFSR integrated crossed dipole antenna with the other low RCS antennas reported in the literature. The proposed study presents the RCS reduction of dual-polarized crossed dipole antenna for the first time in comparison with the single polarization antennas reported [128]−[136]. The proposed design is compact in comparison with reported work in [128, 130, 134]. Further, the design complexity of the proposed structure is less than [128, 129, 134, 135], in terms of lesser quantity of lumped components utilized. Also, the -10 dB RCS reduction bandwidth of the proposed design is more than [128, 133] in the lower band while the RCS reduction bandwidth for the upper band is higher than the work reported in [128, 130, 134]. The average RCS reduction achieved in the proposed design significantly higher in comparison with the reported work [136]. The proposed study achieves the RCS reduction using a 2D AFSR structure in comparison with the 3D FSS structures used in [129, 135]. Furthermore, in contrast to the reported works [128]−[136], the scattered fields for the AFSR integrated antenna are measured in the proposed work at various angles and an average bi-static total RCS reduction of around 80% is experimentally demonstrated for both the TE and TM incident wave.

8.3 Conclusion

In this chapter, an RCS reduction technique is presented by studying an integration strategy of the antenna with the AFSR structure. First, an AFSR structure exhibiting a reflection notch (at 8.2 GHz) between the wide absorbing bands (4.2 to 7.0 GHz and 9.2 to 11.5 GHz) is designed by imprinting a bandstop ring shaped resonator on the back of the top resistive substrate. The crossed dipole antenna designed at the frequency concurrent with the reflecting notch of proposed AFSR structure, is adjusted within a small truncated area at the middle of the AFSR structure with 6 x 6 proposed unit cell array. An average mono-static RCS reduction of 12.51 dB and 12.62 dB is acheived for the TE and TM incidence, respectively in the operating frequency band (4.2−11.5 GHz) for the AFSR based antenna compared with the conventional reflector counterpart. Furthermore, an average total bi-static RCS reduction of around 80% is experimentally demonstrated in reference to the conventional reflector backed antenna.

Chapter 9

Conclusion and Future Scope

9.1 Summary of Research

In this thesis, studies for designing various categories of FSRs have been carried out. The thesis starts from the design of single-layer narrow band rasorbers including multi-band conformal rasorbers. Further various broadband FSRs have been proposed in the thesis which includes rasorbers with A-T, T-A-T, A-T-A, and A-T-A-T behavior. The proposed A-T-A FSR in the thesis is experimentally verified for the RCS reduction of a narrowband patch antenna. The last part of thesis proposes an AFSR structure and integrates as a ground with the crossed dipole antenna for realizing the low RCS radiating system.

Initially, a single-layer FSS based T-A-T rasorber is proposed in the thesis. The rasorber is designed by printing a split-ring resonant structure and a dual bandpass FSS on the front and back of a 0.8 mm thick FR-4 dielectric substrate. The dual bandpass FSS comprising of concentric circular ring slots at the back, achieves two transmission bands at 3.1 and 8.4 GHz. At centre frequency of around 6.2 GHz, the dual bandpass FSS offers high reflection acting as a perfect reflecting surface. A split-ring resonator printed at the front achieves the absorption at 6.2 GHz for which the bandpass FSS acts as a reflecting ground surface. The working principle is illustrated by studying an ECM. The proposed rasorber possesses the feature of being thin single layer structure along with polarisation-insensitive behaviour due its four-fold symmetric design. A study has been carried out to determine the possible range of lower and upper transmission bands, keeping the absorption frequency (f_a) fixed at 6.2 GHz. It has been noted that judicious choice of the parameters of concentric ring etched in the ground plane, can enable tuning of lower transmission band from $0.45f_a$ to $0.72f_a$ and upper transmission band from $1.35f_a$ to $1.69f_a$. Thus the proposed design method help us to tune the relative spacing between absorption and lower/upper transmission band. Further, the results obtained in the simulations have been experimentally verified by carrying out measurements on the fabricated prototype of 21×21 rasorber unit cells. A good agreement is achieved between the simulated and measured results.

An ultra-thin, polarization-insensitive flexible (A-T-T-A/A-T-A-T-A)rasorbers with dual transmission and dual/triple absorption bands are designed on a 0.254 mm thick single layer substrate. The design for dual bandpass FSS is studied and combined with dual-band resonant absorber in such a way that at the absorption frequencies the bandpass FSS possess maximum possible reflection, thus realizing a 2T2A rasorber where the two resonant absorption ($f_{al} = 6.4$ GHz and $f_{au} = 14.7$ GHz) are located on the two sides of dual transmission bands ($f_{tl} = 9.6$ GHz and $f_{tu} = 13.4$ GHz). Further, the structure is modified to 2T3A rasorber in which an additional resonant absorption ($f_{am} = 11.1$ GHz) is obtained in between the two transmission bands. Parametric studies are carried out on the proposed rasorbers for determining the range within which each absorption frequency can be varied in the proposed design by the judicious selection of the corresponding design parameter which controls it. Keeping other performance parameters constant the lower and upper absorption frequency in the 2T2A rasorber can be varied from 4.61 to 6.94 GHz and 14.51 to 15.07 GHz, respectively. In 2T3A rasorber, the middle absorption frequency can be tuned from 10.37 to 12.30 GHz while maintaining the other performance parameters. The working of proposed rasorbers is analysed using an ECM. The results are experimentally verified by carrying out measurements on the fabricated prototype consisting of 17 x 25 unit cell for each of the dual and triple absorptive rasorbers. Furthermore, the conformal property of the proposed rasorbers is experimentally verified by carrying out measurements on the curved prototypes with multiple curvature angles. The proposed ultra-thin flexible rasorbers with absorptions and transmissions in multiple bands, along with conformal behavior can be useful in various potential applications like radar technology and EM shielding.

In the next part, this thesis presents the works on various broadband FSRs. A design technique of a FSR having wide band absorption and a higher transmission band (A-T) is studied. The FSR structure is a two-layer design consisting of resistive and bandpass layers. Increased bandwidth and reduced insertion loss are achieved at the higher transmission band by modifying the design of the bandpass FSS layer from DCS to MDCS. The proposed FSR achieves a broad absorption band ranging from 3.1 to 8.7 GHz with absorptivity greater than 80% and a higher transmission band at 11.46 GHz with insertion loss of 0.7 dB and -10 dB reflection bandwidth of 520 MHz (11.206 to 11.726 GHz). The working principle of the proposed FSR is also illustrated by analyzing a corresponding ECM. The parametric analysis carried on the bandpass FSS reveals that the transmission band of the proposed FSR can be varied from 10.64 to 16.20 GHz, retaining nearly the same broadband absorption property within 3.1 to 8.7 GHz. A prototype of the proposed FSR structure is fabricated and an experimental validation of simulated results is obtained.

A polarization-insensitive T-A-T FSR is proposed by combining the designs of the Jerusalem cross based bandpass FSS with the resistive square loop absorber. The dual resonant characteristics of the Jerusalem cross shaped bandpass FSS is utilized to obtain dual transmission bands (2.1 and 8.8 GHz) with an in-between broad absorption band (3.6 to 7.4 GHz). The proposed FSR is a compact structure having thickness and unit cell size of $0.09\lambda_L$ and $0.026\lambda_L^2$, respectively (λ_L is the lowest frequency of -10 dB reflection). The working principle of the proposed FSR is analyzed using an ECM. The lower and upper transmission bands can be tuned in the range of $0.31f_a$ to $0.46f_a$ and $1.56f_a$ to $1.86f_a$, respectively (f_a is the center frequency of the absorption band) by the judicious choice of the bandpass FSS parameters. A prototype consisting of 10 x 10 FSR unit cells is fabricated and the experimental validation of the performance of the FSR is obtained. The proposed FSR can provide potential application in RCS reduction for a dual-band radiating system.

Further in the thesis, a compact polarization-insensitive A-T-A FSR has been proposed using a MF based resonator, exhibiting higher selectivity at the passband. The proposed FSR is a double-layer structure comprising air-gap separated resistive and bandpass layers. The MF resonator with a cross-slot printed on the front side of resistive layer provides a transmission pole at the frequency corresponding to the transmission frequency of the DCS based bandpass FSS, thus realizing a transmission window (at 8.4 GHz) within a broad absorption band ($3.4-10.8$ GHz). The corner trimming of the square loop resonator on the top resistive layer further achieves the increased absorptivity at the upper absorption band. An ECM corresponding to the proposed FSR is analyzed for understanding the related working principle. A prototype with 17 x 17 proposed unit cells are fabricated, and the corresponding measurements provide the experimental validation of the proposed design. The proposed FSR exhibiting much higher selectivity (Q = 16.25) than the reported FSRs is the most suitable candidate for shielding and EMI/RCS reduction of narrowband radiating systems. Further, the proposed FSR with a 5 x 5 unit cell is integrated with a patch antenna as a superstrate to realize a low RCS system. The measurements carried on the FSR integrated antenna substantiate the RCS reduction outside the antenna's operating frequency. The FSR integrated antenna achieves a maximum monostatic RCS reduction of 23 dB and 10 dB in the upper and lower bands, respectively with an average reduction of 11.92 dB and 5.04 dB in the lower (4−7.5 GHz) and upper (9.2−10.8 GHz) absorption bands, respectively, while maintaining the other antenna parameters. Further, the average normalized total RCS of 0.23 and 0.40 is achieved for the FSR integrated antenna with respect to the conventional antenna in the lower and upper absorption bands, respectively. Thus, the proposed A-T-A FSR co-designed with a narrowband radiating system is experimentally demonstrated for low out-of-band RCS.

As an extension to the concept of A-T-A rasorber design, a polarization-independent dual transmissive FSR has been studied realizing the A-T-A-T response. The proposed design of FSR is a dual-layer structure comprising of resistive and bandpass layers at the top and bottom, respectively. An MF-shaped resonator is studied and incorporated within the resistive layer of the broadband absorber which realizes dual transmission poles within the broad absorption band. The proposed rasorber attains two passbands at 10.4 and 15.2 GHz with the two absorption bands from 5.2 to 10 GHz and 10.7 to 14.4 GHz. Measurements carried on the fabricated 15 x 15 rasorber prototype experimentally validates the design. The proposed FSR exhibiting dual transmission is a potential candidate for the RCS and EMI reduction in the dual-band radiating system. Also, the proposed FSR can be applied suitably as a low RCS radome for the dual-band radiating system having operating bands overlapping with the passbands of A-T-A-T rasorber.

In the last part of thesis, a low RCS dual-polarized crossed dipole antenna is studied for the first time by judiciously integrating with a polarization-insensitive AFSR structure. The AFSR structure exhibiting a reflection notch (at 8.2 GHz) between the wide absorbing bands is designed by imprinting a bandstop ring shaped resonator on the back of the top resistive substrate. The crossed dipole antenna designed at the frequency concurrent with the reflecting notch of proposed AFSR structure, is adjusted within a small truncated area at the middle of the AFSR structure with 6 x 6 proposed unit cell array. The AFSR structure acts as a modified ground for the antenna. Both the mono-static and bi-static measurements performed on the dual-polarized antenna backed with the AFSR structure verify the RCS reduction while the other antenna parameters are observed to be maintained nearly the same. An average mono-static RCS reduction of 12.51 dB and 12.62 dB is achieved for the TE and TM incidence, respectively in the operating frequency band (4.2−11.5 GHz) for the AFSR based antenna compared with the conventional reflector comprising counterpart. Furthermore, an average total bi-static RCS reduction of around 80% is experimentally demonstrated in reference to the conventional reflector backed antenna. The proposed low RCS antenna is a potential candidate in the dual-polarized applications for stealth communication.

9.2 Future Scope

This thesis presents the designs for several type of rasorbers ranging from single-layer narrow band to rasorbers with A-T, T-A-T, A-T-A, A-T-A-T responses. This thesis also discusses the AFSR structure and its integration with the crossed dipole antenna for realizing low RCS system. However, there exists much more scope for carrying out further works. Some of the future scopes related to the work presented in this thesis are given as:

1. The FSR proposed in this thesis can be extended with higher performance like A-T-A-T-A and above.

2. A dual-band antenna can be integrated with the A-T-A-T FSR wherein the operating frequencies of the antenna coincides with the transmission bands of the FSR, thus realizing a low RCS dual-band radiating system.

3. A conformal narrow band rasorber is presented in this thesis. However, the conformal features of the broadband FSR can be investigated in the future which can make them more suitable for practical applications.

4. The reconfigurability features of various FSS structures can be worked out as a future scope. This can enable a single FSS structure to have switchable/tunable absorption/transmission/diffusion characteristics.

Appendix A

Data Sheet CRCW0603200RFKEA Chip Resistor

Standard Thick Film Chip Resistors

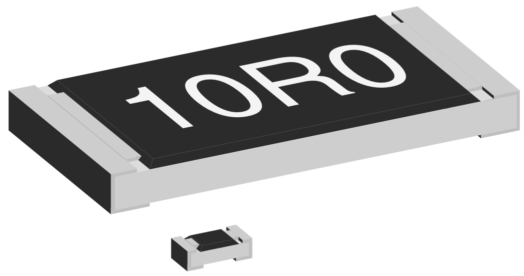

FEATURES

- Stability $\Delta R/R$ = 1 % for 1000 h at 70 ° C
- 2 mm pitch packaging option for 0603 size
- Pure tin solder contacts on Ni barrier layer provides compatibility with lead (Pb)-free and lead containing soldering processes
- Metal glaze on high quality ceramic
- AEC-Q200 qualified
- Material categorization: For definitions of compliance please see www.vishay.com/doc?99912

RoHS COMPLIANT

HALOGEN FREE

STANDARD ELECTRICAL SPECIFICATIONS

MODEL	SIZE		RATED DISSIPATION $P_{70\ °C}$ W	LIMITING ELEMENT VOLTAGE $U_{max.}$ AC/DC	TEMPERATURE COEFFICIENT ppm/K	TOLERANCE %	RESISTANCE RANGE Ω	SERIES
	INCH	METRIC						
D10/CRCW0402	0402	RR 1005M	0.063	50	± 100 ± 200	± 1 ± 5	1R0 to 10M	E24; E96 E24
			Zero-Ohm-Resistor: $R_{max.}$ = 20 mΩ, $I_{max.}$ at 70 °C = 1.5 A					
D11/CRCW0603	0603	RR 1608M	0.10	75	± 100 ± 200	± 1 ± 5	1R0 to 10M	E24; E96 E24
			Zero-Ohm-Resistor: $R_{max.}$ = 20 mΩ, $I_{max.}$ at 70 °C = 2.0 A					
D12/CRCW0805	0805	RR 2012M	0.125	150	± 100 ± 200	± 1 ± 5	1R0 to 10M	E24; E96 E24
			Zero-Ohm-Resistor: $R_{max.}$ = 20 mΩ, $I_{max.}$ at 70 °C = 2.5 A					
D25/CRCW1206	1206	RR 3216M	0.25	200	± 100 ± 200	± 1 ± 5	1R0 to 10M	E24; E96 E24
			Zero-Ohm-Resistor: $R_{max.}$ = 20 mΩ, $I_{max.}$ at 70 °C = 3.5 A					
CRCW1210	1210	RR 3225M	0.5	200	± 100 ± 200	± 1 ± 5	1R0 to 10M	E24; E96 E24
			Zero-Ohm-Resistor: $R_{max.}$ = 20 mΩ, $I_{max.}$ at 70 °C = 5.0 A					
CRCW1218	1218	RR 3246M	1.0	200	± 100 ± 200	± 1 ± 5	1R0 to 2M2	E24; E96 E24
			Zero-Ohm-Resistor: $R_{max.}$ = 20 mΩ, $I_{max.}$ at 70 °C = 7.0 A					
CRCW2010	2010	RR 5025M	0.75	400	± 100 ± 200	± 1 ± 5	1R0 to 10M	E24; E96 E24
			Zero-Ohm-Resistor: $R_{max.}$ = 20 mΩ, $I_{max.}$ at 70 °C = 6.0 A					
CRCW2512	2512	RR 6332M	1.0	500	± 100 ± 200	± 1 ± 5	1R0 to 10M	E24; E96 E24
			Zero-Ohm-Resistor: $R_{max.}$ = 20 mΩ, $I_{max.}$ at 70 °C = 7.0 A					

Notes

- These resistors do not feature a limited lifetime when operated within the permissible limits. However, resistance value drift increasing over operating time may result in exceeding a limit acceptable to the specific application, thereby establishing a functional lifetime.
- Marking: See data sheet "Surface Mount Resistor Marking" (document number 20020).
- Power rating depends on the max. temperature at the solder point, the component placement density and the substrate material.

D/CRCW e3

Vishay

Standard Thick Film Chip Resistors

TECHNICAL SPECIFICATIONS

PARAMETER	UNIT	D10/ CRCW0402	D11/ CRCW0603	D12/ CRCW0805	D25/ CRCW1206	CRCW1210	CRCW1218	CRCW2010	CRCW2512
Rated dissipation P_{70} (1)	W	0.063	0.1	0.125	0.25	0.5	1.0	0.75	1.0
Limiting element voltage $U_{max.}$ AC/DC	V	50	75	150	200	200	200	400	500
Insulation voltage U_{ins} (1 min)	V	> 75	> 100	> 200	> 300	> 300	> 300	> 300	> 300
Insulation resistance	Ω	$> 10^9$							
Category temperature range	°C	- 55 to + 155							
Failure rate	h^{-1}	$< 0.1 \times 10^{-9}$							
Weight	mg	0.65	2	5.5	10	16	29.5	25.5	40.5

Note

(1) The power dissipation on the resistor generates a temperature rise against the local ambient, depending on the heat flow support of the printed-circuit board (thermal resistance). The rated dissipation applies only if the permitted film temperature of 155 °C is not exceeded.

PART NUMBER AND PRODUCT DESCRIPTION

Part Number: CRCW0603562RFKEC

C	R	C	W	0	6	0	3	5	6	2	R	F	K	E	C		

MODEL	VALUE	TOLERANCE	TCR	PACKAGING	SPECIAL
CRCW0402 **CRCW0603** **CRCW0805** **CRCW1206** **CRCW1210** **CRCW1218** **CRCW2010** **CRCW2512**	**R** = Decimal **K** = Thousand **M** = Million **0000** = Jumper	**F** = ± 1.0 % **J** = ± 5.0 % **Z** = Jumper	**K** = ± 100 ppm/K **N** = ± 200 ppm/K **0** = Jumper	**EA, EB,** **EC, ED,** **EE, EF,** **EG, EH,** **EI, EL,** **EK**	Up to 2 digits

Product Description: D11/CRCW0603 100 562R 1 % ET6 e3

D11/CRCW0603	100	562R	1 %	ET6	e3
MODEL	TCR	RESISTANCE VALUE	TOLERANCE	PACKAGING	LEAD (Pb)-FREE
D10/CRCW0402 **D11/CRCW0603** **D12/CRCW0805** **D25/CRCW1206** **CRCW1210** **CRCW1218** **CRCW2010** **CRCW2512**	± **200** ppm/K ± **100** ppm/K	**10R** = 10 Ω **562R** = 562 Ω **10K** = 10 kΩ **1M0** = 1 MΩ **0R0** = Jumper	± **5 %** ± **1 %**	**ET1, ET2,** **ET3, ET4,** **ET5, ET6,** **ET7, ET8,** **ET9, EF4,** **E02, E67,** **E82**	**e3** = Pure tin termination finish

PACKAGING

MODEL	CODE	QUANTITY	CARRIER TAPE	WIDTH	PITCH	REEL DIAMETER
CRCW0402	ED = ET7	10 000	Paper tape acc. to IEC 60068-3 Type I	8 mm	2 mm	180 mm/7"
	EE = EF4	50 000				330 mm/13"
CRCW0603	EI = ET2	5000		8 mm	2 mm	180 mm/7"
	ED = ET3	10 000				180 mm/7"
	EL = ET4	20 000				285 mm/11.25"
	EE = ET8	50 000				330 mm/13"
	EA = ET1	5000		8 mm	4 mm	180 mm/7"
	EB = ET5	10 000				285 mm/11.25"
	EC = ET6	20 000				330 mm/13"
CRCW0805	EA = ET1	5000		8 mm	4 mm	180 mm/7"
	EB = ET5	10 000				285 mm/11.25"
	EC = ET6	20 000				330 mm/13"
CRCW1206	EA = ET1	5000		8 mm	4 mm	180 mm/7"
	EB = ET5	10 000				285 mm/11.25"
	EC = ET6	20 000				330 mm/13"
CRCW1210	EA = ET1	5000		8 mm	4 mm	180 mm/7"
	EB = ET5	10 000				285 mm/11.25"
	EC = ET6	20 000				330 mm/13"
CRCW1218	EK = ET9	4000	Blister tape acc. to IEC 60068-3 Type II	12 mm	4 mm	180 mm/7"
CRCW2010	EF = E02	4000		12 mm	4 mm	180 mm/7"
CRCW2512	EG = E67	2000		12 mm	8 mm	180 mm/7"
	EH = E82	4000			4 mm	

DIMENSIONS

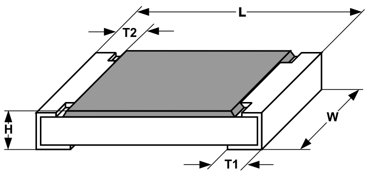

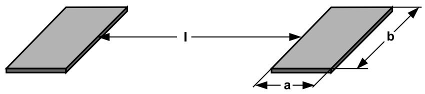

SIZE		DIMENSIONS in millimeters					SOLDER PAD DIMENSIONS in millimeters					
							REFLOW SOLDERING			WAVE SOLDERING		
INCH	METRIC	L	W	H	T1	T2	a	b	l	a	b	l
0402	1005	1.0 ± 0.05	0.5 ± 0.05	0.35 ± 0.05	0.25 ± 0.05	0.2 ± 0.1	0.4	0.6	0.5			
0603	1608	$1.55^{+0.10}_{-0.05}$	0.85 ± 0.1	0.45 ± 0.05	0.3 ± 0.2	0.3 ± 0.2	0.5	0.9	1.0	0.9	0.9	1.0
0805	2012	$2.0^{+0.20}_{-0.10}$	1.25 ± 0.15	0.45 ± 0.05	$0.3^{+0.20}_{-0.10}$	0.3 ± 0.2	0.7	1.3	1.2	0.9	1.3	1.3
1206	3216	$3.2^{+0.10}_{-0.20}$	1.6 ± 0.15	0.55 ± 0.05	0.45 ± 0.2	0.4 ± 0.2	0.9	1.7	2.0	1.1	1.7	2.3
1210	3225	3.2 ± 0.2	2.5 ± 0.2	0.55 ± 0.05	0.45 ± 0.2	0.4 ± 0.2	0.9	2.5	2.0	1.1	2.5	2.2
1218	3246	$3.2^{+0.10}_{-0.20}$	4.6 ± 0.15	0.55 ± 0.05	0.45 ± 0.2	0.4 ± 0.2	1.05	4.9	1.9	1.25	4.8	1.9
2010	5025	5.0 ± 0.15	2.5 ± 0.15	0.6 ± 0.1	0.6 ± 0.2	0.6 ± 0.2	1.0	2.5	3.9	1.2	2.5	3.9
2512	6332	6.3 ± 0.2	3.15 ± 0.15	0.6 ± 0.1	0.6 ± 0.2	0.6 ± 0.2	1.0	3.2	5.2	1.2	3.2	5.2

D/CRCW e3

Vishay

Standard Thick Film Chip Resistors

FUNCTIONAL PERFORMANCE

Single Pulse

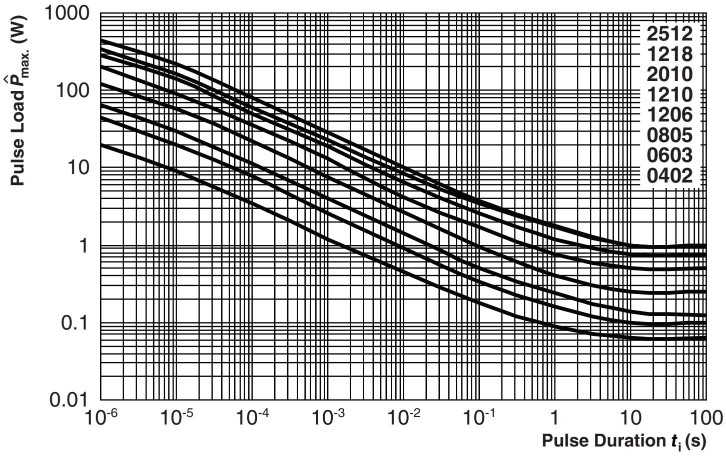

Maximum pulse load, single pulse; applicable if $\bar{P} \rightarrow 0$ and n < 1000 and $\hat{U} \leq \hat{U}_{max.}$;
for permissible resistance change equivalent to 8000 h operation

Continuous Pulse

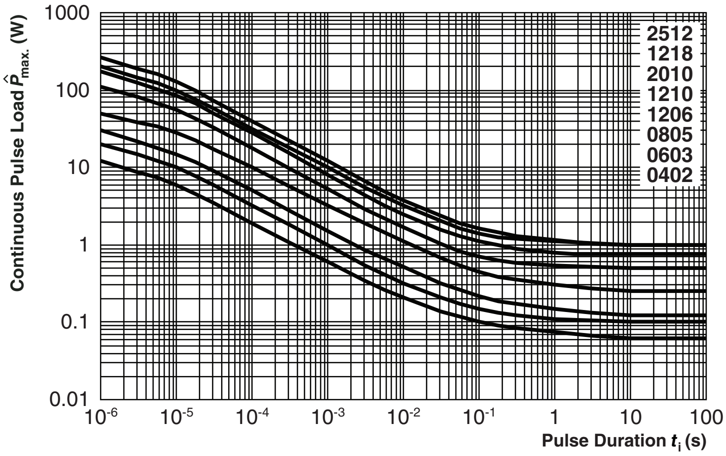

Maximum pulse load, continuous pulses; applicable if $\bar{P} \leq P(\vartheta_{amb})$ and $\hat{U} \leq \hat{U}_{max.}$;
for permissible resistance change equivalent to 8000 h operation

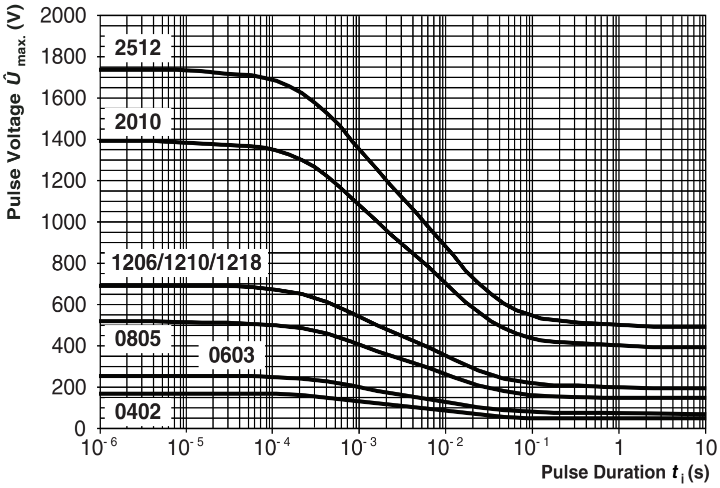

Maximum pulse voltage, single and continuous pulses; applicable if
$\hat{P} \leq \hat{P}_{max.}$; for permissible resistance change equivalent to 8000 h operation

Derating

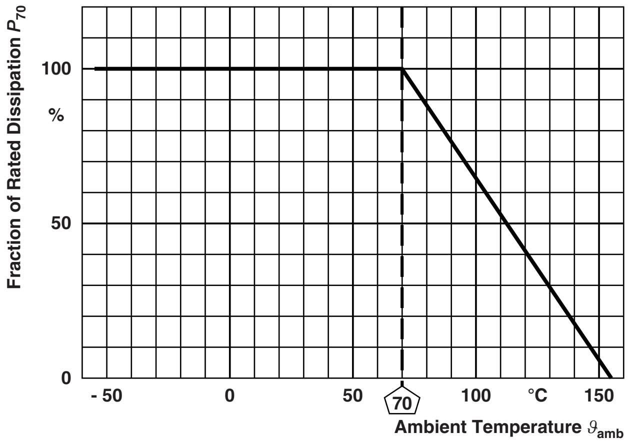
Fraction of Rated Dissipation P_{70}
100
%
50
0
- 50
0
50
70
100
°C
150
Ambient Temperature ϑ_{amb}

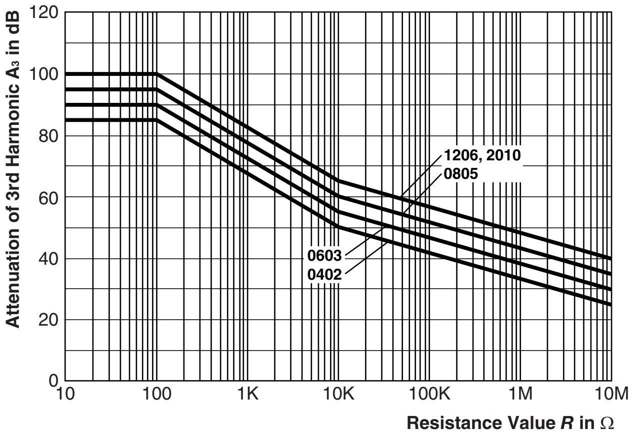
Attenuation of 3rd Harmonic A_3 in dB
120
100
80
60
40
20
0
10
100
1K
10K
100K
1M
10M
1206, 2010
0805
0603
0402
Resistance Value R in Ω

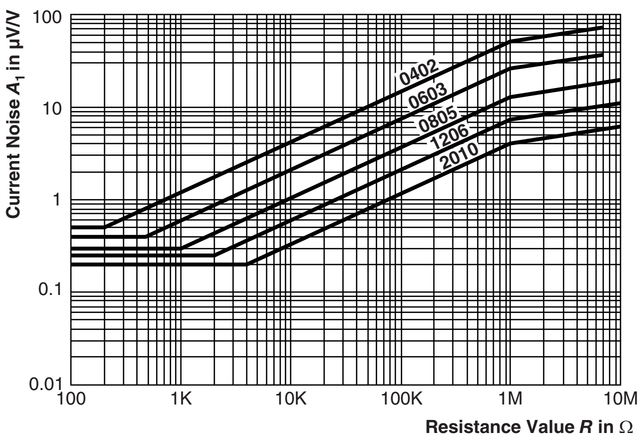
Current Noise A_1 in µV/V
100
10
1
0.1
0.01
100
1K
10K
100K
1M
10M
0402
0603
0805
1206
2010
Resistance Value R in Ω

D/CRCW e3

Vishay

Standard Thick Film Chip Resistors

TEST PROCEDURES AND REQUIREMENTS

EN 60115-1 CLAUSE	IEC 60068-2 TEST METHOD	TEST	PROCEDURE	REQUIREMENTS PERMISSIBLE CHANGE (ΔR) SIZE 0402 to 2512 STABILITY CLASS 1 OR BETTER	STABILITY CLASS 2 OR BETTER
			Stability for product types: **D/CRCW e3**	1 Ω to 10 MΩ	
4.5	-	Resistance	-	± 1 %	± 5 %
4.7	-	Voltage proof	$U = 1.4 \times U_{ins}$; 60 s	No flashover or breakdown	
4.13	-	Short time overload	$U = 2.5 \times \sqrt{P_{70} \times R}$ $\leq 2 \times U_{max.}$; duration: Acc. to style	± (0.25 % R + 0.05 Ω)	± (0.5 % R + 0.05 Ω)
4.17.2	58 (Td)	Solderability	Solder bath method; Sn60Pb40 non activated flux; (235 ± 5) °C (2 ± 0.2) s	Good tinning (≥ 95 % covered) no visible damage	
			Solder bath method; Sn96.5Ag3Cu0.5 non-activated flux; (245 ± 5) °C (3 ± 0.3) s	Good tinning (≥ 95 % covered) no visible damage	
4.8.4.2	-	Temperature coefficient	(20/- 55/20) °C and (20/125/20) °C	± 100 ppm/K	± 200 ppm/K
4.32	21 (Uu_3)	Shear (adhesion)	RR 1608 and smaller: 9 N RR 2012 and larger: 45 N	No visible damage	
4.33	21 (Uu_1)	Substrate bending	Depth 2 mm; 3 times	No visible damage, no open circuit in bent position ± (0.25 % R + 0.05 Ω)	
4.19	14 (Na)	Rapid change of temperature	30 min. at - 55 °C; 30 min. at 125 °C		
			5 cycles	± (0.25 % R + 0.05 Ω)	± (0.5 % R + 0.05 Ω)
			1000 cycles	± (1 % R + 0.05 Ω)	± (1 % R + 0.05 Ω)
4.23	-	Climatic sequence:	-	± (1 % R + 0.05 Ω)	± (2 % R + 0.1 Ω)
4.23.2	2 (Ba)	Dry heat	125 °C; 16 h		
4.23.3	30 (Db)	Damp heat, cyclic	55 °C; ≥ 90 % RH; 24 h; 1 cycle		
4.23.4	1 (Aa)	Cold	- 55 °C; 2 h		
4.23.5	13 (M)	Low air pressure	1 kPa; (25 ± 10) °C; 1 h		
4.23.6	30 (Db)	Damp heat, cyclic	55 °C; ≥ 90 % RH; 24 h; 5 cycles		
4.23.7	-	DC load	$U = \sqrt{P_{70} \times R}$		
4.25.1	-	Endurance at 70 °C	$U = \sqrt{P_{70} \times R} \leq U_{max.}$; 1.5 h on; 0.5 h off;		
			70 °C; 1000 h	± (1 % R + 0.05 Ω)	± (2 % R + 0.1 Ω)
			70 °C; 8000 h	± (2 % R + 0.1 Ω)	± (4 % R + 0.1 Ω)

TEST PROCEDURES AND REQUIREMENTS

EN 60115-1 CLAUSE	IEC 60068-2 TEST METHOD	TEST	PROCEDURE	REQUIREMENTS PERMISSIBLE CHANGE (ΔR) SIZE 0402 to 2512: STABILITY CLASS 1 OR BETTER	STABILITY CLASS 2 OR BETTER
			Stability for product types:		
			D/CRCW e3	1 Ω to 10 MΩ	
4.18.2	58 (Td)	Resistance to soldering heat	Solder bath method (260 ± 5) °C; (10 ± 1) s	± (0.25 % R + 0.05 Ω)	± (0.5 % R + 0.05 Ω)
4.35	-	Flamability, needle flame test	IEC 60695-11-5; 10 s	No burning after 30 s	
4.24	78 (Cab)	Damp heat, steady state	(40 ± 2) °C; (93 ± 3) % RH; 56 days	± (1 % R + 0.05 Ω)	
4.25.3	-	Endurance at upper category temperature	155 °C, 1000 h	± (1 % R + 0.05 Ω)	± (2 % R + 0.1 Ω)
4.40	-	Electrostatic discharge (human body model)	IEC 61340-3-1; 3 pos. + 3 neg. discharges; ESD voltage acc. to size	± (1 % R + 0.05 Ω)	
4.29	45 (XA)	Component solvent resistance	Isopropyl alcohol; 50 °C; method 2	No visible damage	
4.30	45 (XA)	Solvent resistance of marking	Isopropyl alcohol; 50 °C; method 1, toothbrush	Marking legible, no visible damage	
4.22	6 (Fc)	Vibration, endurance by sweeping	f = 10 Hz to 2000 Hz; x, y, z ≤ 1.5 mm; A ≤ 200 m/s^2; 10 sweeps per axis	± (0.25 % R + 0.05 Ω)	± (0.5 % R + 0.05 Ω)
4.37	-	Periodic electric overload	$U = \sqrt{15 \times P_{70} \times R}$ $\leq 2 \times U_{max.}$; 0.1 s on; 2.5 s off; 1000 cycles	± (1 % R + 0.05 Ω)	
4.27	-	Single pulse high voltage overload, 10 µs/700 µs	$\hat{U} = 10 \times \sqrt{P_{70} \times R}$ $\leq 2 \times U_{max.}$; 10 pulses	± (1 % R + 0.05 Ω)	

All tests are carried out in accordance with the following specifications:

- EN 60115-1, generic specification
- EN 140400, sectional specification
- EN 140401-802, detail specification
- IEC 60068-2-x, environmental test procedures

Packaging of components is done in paper or blister tapes according to IEC 60286-3.

Disclaimer

ALL PRODUCT, PRODUCT SPECIFICATIONS AND DATA ARE SUBJECT TO CHANGE WITHOUT NOTICE TO IMPROVE RELIABILITY, FUNCTION OR DESIGN OR OTHERWISE.

Vishay Intertechnology, Inc., its affiliates, agents, and employees, and all persons acting on its or their behalf (collectively, “Vishay”), disclaim any and all liability for any errors, inaccuracies or incompleteness contained in any datasheet or in any other disclosure relating to any product.

Vishay makes no warranty, representation or guarantee regarding the suitability of the products for any particular purpose or the continuing production of any product. To the maximum extent permitted by applicable law, Vishay disclaims (i) any and all liability arising out of the application or use of any product, (ii) any and all liability, including without limitation special, consequential or incidental damages, and (iii) any and all implied warranties, including warranties of fitness for particular purpose, non-infringement and merchantability.

Statements regarding the suitability of products for certain types of applications are based on Vishay’s knowledge of typical requirements that are often placed on Vishay products in generic applications. Such statements are not binding statements about the suitability of products for a particular application. It is the customer’s responsibility to validate that a particular product with the properties described in the product specification is suitable for use in a particular application. Parameters provided in datasheets and / or specifications may vary in different applications and performance may vary over time. All operating parameters, including typical parameters, must be validated for each customer application by the customer’s technical experts. Product specifications do not expand or otherwise modify Vishay’s terms and conditions of purchase, including but not limited to the warranty expressed therein.

Except as expressly indicated in writing, Vishay products are not designed for use in medical, life-saving, or life-sustaining applications or for any other application in which the failure of the Vishay product could result in personal injury or death. Customers using or selling Vishay products not expressly indicated for use in such applications do so at their own risk. Please contact authorized Vishay personnel to obtain written terms and conditions regarding products designed for such applications.

No license, express or implied, by estoppel or otherwise, to any intellectual property rights is granted by this document or by any conduct of Vishay. Product names and markings noted herein may be trademarks of their respective owners.

Bibliography

[1] T. K. Wu, *"Frequency Selective Surface and Grid Array,"* 1st ed. New York, NY, USA: Wiley, 1995.

[2] W. F. Bahret, "The beginnings of stealth technology," *IEEE Trans. Aerosp. Electron. Syst.*, vol. 29, no. 4, pp. 1377–1385, Oct. 1993.

[3] B. A. Munk, *"Frequency Selective Surfaces: Theory and Design,"* 1st ed. New York, NY, USA: Wiley, 2000.

[4] S. W. Lee, "Scattering by dielectric-loaded screen," *IEEE Trans. Antennas Propag.*, vol. 19, pp. 656–665, 1971.

[5] E. Pelton and B. Munk, "A streamlined metallic radome," *IEEE Trans. Antennas Propag.*, vol. 22, no. 6, pp. 799-803, November 1974.

[6] X. Yuan, and X. Yuan,"A transmissive/absorbing radome with double absorbing band," *Microwave Opt Technol Lett.*, vol. 58, no. 8, pp. 2016- 2019, Aug. 2016.

[7] S. Agahi, R. Mittra, "Design of a cascaded frequency selective surface as a dichroic subreflector," *In Proceedings of the Antennas and Propagation Society International Symposium: AP-S Merging Technologies for the 90' (Digest).*, Dallas, TX, USA, 7–11, pp. 88–91, May 1990.

[8] F. Costa, S. Genovesi, A. Monorchio, G. Manara, "A robust differential amplitude codification for chipless RFID," *IEEE Microw. Wireless Compon. Lett.*, vol. 25, pp. 832–834, 2015.

[9] D. Pozar, "Flat lens antenna concept using aperture coupled microstrip patches," *Electron. Lett.*, vol. 32, pp. 2109–2111, 1996.

[10] M. Euler, and V. Fusco, "Frequency selective surface using nested split ring slot elements as a lens with mechanically reconfigurable beam steering capability," *IEEE Trans. Antennas Propag.*, vol. 58, no. 10, pp. 3417-3421, Oct. 2010.

[11] B. Chambers, and K. Ford, "Tunable radar absorbers using frequency selective surfaces," *IEEE Eleventh International Conf. Antennas Propag.*, vol. 2, pp. 593-597, 2001.

[12] P. Yuste, J. M. Rius, J. Romeu, S. Blanch, A. Heldring and E. Ubeda, "A Microwave Invisibility Cloak: The Design, Simulation, and Measurement of a Simple and Effective Frequency-Selective Surface-Based Mantle Cloak," *IEEE Antennas Propag. Mag.*, vol. 60, no. 4, pp. 49-59, Aug. 2018.

[13] W. Tang, Y. Hao and R. Mittra, "Design of a Carpet Cloak to Conceal an Antenna Located Underneath," *IEEE Trans. Antennas Propag.*, vol. 60, no.9, pp. 4444-4449, Sept. 2012.

[14] M. Mahmo odi, L. VanZant and K. M. Donnell, "An Aperture Efficiency Approach for Optimization of FSS-Based Sensor Resolution," *IEEE Trans. Inst. Meas.*, vol. 69, no. 10, pp. 7837-7845, Oct. 2020.

[15] M. Mahmoodi and K. M. Donnell, "Performance Metrics for Frequency Selective Surface-Based Sensors," *IEEE Sensors Lett.*, vol. 1, no. 6, pp. 1-4, Dec. 2017.

[16] S. Milici, J. Lorenzo, A. L azaro, R. Villarino and D. Girbau, "Wireless Breathing Sensor Based on Wearable Modulated Frequency Selective Surface," *IEEE Sensors Journal.*, vol. 17, no. 5, pp. 1285-1292, March, 2017.

[17] M. Saikia, S. Ghosh and K. V. Srivastava, "Design and Analysis of Ultrathin Polarization Rotating Frequency Selective Surface Using V-Shaped Slots," *IEEE Antennas Wireless Propag. Lett.*, vol. 16, pp. 2022-2025, 2017.

[18] L. Li, Y. Li, Z. Wu, F. Huo, Y. Zhang and C. Zhao, "Novel Polarization-Reconfigurable Converter Based on Multilayer Frequency-Selective Sur- faces," *Proc. IEEE.*, vol. 103, no. 7, pp. 1057-1070, July 2015.

[19] M. Fartookzadeh and S. H. Mohseni Armaki, "Dual-Band Reflection-Type Circular Polarizers Based on Anisotropic Impedance Surfaces," *IEEE Trans. Antennas Propag.*, vol. 64, no. 2, pp. 826-830, Feb. 2016.

[20] M. Euler, V. Fusco, R. Cahill and R. Dickie, "325 GHz Single Layer Sub-Millimeter Wave FSS Based Split Slot Ring Linear to Circular Polarization Convertor," *IEEE Trans. Antennas Propag.*, vol. 58, no. 7, pp. 2457-2459, July 2010.

[21] M. Hosseini and S. V. Hum, "A Semianalytical Approach to Designing High-Transparency Low-Profile Circular Polarizers," *IEEE Trans. Antennas Propag.*, vol. 66, no. 12, pp. 7138-7147, Dec. 2018.

[22] E. Arnieri, F. Greco and G. Amendola, "A Broadband, Wide-Angle Scanning, Linear-to-Circular Polarization Converter Based on Standard Jerusalem Cross Frequency Selective Surfaces," *IEEE Trans. Antennas Propag.*, vol. 69, no. 1, pp. 578-583, Jan. 2021.

[23] L. M.-Lopez, J. R.-Cuevas, J. I. M.-Lopez, and A. E. Martynyuk, "A multilayer circular polarizer based on bisected split-ring frequency selective surfaces," *IEEE Antenna Wireless Propag. Lett.*, vol. 13, pp. 153-156, Jan. 2014.

[24] S. H. Abadi, K. Ghaemi, and N. Behdad, "Ultra-wideband, true-time delay reflectarray antennas using ground-plane-backed, miniaturized element frequency selective surfaces," *IEEE Trans. Antennas Propag.*, vol. 63, no. 2, pp. 534-542, Feb. 2015.

[25] S. Celozzi, R. Araneo, and G. Lovat, *"Electromagnetic Shielding,"* 1st ed. New York,NY, USA: Wiley, 2008.

[26] D. Li, T. W.Li, E. P. Li, Y.J. Zhang, "A 2.5-D Angularly Stable Frequency Selective Surface Using Via-Based Structure for 5G EMI Shielding," *IEEE Trans. Electromagn. Compat.*, vol. 60, pp. 768–775, 2018.

[27] A. Tennant, W. Hurley, T. Dias, "Experimental knitted, textile frequency selective surfaces," *Electron. Lett.*, vol. 48, pp. 1386–1388, 2012.

[28] C. N. Chiu, K. P. Chang, "A novel miniaturized-element frequency selective surface having a stable resonance," *IEEE Antennas Wireless Propag. Lett.*, vol. 8, pp. 1175–1177, 2009.

[29] Martinez-Lopez, L. Rodriguez-Cuevas, J. Martinez-Lopez, J.I. Martynyuk, A.E, "A multilayer circular polarizer based on bisected split-ring frequency selective surfaces," *Electron. Lett.*, vol. 13, pp. 153–156, 2014.

[30] A. H. Abdelrahman, A. Z. Elsherbeni, F. Yang, "Transmission phase limit of multilayer frequency-selective surfaces for transmitarray designs," *IEEE Trans. Antennas Propag.*, vol. 62, no. 2, pp. 690-697, Feb. 2014.

[31] S. M. A. Momeni Hasan Abadi, M. Li and N. Behdad, "Harmonic-Suppressed Miniaturized-Element Frequency Selective Surfaces With Higher Order Band-pass Responses," *IEEE Trans. Antennas Propag.*, vol. 62, no. 5, pp. 2562-2571, May 2014.

[32] S. M. A. M. H. Abadi and N. Behdad, "Design of Wideband, FSS-Based MultiBeam Antennas Using the Effective Medium Approach," *IEEE Trans. Antennas Propag.*, vol. 62, no. 11, pp. 5557-5564, Nov. 2014.

[33] N. Xu, J. Gao, J. Zhao, X. Feng, "A novel wideband, low-profile and second order miniaturized band-pass frequency selective surfaces," *AIP Adv.*, vol. 5, 2015.

[34] A. L. P. Campos, E. E. C. de Oliveira, P. H. da Fonseca Silva, "Design of miniaturized frequency selective surfaces using Minkowski island fractal," *J. Microw. Optoelectron. Electromagn. Appl.*, vol. 9, no. 19, pp. 43–49, 2010.

[35] Y. Shi, W. Tang, W.Zhuang, C.Wang, "Miniaturised frequency selective surface based on 2.5-dimensional closed loop," *Electron. Lett.*, vol. 50, pp.1656–1658, 2014.

[36] Y. Yu, C. Chiu, Y. Chiou and T. Wu, "A Novel 2.5-Dimensional Ultraminiaturized-Element Frequency Selective Surface," *IEEE Trans. Antennas Propag.*, vol. 62, no. 7, pp. 3657-3663, July 2014.

[37] B. Li and Z. Shen, "Three-Dimensional Bandpass Frequency-Selective Structures With Multiple Transmission Zeros," *IEEE Trans. Microw. Tech.*, vol. 61, no. 10, pp. 3578-3589, Oct. 2013.

[38] A. K. Rashid, B. Li and Z. Shen, "An overview of three-dimensional frequency-selective structures," *IEEE Antennas Propag. Mag.*, vol. 56, no. 3, pp. 43-67, June 2014.

[39] G. I. Kiani,K. L. Ford, K. P. Esselle, A. R. Weily, C. Panagamuwa, J. C. Batchelor, "Single-layer bandpass active frequency selective surface," *Microw. Opt. Technol. Lett.*, vol. 50, pp. 2149–2151, 2008.

[40] B. Li and Z. Shen, "Bandpass Frequency Selective Structure With Wideband Spurious Rejection," *IEEE Antennas Wirel. Propag. Lett.*, vol. 13, pp. 145-148, 2014.

[41] C. Huang, C. Ji, X. Wu, J. Song and X. Luo, "Combining FSS and EBG Surfaces for High-Efficiency Transmission and Low-Scattering Properties," *IEEE Trans. Antennas Propag.*, vol. 66, no. 3, pp. 1628-1632, March 2018.

[42] L. Sun, H. Cheng, Y. Zhou, J. Wang, "Broadband metamaterial absorber based on coupling resistive frequency selective surface," *Opt. Express.*, vol. 20, pp. 4675–4680, 2012.

[43] R. Anwar, L. Mao, and H. Ning, "Frequency Selective Surfaces: A Review," *Applied Sciences*, vol. 8, no. 9, p. 1689, Sep. 2018.

[44] F. Bilotti, L. Nucci, and L. Vegni, "An SRR based microwave absorber," *Microwave Opt Technol Lett.*, vol. 48, no. 11, pp. 2171-2175, Nov. 2006.

[45] N. I. Landy, S. Sajuyigbe, J. J. Mock, D. R. Smith, and W. J. Padilla, "Perfect metamaterial absorber," *Phys. Rev. Lett.*, vol. 100, p. 207402, May 2008.

[46] H. Li, L. H. Yuan, B. Zhou, X. P. Shen, Q. Cheng, and T. J. Cu, "Ultra-thin multiband gigahertz metamaterial absorbers," *J. Appl. Phys.*, vol. 110, p. 014909, Jul. 2011.

[47] A. K. Singh, M. P. Abegaonkar and S. K. Koul, "Dual- and Triple-Band Polarization Insensitive Ultrathin Conformal Metamaterial Absorbers With Wide Angular Stability," *IEEE Trans. Electromagn. Compat.*, vol. 61, no. 3, pp. 878-886, June 2019.

[48] J. Wang, R. Yang, J. Tian, X. Chen, and W. Zhang, "A dual-band absorber with wide-angle and polarization insensitivity," *IEEE Antennas Wireless Propag. Lett.*, vol. 17, no. 7, pp. 1242–1246, Jul. 2018.

[49] P. Jain, A. K. Singh, J. K. Pandey, S. Garg, S. Bansal, M. Agarwal, S. Kumar, N. Sardana, N. Gupta, and A. K. Singh, "Ultra-thin metamaterial perfect absorbers for single-/dual-/multi-band microwave applications," *IET Microw., Antennas Propag.*, vol. 14, no. 5, pp. 390–396, Apr. 2020.

[50] O. Luukkonen, F. Costa, C. R. Simovski, A. Monorchio, and S. A. Tretyakov, "A thin electromagnetic absorber for wide incidence angles and both polarizations," *IEEE Trans. Antennas Propag.*, vol. 57, no. 10, pp. 3119-3125, Oct. 2009.

[51] S. Bhattacharyya, and K. V. Srivastava, "An ultra thin electric field driven LC resonator structure as metamaterial absorber for dual band applications," *Proc. URSI International Symposium on Electromagnetic Theory (EMTS)*, pp. 722-725, May 20-24, 2013.

[52] M.-H. Li, H.-L. Yang, and X.-W. Hou, "Perfect metamaterial absorber with dual band," *Prog. Electromag. Res.*, vol. 108, pp. 37-49, Sept. 2010.

[53] P. V. Tuong, J. W. Park, J. Y. Rhee, K. W. Kim, W. H. Jang, H. Cheong, and Y. P. Lee, "Polarization-insensitive and polarization-controlled dual-band absorption in metamaterials," *J. Appl. Phys.*, vol. 102, p. 081122, Mar. 2013.

[54] H.-X. Xu, G.-M. Wang, M.-Q. Qi, J.-G. Liang, J.-Q. Gong, and Z.-M. Xu, "Triple- band polarization-insensitive wide-angle ultra-miniature metamaterial transmission line absorber," *Phys. Rev. B*, vol. 86, p. 205104, Nov. 2012.

[55] B. Bian, S. Liu, S. Wang, X. Kong, H. Zhang, B. Ma, and H. Yang, “Novel triple-band polarization-insensitive wide-angle ultra-thin microwave metamaterial absorber,” *J. Appl. Phys.*, vol. 114, p. 194511, Nov. 2013.

[56] D. Chaurasiya, S. Ghosh, S. Bhattacharyya, and K. V. Srivastava, “An ultrathin quad-band polarization-insensitive wide-angle metamaterial absorber,” *Microw. Opt. Technol. Lett.*, vol. 57, no. 3, pp. 697-702, Mar. 2015.

[57] M. Agarwal, A.K. Behera and M.K. Meshram, “Wide-angle quad-band polarisation-insensitive metamaterial absorber,” *Electron. Lett.*, vol. 52, no. 5, pp. 340-342, Jan.2016.

[58] A. Bhattacharya, S. Bhattacharyya, S. Ghosh, D. Chaurasiya, and K. V. Srivastava,“An ultrathin penta-band polarization-insensitive compact metamaterial absorber for airborne radar applications,” *Microw. Opt. Technol. Lett.*, vol. 57, no. 11, pp. 2519-2524, Nov. 2015.

[59] S. Bhattacharyya, S. Ghosh, and K. V. Srivastava, “Bandwidth-enhanced metamaterial absorber using electric field-driven LC resonator for airborne radar applications,” *Microwave Opt Technol Lett.*, vol. 55, no. 9, pp. 2131-2137, Sept 2013.

[60] J. Lee and S. Lim, “Bandwidth-enhanced and polarisation-insensitive metamaterial absorber using double resonance,” *Electron. Lett.*, vol. 47, no. 1, pp. 8–9, Jan. 2011.

[61] D. Wen, H. Yang, Q. Ye, M. Li, L. Guo, and J. Zhang, “Broadband metamaterial absorber based on a multi-layer structure,” *Phys. Scr.*, vol. 88, p. 015402, Jun. 2013.

[62] Y. Z. Cheng, Y. Wang, Y. Nie, R. Zhou Gong, X. Xiong, and X. Wang, “Design, fabrication and measurement of a broadband polarization-insensitive metamaterial absorber based on lumped elements,” *J. Appl. Phys.*, vol. 111, no. 4, p. 044902, 2012.

[63] S. Ghosh, S. Bhattacharyya, and K. V. Srivastava, “Design, characterisation and fabrication of a broadband polarisation-insensitive multi-layer circuit ana-

logue absorber," *Microw., Antennas Propag.*, vol. 10, no. 8, pp. 850–855, May 2016.

[64] N. Hakla, S. Ghosh, and K. V. Srivastava, "Design of low-profile broadband capacitive circuit absorber," *Electron. Lett.*, vol. 52, no. 22, pp. 1825–1826, Oct. 2016.

[65] B. Zhang, C. Jin and Z. Shen, "Low-Profile Broadband Absorber Based on Multimode Resistor-Embedded Metallic Strips," *IEEE Trans. Microw. Theory Techn.*, vol. 68, no. 3, pp. 835-843, March 2020.

[66] W.S.Arceneaux, R.D.Akins, and W.B.May, "absorptive/transmissive radome," *US.Patent* , 5,400,043, May 21,1995.

[67] Bo Yi, Peiguo Liu, Cheng Yang and Yanfei Dong, "Analysis of absorptive and transmissive radome," *IEEE 6th International Symposium on Microwave, Antenna, Propagation, and EMC Technologies (MAPE)*, pp. 616-619, 2015.

[68] Y. Han, Y. Chang and W. Che, "Frequency-Selective Rasorbers: A View of Frequency-Selective Rasorbers and Their Application in Reducing the Radar Cross Sections of Antennas," *IEEE Microwave Magazine*,vol. 23, no. 2, pp. 86-98, Feb. 2022.

[69] A. A. Omar, H. Huang and Z. Shen, "Absorptive Frequency-Selective Reflection/Transmission Structures: A Review and Future Perspectives," *IEEE Antennas and Propagation Magazine*, vol. 62, no. 4, pp. 62-74, Aug. 2020.

[70] P. Mei, X. Q. Lin, J. W. Yu and P. C. Zhang, "A Band-Notched Absorber Designed With High Notch-Band-Edge Selectivity," *IEEE Trans. Antennas Propag.*, vol. 65, no. 7, pp. 3560-3567, July 2017.

[71] Y. Han, L. Zhu, Y. Chang and B. Li, "Dual-Polarized Bandpass and Band-Notched Frequency-Selective Absorbers Under Multimode Resonance," *IEEE Trans. Antennas Propag.*, vol. 66, no. 12, pp. 7449-7454, Dec 2018.

[72] A. Sharma, S. Ghosh and K. V. Srivastava, "A Polarization-Insensitive Band-Notched Absorber for Radar Cross Section Reduction," *IEEE Antennas Wireless Propag. Lett.*, vol. 20, no. 2, pp. 259-263, Feb 2021.

[73] H. Huang and Z. Shen, "Low-RCS Reflectarray With Phase Controllable Absorptive Frequency-Selective Reflector," *IEEE Trans. Antennas Propag.*, vol. 67, no. 1, pp. 190-198, Jan 2019.

[74] B. Zhang, C. Jin and Z. Shen, "Absorptive Frequency-Selective Reflector Based on Bent Metallic Strip Embedded With Chip-Resistor," *IEEE Trans. Antennas Propag.*, vol. 68, no. 7, pp. 5736-5741, July 2020.

[75] B. Zhang, C. Jin, Q. Lv, J. Chen and Y. Tang, "Low-RCS and Wideband Reflectarray Antenna With High Radiation Efficiency," *IEEE Trans. Antennas Propag.*, vol. 69, no. 7, pp. 4212-4216, July 2021.

[76] F. Costa and A. Monorchio, "A frequency selective radome with wideband absorbing properties," *IEEE Trans. Antennas Propag.*, vol. 60, no. 6, pp. 2740–2747, Jun. 2012.

[77] W. Yu et al., "Dual-Polarized Band-Absorptive Frequency Selective Rasorber Using Meander-Line and Lumped Resistors," *IEEE Trans. Antennas Propag.*, vol. 67, no. 2, pp. 1318-1322, Feb. 2019.

[78] G. Q. Luo, W. Yu, Y. Yu, H. Jin, K. Fan, and F. Zhu, "Broadband dual polarized band-absorptive frequency-selective rasorber using absorptive Transmission/Reflection surface," *IEEE Trans. Antennas Propag.*, vol. 68, no. 12, pp. 7969–7977, Dec. 2020.

[79] Y. Yu, Z. Shen, T. Deng, and G. Luo, "3-D frequency-selective rasorber with wide upper absorption band," *IEEE Trans. Antennas Propag.*, vol. 65, no. 8, pp. 4363–4367, Aug. 2017.

[80] A. Motevasselian and B. L. G. Jonsson, "Design of a wideband rasorber with a polarisation-sensitive transparent window," *IET Microw. Antennas Propag.*, vol. 6, no. 7, pp. 747–755, 2012.

[81] Q. Chen, J. Bai, L. Chen, and Y. Fu, "A miniaturized absorptive frequency selective surface," *IEEE Antennas Wireless Propag. Lett.*, vol. 14, pp. 80–83, 2014.

[82] Q. Chen, L. Liu, L. Chen, J. Bai, and Y. Fu, "Absorptive frequency selective surface using parallel LC resonance," *Electron. Lett.*, vol. 52, no. 6, pp. 418–419, 2016.

[83] Z. Wang et al., "A High-Transmittance Frequency-Selective Rasorber Based on Dipole Arrays," *IEEE Access*, vol. 6, pp. 31367-31374, 2018.

[84] Q. Chen, D. Sang, M. Guo, and Y. Fu, "Miniaturized frequency-selective rasorber with a wide transmission band using circular spiral resonator," *IEEE Trans. Antennas Propag.*, vol. 67, no. 2, pp. 1045–1052, Feb. 2019.

[85] M. Guo, Z. Sun, D. Sang, X. Jia and Y. Fu, "Design of Frequency-Selective Rasorbers Based on Centrosymmetric Bended-Strip Resonator," *IEEE Access*, vol. 7, pp. 24964-24970, 2019.

[86] Z. Wang, J. Fu, Q. Zeng, M. Song and T. A. Denidni, "Wideband Transmissive Frequency-Selective Absorber," *IEEE Antennas Wireless Propag. Lett.*, vol. 18, no. 7, pp. 1443-1447, July 2019.

[87] Q. Chen, M. Guo, Z. Sun, D. Sang, and Y. Fu, "Polarization-independent frequency-selective rasorber with a broadened absorption band," *Int. J. Electron. Commun.*, vol. 96, pp. 178–183, 2018.

[88] Y. Han and L. Xu, "Dual-polarized frequency-selective absorber with wide transmission band," *Microw. Opt. Technol. Lett.*, vol. 62, no. 3, pp. 1270–1274, 2020.

[89] Q. Chen, L. Chen, J. Bai, and Y. Fu, "Design of absorptive frequency selective surface with good transmission at high frequency," *Electron. Lett.*, vol. 51, no. 12, pp. 885–886, 2015.

[90] K. Zhang, W. Jiang, and S. Gong, "Design bandpass frequency selective surface absorber using LC resonators," *IEEE Antennas Wireless Propag. Lett.*, vol. 16, pp. 2586–2589, 2017.

[91] M. Qu, S. Sun, L. Deng and S. Li, "Design of a Frequency-Selective Rasorber Based on Notch Structure," *IEEE Access*, vol. 7, pp. 3704-3711, 2019.

[92] J. Xia et al., “Design of a Wideband Absorption Frequency Selective Rasorber Based on Double Lossy Layers,” *IEEE Trans. Antennas Propag.*, vol. 68, no. 7, pp. 5718-5723, July 2020.

[93] H. Ye, W. Dai, X. Chen, H. Zhang, S. Bie and J. Jiang,“High-Selectivity Frequency-Selective Rasorber Based on Low-Profile Bandpass Filter,” *IEEE Antennas and Wireless Propag. Lett.*, vol. 20, no. 2, pp. 150-154, Feb. 2021.

[94] M. Guo, T. Guo, Q. Cheng, Y. Zheng and Y. Fu,“Frequency Selective Rasorber With Anisotropic Transmission Band,” *IEEE Antennas and Wireless Propag. Lett.*, vol. 20, no. 2, pp. 155-159, Feb. 2021.

[95] S. C. Bakshi, D. Mitra and F. L. Teixeira, “Wide-Angle Broadband Rasorber for Switchable and Conformal Application,” *IEEE Trans. Microw. Theory Techn.* , vol. 69, no. 2, pp. 1205-1216, Feb. 2021.

[96] H. Ye, J. Wei, L. Lin, F. Liu, L. Miao, S. Bie, and J. Jiang, “A frequency selective surface rasorber based on four functional layers,” *IEEE Trans. Antennas Propag.*, vol. 69, no. 5, pp. 2768–2778, May 2021.

[97] Q. Guo, J. Su, Z. Li, J. Song, and Y. Guan, “Miniaturized-element frequency-selective rasorber design using characteristic modes analysis,” *IEEE Trans. Antennas Propag.*, vol. 68, no. 9, pp. 6683–6694, Sep. 2020.

[98] Q. Chen, S. Yang, J. Bai and Y. Fu, ”Design of Absorptive/Transmissive Frequency-Selective Surface Based on Parallel Resonance,” *IEEE Trans. Antennas Propag.*, vol. 65, no. 9, pp. 4897-4902, Sept. 2017.

[99] A. Sharma, M. Saikia, S. Malik, S. Ghosh, and K. V. Srivastava, “A polarization insensitive broadband rasorber with in-band transmission response,” *Microw. Opt. Technol. Lett.*, vol. 62, no. 12, pp. 3668-3676, 2020.

[100] Q. Guo, Z. Li, J. Su, L. Y. Yang and J. Song, ”Dual-Polarization Absorptive/Transmissive Frequency Selective Surface Based on Tripole Elements,” *IEEE Antennas and Wireless Propag. Lett.*, vol. 18, no. 5, pp. 961-965, May 2019.

[101] A. Parameswaran, D. Kundu and H. S. Sonalikar, "A Dual-Polarized Wideband Frequency-Selective Rasorber With Low in-Band Insertion Loss and High Oblique Incidence Stability," *IEEE Trans. Electromagn. Compat.*, vol. 63, no. 6, pp. 1820-1828, Dec. 2021.

[102] Q. Yu et al., "Miniaturized Wide-Angle Rasorber With a Wide Interabsorption High Transparent Bandpass Based on Multiple 2.5-D Resonators," in *IEEE Antennas and Wireless Propag. Lett.*, vol. 21, no. 2, pp. 416-420, Feb. 2022.

[103] M. Guo et al., "Broadband Absorptive Frequency-Selective Rasorber Based on Multilayer Resistive Sheets Using Multilayer Resonator," *IEEE Trans. Antennas Propag.*, vol. 70, no. 3, pp. 2009-2022, March 2022.

[104] W. Wan et al., "Chiral Absorber-Based Frequency Selective Rasorber With Identical Filtering Characteristics for Distinct Polarizations," *IEEE Trans. Antennas Propag.*, vol. 70, no. 5, pp. 3506-3514, May 2022.

[105] Y. Shang, Z. Shen, and S. Xiao, "Frequency-selective rasorber based on square-loop and cross-dipole arrays," *IEEE Trans. Antennas Propag.*, vol. 62, no. 11, pp. 5581–5589, Nov. 2014.

[106] Y. Han, L. Zhu, Y. Chang, and B. Li, "Dual-polarized bandpass and band-notched frequency-selective absorbers under multimode resonance," *IEEE Trans. Antennas Propag.*, vol. 66, no. 12, pp. 7449–7454, Dec. 2018.

[107] X. Xiu, W. Che, W. Yang, Y. Han, and Q. Xue, "A highly selective rasorber based on second-order resonance," *IEEE Trans. Antennas Propag.*, vol. 19, no. 2, pp. 223–227, Feb. 2020.

[108] M. Guo, Q. Chen, Z. Sun, D. Sang and Y. Fu, "Design of Dual-Band Frequency-Selective Rasorber," *IEEE Antennas and Wireless Propag. Lett.*, vol. 18, no. 5, pp. 841-845, May 2019.

[109] X. Zhang, W. Wu, J. Huang, W. Zhang, Y. Ye and N. Yuan, "Dual-Polarized Frequency Selective Rasorber With Two Transmission Bands," *IEEE Access*, vol. 7, pp. 139795-139801, 2019.

[110] Y. Jia, A. Wu, Y. Liu, W. Zhang and Z. Zhou, "Dual-Polarization Frequency-Selective Rasorber With Independently Controlled Dual-Band Transmission Response," *IEEE Antennas and Wireless Propag. Lett.*, vol. 19, no. 5, pp. 831-835, May 2019.

[111] X. Xiu, W. Che, W. Yang, Y. Han, and Q. Xue, "Double-polarized dual passband absorptive frequency-selective transmission structure," *IEEE Trans. Electromagn. Compat.*, vol. 62, no. 5, pp. 1951–1960, Oct. 2020.

[112] S. Hu et al., "Backscattering cross section of ultrawideband antennas," *IEEE Antennas Wireless Propag Lett.*, vol. 6, pp. 70-73, 2007.

[113] W. Jiang, Y. Liu, S. Gong, and T. Hong, "Application of bionics in antenna radar cross section reduction," *IEEE Antennas Wireless Propag Lett.*, vol. 8, pp. 1275-1278, 2009.

[114] Y. B. Thakare et al., "Design of fractal patch antenna for size and radar cross-section reduction," *IET Microw., Antennas Propag.*, vol. 4, no. 2, pp. 175-181, 2010.

[115] W. Wang, S. Gong, X. Wang, Y. Guan, and W. Jiang, "Differential evolution algorithm and method of moments for the design of low-RCS antenna," *IEEE Antennas Wireless Propag Lett.*, vol. 9, pp. 295-298, 2010.

[116] Y. Liu and X. Zhao, "Perfect absorber metamaterial for deigning low RCS patch antenna," *IEEE Antennas Wireless Propag Lett.*, vol. 13, pp. 1473–1476, 2014.

[117] Y. Q. Li, H. Zhang, Y. Q. Fu, and N. C. Yuan, "RCS reduction of ridged waveguide slot antenna array using EBG radar absorbing material," *IEEE Antennas Wireless Propag Lett.*, vol. 7, pp. 473–476, 2008.

[118] T. Liu, X. Cao, J. Gao, Q. Zheng, W. Li, and H. Yang, "RCS reduction of waveguide slot antenna with metamaterial absorber," *IEEE Trans. Antennas Propag.*, vol. 61, no. 3, pp. 1479–1484, 2013.

[119] D. Xie, X. Liu, H. Guo, X. Yang, C. Liu, and L. Zhu, "A wideband absorber with a multiresonant gridded-square FSS for antenna RCS reduction," *IEEE Antennas Wireless Propag Lett.*, vol. 16, pp. 629–632, 2017.

[120] H. B. Baskey, E. Johari, and M. J. Akhtar, "Metamaterial structure integrated with a dielectric absorber for wideband reduction of antennas radar cross section," *IEEE Trans. Electromagn. Compat.*, vol. 59, no. 4, pp. 1060–1069, Aug. 2017.

[121] Y. Li, K. Zheng, L. Yang, and L. Du, "Wide-band radar cross-section reduction for antenna using frequency selective absorber," *Electron. Lett.*, vol. 52, no. 21, pp. 1809–1811, Oct. 2016.

[122] Y. Liu, K. Li, Y. Jia, Y. Hao, S. Gong, and Y. J. Guo, "Wideband RCS reduction of a slot array antenna using polarization conversion metasurfaces," *IEEE Trans. Antennas Propag.*, vol. 64, no. 1, pp. 326–331, Jan. 2016.

[123] Y. Liu, Y. Hao, K. Li, and S. Gong, "Wideband and polarization independent radar cross section reduction using holographic metasurface," *IEEE Antennas Wireless Propag. Lett.*, vol. 15, pp. 1028–1031, 2016.

[124] Y. Liu, Y. Hao, K. Li, and S. Gong, "Radar cross section reduction of a microstrip antenna based on polarization conversion metamaterial," *IEEE Antennas Wireless Propag. Lett.*, vol. 15, pp. 80–83, 2016.

[125] Y. Zheng, J. Gao, X. Cao, Z. Yuan, and H. Yang, "Wideband RCS reduction of a microstrip antenna using artificial magnetic conductor structures," *IEEE Antennas Wireless Propag. Lett.*, vol. 14, pp. 1582–1585, 2015.

[126] Y. Zhao, X.-Y. Cao, J. Gao, and W.-Q. Li, "Broadband RCS reduction and high gain waveguide slot antenna with orthogonal array of polarisation-dependent AMC," *Electron. Lett.*, vol. 49, no. 21, pp. 1312–1313, Oct. 2013.

[127] P. Mei, X. Q. Lin, J. W. Yu, P. C. Zhang and A. Boukarkar, "A Low Radar Cross Section and Low Profile Antenna Co-Designed With Absorbent Frequency Selective Radome," *IEEE Trans. Antennas Propag.*, vol. 66, no. 1, pp. 409-413, Jan. 2018.

[128] P. Mei, X. Q. Lin, J. W. Yu, A. Boukarkar, P. C. Zhang and Z. Q. Yang, "Development of a Low Radar Cross Section Antenna With Band-Notched Absorber," *IEEE Trans. Antennas Propag.*, vol. 66, no. 2, pp. 582-589, Feb 2018.

[129] H. Huang, Z. Shen and A. A. Omar, "3-D Absorptive Frequency Selective Reflector for Antenna Radar Cross Section Reduction," *IEEE Trans. Antennas Propag.*, vol. 65, no. 11, pp. 5908-5917, Nov. 2017.

[130] Q. Chen, M. Guo, D. Sang, Z. Sun and Y. Fu, "RCS Reduction of Patch Array Antenna Using Anisotropic Resistive Metasurface," *IEEE Antennas and Wireless Propag. Lett.*, vol. 18, no. 6, pp. 1223-1227, June 2019.

[131] Y. Han, L. Zhu, Y. Bo, W. Che and B. Li, "Novel Low-RCS Circularly Polarized Antenna Arrays via Frequency-Selective Absorber," *IEEE Trans. Antennas Propag.*, vol. 68, no. 1, pp. 287-296, Jan. 2020.

[132] Y. Liu, Y. Jia, W. Zhang and F. Li, "Wideband RCS Reduction of a Slot Array Antenna Using a Hybrid Metasurface," *IEEE Trans. Antennas Propag.*, vol. 68, no. 5, pp. 3644-3652, May 2020.

[133] W. Yu, Y. Yu, W. Wang, X. H. Zhang and G. Q. Luo, "Low-RCS and Gain-Enhanced Antenna Using Absorptive/Transmissive Frequency Selective Structure," *IEEE Trans. Antennas Propag.*, vol. 69, no. 11, pp. 7912-7917, Nov. 2021.

[134] B. Zhang, L. Li, C. Jin, Q. Lv and R. Mittra, "Wideband Low RCS Antenna Based on Hybrid Absorptive-Diffusive Frequency Selective Reflector," *IEEE Access*, vol. 9, pp. 77863-77872, June 2021.

[135] Y. Yu, W. Yu, G. Xie, J. Tong and G. Q. Luo, "Wideband RCS Reduction of Slot Array Antenna Utilizing 3-D Absorptive Frequency-Selective Structure," *IEEE Antennas Wireless Propag. Lett.*, vol. 21, no. 1, pp. 64-68, Jan 2022.

[136] K. Zhang, R. Tan, Z. H. Jiang, Y. Huang, L. Tang and W. Hong, "A Compact, Ultra-Wideband Dual-Polarized Vivaldi Antenna with Radar Cross Section Reduction," *IEEE Antennas Wireless Propag. Lett.*, Early Access.

[137] S. Ghosh and K. V. Srivastava, “An Equivalent Circuit Model of FSS-Based Metamaterial Absorber Using Coupled Line Theory,” *IEEE Antennas Wireless Propag. Lett.*, vol. 14, pp. 511-514, 2015.

[138] Ben A. Munk, “On Radar Cross Section of Antennas in General,” *Finite Antenna Arrays and FSS, Wiley-IEEE Press* , pp. 15-55, 2003.

[139] P. Alitalo, A. E. Culhaoglu, A. V. Osipov et al., “Experimental Characterization of a Broadband Transmission-Line Cloak in Free Space,” *IEEE Trans. Antennas Propag.*, vol. 60, no. 10, pp. 4963-4968, Oct. 2012.

[140] K. Saurav, D. Sarkar and K. V. Srivastava, “CRLH Unit-Cell Loaded Multiband Printed Dipole Antenna,” *IEEE Antennas Wireless Propag. Lett.*, vol. 13, pp. 852-855, April 2014.

List of publications

Journals

1. **M. M. Zargar**, A. Rajput, K. Saurav and S. K. Koul, "Polarisation insensitive dual-band transmissive rasorber designed on a single layer substrate," ***IET Microwaves, Antennas Propagation***, vol. 14, no. 11, pp. 1296-1303, Sept. 2020, doi: 10.1049/iet-map.2020.0283.

2. **M. M. Zargar**, A. Rajput, K. Saurav and S. K. Koul, "Polarization-insensitive frequency selective rasorber with higher transmission band using modified double cross slot based bandpass layer," ***Wiley International Journal of RF and Microwave Computer-Aided Engineering***, vol. 31, no. 8, e22733, 2021, doi: 10.1002/mmce.22733

3. **M. M. Zargar**, A. Rajput, K. Saurav and S. K. Koul, "Polarization-insensitive frequency selective rasorber with broad absorption band and two-sided transmission bands," ***Wiley International Journal of RF and Microwave Computer-Aided Engineering***, vol. 32, no. 4, e23067, 2022, 10.1002/mmce.23067.

4. **M. M. Zargar**, A. Rajput, K. Saurav and S. K. Koul, "Single-Layered Flexible Dual Transmissive Rasorbers With Dual/Triple Absorption Bands for Conformal Applications," ***IEEE Access***, vol. 9, pp. 150426-150442, 2021, doi: 10.1109/ACCESS.2021.3126197.

5. **M. M. Zargar**, A. Rajput, K. Saurav and S. K. Koul, "Frequency-Selective Rasorber Based on High-Q Minkowski Fractal-Shaped Resonator for Realizing a Low Radar Cross-Section Radiating System," ***IEEE Transactions on Electromagnetic Compatibility***, vol. 64, no. 5, pp. 1574-1584, 2022. doi: 10.1109/ TEMC.2022.3179514.

6. **M. M. Zargar**, A. Rajput, K. Saurav and S. K. Koul, “Low RCS Dual-Polarized Crossed Dipole Antenna Co-Designed with Absorptive Frequency-Selective Reflection Structure,” ***IEEE Access***, Early Access 2022. doi: 10.1109/ACCESS.2022.3220672.

Conferences

1. **M. M. Zargar**, A. Rajput, K. Saurav and S. K. Koul, “A Polarization-Insensitive Frequency Selective Surface Based Rasorber with Narrow-Band Absorption Between Two Transmission Bands,” ***2020 50th European Microwave Conference (EuMC)***, Utrecht, Netherland, 2021, pp. 503-505, doi: 10.23919/EuMC48046.2021.9338010.

2. **M. M. Zargar**, A. Rajput, K. Saurav and S. K. Koul, ”Low Radar Cross Section Dipole Antenna Integrated with Absorptive Frequency Selective Reflection Structure,” ***2022 16th European Conference on Antennas and Propagation (EuCAP)***, Madrid, Spain, 2022, pp. 1-4, doi: 10.23919/EuCAP53622.2022.9769385.

3. **M. M. Zargar**, A. Rajput, K. Saurav and S. K. Koul, ”Dual Transmissive Frequency Selective Rasorber Designed Using Minkowski Fractal Shaped Resonator,” Accepted for Presentation in ***IEEE Microwave, Antennas and Propagation Conference-2022***, December 2022, Banglore, India.

About the Author

Mehran Manzoor Zargar was born in Srinagar, Jammu and Kashmir, India in October 1990. He has received the Bachelor of Technology (B.Tech.) degree in Electronics and Communication Engineering from *Department of Electronics and Instrumentation Technology, University of Kashmir* in 2014. He has completed the Master of Technology (M.Tech.) degree in Microelectronics from *National Institute of Technology Srinagar* in 2018. He has joined the Doctor of Philosophy (Ph.D.) program in the *Department of Electrical Engineering, Indian Institute of Technology Jammu* in December 2018. He has done his Pre-Ph.D. course work at *Indian Institute of Technology Delhi* from December 2018 to May 2019. His current research interest includes Frequency Selective Rasorbers for RCS reduction.